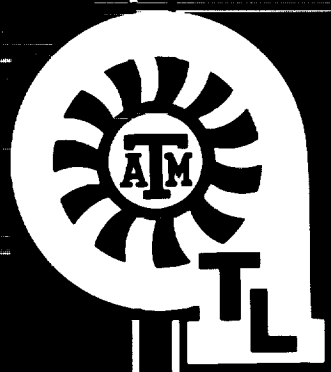

September 1993
NASA MSFC Contract No. NAS8-37821
Technical Monitor: James Cannon

**FINAL REPORT**

# A FINITE-ELEMENT-BASED PERTURBATION MODEL FOR THE ROTORDYNAMIC ANALYSIS OF SHROUDED PUMP IMPELLERS :

## PART 1: MODEL DEVELOPMENT AND APPLICATIONS

Erian A. Baskharone
Principal Investigator
Department of Mechanical Engineering
Texas A&M University

Turbomachinery Laboratory

September 1993

NASA MSFC Contract No. NAS8-37821

Technical Monitor: James Cannon

FINAL REPORT

# A FINITE-ELEMENT-BASED PERTURBATION MODEL FOR THE ROTORDYNAMIC ANALYSIS OF SHROUDED PUMP IMPELLERS :

## PART 1: MODEL DEVELOPMENT AND APPLICATIONS

Erian A. Baskharone

Principal Investigator

Department of Mechanical Engineering

Texas A&M University

## TABLE OF CONTENTS

## SUMMARY

This study concerns the rotordynamic characteristics of fluid–encompassed rotors, with special emphasis on shrouded pump impellers. The core of the study is a versatile and categorically new finite–element–based perturbation model, which is based on a rigorous flow analysis and what we have generically termed the "virtually" deformable finite–element approach. The model is first applied to the case of a smooth annular seal for verification purposes. The rotor excitation components, in this sample problem, give rise a purely cylindrical, purely conical and a simultaneous cylindrical/conical rotor whirl around the housing centerline. In all cases, the computed results are compared to existing experimental and analytical data involving the same seal geometry and operating conditions. Next, two labyrinth–seal configurations, which share the same tooth–to–tooth chamber geometry but differ in the total number of chambers, were investigated. The results, in this case, are compared to experimental measurements. for both seal configurations. The focus is finally shifted to the shrouded–impeller problem, where the stability effects of the leakage flow in the shroud–to–housing secondary passage are investigated. To this end, the computational model is applied to a typical shrouded–impeller pump stage, fabricated and rotordynamically tested by Sulzer Bros., and the results compared to to those of a simplified "bulk–flow" analysis and Sulzer Bros.' test data. In addition to assessing the computed rotordynamic coefficients, the shrouded–impeller study also covers a controversial topic; namely that of the leakage–passage inlet swirl, which was previously cited as the origin of highly unconventional (resonance–like) trends of the fluid–exerted forces. In order to validate this claim, a "microscopic" study of the fluid/shroud interaction mechanism is conducted, with the focus being on the structure of the perturbed flow field associated with the impeller whirl. The conclusions of this study were solidified by the outcome of a numerical–certainty exercise, where the grid dependency of the numerical results is objectively examined. The final phase of the shrouded–impeller investigation involves the validation of a built–in assumption, in all other perturbation models, whereby single–harmonic tangential distributions of all the flow thermophysical properties are imposed. Grid dependency of the fluid–induced The last phase of the investigation course is aimed at verifying the fine details of the perturbed flow field in light of recent set of detailed LDA measurements in a smooth annular seal. Grid dependency of the fluid–induced forces is also investigated, and specific recommendations made.

## OVERVIEW AND REPORT STRUCTURE

This report presents the development, verification, and applications of a categorically unprecedented perturbation approach to the rotordynamic problem arising from the fluid/rotor interaction in turbomachinery applications. This is a finite–element–based approach, which is based on the perception that the fluid reaction forces developed in the rotor–to–housing gap as a result of the rotor whirl, arise from infinitesimally small deformations of the finite elements in this gap. Although the research tasks were all focused on the rotordynamic characteristics of shrouded impellers (Fig. 1a), the problem formulation is sufficiently general to embrace other conceptually similar problems, all belonging to the isolated–seal category.

Since many aspects of the current study have already been published, or submitted for publication, and for the sake of compactness, the reader is referred to the manuscript of a specific paper, in one of the two appendices, each time reference is made to the subject of this paper. These two appendices contain already published journal articles, and those which are currently under review, respectively. Once the reader is referred to one of these papers, only the relevant contents of the paper are recited in the core of the report, should that serve the purpose of clarity. The appendices, in this sense, are hardly peripheral, but constitute an equally essential segments of the text.

Among the segments which were overridden in the report core is that concerning the mathematical development of the "virtually" deformable finite–element–based perturbation model. This tedious and predominantly mathematical subject is presented in the subsection "Paper# 1" of Appendix 1 for the reader who might be interested in the mathematical foundation of the model, and the finite–element formulation of the general problem of fluid/rotor interaction. Other papers of the appendices involve exhaustive discussions of certain applications of the model, and as such, may distract the user from the main application focus, being that of shrouded impellers, had they been included in the report core. Of these, Paper# 2 concerns the model application to the case of a smooth annular seal with a cylindrically whirling rotor, and confirms the traditional assumption of a single–harmonic variation of the shroud pressure perturbation around the circumference. This assumption is indicative of a set of restrictions that has been (almost blindly) common among all of the existing models in this engineering discipline, regardless of the physics of the problem (the reader is alerted to the implied fact here, that such an assumption is not made in the current computational model). Next, Paper# 3, in the same appendix, expands the model to the unstable seal operation mode involving a conical rotor whirl, again in a smooth annular seal. The two degrees–of–freedom of the rotor axis, meaning the linear and angular displacements, are then lumped together and applied to the same seal configuration. The resulting cylindrical and conical whirl components of the rotor axis were analyzed as occurring simultaneously, and the results appraised in Paper# 4 of Appendix 1. The last paper (# 5) in this appendix marks the beginning of the process where the unstable operation of a shrouded pump impeller is investigated. This paper presents the highly irregular features of the unperturbed (zeroth–order) flow fields in two typical leakage–passage configurations, with two, conventional wear–ring and face, seals

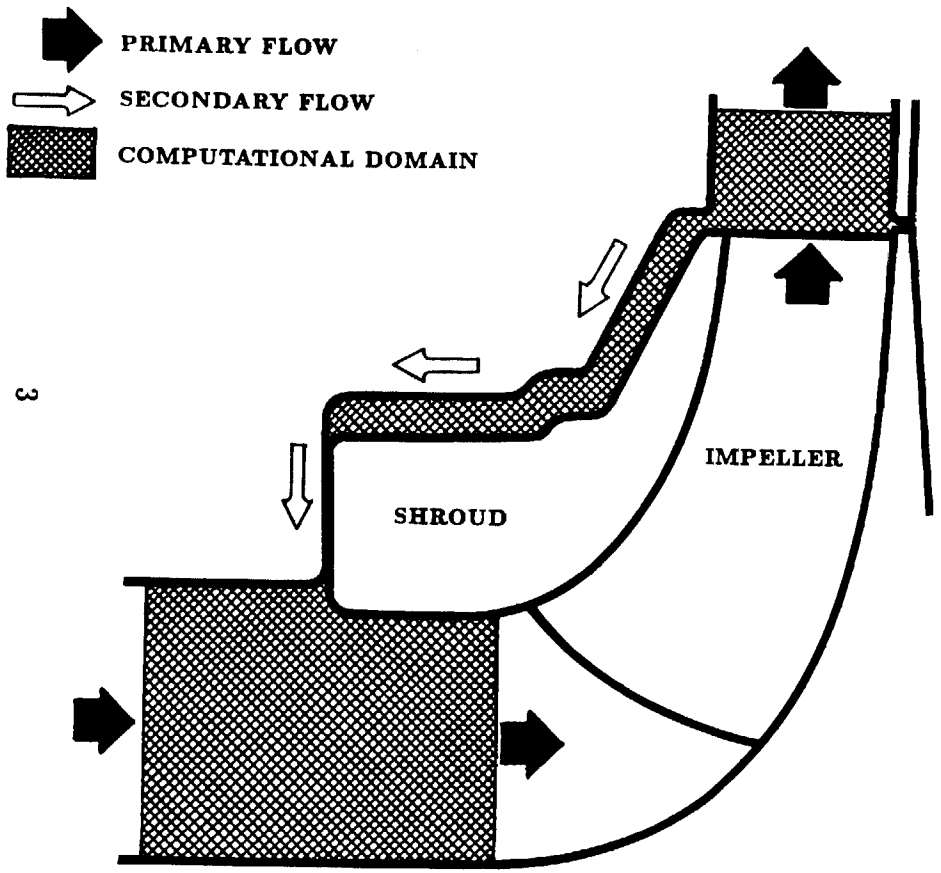


a) PUMP GEOMETRY

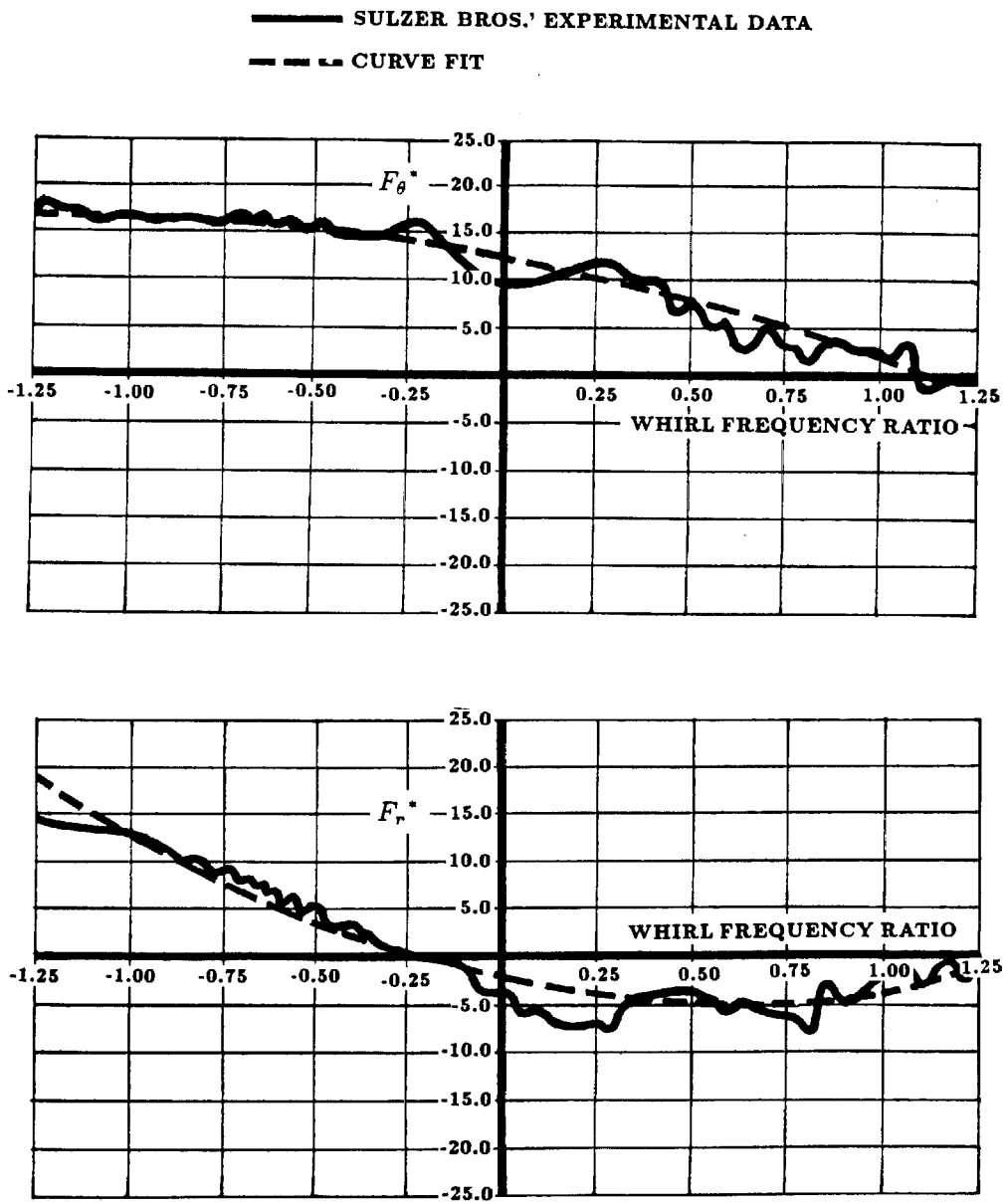


b) EXPERIMENTAL DATA

**Fig. 1 Rotordynamic force measurements in the Sulzer Bros. face–seal pump configuration**

comprising the passage tight-clearance regions. A comprehensive comparison between the leakage (or secondary) flow fields, associated with these seal categories, is made in this paper, with a special emphasis on rotordynamics-related aspects such as the leakage-passage inlet swirl angle.

Appendix 2 in this report contains three recent papers which are currently at different phases of the review process for publication. The first of these papers is a natural continuation of Paper# 4 in Appendix 1. This paper contains the rotordynamic coefficients associated with one of the two seal configurations mentioned above, namely the face-seal configuration. The paper also contains a comparison between the computed coefficients versus a bulk-flow solution (Childs, 1989) and the experimental data of Sulzer Bros. (Bolleter et al., 1989). Next, the current perturbation approach is applied to the category of labyrinth seals, where the basic issue of the tooth-to-tooth chamber count impact on the seal stability is investigated. The last paper (# 3) in Appendix 2 makes use of recent LDA measurements, by Morrison et al. (1992), in assessing the computed perturbations of the flow-velocity components throughout an annular seal with a cylindrically whirling rotor. The paper shows that there indeed is a notable agreement between the two sets of results in the downstream seal segment, and that the most observable agreement is progressively attained as the seal-discharge station is approached. This, as stated in the paper, is a comprehendable finding, in the sense that this downstream segment of the seal is where the real admission effects, in the actual rig, have diminished, allowing a one-to-one comparison of the computed and measured sets of data.

The core segment of this report addresses a certain critical issue, all related to the major application of the current computational model, namely that of the shrouded pump impeller. The issue here was raised by Childs (1989), who that an inlet swirl ratio (leakage-passage inlet swirl component/impeller tip speed) that is above 0.5 is sure to produce abrupt fluctuations in the fluid reaction forces in a narrow range of positive whirl ratios. Childs' conclusions were based on a simplified bulk-flow analysis, and perhaps are limited to the Sulzer Bros.' pump impeller. Since such fluctuations would greatly influence the impeller rotordynamic coefficients, as well as prohibit the use of a simple quadratic interpolation of the fluid-exerted force components, at least in the disputed whirl frequency range, a thorough investigation of this phenomenon was warranted. Lack of conclusiveness, meanwhile, was caused by Guinzburg's experimental results (1992) which dismissed Childs' observation. Although Guinzburg's rig design did not allow, or even simulate, any primary flow effects, the categorical denial of this "resonance-like" phenomenon was, at least, surprising. Seriousness of this issue was further established, when a careful review of Sulzer Bros.' experimental measurements revealed that the fluid-forces versus whirl-frequency indeed exhibit some fluctuations (Fig. 1b), although the latter were much milder by comparison. Vagueness of the entire issue was later concluded, as the preliminary results of the current perturbation model came to support the existence of such force fluctuations, with the exception that the severity of these fluctuations was closer to those of Sulzer Bros. than they were to Childs' force trends. A full-scale investigation of the issue was then conducted. It is exclusively this investigation which is emphasized in the core segment of this report.

Investigation of the fluid–exerted forces in the Sulzer Bros.' pump case involved several potentially–contributing factors concerning the current model as well as the bulk–flow model. These factors were as follows:

1. Grid dependency of the fluid–exerted forces in our analysis (Fig. 2).

2. The manner in which the shroud pressure perturbations are altered during the transition from negative (backward) to positive (forward) whirl.

3. Effect of the leakage passage inlet swirl velocity on our computed forces.

4. Validity of the bulk–flow–model assumption that the perturbations of the flow properties (particularly the shroud pressure) are expressible via a single harmonic in the circumferential direction.

The last section of the report–core segment concerns proposed research tasks which are aimed at continuing the code validation process, on one hand, and expanding the current perturbation model towards either more prediction accuracy or new applications, on the other. One of the proposed topics is a bench–mark test case, and involves numerical simulation of the Cal. Tech. test rig (Guinzburg, 1992). This rig was designed with the intention of testing the rotordynamic consequences of the isolated leakage passage. The passage inlet swirl in this case was varied from -200% to +200% of the rotor tip speed, and no indication of force fluctuation was observed throughout the entire inlet swirl range.

Also proposed is another related study, which has to do with the flow domain with which the shroud interacts. As seen in Fig. 1a, we have so far simulated the primary/leakage flow interaction at the impeller inlet and discharge stations. This is obviously an upgrade to the common approach where the leakage passage is totally isolated, and fictitiously uniform boundary conditions are specified at both ends. Nevertheless, we believe that a much more realistic model of the fluid/shroud interaction can be attained by physically including the impeller primary passage as part of the computational domain. In this case, contributions to the shroud forces will (as they should) be produced in both flow passages. Implementation of this upgrade will undoubtedly improve the accuracy of the computed rotordynamic coefficients.

A major expansion of our perturbation model is that concerning the hydrostatic bearing rotordynamics problem. Numerical models which were developed over the past three years were generally based on the bulk–flow theory in which inertia domination (at the recess edges and in the film land) were simulated through simple one–dimensional means, and the flow turbulence was recognized only at the walls. These models, more or less, uncoupled the recess and film–land contributions to the journal forces and, consequently, treated the fluid/journal interaction problem in a steady–state sense. Our approach, on the other hand, is that of repeatedly marching in time through a circumferential "pitch" between two successive recesses, and computing the instantaneous fluid–exerted forces during the process until until convergence (in terms of a fixed cyclic force pattern) is achieved. Moreover, contrary to the existing models, where no journal–to–housing flow gradients

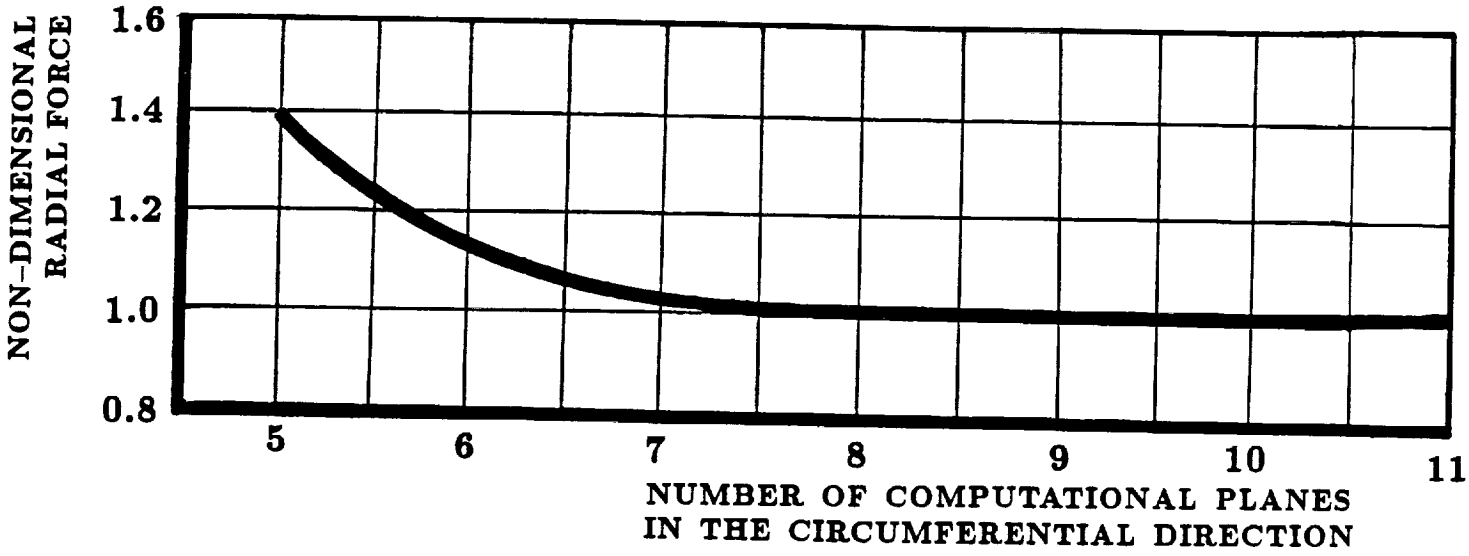


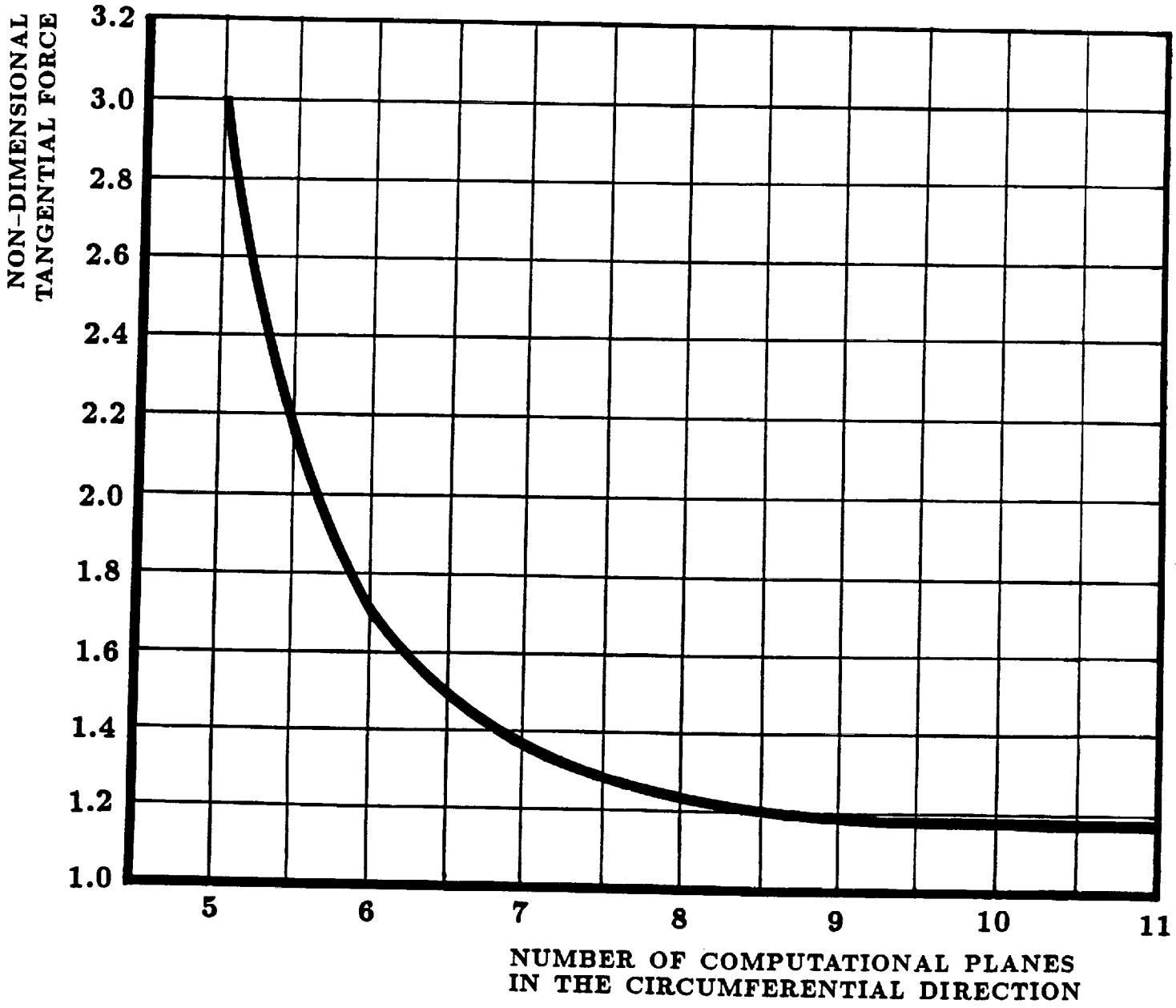


**Fig. 2 Dependency of the fluid–exerted forces on the grid resolution in the circumferential direction**

are taken into account, the proposed model is based on the fully three–dimensional flow–governing equations, coupled with a provenly accurate combination of turbulence closure and near–wall flow analysis.

## COMPUTATIONAL PROCEDURE

Analysis of the fluid/shroud interaction within a pump stage, is based on what we interimly termed the "virtually" deformable finite–element concept (Baskharone and Hensel, 1991).Under this approach, perturbations in the fluid thermophysical properties including, in particular, the shroud pressure are perceived as a direct result of varied distortions in the finite element assembly occupying the shroud–to–housing gap as the impeller undergoes a whirling motion.

The computational process is initialized by solving the centered–impeller flow field throughout the computational domain shown in Fig. 3. This "zeroth–order" flow solution is then used as input to the perturbation model. This step physically corresponds to the point when the impeller whirl (defined by a virtual impeller eccentricity $\epsilon$ and a finite whirl frequency $\Omega$) is recognized (Fig. 4). This is also when the computational domain becomes totally three–dimensional due to the impeller eccentricity. The finite–element discretization unit, in this case, is the twenty–noded curve–sided isoparametric element shown in Fig. 5, with the frame of reference being attached to the impeller and whirling with it (Fig. 6) in order to eliminate the time–dependency of the shroud–to–housing flow field. Expansion of the finite–element equations (on an element–by–element basis) in terms of the nodal values of displacement, eventually gives rise (once assembled into the global system) to an equivalent set of equations the unknowns in which are $[\partial P_i/\partial\epsilon,\ i = 1,2,...,N]$, where $p_i$ is a general flow property (e.g velocity component or pressure) at the computational node "i". Of these, the shroud pressure perturbations are extracted and integrated over the entire shroud surface, giving rise to the rate (with respect to $\epsilon$) at which the fluid forces on the shroud are developed. These forces are, in the end, used to compute the direct and cross–coupled stiffness, damping and inertia (added mass) coefficients of the fluid/shroud interaction.

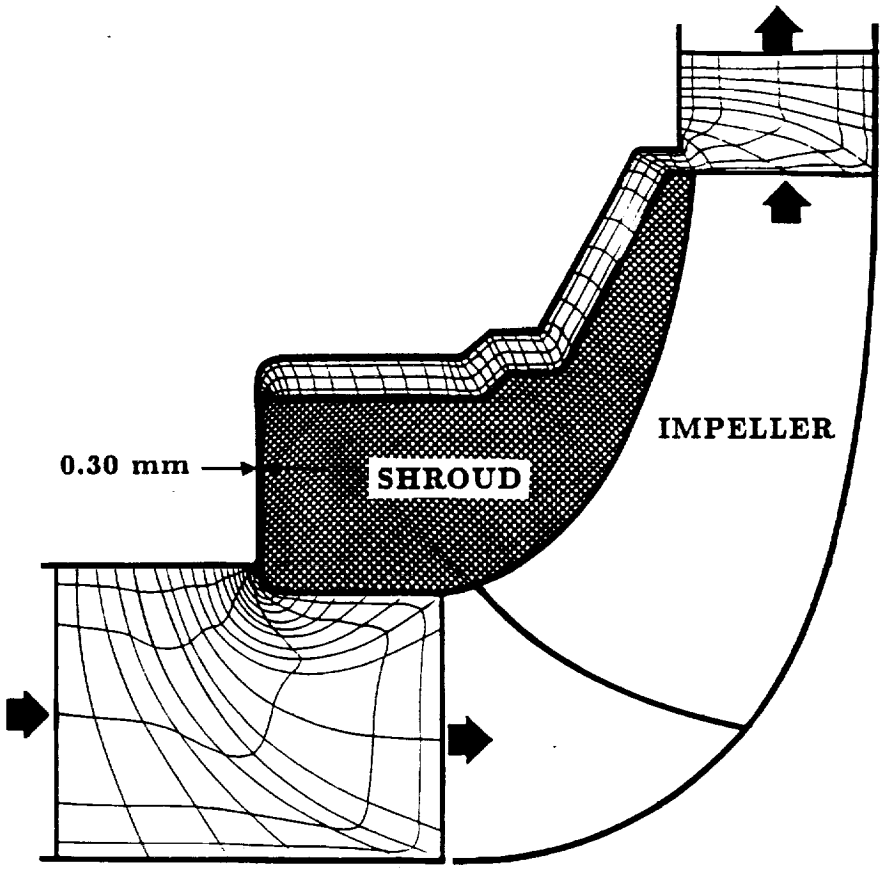


**Fig. 3 Finite–element discretization model for the centered–impeller operation mode**

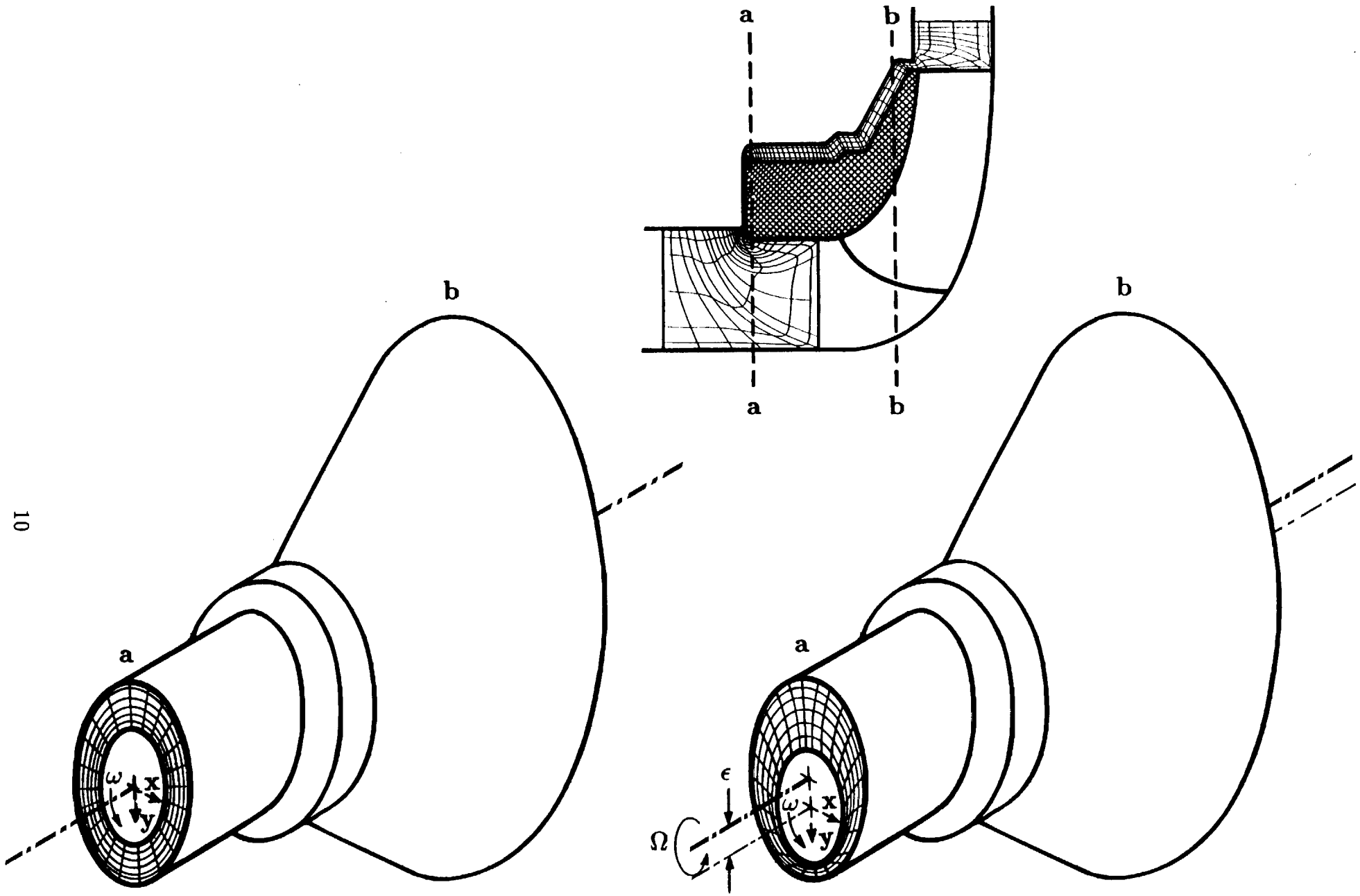


CENTERED–IMPELLER OPERATION MODE

WHIRLING–IMPELLER OPERATION MODE

**Fig. 4 Distortion of the shroud–to–housing finite element assembly due to the impeller whirl**

- VELOCITY IS A DEGREE OF FREEDOM
- VELOCITY AND PRESSURE ARE DEGREES OF FREEDOM

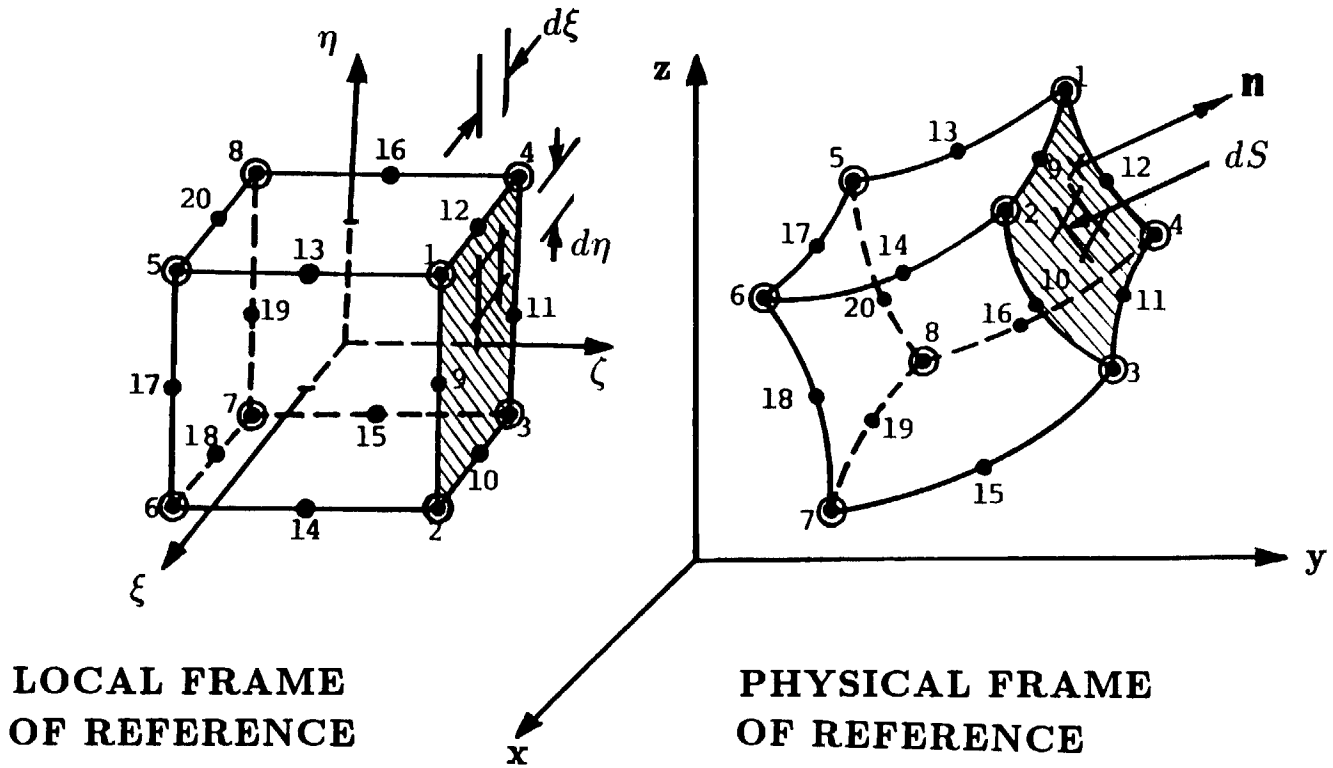


Fig. 5 Quadrilateral curve–sided isoparametric finite element for analyzing the perturbed flow field

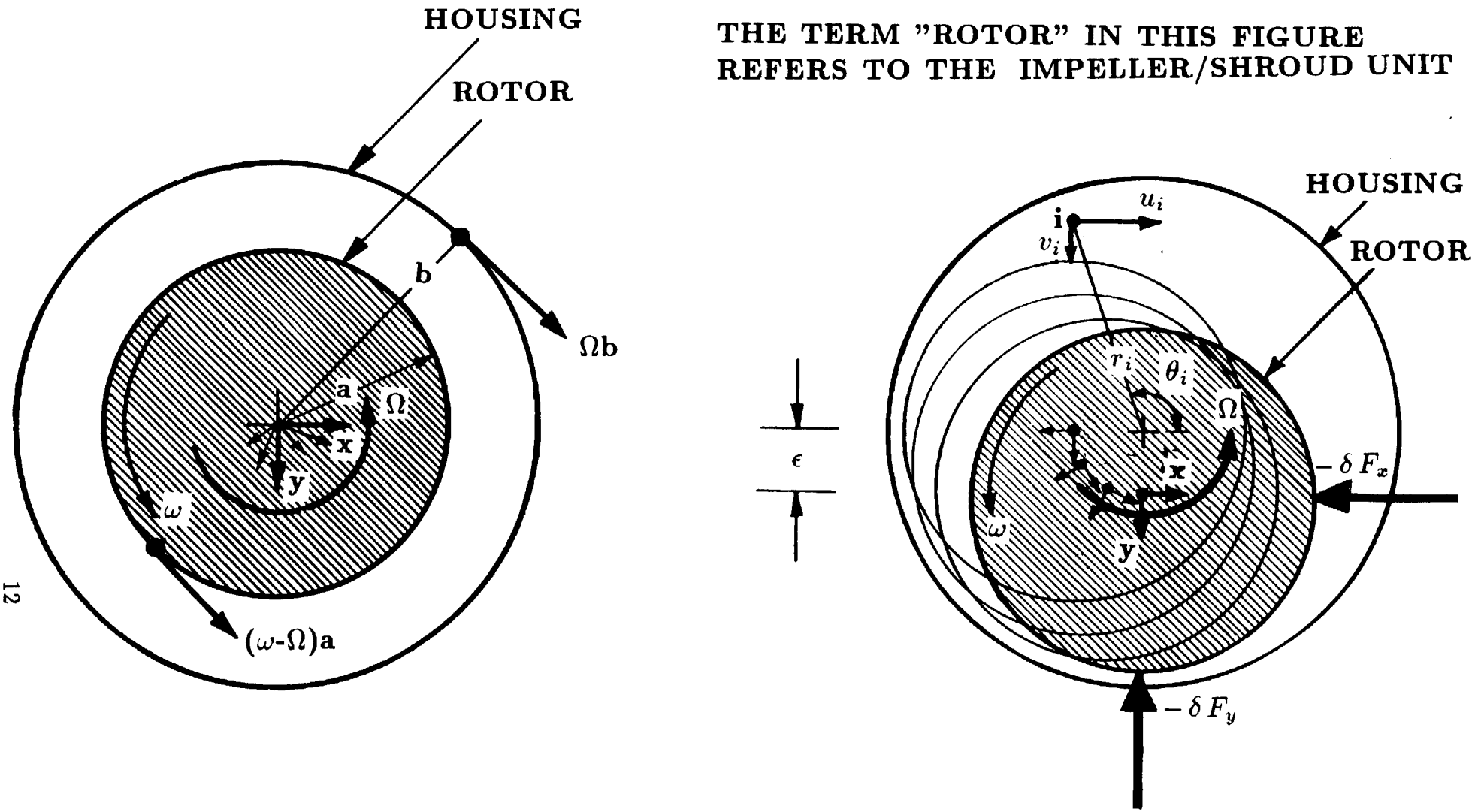


a. CENTERED ROTOR

b. ECCENTRIC ROTOR

Fig. 6 Lateral motion of the coordinate axes as a result of the rotor whirl

## UNIQUENESS AND IMPACT OF THE NEW APPROACH

Judging by the initial impression of a typical discusser (e.g. a paper reviewer, a conference attendee,...etc), the very foundation of the current perturbation model can easily be misconceived. For instance, referring to the use of the finite–element method (in conjunction with the model) as a means of solving the "perturbed flow field" or solving "the perturbation equations" is misleading and totally wrong, respectively. The fact (by reference to Paper# 1 in Appendix 1) is that the perturbed–field equations themselves arise from physical displacements, velocities and acceleration components which are viewd from a moving (rotating and translating) frame of reference, as a result of the rotor whirl (Fig. 6). These are carefully superimposed on the unperturbed flow field, giving rise to a new system (governing equations and boundary conditions) under which the fluid response is totally unrestricted. When this approach is compared to existing perturbation models (where the circumferential variation of the fluid response is externally imposed as a single harmonic), the question becomes: "what if the flow physics do not naturally lend themselves to such pre–specifed response", or, "what if the circumferential variation of the clearance width (itself) is not a single harmonic (such as the case of a tagentially–deformed shroud or a hydrostatic bearing)".

The process of "adding" whirl–related terms to the unperturbed flow field (above) involves all of the flow kinematical properties, with the common factor being the rotor eccentricity "$\epsilon$". For instance, the added displacements are those of the nodal points (relative to an observer at the origin of the whirling frame of reference, Fig. 4), the added velocity components are, for instance, those of a node on the housing surface (since the housing is non–stationary in this frame of reference, and the added acceleration components are those of the Coriolis and Centriputal types, and appear as a result of the origin motion, since the latter is attached to the rotor (Fig. 4).

The problem formulation (above) is hardly a mere mathematical alteration of existing perturbation models. The critical issue here is "whether one should define the rotor eccentric motion and the fluid response to it." To the author, the answer is "not always, unless the problem is the simplest possible (e.g. the case of a straight annular seal)." In fact, such a pre–imposed response (namely that of the single–harmonic type) is proven (later in this report) to produce an error that is as high as 21% within regions in the leakage path of a pump, where such an assumption is inconsistent with the local flow physics.

In view of the above, a traditional question calling for a comparison between the finite–element technique and other methods, is perhaps less relevant to this study than the asker might think.

## RESULTS AND DISCUSSION

### Origin of the Rotordynamic Force Fluctuations:

The study outlined in Appendix 1, Paper# 4 concerns the centered–impeller flow field in the Sulzer Bros. face–seal pump configuration, and compares it to a twin pump geometry where the leakage–control device is of the conventional wear–ring type. Of particular interest in this paper is the swirl velocity distribution in the secondary–flow passage leading to the seal (Figs.6 & 9 of the Appendix). Comparison of the seal–inlet swirl velocity ratios, in both pump configurations, with those of Childs (1989), revealed one possible reason why the shroud forces in Childs' study had the nearly resonance–type trends. The reason, we believe, is that the seal–inlet swirl velocity (obtained through simplified matching means in Childs' analysis) was approximately double our computed values. Note that this swirl ratio in our analysis is an internal variable that is totally unrestricted.

Fig. 2 contains our rotordynamic results for the face–seal pump configuration using the centered–impeller flow solution, mentioned above, as input. The results in this Figure was particularly revealing to us. The reason is that initially–obtained shroud forces were the outcome of a finite–element model with only seven computational planes in the circumferential direction. This, by reference to the Figure, is much less than the number required for grid independency.

### Effect of the Leakage–passage Inlet Swirl

A test case, involving a modified version of Sulzer Bros.' face–seal pump configuration (Fig. 3), was investigated. The intention here was to investigate the effect of the leakage–passage inlet swirl on the impeller rotordynamic characteristics. In this case, the inlet swirl was totally destryed, a situation that is physically achievable by inserting a swirl brake at the leakage–passage inlet station, or through the use of a cascade of deswirl vanes in the primary passage downstream from the impeller (Fig. 7).

Results of the centered–impeller flow analysis, in the absence of leakage–passage inlet swirl, are shown in Figs. 8,9 &10. These are vector and contour plots of the velocity and pressure fields. The plots in this Figure were then compared to their counterparts in Appendix 1, Paper# 4, with the latter corresponding to the design–point value of the leakage–passage inlet swirl (Figs. 8,9 &10 in Appendix 1, Paper# 4). The conclusion was that "killing" the inlet swirl had no appreciable effect on the meridional velocity vectors throughout the leakage passage. This was, to some extent, anticipated since the recirculatory motion in this passage is primarily controlled by two other factors; namely the fluid migration radially outwards (near the shroud) as a result of the centrifugal force, and inwards (near the housing) due to the streamwise static pressure differential. However, the swirl–velocity/tip–speed ratio shown in Fig. 9 seems to remain much smaller throughout the leakage passage by comparison. This, to us, was the most significant difference between the two sets of results, and was regarded as a sufficient reason to expect significant

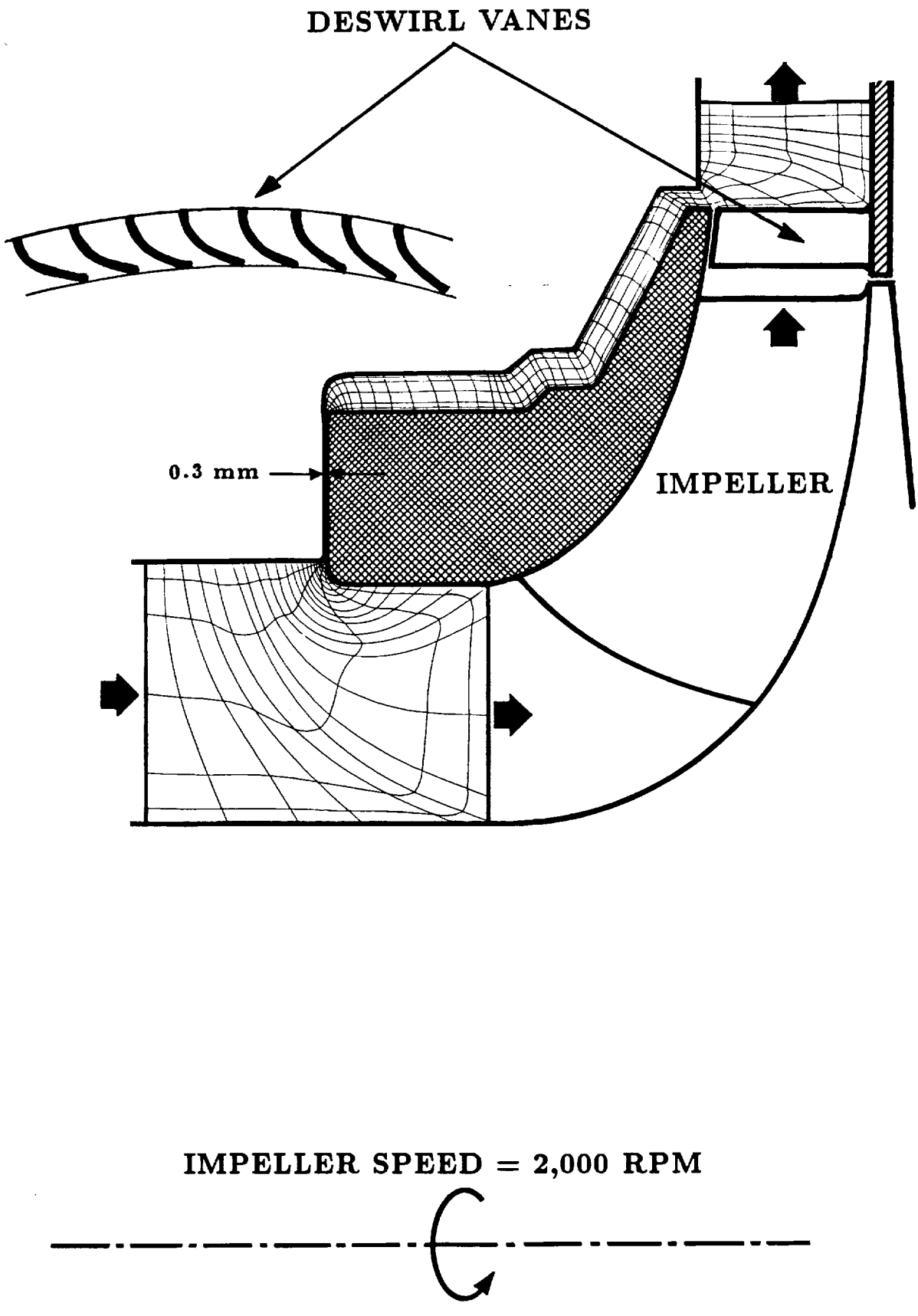


**Fig. 7 Deswirl vanes as a means of eliminating the leakage–passage inlet swirl**

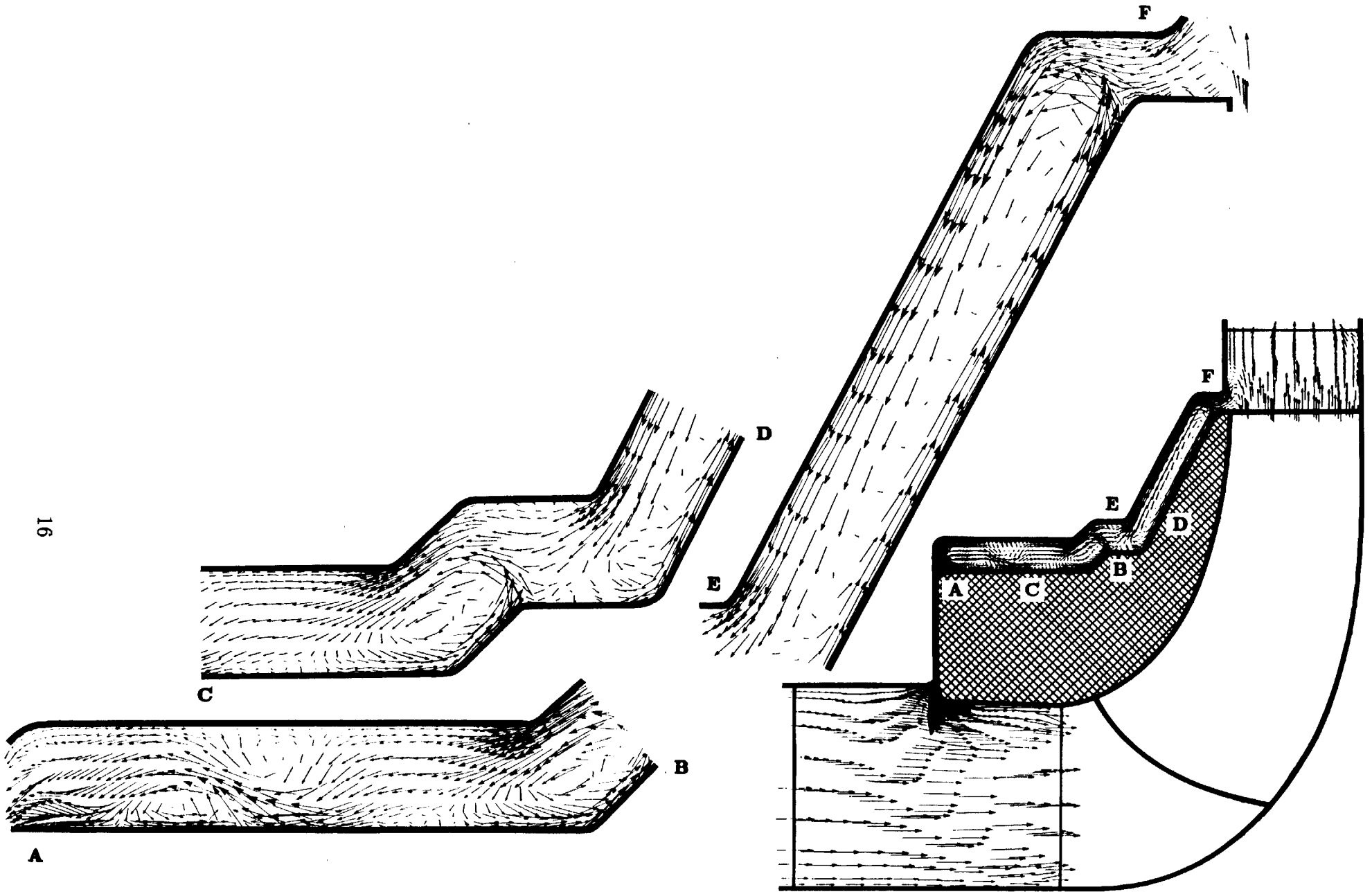


Fig. 8 Meridional velocity vector plot for zero preswirl in the leakage passage

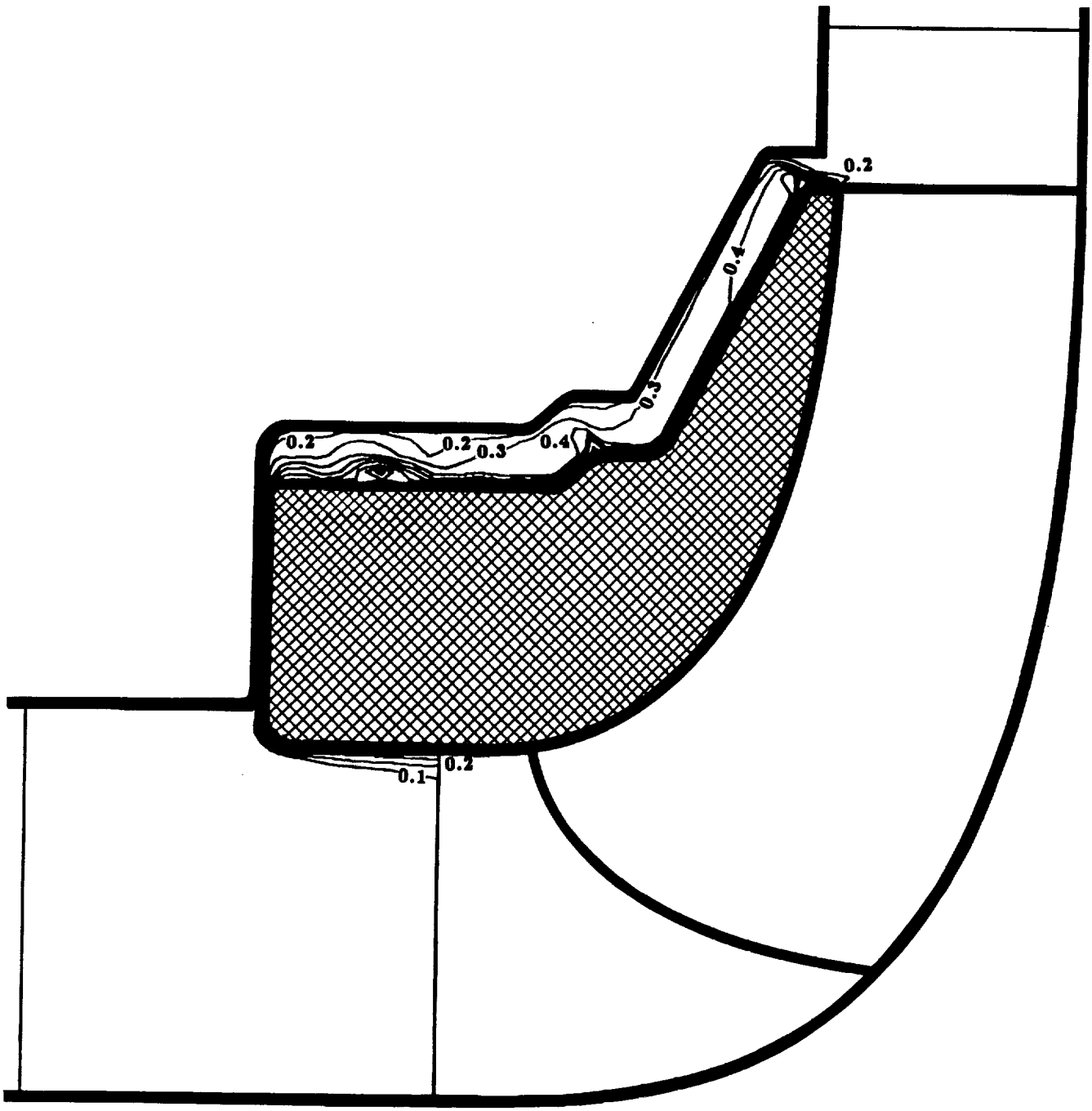


Fig. 9 Contours of the nondimensional swirl velocity for the zero leakage–passage preswirl case

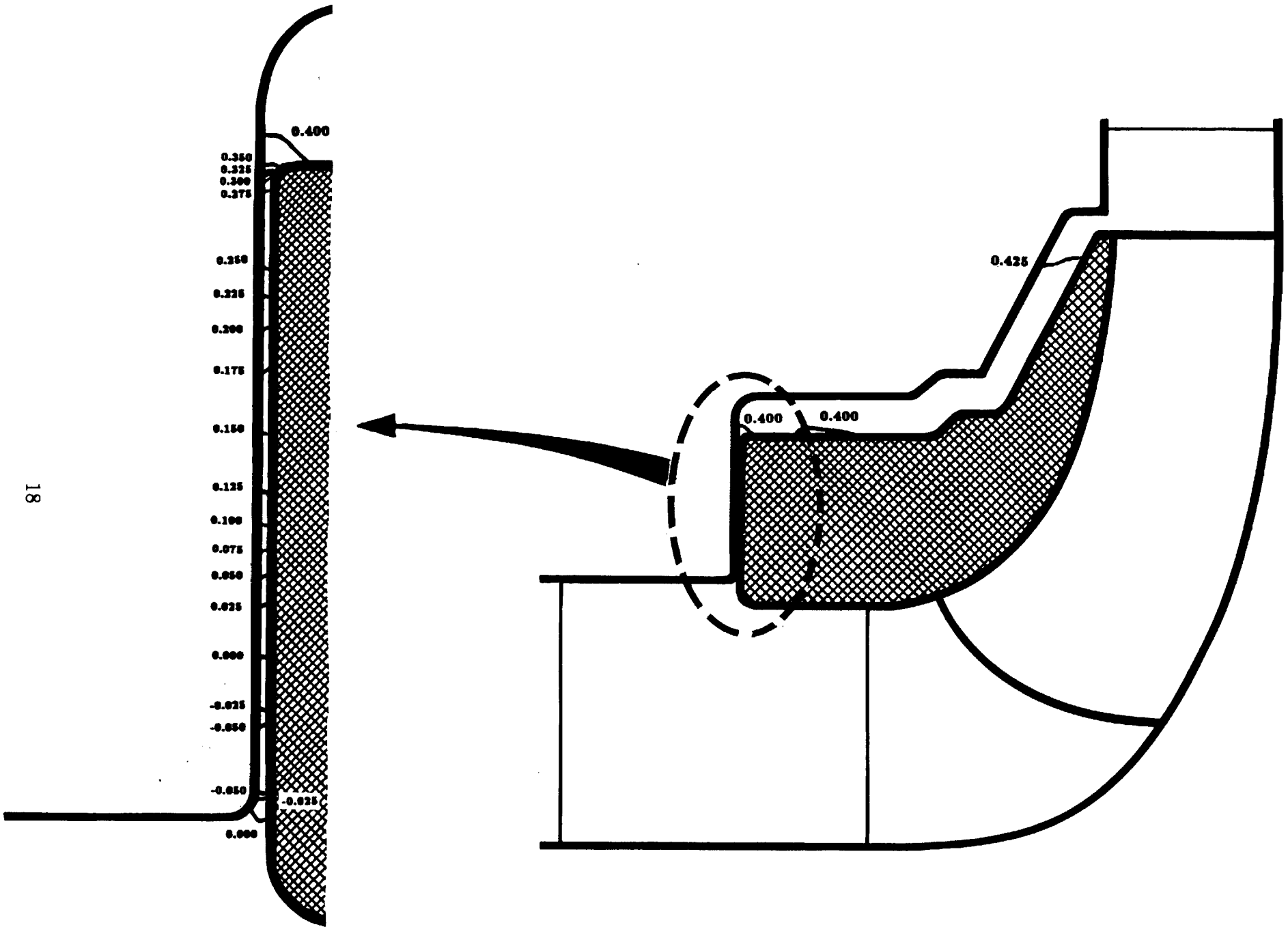


Fig. 10 Contours of the nondimensional static pressure for the zero leakage–passage preswirl case

improvements in the stability-related rotordynamic coefficients. As for the static pressure distributions (Fig. 10 and Fig. 10 in Appendix 1, Paper# 4), no major gain seems to have been obtained by destroying the leakage-passage inlet swirl velocity, with the exception that the secondary passage segment leading to the seal now shares the streamwise pressure differential with the seal, more so than the case was under the design-point preswirl (Fig. 10 in Appendix 1, Paper# 4). This feature is desirable from a design standpoint in the sense that utilization of a lower-resistance seal would, in this case, be allowed. Finally, the swirl velocity profiles slightly downstream from the leakage-passage inlet station (Fig. 11 and Fig. 5 in Appendix 1, Paper# 4) were compared. As expected, a rather thick boundary-layer type region exists near the shroud, under the no-preswirl pump operation, where the swirl velocity is notably high as a result of excessive flow recirculation in this region. Note that the swirl velocity component in Figs. 9 & 11 is non-dimensionalized using the impeller tip speed. The non-dimensional pressure in Fig. 10, on the other hand, is defined as follows:

$$\bar{p} = \frac{(p - p_i)}{\rho U_t^{\,2}}$$

where $p$ and $p_i$ are the local and stage-inlet static pressures, respectively, $\rho$ is the fluid density and $U_t$ is the impeller tip speed.

The "no-preswirl" zeroth-order flow solution was then used to compute the fluid-exerted forces over a range of whirl frequencies between -125% and +125% of the impeller speed. The results are shown in Fig. 12, together with the computed forces and experimental data, both of which corresponding to the design-point value of the leakage-passage inlet swirl. The first impression one would have by examining the tangential-force curve in this Figure is that the no-preswirl pump operation is comparatively more stable (as anticipated) judging by the smaller range of positive whirl frequency within which the tangential force is positive.

The impeller rotordynamic coefficients, corresponding to zero leakage-passage preswirl, are compared to the numerical and experimental data, associated with the design-point preswirl, in Table 1. All three sets of data in this table were obtained through a quadratic least-square fit of the fluid-exerted forces, as outlined by Baskharone and Hensel, 1991. Referring to Table 1, and limiting the comparison to the computed coefficients (last two columns of the Table), it is clear that the zero leakage-passage preswirl gives rise to a much stable impeller operation. While the direct damping coefficient "C" remains almost unaffected, the cross-coupled stiffness coefficient "k" becomes negative (thus stabilizing) in the zero-preswirl operation mode.

### Examination of the Perturbed Flow Field:

In an attempt to understand the origin of rotordynamic forces, we developed a post-processor which, in effect, "unwraps" the shroud surface, in the manner illustrated in Fig. 13, and displays the distribution of pressure perturbations (i.e. $\partial p/\partial \epsilon$ over the "unwrapped" surface, where "$\epsilon$" is the impeller eccentricity. Note that integration of the

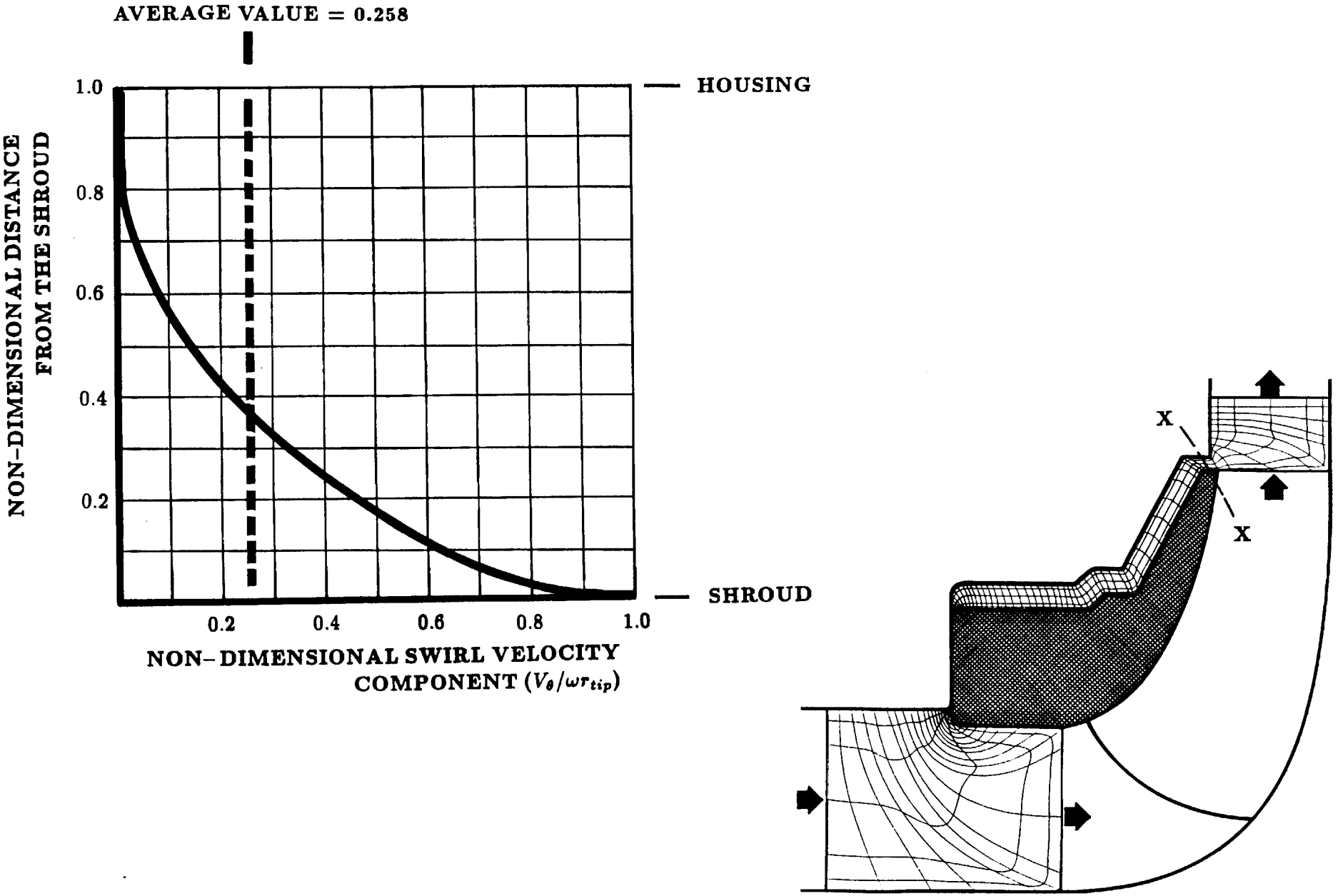


Fig. 11 Profile of the nondimensional swirl velocity near the leakage–passage inlet station for the zero–preswirl case

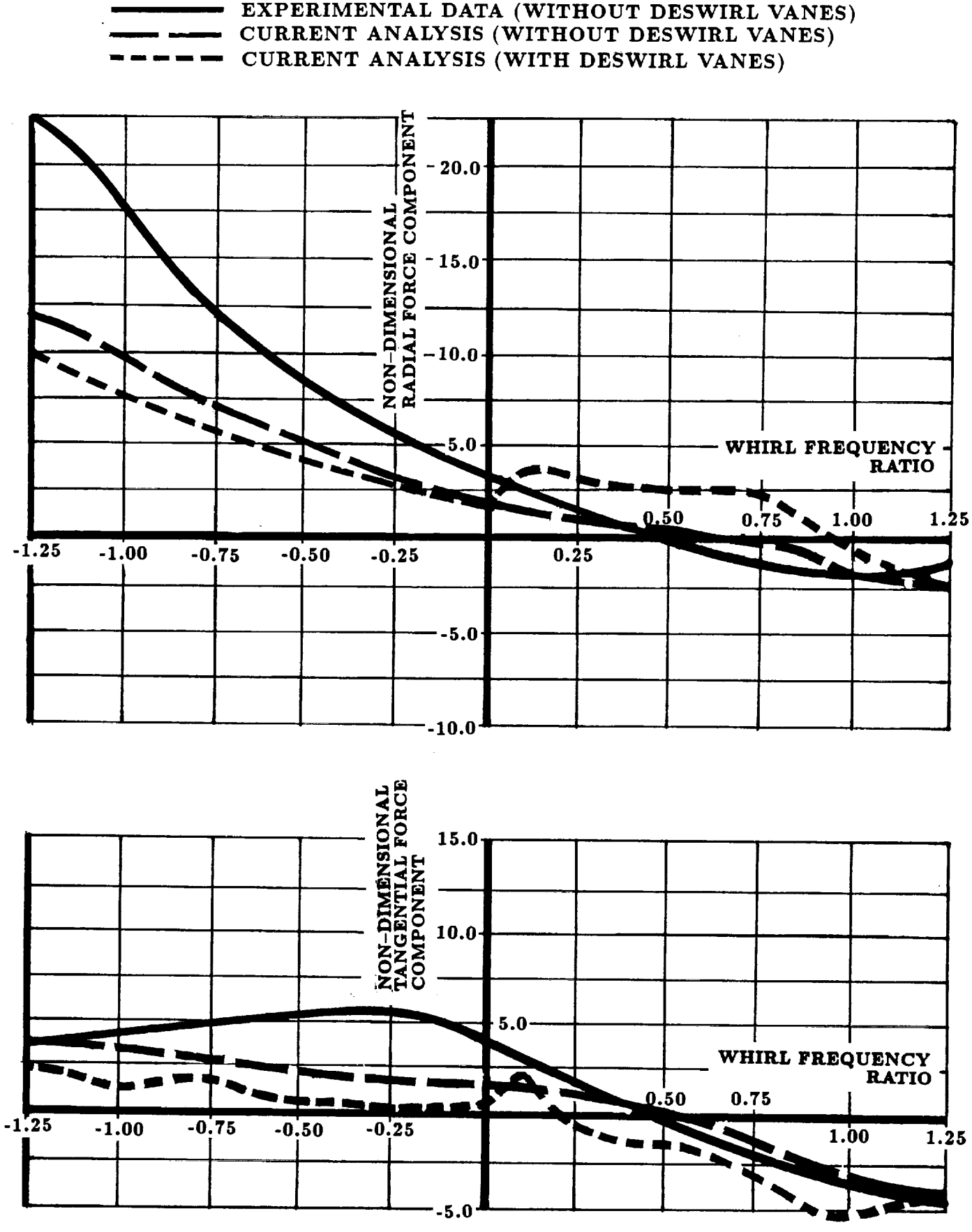


**Fig. 12 Comparison of the fluid exerted forces with and without deswirl vanes**

pressure perturbations over the entire shroud surface yields the net fluid–exerted force which, in turn, is resolved in the radial and tangential directions. The pump operation with and without leakage–passage preswirl were both under consideration in a range of whirl frequency ratios between -0.2 and +0.3. The main objective here was to see whether there are any redistribution of the pressure perturbation contours as the impeller shifts from slightly negative to slightly positive whirl frequencies.

Fig. 14 (on three successive pages) shows the pressure perturbation contours in the selected whirl–frequency range. For backward whirl (first two whirl frequency ratios), the Figure shows that the zero–preswirl pressure perturbations peak, more or less, at the minimum–clearance position (circumferential position c–c in Fig. 13). The Figure also shows that the design–point preswirl pump operation gives rise to pressure perturbation peaks which are clearly ahead of the minimum–clearance position in the direction of rotation. The relatively symmetric distribution of the pressure perturbation in the zero–preswirl case is perhaps the reason why the tangential force in Fig. 12 is comparatively small in this negative whirl–frequency range.

Proceeding to the positive whirl–frequency ratios in Fig. 14, it is seen that both pump operation modes give rise to peak pressure perturbations ahead of the minimum–clearance position in the direction of rotation. This occurs in the whirl frequency ratio range between 0.0 and +0.2, and indeed represents a shift in the case of the zero–preswirl case. This shift causes the notably rise in the tangential force curve (Fig. 12) in this frequency range. While the pressure perturbation peak in Fig. 14 continues to exist ahead of the minimum–clearance position (c–c) for the pump operation with inlet preswirl, a rather surprising contour redistribution occurs for the zero–preswirl operation, whereby the pressure perturbation peak is now at a circumferential location that is lagging the minimum–clearance position (relative to the direction of rotation) at $\Omega/\omega = +0.3$. Referring to Fig. 12, note that this shift causes the tangential force (for zero–preswirl) to be negative and, therefore, stabilizing.

The foregoing discussion illustrates the significance of the peak pressure–perturbation position (on the shroud surface), but lacks experimental validation. Fortunately, a recent set of LDA velocity measurements by Morrison et al. (1992) made a qualitative verification of our results possible. Fig. 15 shows a typical contour plot of the non–dimensional through–flow velocity which was obtained in this experimental study for an annular seal with a synchronously whirling rotor ($\Omega/\omega = 1.0$. Shown in the same Figure is our computed non–dimensional axial–velocity perturbation contours in the leakage passage at the location marked x–x for a synchronous whirl–frequency ratio. Note that this Figure does not allow a one–to–one comparison, for the simple reason that Morrison's contours are those of the non–dimensional through–flow velocity:

$$\frac{V_z}{V_{z,in}}$$

while our contours are those of the non–dimensional perturbation:

$$\frac{c}{V_{z,av}} \times \frac{\partial V_z}{\partial \epsilon}$$

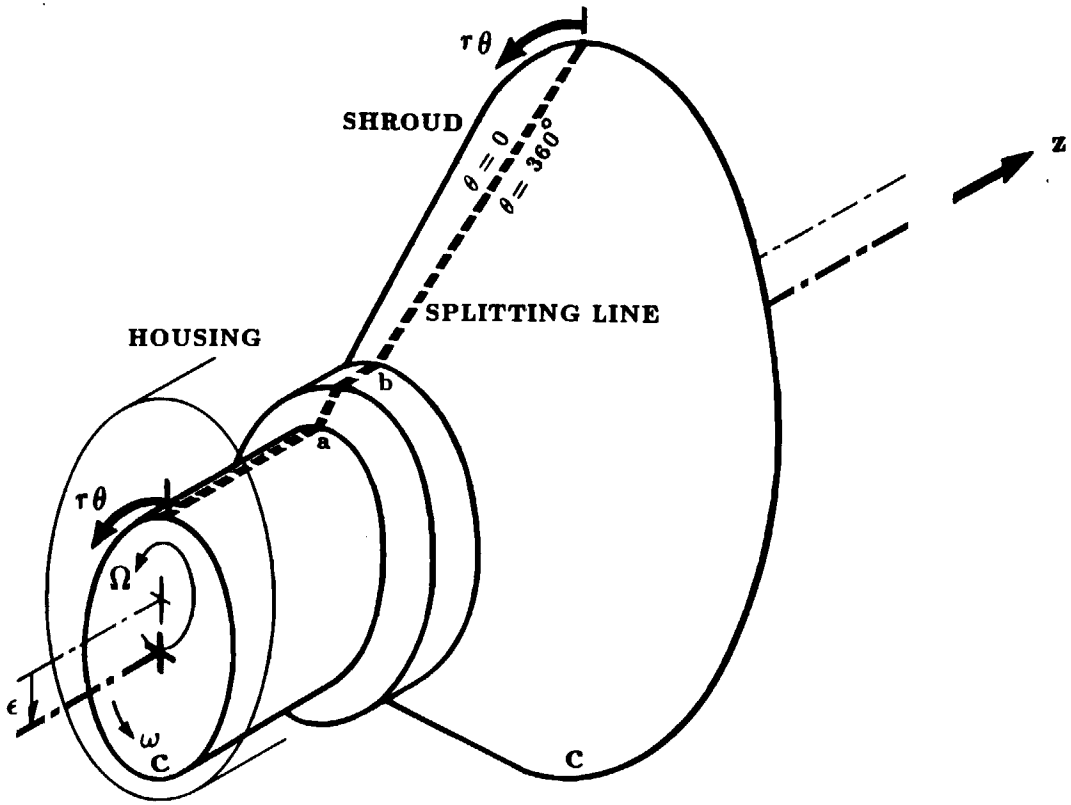


Fig. 13 Splitting and unwrapping the shroud surface

PRINTED VALUES ARE IN MN/m$^3$

WITH INLET PRESWIRL

WITHOUT INLET PRESWIRL

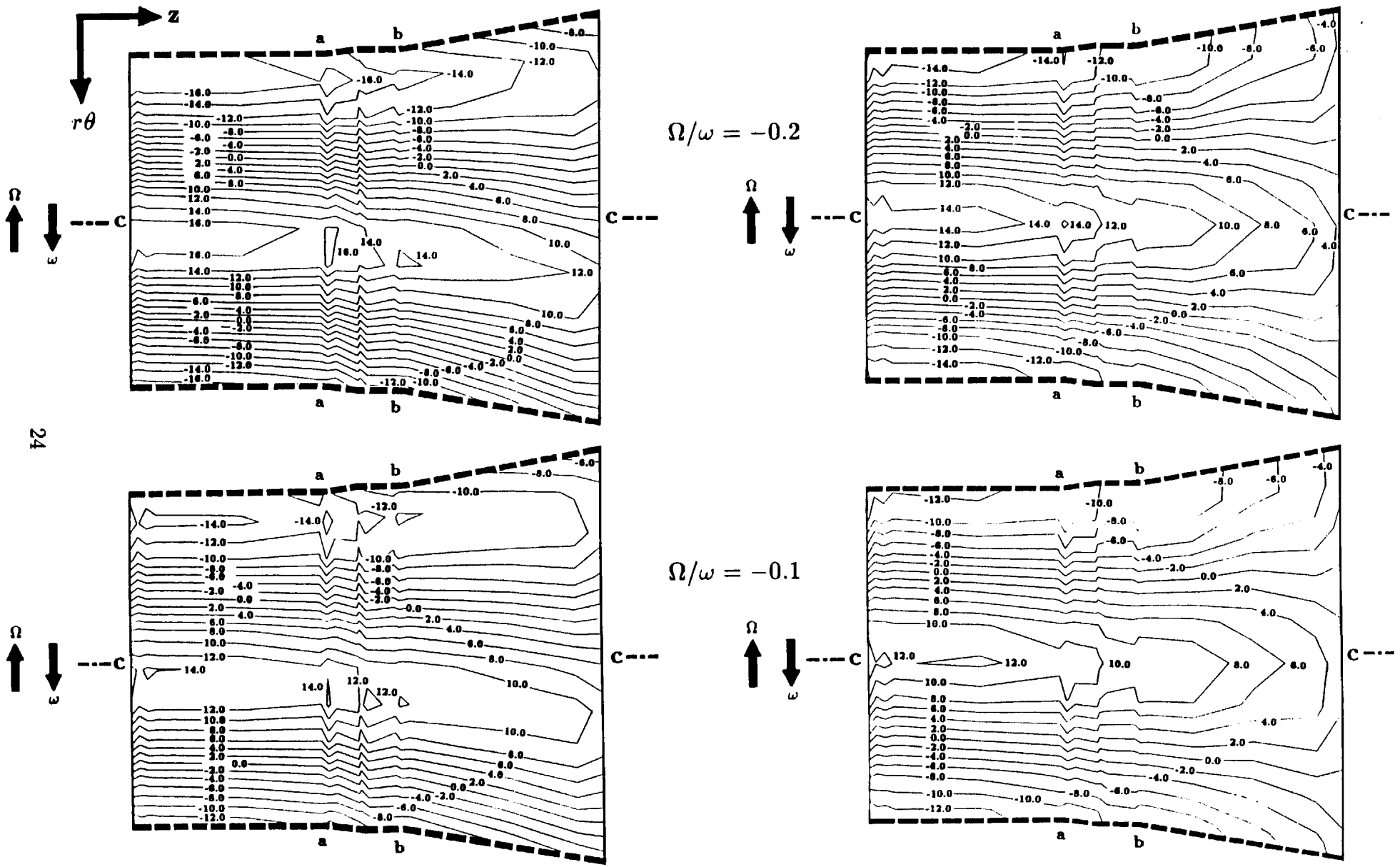




Fig. 14 Shroud pressure perturbation contours with and without inlet preswirl

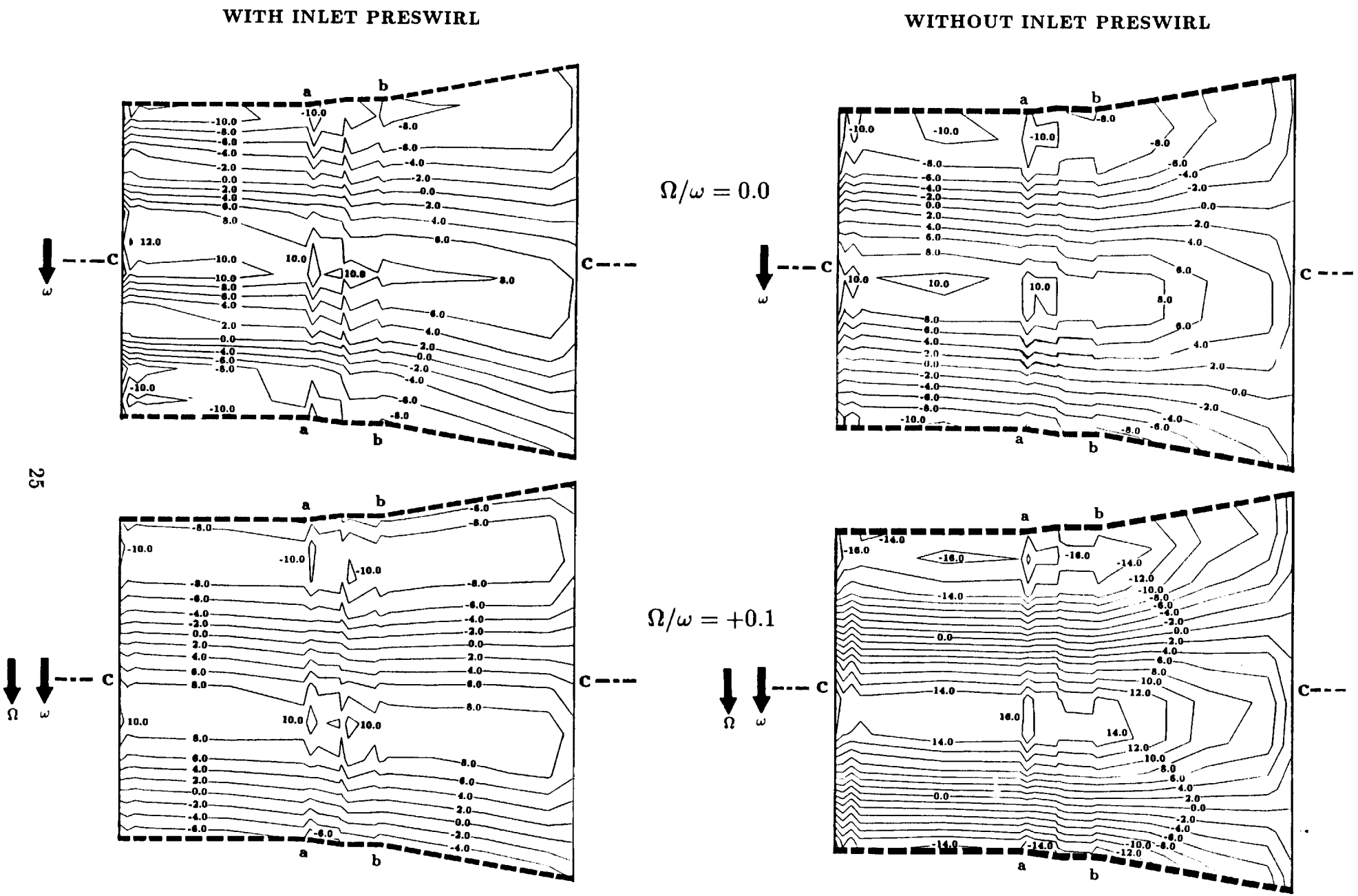
WITH INLET PRESWIRL
WITHOUT INLET PRESWIRL
Ω/ω = 0.0
Ω/ω = +0.1
a
b
c
ω
Ω

Fig. 14 Cont.

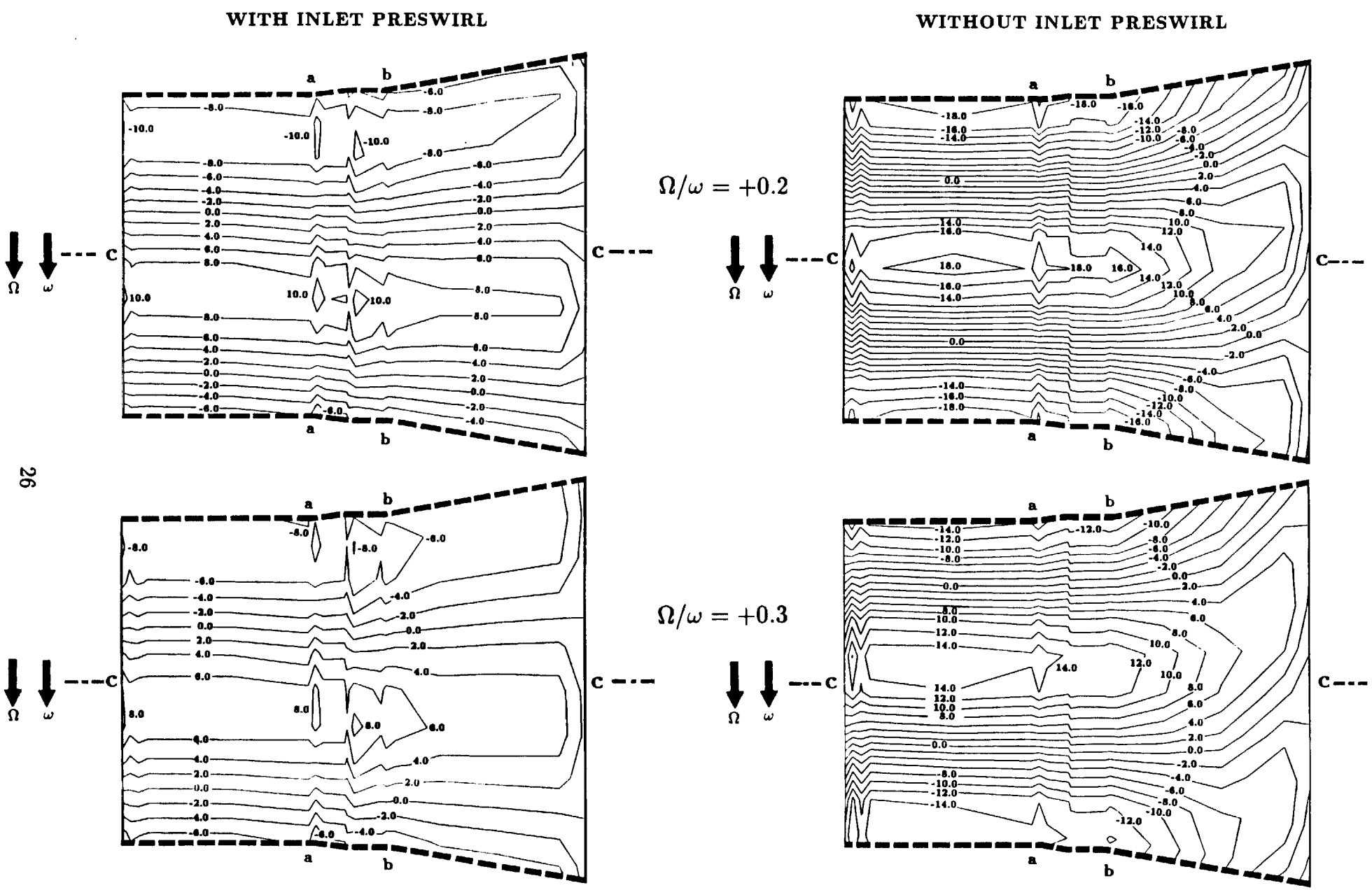
WITH INLET PRESWIRL
WITHOUT INLET PRESWIRL
Ω/ω = +0.2
Ω/ω = +0.3
a
b
c
Ω
ω

Fig. 14 Cont.

NON-DIMENSIONAL THROUGH-FLOW VELOCITY

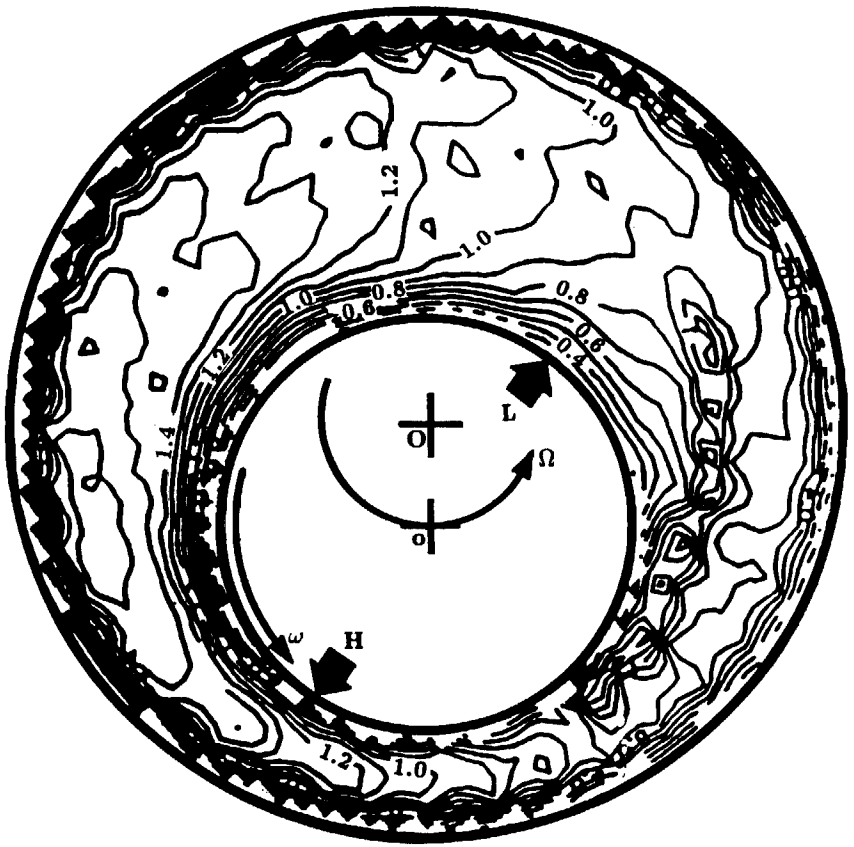


MORRISON'S SEAL MEASUREMENTS

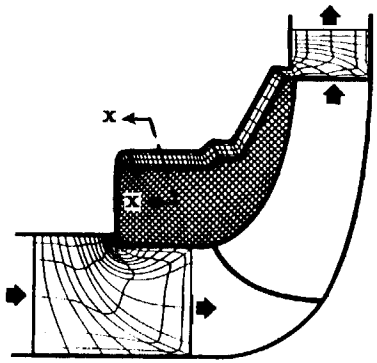


NON-DIMENSIONAL THROUGH-FLOW VELOCITY PERTURBATIONS

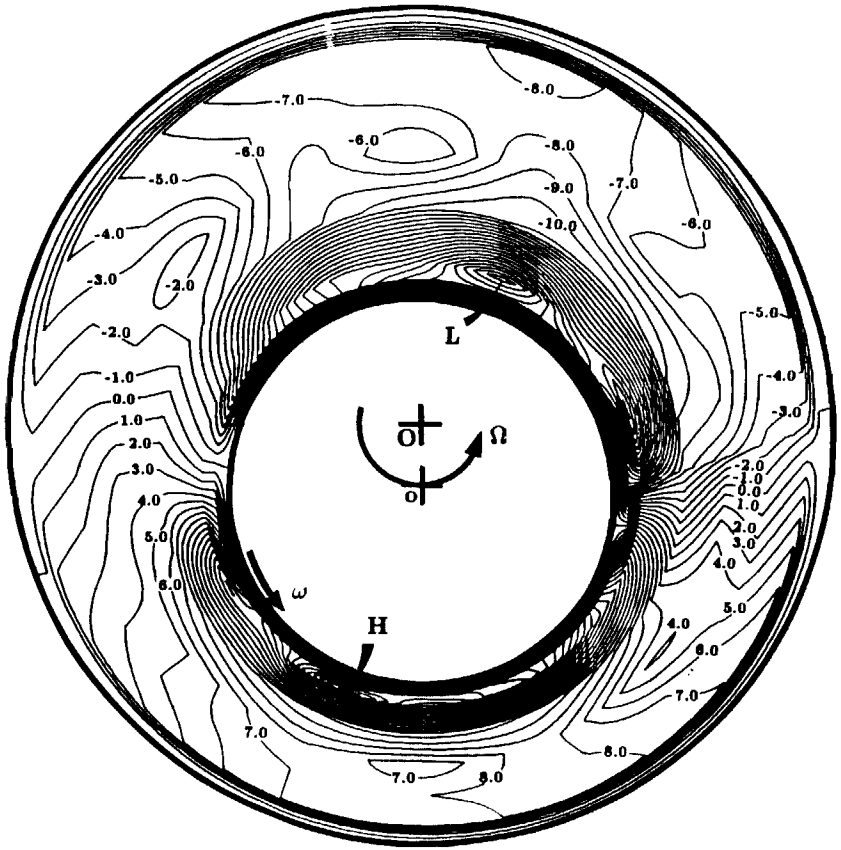


CURRENT SHROUDED-IMPELLER ANALYSIS

Fig. 15 Comparison with Morrison's seal measurements

where $V_{z,in}$ is the seal-inlet through-flow velocity (in Morrison's rig), and $c$ is the local clearance at the location x-x (in our case). Nevertheless, The Figure provides a means for qualitative comparison, particularly in regards to the tangential position of the peak value of through-flow velocity. Both the experimental and computed contours in Fig. 15 clearly indicate that the maximum disturbance position (marked "H" in Fig. 15) is at a tangential location in the opposite direction (relative to the rotor speed) from the minimum-clearance position. Pursuing this qualitative comparison, the shroud-surface pressure perturbation contours were also generated, and are shown in Fig. 16 (also for a synchronously-whirling impeller). Examination of this Figure again reveals that the maximum disturbance point does, in this case, exist at a tangential location that is lagging the minimum-clearance point (relative to the impeller speed). It should be emphasized, however, that our objective here was no more than a qualitative assessment of our results, particularly in view of the fact that no pressure measurements were reported for a whirling seal rotor neither by Morrison nor by any other experimentalist to the author's best knowledge.

**Validation of the Single-Harmonic Perturbation Assumption:**

The assumption that perturbations in each flow property is expressible via a single-harmonic tangential distribution, has commonly been used in all perturbation models existing today [e.g. Childs (1989), Dietzen and Nordmann (1987),...]. The current perturbation model, on the contrary, does not pre-impose any such restriction.

In order to investigate the validity of this assumption, the circumferential distribution of the shroud pressure perturbation was expressed at each through-flow location (using the already-computed nodal values) as a Fourier series as follows:

$$\frac{\partial p_i}{\partial \epsilon} = a_0 + \sum_n a_n \cos(n\theta) + \sum_n b_n \sin(n\theta)$$

where "$\theta$" is the angular coordinate. The number of sine and cosine waves "$n$" in this expression was arbitrarily set equal to three. The ratios $(a_n/a_1)$ and $(b_n/b_1)$ were then examined for $n = 2\&3$. The outcome of this study was that these ratios were sufficiently close to zero (meaning a valid single-harmonic assumption) at locations away from the leakage-passage inlet and exit stations and away from the passage segments where excessive flow recirculation and vortex breakdown occur (Fig. 8). In fact, the ratios $a_n/a_1$ and $b_n/b_1$, where $n = 2\&3$, can be as high, in the latter subdomains, as 21%. Fig. 17 shows the shroud segments where the single-harmonic assumption is hardly accurate.

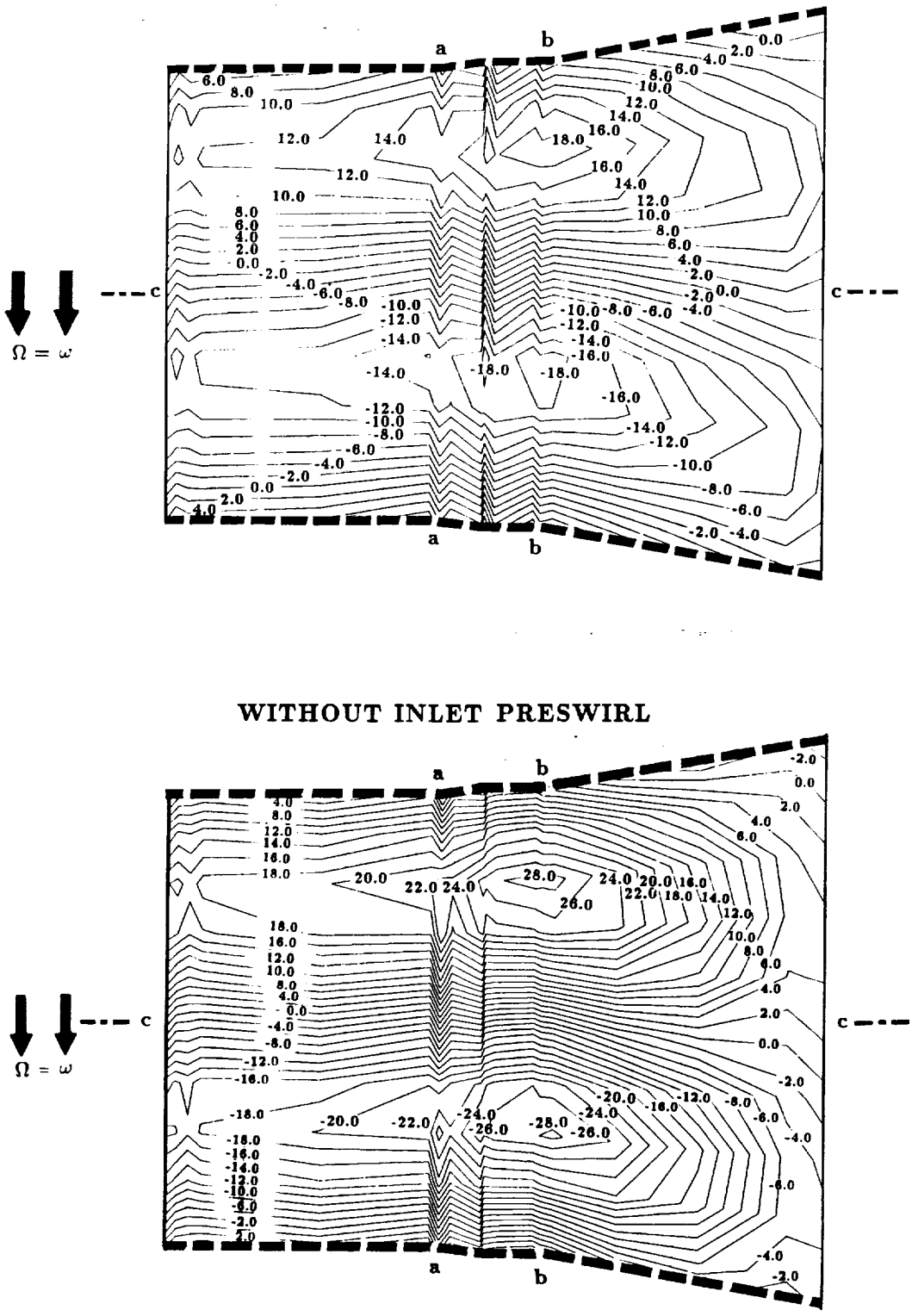


**Fig. 16 Contour plot of the shroud–surface pressure perturbations for a synchronously–whirling impeller**

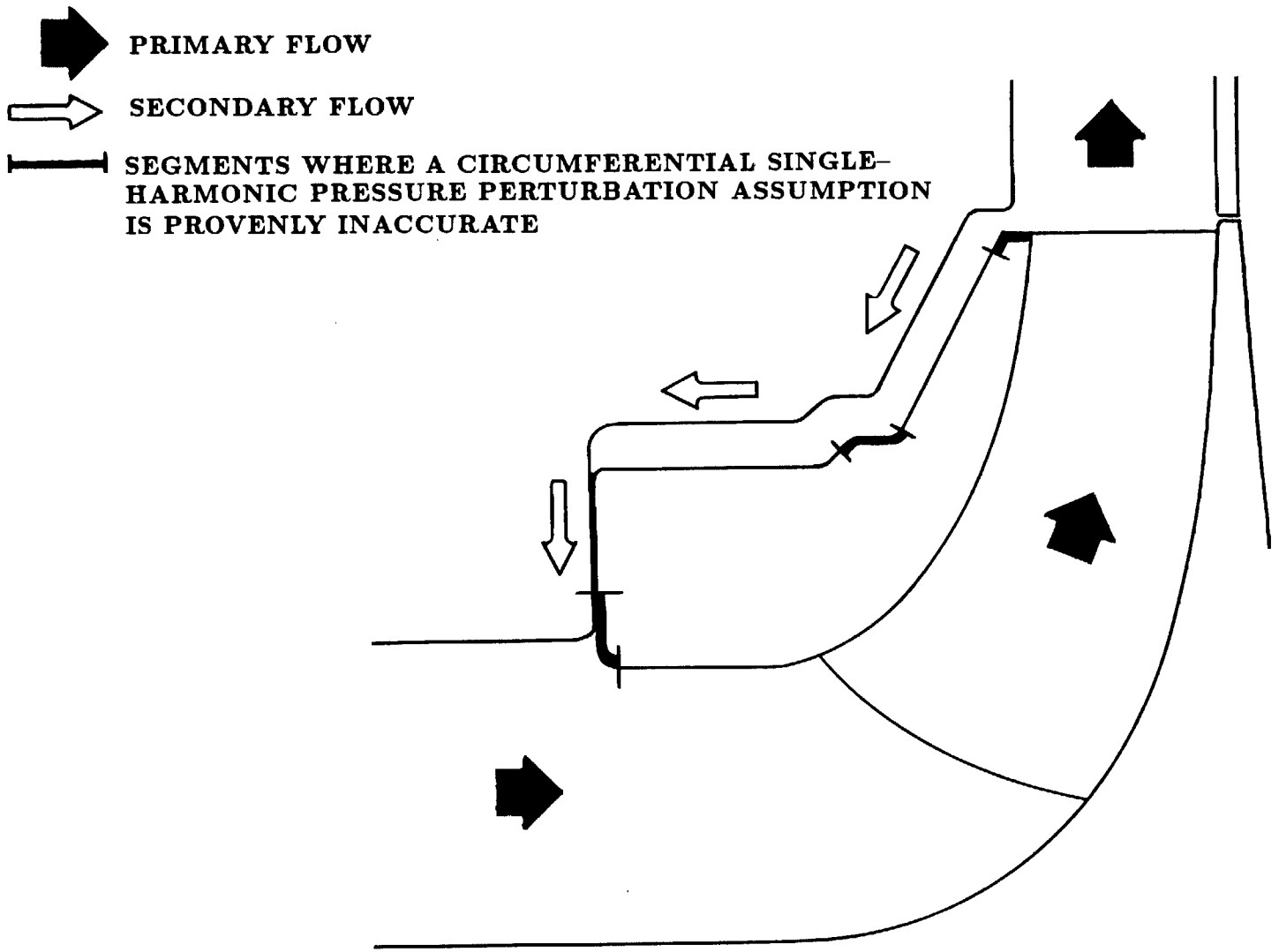


Fig. 17 Leakage passage segments where the single–harmonic perturbation variation assumption is inaccurate

## PROPOSED WORK

Falling under the category of rotordynamics, three different expansion studies are proposed. Of these, the first proposed study concerns creation of a new and desirable mode of code execution, whereby the phase of solving the centered–rotor flow field is by–passed, and a pre–existing flow solution used instead. The second study concerns an upgrade of the perturbation model to account for contributions of the primary flow to the shroud forces. The third proposed study involves what promises to be the most rigorous rotordynamic analysis of hydrostatic bearings. A summary of the objectives and approach in each study is given hereafter.

### 1. Insertion of an Existing Unperturbed Flow Field:

As described in Part 2 of this report, a new option (in executing the computational model) is proposed, whereby the user may make use of an existing centered–rotor (axisymmetric) flow solution [or, more importantly, centered–rotor flow measurements (if available)] as input to the perturbation model. The user, in this case, would be overriding the subprogram which is responsible for securing this "zeroth–order" flow solution. Due to the vast differences in the grid structure and the computed (or measured) flow variables there can be (let alone the format of the user's files), the author realizes the difficulty in "universalizing" this option. The focus will therefore be on providing the user with a systematic procedure whereby he/she could write his/her own interface code (usually short and simple), which would convert the grid (and, occasionally, the flow variables) into the form and format that is acceptable to the current perturbation analysis subprogram. In addition, at least one example of such interface code, the present outcome of which is the middle grid in Fig. 18, will be provided in the final version of the User's Manual. Nevertheless, it is important to point out that the user would (from a practical standpoint) resort to this option only if he/she has a good reason to (e.g. availability of reliable experimental data, or a highly accurate axisymmetric flow solver featuring, for instance, a state–of–the–art turbulence closure,...etc.). Otherwise, the user is generally advised to use the existing centered–rotor flow solver.

Included in this first proposed study is also the execution of a bench–mark test case, which was recently reported by Cal. Tech. (Guinzburg, 1992). The significance of Cal. Tech.'s rotordynamic measurements stems from the fact that the rig was designed to exclusively account for the leakage flow effects only, meaning that the primary (impeller) flow in this rig was non–existing (Fig. 19). As reported by Cal. Tech., the fluid–exerted forces on the rotor were parabolic and fluctuation–free, when plotted versus the whirl frequency. The author believes that this test case will complement the ongoing code verification process, and have actually started the rig simulation process by creating the centered–rotor finite element grid (Fig. 19).

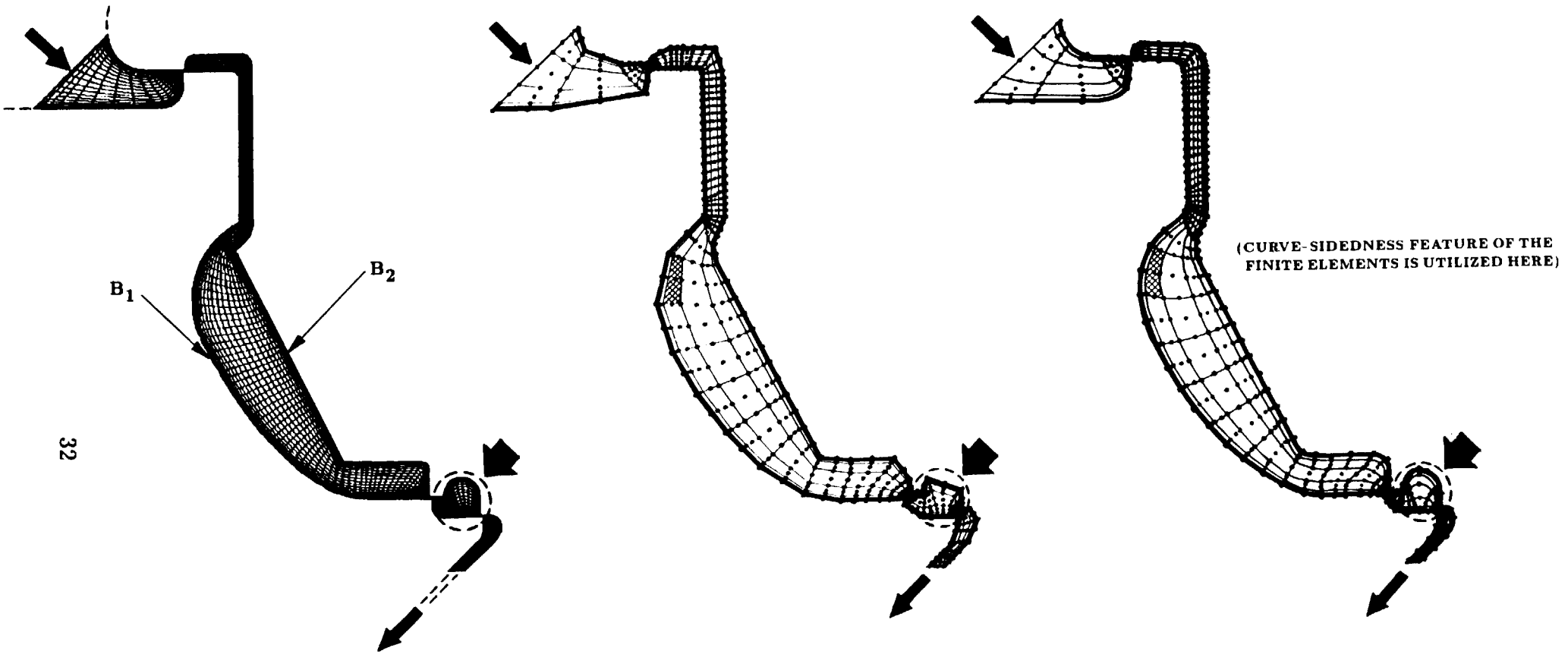


(A) NASA-GENERATED GRID FOR THE FINITE-VOLUME ZEROTH-ORDER FLOW SOLUTION

(B) FINITE-ELEMENT MODEL CREATED BY THE CURRENTLY EXISTING INTERFACE CODE

(C) ANTICIPATED ENHANCEMENT WITH THE PROPOSED INTERFACE CODE



**Fig. 18 Conversion of a finite–volume into a finite–element grid**

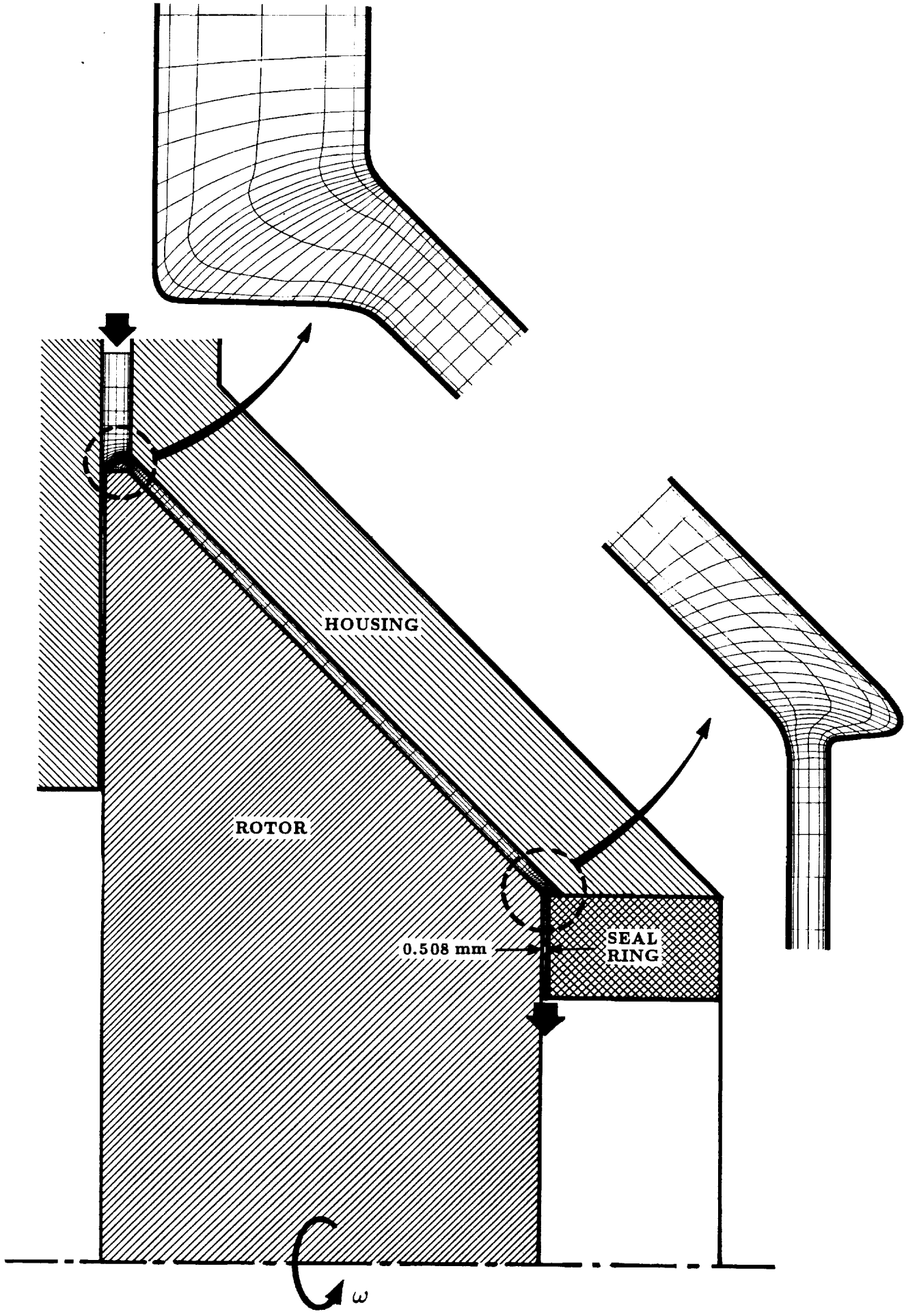


**Fig. 19 Finite–element discretization model of Cal. Tech.'s test rig**

### Inclusion of the Primary Flow Passage in the Analysis:

The current version of the currentperturbation model only accounts for the shroud forces developed in the secondary (leakage) passage (Fig. 1a). Since the inner shroud surface is also exposed to the flowing medium, it would be inaccurate to extract the latter from the flow domain with which the shroud interacts.

We are proposing a two–phase study to account for the primary flow passage effects on the shrouded–impeller rotordynamic characteristics. Referring to Fig. 20, these two phases are as follows:

a) Full guidedness of the impeller flow will first be assumed, whereby the swirl velocity at any finite–element node within the primary–flow passage (Fig. 20) will be determined from an already computed meridional (r–z) velocity and the assumption that the total velocity vector is tangent to the impeller blade. This is an iterative procedure the outcome of which will be combined with the leakage–passage flow field prior to executing the perturbation model.

b) A new computational capability, which we have just developed, will be utilized for a more realistic simulation of the primary–passage flow field. This capability is a blade–to–blade turbulent flow analysis code for a centrifugal pump impeller. The code is now operational, and a sample pump impeller case for which experimental data, by Lanes (1982), was provided. This study has already been concluded (Hlavaty, 1993) under the author's supervision. Results of this code, for a given impeller geometry and operating conditions, will be used to compute the circumferentially–averaged swirl velocity component which, in turn, will will be used in the axisymmetric–flow governing equations to compute a comparatively accurate zeroth–order flow solution in the primary–flow passage. This solution will then be merged with the leakage–passage axisymmetric flow solution, with the outcome being a valid input to the perturbation model.

As indicated above, we do have the computational means of implementing these lower– and higher–order modeling phases. In the end, we will be in a position to assess the contribution of the combined primary/secondary flow passages, in a real pump situation, versus the contribution of only the leakage–flow passage.

### Rotordynamic Characteristics of Hydrostatic Bearings:

This is perhaps the most aggressive, yet very much achievable, proposed task. The proposed approach (summarized hereafter) is currently under consideration, and should cover a range of bearing between outlined hereafter is applicable to a range of bearings between totally pressurized (hydrostatic) to hydrodynamic bearings including, in particular, the hybrid bearing category. In our model, there will be no assumption of viscosity–dominated (low Reynolds' number) flow anywhere, since the inertia terms will always be retained, no compromise of the flow turbulence anywhere (and not only over solid walls), and no compromise of the journal–to–housing gradients of the flow variables. In the sense that

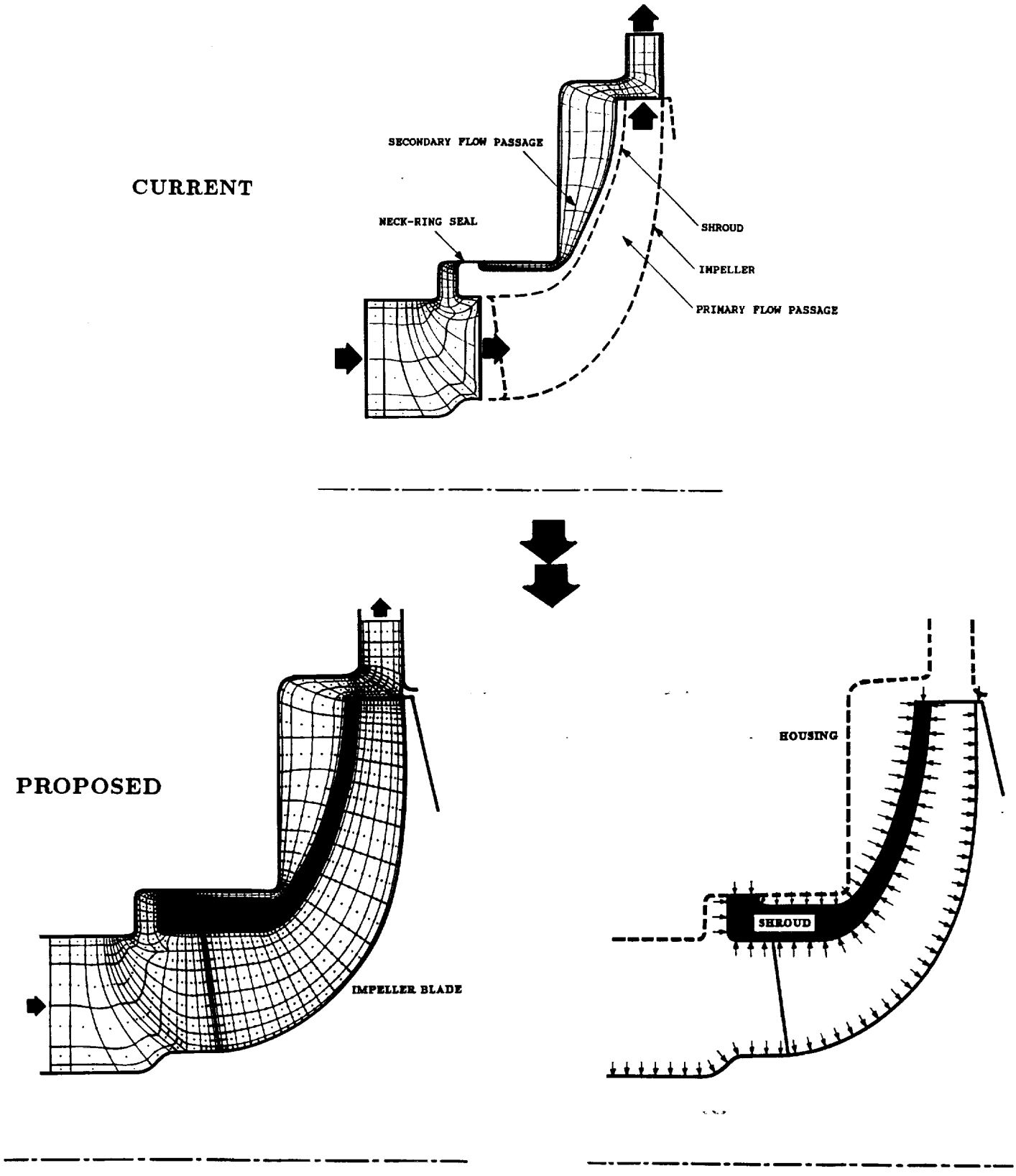


**Fig. 20 Inclusion of the primary flow passage as part of the computational domain**

the model is a natural extension of what we generically termed the "virtually" deformable finite–element approach, it should also be emphasized that utilization of the finite–element method in the current analysis is not only meant to solve one or more orders of the flow perturbation equations, but is also the means with which these equations come to existence. This is true in the sense that the perturbation equations, in the current model, emerge from expansion of the flow–governing equations in their discrete finite–element form, as opposed to the differential form in any existing perturbation model. This feature is the reason behind the model unmatched versatility, especially when it comes to the three–dimensionality of the flow domain.

In the proposed model, a time–accurate algorithm is utilized to determine the history of the lubricant–exerted forces on the journal, as the latter traverses over a tangential "pitch" between two successive recesses. This will make it possible to compute a set of rotordynamic coefficients, which are based on the time–averaged fluid–exerted forces, and another set of "conservative" coefficients which correspond to the instance at which the destabilizing/stabilizing journal–force ratio is maximum. In the following, the proposed approach will be summarized with reference to Fig. 21, which shows the NLS Fuel Pump hydrostatic bearing as an example.

First, the reader is reminded of some relevant details concerning the current perturbation model. Referring to Fig. 22, the frame of reference in which the "unperturbed" flow field is described consists of the z-axis (which at this point is coincident with the housing centerline) with the x and y axes rotating at an angular speed that is identical to the whirl frequency $\Omega$. Recalling that the journal whirl has not physically occurred yet, it is seen that this coordinate system is highly untraditional but is, nevertheless, legitimate. The reason for this choice is that once the governing equations and boundary conditions are cast in this coordinate system, the only physical component that is missing from the whirling motion is the journal eccentricity $\epsilon$. In other words, if the journal whirl is thought of as a journal eccentricity coupled with a whirl frequency, then the latter is taken into account in the early step of defining the centered–journal flow field. Furthermore, because the flow variables (including the velocity) are relative to this coordinate system, it is actually the housing which undergoes the rotational motion at this point. This is simply due to the fact that the flow variables and boundary conditions are those which would appear to an observer in this rotating frame of reference. Fig. 6 shows the solid–wall boundary conditions relative to that observer.

With the preceding logic in mind, and referring to the hydrostatic bearing problem (Fig. 22), all one has to do for determining the perturbations in the fluid properties (particularly those of the journal–surface pressure) is to construct a centered–journal (zeroth–order) flow problem that is consistent with that associated with the position of the whirling journal at any given point in time. The consistency here includes the instantaneous orientation of the coordinate axes and the whirl frequency $\Omega$ as shown in the upper row of Fig. 22. Superimposition of the journal lateral eccentricity $\epsilon$ (lower row of Fig. 22) would then complete the requirements for the whirling motion (at the corresponding point in time) to prevail. The procedure is therefore one of marching in time, in which the journal

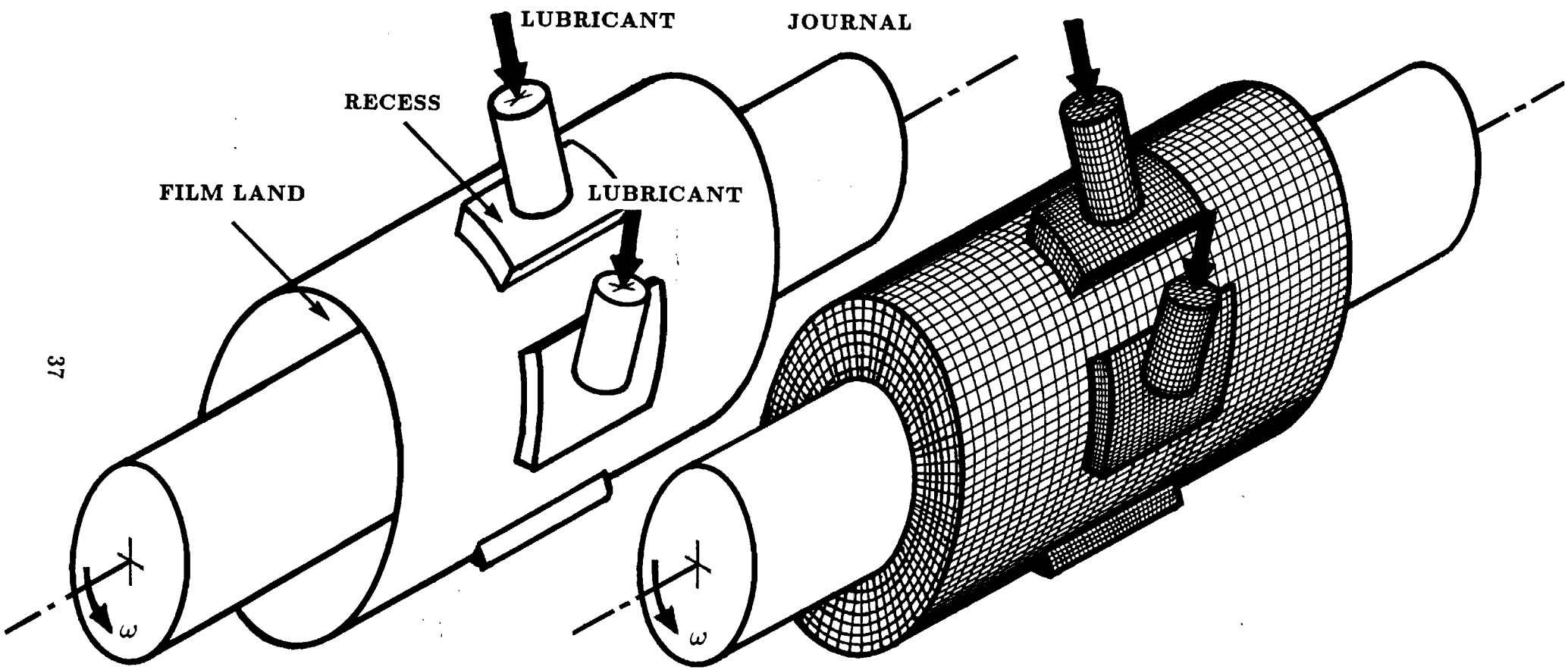


Fig. 21 Hydrostatic bearing geometry and finite–element model

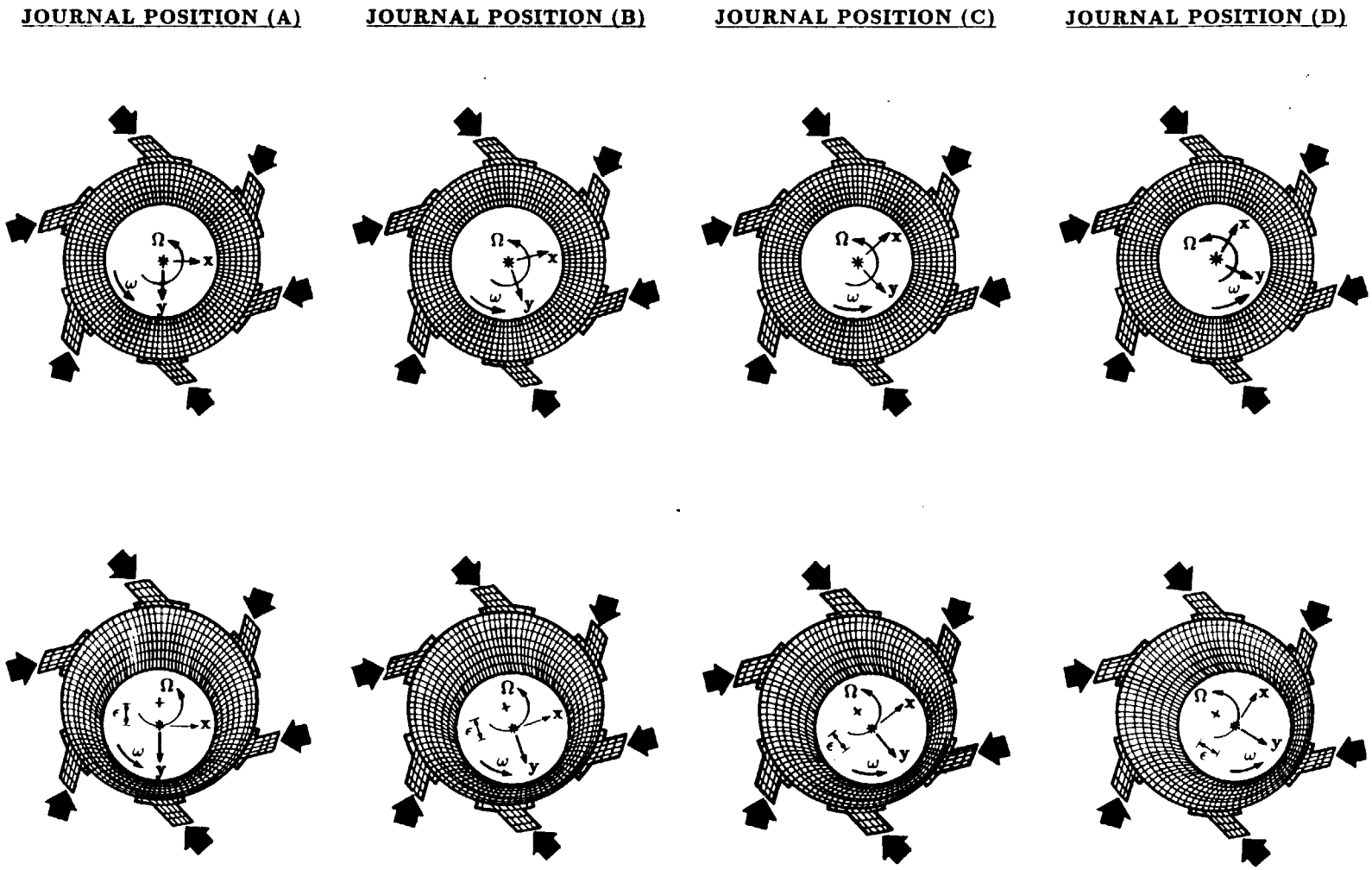


**Fig. 22 Instantaneous positions of the coordinate axes over one angular pitch between two successive recesses in a hydrostatic bearing**

repeatedly sweeps (in its whirling motion) the angular spacing between two successive recesses (Fig. 22), until fixed cyclic patterns of the fluid reaction forces are achieved. During the marching process, a "centered–journal" flow field is first obtained for any given angular position of the journal axis (upper row in Fig. 22). Subsequent application of the "virtually" deformable finite element concept (Baskharone and Hensel, 1991a) to this zeroth–order flow field will then produce the perturbations of the flow variables. Of these, the journal–surface pressure perturbations are extracted and integrated over the journal surface to attain the instantaneous radial and tangential components ($F_r$ and $F_\theta$) of the journal/fluid interaction force.

The procedure described above will produce the history of the fluid–reaction force components as the journal whirls through a complete angular "pitch" between two successive recesses, which is 60 deg. in Fig. 22. The time–averaged values of these force components can then be computed and used in a traditional rotordynamic analysis, as outlined earlier. Note that the proposed approach compromises none of the real flow effects, and fully accounts for the three–dimensionality of the journal–to–housing domain. It is also important to point out that despite the generality and rigorousness of the proposed approach, the size of the model (in terms of computational resources) is not expected to be much different from that of the shrouded–impeller rotordynamics problem, which we have successfully solved.

## REFERENCES

Baskharone, E.A. and Hensel, S.J., 1991, "A Finite-Element Perturbation Approach to
Fluid/Rotor Interaction in Turbomachinery Elements. Part 1: Theory," J. of Fluids Engineering (ASME Trans.), Vol.113, No. 3, pp. 362-367.

Bolleter, U., Leibundgut, E. and Sturchler, R., 1989, "Hydraulic Interaction and Excitation Forces of High Head Pump Impellers," presented at the Third Joint ASCE/ASME Mechanics Conference, University of California, La Jolla, California.

Childs, D.W., 1989, "Fluid-Structure Interaction Forces at Pump-Impeller-Shroud Surfaces for Rotordynamic Calculations," ASME J. of Vibration, Stress and Reliability in Design, Vol. 111, pp. 216-225.

Dietzen, F.G. and Nordmann, R., 1987, "Calculating Rotordynamic Coefficients of Seals by Finite Difference Techniques," ASME J. of Tribology, Vol. 109, pp. 388-394.

Guinzburg, A., 1992,"Rotordynamic Forces Generated by Discharge-to-Suction Leakage Flow in Centrifugal Pumps," Ph.D. Dissertation, California Institute of Technology.
Hlavaty, S.T., 1993, "A Finite-Element Model of the Turbulent Flow in Centrifugal Impellers," M.S. Thesis, Texas A&M University.

Lanes, R.F., 1982, "The Design, Construction, and Testing of a Plexiglas Centrifugal Pump for Use with Laser Velocimetry,"

# APPENDIX 1

## PAPERS PUBLISHED DURING THE FUNDING PERIOD

**PAPER# 1**

# A Finite-Element Perturbation Approach to Fluid/Rotor Interaction in Turbomachinery Elements. Part 1: Theory

**E. A. Baskharone**
Associate Professor.
Mem. ASME

**S. J. Hensel**[1]
Mem. ASME

Department of Mechanical Engineering,
Texas A&M University,
College Station, Texas 77843

*The vibrational characteristics of a rotor that is in contact with a fluid in an annular clearance gap, as dictated by the fluid forces in the gap, are investigated. The "rotor" here is a general term that may refer to the shaft segment within the housing of an annular seal, on the simple end of the application spectrum, or the shroud-seal assembly in a shrouded-impeller stage of a turbomachine, on the complex end. The disturbance under consideration involves the axis of rotation, and includes a virtual lateral eccentricity, together with a whirling motion around the housing centerline. Uniqueness of the computational model stems from the manner in which the rotor eccentricity is physically perceived and subsequently incorporated. It is first established that the fluid reaction components arise from infinitesimally small deformations with varied magnitudes which are experienced by an assembly of finite elements in the rotor-to-housing gap as the gap becomes distorted due to the rotor virtual eccentricity. The idea is then cast into a perturbation model in which the perturbation equations emerge from the flow-governing equations in their discrete finite-element form as opposed to the differential form, which is traditionally the case. As a result, restrictions on the rotor-to-housing gap geometry, or the manner in which the rotor virtual eccentricity occurs are practically nonexisting. While the emphasis in this paper is on the theoretical model, a representative application of the model and assessment of the numerical results are the focus of a companion paper that is being published concurrently.*

## Introduction

Reliable modeling of the rotordynamic characteristics of fluid-encompassed elements in turbomachines, such as the annular seal rotor in Fig. 1, started fairly recently. The bulk-flow model devised by Childs (1983) is an example of some widely used predictive tools in this area. This technique was used to compute both the direct and cross-coupled rotordynamic coefficients for an annular seal (Childs, 1985) and further extended by Nelson (1985) to account for the flow compressibility and the seal taper. However, the accuracy of this model would naturally decline in the case of a generally shaped annular flow passage, such as the secondary passage of the shrouded impeller in Fig. 2, where lateral (rotor-to-housing) flow stresses become comparable to those at the solid walls. Besides, the analysis is conceptually incapable of simulating the effects of flow separation and recirculation in such a complex flow passage, but has been remarkably successful otherwise (Childs, 1989).

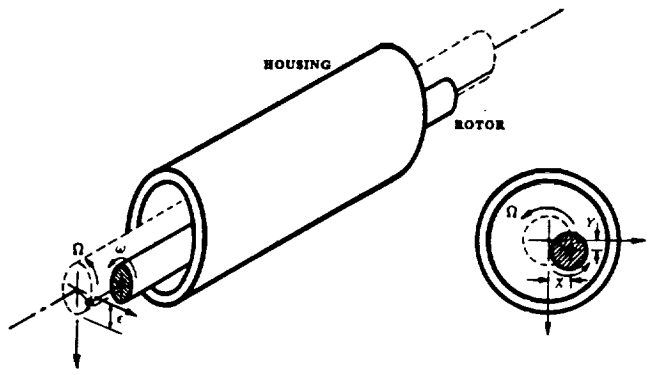


Fig. 1 Cylindrical whirl of a rotor inside a housing

Recently, a more rigorous finite difference-based perturbation model was developed by Dietzen et al. (1987) and applied to an annular seal. The distorted seal annulus for the displaced shaft configuration, in this case, was mapped into a fictitious frame of reference, reducing the problem into that of a centered shaft rotation. A traditional hypothesis was then made that perturbations of the flow variables vary sinusoidally with the tangential coordinate around the circumference in the

[1]Graduate Research Assistant, currently a Senior Engineer at Westinghouse Savannah River Laboratory, Aiken, South Carolina.

Contributed by the Fluids Engineering Division for publication in the JOURNAL OF FLUIDS ENGINEERING. Manuscript received by the Fluids Engineering Division March 27, 1990.

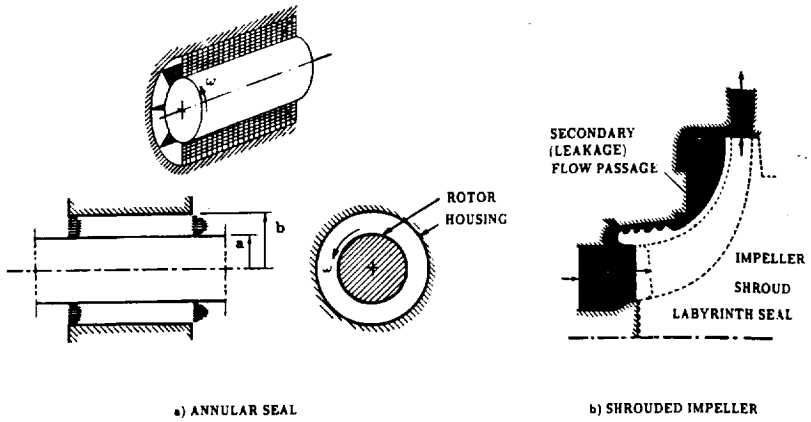


a) ANNULAR SEAL b) SHROUDED IMPELLER

**Fig. 2 Two representative problems of turbomachinery rotating elements**

fictitious space, with only the first harmonic wave taken into account. Based on this assumption, a perturbation analysis of Navier-Stokes equations was then performed and the rotordynamic coefficients, in the end, obtained. Despite the apparent generality and complex nature of this analysis, it involves geometry-related restrictions and is limited to a uniform lateral eccentricity of the rotor axis. Other existing models for annular and labyrinth seals, e.g., those by Dietzen and Nordmann (1988) and Hensel (1986), do not utilize the perturbation concept and are therefore tedious as well as costly, for they require solution of the fully three-dimensional Navier-Stokes equations in the distorted flow domain.

In this paper, a new finite element-based perturbation model is presented. The model introduces what may be referred to as the "virtually deformable" finite element concept, as a means of determining the fluid-exerted forces in the rotor-to-housing gap, and whether such forces would sustain or suppress a rotor whirling motion of the cylindrical type, as depicted in Fig. 1 for a simple annular seal. Originality and versatility of the new model both stem from the fact that the perturbation equations emerge from the discrete finite-element flow equations as opposed to the flow-governing equations in their differential form as is traditionally the case.

## Analysis

The governing equations are grouped as pertinent to the fundamental rotordynamics basis, the flow kinetics in the undisturbed operation mode and, finally, the perturbation model. In all phases, reference is made to a general fluid domain with which the rotor is in contact. Two examples of such domain, namely that of an annular seal and shrouded pump impeller (Fig. 2), are given.

**Definition of the Rotordynamic Coefficients.** Evaluation of the force coefficients is initialized by considering the rotor lateral eccentricity "$\epsilon$" coupled with a circular whirling motion around the housing centerline (Fig. 1). The locus of the rotor axis, in this case, can parametrically be described as follows:

$$X = \epsilon\sin(\Omega t), Y = \epsilon\cos(\Omega t) \tag{1}$$

where "$X$" and "$Y$" are the eccentricity components of the rotor axis (Fig. 1), "$\Omega$" is the whirl frequency and "$t$" refers to time. Noting that the direction of "$\Omega$" in Fig. 3($a$) is negative, the rotor equation of motion can be written as follows:

$$-\begin{Bmatrix}\delta F_x\\ \delta F_y\end{Bmatrix} = \begin{bmatrix}K & -k\\ k & K\end{bmatrix}\begin{Bmatrix}X\\ Y\end{Bmatrix} + \begin{bmatrix}C & -c\\ c & C\end{bmatrix}\begin{Bmatrix}\dot{X}\\ \dot{Y}\end{Bmatrix} + \begin{bmatrix}M & -m\\ m & M\end{bmatrix}\begin{Bmatrix}\ddot{X}\\ \ddot{Y}\end{Bmatrix} \tag{2}$$

where

$\delta F_x$, $\delta F_y$ are the incremental changes in the rotor force components as a result of the rotor disturbance,

$K$, $k$ are the direct and cross-coupled stiffness coefficients of the fluid/structure system,

$C$, $c$ are the damping coefficients,

$M$, $m$ are the inertia (or added mass) coefficients,

Assuming cylindrical whirl around the housing centerline at

## Nomenclature

$[A]$, $[a]$ = global and elemental matrices of influence coefficients in the finite element equations

$\{B\}$, $\{b\}$ = global and elemental load vectors in the finite element equations

$\mathbf{F}, \mathbf{G}, \mathbf{H}, \mathbf{I}, \mathbf{J}, \mathbf{K}$ = linear operators defined in the element local frame of reference

$K, k, C, c, M, m$ = direct and cross-coupled stiffness, damping and inertia coefficients

$M_i(\zeta, \eta, \xi)$ = linear shape function associated with the $i$th corner node of a finite element

$N_i(\zeta, \eta, \xi)$ = quadratic shape function associated with the $i$th corner or midside node of a finite element

$p$ = static pressure

$u, v, w$ = velocity components in the cartesian frame of reference

$W_i$ = weight function in the Petrov-Galerkin weighted-residual analysis

$x, y, z$ = cartesian coordinates

$\epsilon$ = lateral eccentricity of the rotor axis

$\zeta, \eta, \xi$ = coordinates in the element local frame of reference

$\nu$ = kinematic viscosity

$\rho$ = density

$\{\Phi\}$, $\{\phi\}$ = global and elemental vector of unknown velocity components and pressure

$\Omega$ = whirl frequency

$\omega$ = rotor operating speed

**Other Symbols**

overbar = perturbation in a quantity due to the rotor eccentricity

$(^*)$ = a quantity that is known from a previous iteration or an initial guess

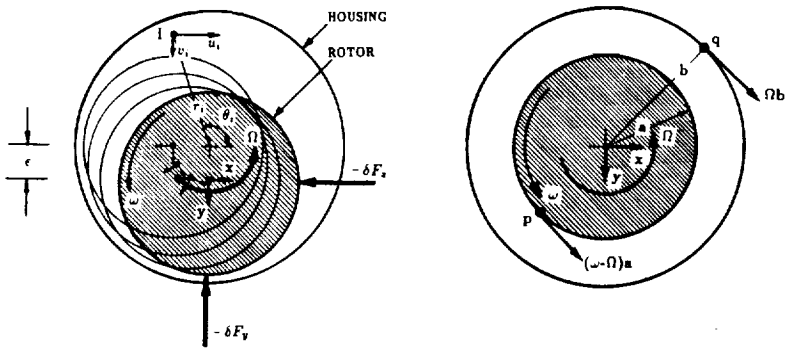


**Fig. 3 Definition of the rotating-translating axes and solid-wall boundary conditions**

a constant whirl frequency "Ω", and refering to Fig. 1, consider the position of the rotor axis that is vertically underneath the housing centerline. The axis location, linear velocity and acceleration at this position are:

$$X=0 \quad Y=\epsilon$$
$$\dot{X}=\Omega\epsilon \quad \dot{Y}=0$$
$$\ddot{X}=0 \quad \ddot{Y}=-\Omega^2\epsilon$$

Substituting these into the expanded form of the matrix Eq. (2), and taking the limit as "$\epsilon$" tends to zero, the following equations are obtained:

$$\frac{\partial F_x}{\partial \epsilon}=\lim_{\epsilon\to 0}\left(\frac{\delta F_x}{\epsilon}\right)=k-\Omega C-\Omega^2 m \tag{3}$$

$$\frac{\partial F_y}{\partial \epsilon}=\lim_{\epsilon\to 0}\left(\frac{\delta F_y}{\epsilon}\right)=-K-\Omega c+\Omega^2 M \tag{4}$$

Determination of the rotordynamic coefficients in Eqs. (3) and (4) requires computation of the derivatives $\frac{\partial F_x}{\partial \epsilon}$ and $\frac{\partial F_y}{\partial \epsilon}$ at a minimum of three different values of the whirl frequency "Ω." Interpolation of these two derivatives as parabolic expressions of "Ω," using curve fitting techniques, leads to the rotordynamic coefficients by simply equating the different terms in these expressions to those on the right-hand sides of Eqs. (3) and (4). It is therefore clear that the fundamental problem here is that of computing the rate (with respect to the virtual eccentricity "$\epsilon$") at which the fluid reaction forces are developed on the whirling rotor (Fig. 1). The procedure is initialized by solving the flow-governing equations in the undisturbed rotation mode as presented next.

**Choice of the Coordinate Axes.** The flow equations are cast in a frame of reference that is consistent with the annular gap geometry in the disturbed-rotor operation mode. As shown in Fig. 3(*a*), the reference axes are attached to the displaced rotor and are, therefore, of the rotating-translating, or simply whirling, type. The rotational speed, in this case, is numerically equal to the whirl frequency "Ω" and the translation is identical to that of the rotor axis. As seen, the clearance gap flow field, viewed in this frame of reference, is now steady at all times, despite the apparent time dependency of the absolute flow field when viewed in a stationary frame of reference.

Motion of the coordinate axes, in the general manner just described, takes place only after the rotor has entered its eccentric operation mode. However, it is only the axes rotation that prevails in the centered-rotor mode (Fig. 3(*b*)), in which case "Ω" is to be viewed as an arbitrary frequency.

The choice of a rotating-translating frame of reference does not imply the need to solve the flow-governing equations in the physically distorted clearance gap (e.g., Dietzen et al., (1987). The fact, however, is that this choice, despite the complex nature of the flow equations it produces (as will be seen next), makes it easier to develop the perturbation model as it ensures consistency of the unperturbed and perturbed flow fields, with the difference between the two fields being a result of only the rotor eccentricity (Fig. 3). Note that this consistency requirement can alternately be ensured by solving the simple axisymmetric flow field in the undistorted passage (Baskharone and Hensel, 1991) and then casting this "zeroth-order" solution in the frame of reference defined above (Hensel, 1990). This procedure was implemented during execution of the computer code for the substantial reduction in the core and CPU time consumption it provides.

**Flow-Governing Equations.** The swirling flow in the undistorted rotor-to-housing gap (Fig. 3(*b*)) is assumed adiabatic, incompressible and generally turbulent. The momentum and mass conservation equations can therefore be expressed in the rotating frame of reference (noting that "Ω" in Fig. 3(*b*) is negative) as follows:

$$\hat{u}\frac{\partial u}{\partial x}+\hat{v}\frac{\partial u}{\partial y}+\hat{w}\frac{\partial u}{\partial z}+2\Omega v-\Omega^2 x=-\frac{1}{\rho}\frac{\partial p}{\partial x}+\nu_e\nabla^2 u$$
$$+2\frac{\partial \nu_t}{\partial x}\frac{\partial u}{\partial x}+\frac{\partial \nu_t}{\partial y}\left(\frac{\partial u}{\partial y}+\frac{\partial v}{\partial x}\right)+\frac{\partial \nu_t}{\partial z}\left(\frac{\partial u}{\partial z}+\frac{\partial w}{\partial x}\right) \tag{5}$$

$$\hat{u}\frac{\partial v}{\partial x}+\hat{v}\frac{\partial v}{\partial y}+\hat{w}\frac{\partial v}{\partial z}-2\Omega u-\Omega^2 y=-\frac{1}{\rho}\frac{\partial p}{\partial x}+\nu_e\nabla^2 v$$
$$+2\frac{\partial \nu_t}{\partial y}\frac{\partial v}{\partial y}+\frac{\partial \nu_t}{\partial x}\left(\frac{\partial u}{\partial y}+\frac{\partial v}{\partial x}\right)+\frac{\partial \nu_t}{\partial z}\left(\frac{\partial v}{\partial z}+\frac{\partial w}{\partial y}\right) \tag{6}$$

$$\hat{u}\frac{\partial w}{\partial x}+\hat{v}\frac{\partial w}{\partial y}+\hat{w}\frac{\partial w}{\partial z}=-\frac{1}{\rho}\frac{\partial p}{\partial z}+\nu_e\nabla^2 w$$
$$+2\frac{\partial \nu_t}{\partial z}\frac{\partial w}{\partial z}+\frac{\partial \nu_t}{\partial x}\left(\frac{\partial u}{\partial z}+\frac{\partial w}{\partial x}\right) \tag{7}$$

$$\frac{\partial u}{\partial x}+\frac{\partial v}{\partial y}+\frac{\partial w}{\partial z}=0 \tag{8}$$

where

$u$, $v$, $w$ are the relative velocity components
$p$ is the static pressure
Ω is the rotational frequency of the coordinate axes (to be set equal to the rotor whirl frequency once the rotor eccentricity prevails)
$\nu_t$, $\nu_e$ are the eddy and effective coefficients of kinematic viscosity, respectively

with the symbol (^) designating values that are carried over from a previous iteration or an initial guess for the purpose of successively linearizing the momentum equations. As seen, the axes rotational frequency "Ω" is part of these equations, which is a result of including the centripetal and Coriolis acceleration effects in this case.

**Turbulence Closure.** Simulation of the flow turbulence is based on the algebraic eddy-viscosity turbulence model by Baldwin and Lomax (1978). However, an adjustment in this vorticity-based model was implemented whereby the relative, as opposed to the absolute, vorticity was used to calculate the mixing length in the fluid layer that is adjacent to a solid surface. Equally important in implementing the turbulence model was the analysis of the near-wall zone which was conceptually based on the approach by Benim and Zinser (1985). Further details of the turbulence closure and the near-wall flow analysis are covered by Baskharone and Hensel (1991).

**Boundary Conditions.** The major difference between the two problem configurations in Fig. 2 is in the multiple entry/departure nature of the flow domain associated with the centrifugal impeller case. Uniqueness of the solution, under such circumstances, was described and attained by Baskharone and Hensel (1989) through a specific set of boundary conditions over the flow-permeable segments of the domain boundary. Boundary conditions pertaining to the annular seal problem include known profiles of inlet velocity components and zero streamwise diffusion of the exit velocity vector. The latter replaces a zero velocity gradient exit condition which would imply a fully developed flow at this station and may, in this sense, be accurate only for sufficiently long seals.

The last category of boundary conditions concerns the rotor and housing surfaces and is created by the rotation of the coordinate axes. Referring to Fig. 3(*b*), the housing surface to an observer in the rotating frame of reference, will no longer appear stationary, but will rather possess a relative velocity component "$\Omega b$" as indicated in the figure, where "$b$" is the housing radius. Considering the case of what would amount to forward whirl (as the rotor axis becomes eccentric), the rotor surface in Fig. 3(*b*) would appear to the same observer as rotating at an angular speed that is less than the rotor operating speed "$\omega$" by the amount "$\Omega$." The rotor surface velocity in this case is $(\omega - \Omega)a$, where "$a$" is the rotor radius.

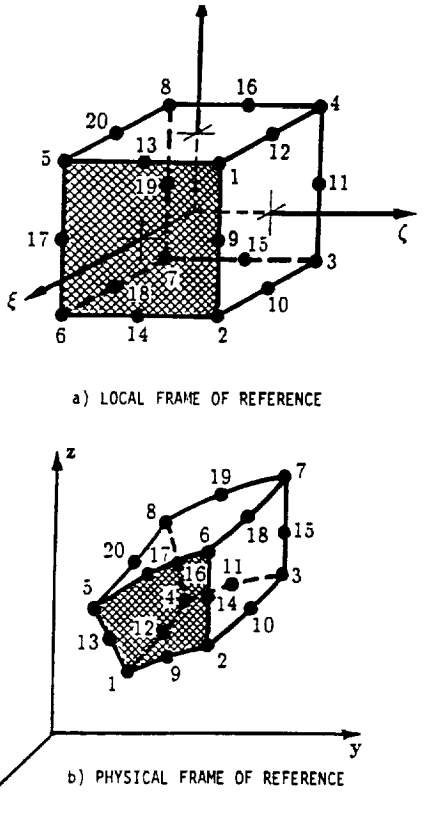


Fig. 4 Quadrilateral curve-sided isoparametric finite element

**Finite-Element Formulation.** The finite-element model is constructed with the twenty-node quadrilateral element in Fig. 4 as the discretization unit. The procedure is initiated by creating the finite-element discretization model corresponding to the centered-rotor operation mode as shown in Fig. 5(*a*) for a generally-shaped rotor. Within a typical "undistorted" finite element in this figure, let the cartesian-to-local spatial coordinate mapping (Fig. 4) be defined as follows:

$$x = \sum_{i=1}^{20} N_i x_i, \quad y = \sum_{i=1}^{20} N_i y_i, \quad z = \sum_{i=1}^{20} N_i z_i \tag{9}$$

where $N_i$ are quadratic "shape" functions (Zienkiewicz, 1971) of the local coordinates $\zeta$, $\eta$, and $\xi$ (Fig. 4). Conversion of the spatial derivatives is, in this case, defined as follows:

$$\begin{Bmatrix} \frac{\partial}{\partial x} \\ \frac{\partial}{\partial y} \\ \frac{\partial}{\partial z} \end{Bmatrix} = [T] \begin{Bmatrix} \frac{\partial}{\partial \zeta} \\ \frac{\partial}{\partial \eta} \\ \frac{\partial}{\partial \xi} \end{Bmatrix} \tag{10}$$

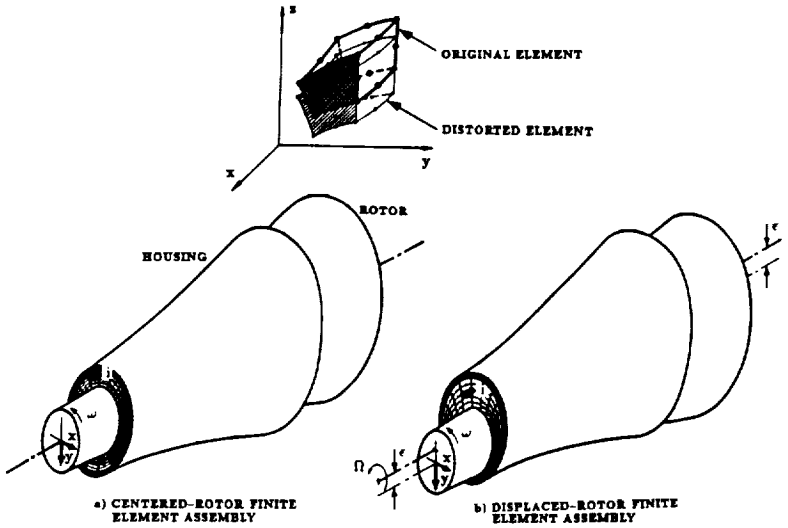


Fig. 5 Distortion of the finite elements as a result of the rotor eccentricity in a general fluid/rotor interaction problem

where the components of the matrix $[T]$ are as follows:

$$T_{11}=\frac{1}{|J|}\left(\sum_{i=1}^{20}\frac{\partial N_i}{\partial\eta}y_i\sum_{i=1}^{20}\frac{\partial N_i}{\partial\xi}z_i-\sum_{i=1}^{20}\frac{\partial N_i}{\partial\xi}y_i\sum_{i=1}^{20}\frac{\partial N_i}{\partial\eta}z_i\right)$$

$$T_{12}=\frac{1}{|J|}\left(\sum_{i=1}^{20}\frac{\partial N_i}{\partial\xi}y_i\sum_{i=1}^{20}\frac{\partial N_i}{\partial\zeta}z_i-\sum_{i=1}^{20}\frac{\partial N_i}{\partial\zeta}y_i\sum_{i=1}^{20}\frac{\partial N_i}{\partial\xi}z_i\right)$$

$$T_{13}=\frac{1}{|J|}\left(\sum_{i=1}^{20}\frac{\partial N_i}{\partial\zeta}y_i\sum_{i=1}^{20}\frac{\partial N_i}{\partial\eta}z_i-\sum_{i=1}^{20}\frac{\partial N_i}{\partial\eta}y_i\sum_{i=1}^{20}\frac{\partial N_i}{\partial\zeta}z_i\right)$$

$$T_{21}=\frac{1}{|J|}\left(\sum_{i=1}^{20}\frac{\partial N_i}{\partial\xi}x_i\sum_{i=1}^{20}\frac{\partial N_i}{\partial\eta}z_i-\sum_{i=1}^{20}\frac{\partial N_i}{\partial\eta}x_i\sum_{i=1}^{20}\frac{\partial N_i}{\partial\xi}z_i\right)$$

$$T_{22}=\frac{1}{|J|}\left(\sum_{i=1}^{20}\frac{\partial N_i}{\partial\zeta}x_i\sum_{i=1}^{20}\frac{\partial N_i}{\partial\xi}z_i-\sum_{i=1}^{20}\frac{\partial N_i}{\partial\xi}x_i\sum_{i=1}^{20}\frac{\partial N_i}{\partial\zeta}z_i\right)$$

$$T_{23}=\frac{1}{|J|}\left(\sum_{i=1}^{20}\frac{\partial N_i}{\partial\eta}x_i\sum_{i=1}^{20}\frac{\partial N_i}{\partial\zeta}z_i-\sum_{i=1}^{20}\frac{\partial N_i}{\partial\zeta}x_i\sum_{i=1}^{20}\frac{\partial N_i}{\partial\eta}z_i\right)$$

$$T_{31}=\frac{1}{|J|}\left(\sum_{i=1}^{20}\frac{\partial N_i}{\partial\eta}x_i\sum_{i=1}^{20}\frac{\partial N_i}{\partial\xi}y_i-\sum_{i=1}^{20}\frac{\partial N_i}{\partial\xi}x_i\sum_{i=1}^{20}\frac{\partial N_i}{\partial\eta}y_i\right)$$

$$T_{32}=\frac{1}{|J|}\left(\sum_{i=1}^{20}\frac{\partial N_i}{\partial\xi}x_i\sum_{i=1}^{20}\frac{\partial N_i}{\partial\zeta}y_i-\sum_{i=1}^{20}\frac{\partial N_i}{\partial\zeta}x_i\sum_{i=1}^{20}\frac{\partial N_i}{\partial\xi}y_i\right)$$

$$T_{33}=\frac{1}{|J|}\left(\sum_{i=1}^{20}\frac{\partial N_i}{\partial\zeta}x_i\sum_{i=1}^{20}\frac{\partial N_i}{\partial\eta}y_i-\sum_{i=1}^{20}\frac{\partial N_i}{\partial\eta}x_i\sum_{i=1}^{20}\frac{\partial N_i}{\partial\zeta}y_i\right)$$

with $|J|$ being the Jacobian of transformation.

Next the flow variables are interpolated within the typical element in a similar fashion. Guided by the Ladyshenskaya-Babuska-Brezzi compatibility requirements (Carey and Oden, 1986), as applied to the current problem, the velocity components and pressure are expressed as follows:

$$u=\sum_{i=1}^{20}N_iu_i,\quad v=\sum_{i=1}^{20}N_iv_i,$$

$$w=\sum_{i=1}^{20}N_iw_i,\quad p=\sum_{k=1}^{8}M_kp_k \tag{11}$$

where the interpolants "$M_k$" appearing in the pressure expressions are the linear shape functions associated with the finite element corner nodes (Zienkiewwicz, 1971).

The error functions produced by the unperturbed flow governing equations as a result of the interpolation expressions above, are then made orthogonal to a special set of weight functions $W_i$ throughout the finite element. In constructing these functions, the so-called error consistency criterion of Hood and Taylor (1974) is implemented, whereby the element linear shape functions, $M_i$, are used in conjunction with the continuity equation. The weight functions used with the momentum equations, on the other hand, are of the upwind form (Baskharone and Hensel, 1991) when applied to the convection terms, and are identical to the element quadratic shape functions "$N_i$" for all other terms.

The orthogonality conditions stated above constitute the elemental set of finite element equations, which can be written as follows:

$$[a_1]\{u\}+[a_2]\{v\}+[a_3]\{w\}+[a_4]\{p\}=\{b_1\} \tag{12}$$

$$[a_5]\{u\}+[a_6]\{v\}+[a_7]\{w\}+[a_8]\{p\}=\{b_2\} \tag{13}$$

$$[a_9]\{u\}+[a_{10}]\{v\}+[a_{11}]\{w\}+[a_{12}]\{p\}=\{b_3\} \tag{14}$$

$$[a_{13}]\{u\}+[a_{14}]\{v\}+[a_{15}]\{w\}=0 \tag{15}$$

where:

$$a_1)_{i,j}=\int_{V(e)}\{\hat{\nu}_e[\mathbf{F}(N_i)\mathbf{F}(N_j)+\mathbf{G}(N_i)\mathbf{G}(N_j)+\mathbf{H}(N_i)\mathbf{H}(N_j)]$$
$$-N_i[\mathbf{G}(\hat{\nu}_t)\mathbf{G}(N_j)+\mathbf{H}(\hat{\nu}_t)\mathbf{H}(N_j)+2\mathbf{F}(\hat{\nu}_t)\mathbf{F}(N_j)]$$
$$+W_i[\hat{u}\mathbf{F}(N_j)+\hat{v}\mathbf{G}(N_j)+\hat{w}\mathbf{H}(N_j)]\}dV$$

$$a_2)_{i,j}=\int_{V(e)}-N_i[\mathbf{G}(\hat{\nu}_t)\mathbf{F}(N_j)-2\Omega N_j]dV$$

$$a_3)_{i,j}=\int_{V(e)}-N_i\mathbf{H}(\hat{\nu}_t)\mathbf{F}(N_j)dV$$

$$a_4)_{i,k}=\int_{V(e)}\frac{1}{\rho}N_i\mathbf{F}(M_k)dV$$

$$a_5)_{i,j}=\int_{V(e)}-N_i[\mathbf{F}(\hat{\nu}_t)\mathbf{G}(N_j)+2\Omega N_j]dV$$

$$a_6)_{i,j}=\int_{V(e)}\{\hat{\nu}_e[\mathbf{F}(N_i)\mathbf{F}(N_j)+\mathbf{G}(N_i)\mathbf{G}(N_j)+\mathbf{H}(N_i)\mathbf{H}(N_j)]$$
$$-N_i[\mathbf{F}(\hat{\nu}_t)\mathbf{F}(N_j)+\mathbf{H}(\hat{\nu}_t)\mathbf{H}(N_j)+2\mathbf{G}(\hat{\nu}_t)\mathbf{G}(N_j)]$$
$$+W_i[\hat{u}\mathbf{F}(N_j)+\hat{v}\mathbf{G}(N_j)+\hat{w}\mathbf{H}(N_j)]\}dV$$

$$a_7)_{i,j}=\int_{V(e)}-N_i\mathbf{H}(\hat{\nu}_t)\mathbf{G}(N_j)dV$$

$$a_8)_{i,k}=\int_{V(e)}\frac{1}{\rho}N_i\mathbf{G}(M_k)dV$$

$$a_9)_{i,j}=\int_{V(e)}-N_i\mathbf{F}(\hat{\nu}_t)\mathbf{H}(N_j)dV$$

$$a_{10})_{i,j}=\int_{V(e)}-N_i\mathbf{G}(\hat{\nu}_t)\mathbf{H}(N_j)dV$$

$$a_{11})_{i,j}=\int_{V(e)}\{\hat{\nu}_e[\mathbf{F}(N_i)\mathbf{F}(N_j)+\mathbf{G}(N_i)\mathbf{G}(N_j)+\mathbf{H}(N_i)\mathbf{H}(N_j)]$$
$$-N_i[\mathbf{F}(\hat{\nu}_t)\mathbf{F}(N_j)+\mathbf{G}(\hat{\nu}_t)\mathbf{G}(N_j)+2\mathbf{H}(\hat{\nu}_t)\mathbf{H}(N_j)]$$
$$+W_i[\hat{u}\mathbf{F}(N_j)+\hat{v}\mathbf{G}(N_j)+\hat{w}\mathbf{H}(N_j)]\}dV$$

$$a_{12})_{i,k}=\int_{V(e)}\frac{1}{\rho}N_i\mathbf{H}(M_k)dV$$

$$a_{13})_{k,j}=\int_{V(e)}M_k\mathbf{F}(N_j)dV$$

$$a_{14})_{k,j}=\int_{V(e)}M_k\mathbf{G}(N_j)dV$$

$$a_{15})_{k,j}=\int_{V(e)}M_k\mathbf{H}(N_j)dV$$

$$b_1)_i=\int_{S(e)}\hat{\nu}_eN_i(\mathbf{n}\cdot\nabla u)dS+\Omega^2\int_{V(e)}N_i\left(\sum_{l=1}^{20}N_lx_l\right)dV$$

$$b_2)_i=\int_{S(e)}\hat{\nu}_eN_i(\mathbf{n}\cdot\nabla v)dS+\Omega^2\int_{V(e)}N_i\left(\sum_{l=1}^{20}N_ly_l\right)dV$$

$$b_3)_i=\int_{S(e)}\hat{\nu}_eN_i(\mathbf{n}\cdot\nabla w)dS$$

where $(e)$ refers to a typical finite element, $i=1,2,\ldots,20$, $j=1,2,\ldots,20$, $k=1,2,\ldots,8$, the superscript $(\hat{})$ refers to a value that is known from a previous iteration or an initial guess, $dS$ is the differential element of surface area and $\mathbf{n}$ is the local unit vector normal to the boundary (Fig. 4). Also, the volume differential $dV$ and the operators $\mathbf{F}$, $\mathbf{G}$, and $\mathbf{H}$ are defined as follows:

$$dV=|J|d\zeta d\eta d\xi$$

$$\mathbf{F}=T_{11}\frac{\partial}{\partial\zeta}+T_{12}\frac{\partial}{\partial\eta}+T_{13}\frac{\partial}{\partial\xi} \tag{16}$$

$$\mathbf{G} = T_{21}\frac{\partial}{\partial\zeta} + T_{22}\frac{\partial}{\partial\eta} + T_{23}\frac{\partial}{\partial\xi} \tag{17}$$

$$\mathbf{H} = T_{31}\frac{\partial}{\partial\zeta} + T_{32}\frac{\partial}{\partial\eta} + T_{33}\frac{\partial}{\partial\xi} \tag{18}$$

It should be pointed out that expanding the finite element equations in terms of the operators **F**, **G**, and **H**, defined above, is consistent with, and indeed simplifies, the procedure leading to the perturbed version of the flow equations, as will be seen later in this section.

Equations (12) through (15) can be rewritten in the following compact form:

$$[a]\{\phi\} = \{b\} \tag{19}$$

where the vector $\{\phi\}$ contains the nodal values of velocity components and static pressure that are associated with the typical element "$e$." The global form of the elemental set of Eqs. (19) is obtained by assembling all finite element contributions, and introducing the various boundary conditions, at which point the equations are expressible in the following form:

$$[A]\{\Phi\} = \{B\} \tag{20}$$

**Perturbation Model.** Referring to Eqs. (3) and (4), determination of the rotordynamic coefficients reduces to the fundamental problem of computing the rate (with respect to the virtual eccentricity "$\epsilon$") at which the fluid forces are exerted on a cylindrically-whirling rotor. This objective is achieved through the perturbation analysis outlined next.

The current model is centered around the manner in which the finite-element Eqs. (20) are altered as a result of the rotor virtual eccentricity "$\epsilon$" (Fig. 5). Under such eccentricity, each finite element will yield a perturbed set of equations. The assembled form of these equations can generally be written as follows:

$$([A] + \epsilon[\bar{A}])(\{\Phi\} + \{\delta\Phi\}) = (\{B\} + \epsilon\{\bar{B}\}) \tag{21}$$

where $\{\Phi\}$ is the global vector containing the nodal values of the velocity components and pressure. Combination of Eqs. (20) and (21) gives rise to the following:

$$\frac{\partial\{\Phi\}}{\partial\epsilon} = \lim_{\epsilon\to 0}\left\{\frac{\delta\Phi}{\epsilon}\right\} = [A]^{-1}(\{\bar{B}\} - [\bar{A}]\{\Phi\}) \tag{22}$$

Equation (22) reveals that the differential changes by which the flow variables, namely the velocity components and pressure, vary as a result of the rotor eccentricity can be achieved knowing the undisturbed flow solution vector $\{\Phi\}$ which is known at this point, a matrix $[\bar{A}]$ and a vector $\{\bar{B}\}$ with the latter two arrays representing, respectively, the effect of distorting the finite elements, and the changes in the flow kinematics as a result of the whirling motion of the coordinate axes (Fig. 3($a$)). The arrays $[\bar{A}]$ and $\{\bar{B}\}$ are derived next as part of the procedure to compute the rotordynamic coefficients.

Consider a distorted finite element in the clearance gap corresponding to the eccentric-rotor operation mode (Fig. 5). To an observer in the whirling frame of reference, the typical node "$i$" of this element will now be displaced by an amount that is a function of the rotor virtual eccentricity "$\epsilon$" and the node original location in the cross-flow plane. Referred to the displaced axes position in Fig. 5($b$), the new nodal coordinates $\mathbf{x}_i$, $\mathbf{y}_i$, and $\mathbf{z}_i$ can be related to those prior to the rotor eccentricity as follows:

$$\mathbf{x}_i = x_i, \quad \mathbf{y}_i = y_i + \lambda_i\epsilon \quad \text{and} \quad \mathbf{z}_i = z_i$$

where $\lambda_i$ is a fraction that varies from zero, for nodes on the rotor surface, to $-1.0$ for those on the housing surface, since the housing, to an observer in the whirling frame of reference, is the surface that undergoes the virtual displacement (note the positive direction of the $y$-axis in Fig. 4). The local-to-cartesian transformation Jacobian $|J|$ can correspondingly be written for a distorted finite element as $|J_1|$ where:

$$|J_1| = |J| + \epsilon|\bar{J}| \tag{24}$$

in which the Jacobian $|J|$ is that of the undistorted element, and $|\bar{J}|$ is as follows:

$$|\bar{J}| = \begin{vmatrix} \sum_{i=1}^{20}\frac{\partial N_i}{\partial\zeta}x_i & \sum_{i=1}^{20}\frac{\partial N_i}{\partial\zeta}\lambda_i & \sum_{i=1}^{20}\frac{\partial N_i}{\partial\zeta}z_i \\ \sum_{i=1}^{20}\frac{\partial N_i}{\partial\eta}x_i & \sum_{i=1}^{20}\frac{\partial N_i}{\partial\eta}\lambda_i & \sum_{i=1}^{20}\frac{\partial N_i}{\partial\eta}z_i \\ \sum_{i=1}^{20}\frac{\partial N_i}{\partial\xi}x_i & \sum_{i=1}^{20}\frac{\partial N_i}{\partial\xi}\lambda_i & \sum_{i=1}^{20}\frac{\partial N_i}{\partial\xi}z_i \end{vmatrix}$$

A new spatial derivative operator, that is equivalent to that in Eq. (10), can now be derived as follows:

$$\begin{Bmatrix} \frac{\partial}{\partial x} \\ \frac{\partial}{\partial y} \\ \frac{\partial}{\partial z} \end{Bmatrix} = ([T] + \epsilon[P]) \begin{Bmatrix} \frac{\partial}{\partial\zeta} \\ \frac{\partial}{\partial\eta} \\ \frac{\partial}{\partial\xi} \end{Bmatrix} \tag{25}$$

where the matrix $[T]$ is the same as described in conjunction with Eq. (10), while the matrix $[P]$ is defined as follows:

$$P_{11} = \frac{1}{|J|}\left(\sum_{i=1}^{20}\frac{\partial N_i}{\partial\eta}\lambda_i\sum_{i=1}^{20}\frac{\partial N_i}{\partial\xi}z_i - \sum_{i=1}^{20}\frac{\partial N_i}{\partial\xi}\lambda_i\sum_{i=1}^{20}\frac{\partial N_i}{\partial\eta}z_i\right) - \frac{|\bar{J}|}{|J|^2}T_{11}$$

$$P_{12} = \frac{1}{|J|}\left(\sum_{i=1}^{20}\frac{\partial N_i}{\partial\xi}\lambda_i\sum_{i=1}^{20}\frac{\partial N_i}{\partial\zeta}z_i - \sum_{i=1}^{20}\frac{\partial N_i}{\partial\zeta}\lambda_i\sum_{i=1}^{20}\frac{\partial N_i}{\partial\xi}z_i\right) - \frac{|\bar{J}|}{|J|^2}T_{12}$$

$$P_{13} = \frac{1}{|J|}\left(\sum_{i=1}^{20}\frac{\partial N_i}{\partial\zeta}\lambda_i\sum_{i=1}^{20}\frac{\partial N_i}{\partial\eta}z_i - \sum_{i=1}^{20}\frac{\partial N_i}{\partial\eta}\lambda_i\sum_{i=1}^{20}\frac{\partial N_i}{\partial\zeta}z_i\right) - \frac{|\bar{J}|}{|J|^2}T_{13}$$

$$P_{21} = -\frac{|\bar{J}|}{|J|^2}T_{21}$$

$$P_{22} = -\frac{|\bar{J}|}{|J|^2}T_{22}$$

$$P_{23} = -\frac{|\bar{J}|}{|J|^2}T_{23}$$

$$P_{31} = \frac{1}{|J|}\left(\sum_{i=1}^{20}\frac{\partial N_i}{\partial\eta}x_i\sum_{i=1}^{20}\frac{\partial N_i}{\partial\xi}\lambda_i - \sum_{i=1}^{20}\frac{\partial N_i}{\partial\xi}x_i\sum_{i=1}^{20}\frac{\partial N_i}{\partial\eta}\lambda_i\right) - \frac{|\bar{J}|}{|J|^2}T_{31}$$

$$P_{32} = \frac{1}{|J|}\left(\sum_{i=1}^{20}\frac{\partial N_i}{\partial\xi}x_i\sum_{i=1}^{20}\frac{\partial N_i}{\partial\zeta}\lambda_i - \sum_{i=1}^{20}\frac{\partial N_i}{\partial\zeta}x_i\sum_{i=1}^{20}\frac{\partial N_i}{\partial\xi}\lambda_i\right) - \frac{|\bar{J}|}{|J|^2}T_{32}$$

$$P_{33} = \frac{1}{|J|}\left(\sum_{i=1}^{20}\frac{\partial N_i}{\partial\zeta}x_i\sum_{i=1}^{20}\frac{\partial N_i}{\partial\eta}\lambda_i - \sum_{i=1}^{20}\frac{\partial N_i}{\partial\eta}x_i\sum_{i=1}^{20}\frac{\partial N_i}{\partial\zeta}\lambda_i\right) - \frac{|\bar{J}|}{|J|^2}T_{33}$$

Using the Jacobian of coordinate transformation and operator of spatial derivatives for the distorted element (Eqs. (24) and (25), respectively) as well as the general interpolation expressions (11), in the flow-governing Eqs. (5 through 8), and reapplying the weighted-residual procedure, the distorted element equations can be written (upon separation of terms containing "$\epsilon$" and ignoring high order terms) as follows:

$$([a]+\epsilon[\bar{a}])(\{\phi\}+\{\delta\phi\})=(\{b\}+\epsilon\{\bar{b}\}) \tag{26}$$

where the matrix $\{\bar{a}\}$ and the vector $\{\bar{b}\}$ are produced by the distortion in the finite element shape, while the non-zero entries of the vector $\{\bar{b}\}$ are associated with some distortion-related entries which are explained later in this section. The vector $\{\bar{b}\}$ also contains the effect of an additional acceleration component that is created by the motion of the coordinate axes origin around the housing centerline. The vector $\{\delta\phi\}$ in Eq. (26) contains the differential changes in the nodal values of velocity components and pressure that are created by the virtual eccentricity.

Noting that the matrix $[\bar{a}]$ is similar, in construction, to $[a]$ in Eq. (19), the earlier can consistently be viewed as composed of submatrices $[\bar{a}_1]$ through $[\bar{a}_{15}]$, which correspond to those in Eqs. (12) through (15), and are defined as follows:

$$\begin{aligned}\bar{a}_1)_{i,j}=a_1^*)_{i,j}+\int_{V(e)}\{&\hat{\nu}_e[\mathbf{F}(N_i)\mathbf{I}(N_j)\\&+\mathbf{I}(N_i)\mathbf{F}(N_j)+\mathbf{G}(N_i)\mathbf{J}(N_j)\\&+\mathbf{J}(N_i)\mathbf{G}(N_j)+\mathbf{H}(N_i)\mathbf{K}(N_j)+\mathbf{K}(N_i)\mathbf{H}(N_j)]-N_i[\mathbf{G}(\hat{\nu}_t)\mathbf{J}(N_j)\\&+\mathbf{J}(\hat{\nu}_t)\mathbf{G}(N_j)+\mathbf{H}(\hat{\nu}_t)\mathbf{K}(N_j)+\mathbf{K}(\hat{\nu}_t)\mathbf{H}(N_j)\\&+2\mathbf{F}(\hat{\nu}_t)\mathbf{I}(N_j)+2\mathbf{I}(\hat{\nu}_t)\mathbf{F}(N_j)]+W_i[\hat{u}\mathbf{I}(N_j)\\&+\hat{v}\mathbf{J}(N_j)+\hat{w}\mathbf{K}(N_j)]\}dV\end{aligned}$$

$$\bar{a}_2)_{i,j}=a_2^*)_{i,j}-\int_{V(e)}N_i[\mathbf{G}(\hat{\nu}_t)\mathbf{I}(N_j)+\mathbf{J}(\hat{\nu}_t)\mathbf{F}(N_j)]dV$$

$$\bar{a}_3)_{i,j}=a_3^*)_{i,j}-\int_{V(e)}N_i[\mathbf{H}(\hat{\nu}_t)\mathbf{I}(N_j)+\mathbf{K}(\hat{\nu}_t)\mathbf{F}(N_j)]dV$$

$$\bar{a}_4)_{i,k}=a_4^*)_{i,k}+\int_{V(e)}\frac{1}{\rho}N_i\mathbf{I}(M_k)dV$$

$$\bar{a}_5)_{i,j}=a_5^*)_{i,j}-\int_{V(e)}N_i[\mathbf{F}(\hat{\nu}_t)\mathbf{J}(N_j)+\mathbf{I}(\hat{\nu}_t)\mathbf{G}(N_j)]dV$$

$$\begin{aligned}\bar{a}_6)_{i,j}=a_6^*)_{i,j}+\int_{V(e)}\{&\hat{\nu}_e[\mathbf{F}(N_i)\mathbf{I}(N_j)\\&+\mathbf{I}(N_i)\mathbf{F}(N_j)+\mathbf{G}(N_i)\mathbf{J}(N_j)\\&+\mathbf{J}(N_i)\mathbf{G}(N_j)+\mathbf{H}(N_i)\mathbf{K}(N_j)+\mathbf{K}(N_i)\mathbf{H}(N_j)]-N_i[\mathbf{F}(\hat{\nu}_t)\mathbf{I}(N_j)\\&+\mathbf{I}(\hat{\nu}_t)\mathbf{F}(N_j)+\mathbf{H}(\hat{\nu}_t)\mathbf{K}(N_j)+\mathbf{K}(\hat{\nu}_t)\mathbf{H}(N_j)\\&+2\mathbf{G}(\hat{\nu}_t)\mathbf{J}(N_j)+2\mathbf{J}(\hat{\nu}_t)\mathbf{G}(N_j)]+W_i[\hat{u}\mathbf{I}(N_j)\\&+\hat{v}\mathbf{J}(N_j)+\hat{w}\mathbf{K}(N_j)]\}dV\end{aligned}$$

$$\bar{a}_7)_{i,j}=a_7^*)_{i,j}-\int_{V(e)}N_i[\mathbf{H}(\hat{\nu}_t)\mathbf{J}(N_j)+\mathbf{K}(\hat{\nu}_t)\mathbf{G}(N_j)]dV$$

$$\bar{a}_8)_{i,k}=a_8^*)_{i,k}-\int_{V(e)}\frac{1}{\rho}N_i\mathbf{J}(M_k)dV$$

$$\bar{a}_9)_{i,j}=a_9^*)_{i,j}-\int_{V(e)}N_i[\mathbf{F}(\hat{\nu}_t)\mathbf{K}(N_j)+\mathbf{I}(\hat{\nu}_t)\mathbf{H}(N_j)]dV$$

$$\bar{a}_{10})_{i,j}=a_{10}^*)_{i,j}-\int_{V(e)}N_i[\mathbf{G}(\hat{\nu}_t)\mathbf{K}(N_j)+\mathbf{J}(\hat{\nu}_t)\mathbf{H}(N_j)]dV$$

$$\begin{aligned}\bar{a}_{11})_{i,j}=a_{11}^*)_{i,j}+\int_{V(e)}\{&\hat{\nu}_e[\mathbf{F}(N_i)\mathbf{I}(N_j)\\&+\mathbf{I}(N_i)\mathbf{F}(N_j)+\mathbf{G}(N_i)\mathbf{J}(N_j)\\&+\mathbf{J}(N_i)\mathbf{G}(N_j)+\mathbf{H}(N_i)\mathbf{K}(N_j)+\mathbf{K}(N_i)\mathbf{H}(N_j)]-N_i[\mathbf{F}(\hat{\nu}_t)\mathbf{I}(N_j)\\&+\mathbf{I}(\hat{\nu}_t)\mathbf{F}(N_j)+\mathbf{G}(\hat{\nu}_t)\mathbf{J}(N_j)+\mathbf{J}(\hat{\nu}_t)\mathbf{G}(N_j)\\&+2\mathbf{H}(\hat{\nu}_t)\mathbf{K}(N_j)+2\mathbf{K}(\hat{\nu}_t)\mathbf{H}(N_j)]+W_i[\hat{u}\mathbf{I}(N_j)\\&+\hat{v}\mathbf{J}(N_j)+\hat{w}\mathbf{K}(N_j)]\}dV\end{aligned}$$

$$\bar{a}_{12})_{i,k}=a_{12}^*)_{i,k}+\int_{V(e)}\frac{1}{\rho}N_i\mathbf{K}(M_k)dV$$

$$\bar{a}_{13})_{k,j}=a_{13}^*)_{k,j}+\int_{V(e)}M_k\mathbf{I}(N_j)dV$$

$$\bar{a}_{14})_{k,j}=a_{14}^*)_{k,j}+\int_{V(e)}M_k\mathbf{J}(N_j)dV$$

$$\bar{a}_{15})_{k,j}=a_{15}^*)_{k,j}+\int_{V(e)}M_k\mathbf{K}(N_j)dV$$

where

$$dV=|J|d\zeta d\eta d\xi$$

In the these expressions, a matrix entry with an asterisk has the same form as that in Eqs. (12) through (15), with the exception that the Jacobian $|J|$ is now replaced by $|\bar{J}|$ as defined in conjunction with Eq. (24). The vector $\{\bar{b}\}$ in Eq. (26) can similarly be defined by the subvectors $\{\bar{b}_1\}$ and $\{\bar{b}_2\}$, as in Eqs. (12) through (15), as follows:

$$\bar{b}_1)_i=\Omega^2\int_{V(e)}N_i\left(\sum_{l=1}^{20}N_l x_l\right)|\bar{J}|d\zeta d\eta d\xi$$

$$\bar{b}_2)_i=\Omega^2\int_{V(e)}N_i\left(\sum_{l=1}^{20}N_l y_l\right)|\bar{J}|d\zeta d\eta d\xi$$

$$-\Omega^2\int_{V(e)}N_i\left(\sum_{l=1}^{20}N_l\lambda_l\right)dV+\Omega^2\int_{V(e)}N_i dV$$

$$\bar{b}_3)_i=0$$

where $i$ and $j$ vary from 1 to 20, while $k$ varies from 1 to 8. With the operator **F**, **G**, and **H** being those defined by Eqs. (16) through (18), the new operators **I**, **J**, and **K** are defined as follows:

$$\mathbf{I}=P_{11}\frac{\partial}{\partial\zeta}+P_{12}\frac{\partial}{\partial\eta}+P_{13}\frac{\partial}{\partial\xi} \tag{27}$$

$$\mathbf{J}=P_{21}\frac{\partial}{\partial\zeta}+P_{22}\frac{\partial}{\partial\eta}+P_{23}\frac{\partial}{\partial\xi} \tag{28}$$

$$\mathbf{K}=P_{31}\frac{\partial}{\partial\zeta}+P_{32}\frac{\partial}{\partial\eta}+P_{33}\frac{\partial}{\partial\xi} \tag{29}$$

The matrix $[P]$ is the same as defined in conjunction with Eq. (25). Of particular interest here is the construction of $\bar{b}_1)_i$, $\bar{b}_2)_i$ and $\bar{b}_3)_i$ above, as compared to that of $b_1)_i$, $b_2)_i$ and $b_3)_i$ in Eqs. (12) through (14). First, it is noted that the perturbations of the surface integrals in $b_1)_i$ and $b_2)_i$ are nonexisting in $\bar{b}_1$ and $\bar{b}_2$ since these surface integrals would have nonzero values only in the case where a nonzero normal derivative of, respectively, "$u$" or "$v$" is prescribed as a boundary condition, a situation which is not encountered in formulating the undisturbed-flow problem. Secondly, it is due to the centripetal acceleration of the rotating axes origin around the housing centerline that the last term in the $\bar{b}_2)_i$ is produced, while the other terms, in $b_1)_i$ and $b_2)_i$, result from infinitesimally-small distortions in the finite element shape as a result of the rotor eccentricity.

**Calculation of the Rotordynamic Coefficients.** Equation (22) can be rewritten in the following detailed form:

$$\frac{\partial\{\Phi\}}{\partial\epsilon}=\frac{\partial}{\partial\epsilon}\begin{Bmatrix}\{U\}\\\{V\}\\\{W\}\\\{P\}\end{Bmatrix}=[A]^{-1}(\{\bar{B}\}-[\bar{A}]\{\Phi\}) \tag{30}$$

where $\{U\}$, $\{V\}$, $\{W\}$, and $\{P\}$ are vectors containing the nodal values of the velocity components and static pressure, respectively, with the overbars signifying quantities that are associated with the perturbation in the rotor-to-housing flow field. Of all the pressure nodal values in the vector $\{P\}$ above, define a subvector $\{\mathcal{P}\}$ as composed of the pressure values at the rotor surface nodes, i.e.,

$$\{\mathcal{P}\}=\{p_i, i=1,N_s\}\subset\{P\} \tag{31}$$

where $N_s$ is the total number of corner nodes existing on the rotor surface. It is true, in this case, that $\left\{\frac{\partial\mathcal{P}}{\partial\epsilon}\right\}=\left\{\left(\frac{\partial p}{\partial\epsilon}\right)_i, i=1, N_s\right\}$ is but a subvector of the already computed global vector $\left\{\frac{\partial\Phi}{\partial\epsilon}\right\}$ in Eq. (30) and is, therefore, known as this computational step.

Next, consider the finite element face "$s$" in Fig. 6 which exists on the rotor surface in its displaced position. The pressure derivative $p_{,\epsilon}^{(s)}$ over this surface element can now be interpolated in terms of the known pressure derivatives at the four corner nodes of "$s$" as follows:

$$p_{,\epsilon}^{(s)}=\sum_{i=1}^{4}M_i(1,\eta,\xi)\left(\frac{\partial p}{\partial\epsilon}\right)_i \tag{32}$$

Summation of $p_{,\epsilon}^{(s)}$, as contributed by all finite elements sharing faces with the rotor, over the entire rotor surface yields the rate (with respect to "$\epsilon$") at which the fluid force is exerted on the rotor. This can be resolved in the "$x$" and "$y$" directions to produce the derivatives $\frac{\partial F_x}{\partial\epsilon}$ and $\frac{\partial F_y}{\partial\epsilon}$ as follows:

$$\frac{\partial F_x}{\partial\epsilon}=\sum_{i=1}^{N_s}\int_{-1}^{+1}\int_{-1}^{+1}n_x(\eta,\xi)p_{,\epsilon}(\eta,\xi)G(\eta,\xi)d\eta d\xi \tag{33}$$

$$\frac{\partial F_y}{\partial\epsilon}=\sum_{i=1}^{N_s}\int_{-1}^{+1}\int_{-1}^{+1}n_y(\eta,\xi)p_{,\epsilon}(\eta,\xi)G(\eta,\xi)d\eta d\xi \tag{34}$$

where $n_x$ and $n_y$ are the components of the local unit vector that is normal to the rotor surface (Fig. 6). Also, the parameter $G(\eta, \xi)$ is a Jacobian-like function for cartesian-to-local area transformation, and was previously derived by Baskharone (1979) as follows:

$$G(\eta,\xi)=\left[\left(\frac{\partial y}{\partial\eta}\frac{\partial z}{\partial\xi}-\frac{\partial y}{\partial\xi}\frac{\partial z}{\partial\eta}\right)^2+\left(\frac{\partial x}{\partial\xi}\frac{\partial z}{\partial\eta}-\frac{\partial x}{\partial\eta}\frac{\partial z}{\partial\xi}\right)^2+\left(\frac{\partial x}{\partial\eta}\frac{\partial y}{\partial\xi}-\frac{\partial x}{\partial\xi}\frac{\partial y}{\partial\eta}\right)^2\right]^{1/2}$$

where the derivatives on the right-hand side are evaluated using the interpolation expressions (9) for a "$\zeta$" value of 1.0 (Fig. 6). Having computed the force derivatives (Eqs. (33) and (34) above), the requirements for computing the force coefficients ($K$, $k$, $C$, $c$, $M$, $m$) are, by reference to Eqs. (3) and (4), complete.

## Concluding Remarks

The virtually deformable finite element concept introduced in this paper offers a new and powerful tool with which the fluid/structure interaction effects can be captured. Versatility of the computational model was illustrated through two typical problem categories where a cylindrically whirling rotor was analyzed. In this, and all similar disturbance modes, the object of the perturbation analysis is the finite-element equivalent of the flow governing equations in the rotor-to-housing gap.

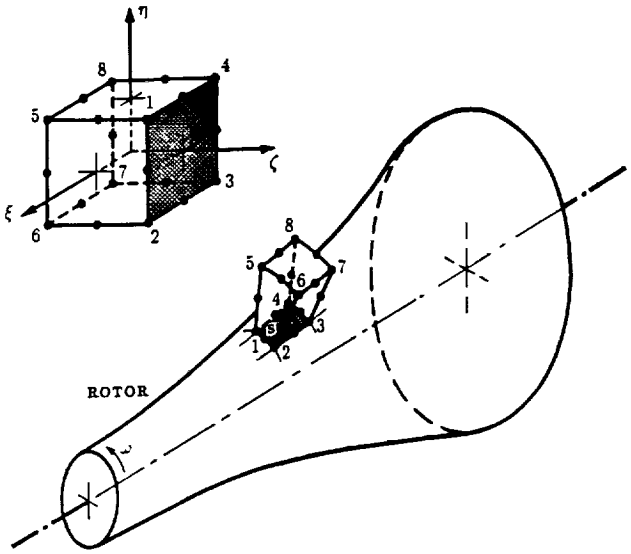


Fig. 6 Pressure integration segment over the surface of a generally shaped rotor

Sample results of the current analysis are contained in a companion paper (Baskharone and Hensel, 1991). Under focus in this paper is the rotordynamic coefficient of an annular seal under a cylindrical type of rotor whirl. It is undoubtedly clear, at this point, that tilting-related, or simply moment, coefficients of a conically-whirling rotor would equally be calculable using the virtual finite-element distortion concept developed in the current study. Utilization of the concept in this case would lead to the differential changes in the fluid forces along the rotor axis which, in turn, exert differential moments around two perpendicular axes at the center of the tilting motion. The moment coefficients are eventually computed by integrating these moments along the axis and relating the outcome to the rotor angular displacement and its time derivatives. It is further emphasized that the same concept is potentially applicable to other modes of fluid-induced vibrations. An example of these modes is the axial oscillation of the impeller-shroud assembly of the centrifugal pump to which reference was made in this paper. The oscillatory motion is, in this case, caused by the fluid forces on the front (or shroud) side of the impeller as well as the back face of the impeller disk. An equally detailed computational model that is capable of analyzing such vibration modes is currently non-existing in the open literature.

## Acknowledgment

This study was funded by NASA-Marshall Space Flight Center (Huntsville, Alabama), contract no. NAS8-37821, NASA monitor: James Cannon. Partial funding was also provided by the Houston Advanced Rsearch Center (The Woodlands, Texas), grant no. 88-025.

## References

Baldwin, B. S., and Lomax, H., 1978, "Thin Layer Approximation and Algebraic Model for Separated Turbulent Flow," AIAA Paper No. 78-257.

Baskharone, E., 1979, "A New Approach in Turbomachinery Flow Analysis Using the Finite Element Method," Ph.D. dissertation, University of Cincinnati.

Baskharone, E. A., and Hensel, S. J., 1989, "A New Model for Leakage Prediction in Shrouded-Impeller Turbopumps," ASME JOURNAL OF FLUIDS ENGINEERING, Vol. 111, pp. 118-123.

Baskharone, E. A., and Hensel, S. J., 1991, "A Finite-Element Perturbation

Approach to Fluid/Rotor Interaction in Turbomachinery Elements. Part 2: Application," ASME JOURNAL OF FLUIDS ENGINEERING, published in this issue, pp. 362-367.

Benim, A. C., and Zinser, W., 1985, "Investigation into the Finite Element Analysis of Confined Turbulent Flow Using a $k$-$\epsilon$ Model of Turbulence," *Computer Methods in Applied Mechanics and Engineering*, Vol. 51, pp. 507-523.

Carey, G. F., and Oden, J. T., 1986, "Finite Elements: Fluid Mechanics," *The Texas Finite Element Series*, Vol. IV, Prentice-Hall.

Childs, D. W., 1983, "Finite Length Solutions for Rotordynamic Coefficients of Turbulent Annular Seals," ASME *Journal of Lubrication Technology*, Vol. 105, pp. 437-445.

Childs, D. W., 1989, "Fluid-Structure Interaction Forces at Pump-Impeller-Shroud Surfaces for Rotordynamic Calculations," ASME *Journal of Vibration, Stress and Reliability in Design*, Vol. 111, pp. 216-225.

Childs, D., and Kim, C. H., 1985, "Analysis and Testing for Rotordynamic Coefficients of Turbulent Annular Seals with Different Homogeneous Surface Roughness Treatment for Rotor and Stator Elements," ASME *Journal of Tribology*, Vol. 107, pp. 296-306.

Dietzen, F. J., and Nordmann, R., 1987, "Calculating Rotordynamic Coefficients of Seals by Finite Difference Techniques," ASME *Journal of Tribology*, Vol. 109, pp. 388-394.

Dietzen, F. J., and Nordmann, R., 1988, "A 3-Dimensional Finite-Difference Method for Calculating the Dynamic Coefficients of Seals," Presented at the Workshop on Rotordynamic Instability in High Performance Turbomachinery, Texas A&M University.

Hensel, S. J., 1986, "Rotordynamic Forces on Labyrinth Seals," M.S. thesis, Texas A&M University.

Hensel, S. J., 1990, "A New Method for Determining Rotordynamic Forces on Liquid Annular Seals," Ph.D. dissertation, Texas A&M University.

Hood, P., and Taylor, C., 1974, "Navier-Stokes Equations Using Mixed Interpolation," *Proceedings of the International Symposium on Finite Element Methods in Flow Problems*, University of Wales, Swansea, United Kingdom.

Nelson, C. C., 1985, "Rotordynamic Coefficients for Compressible Flow in Tapered Annular Seals," ASME *Journal of Tribology*, Vol. 107, pp. 318-325.

Zienkiewicz, O. C., 1971, *The Finite Element Method in Engineering Science*, McGraw-Hill.

**PAPER# 2**

# A Finite-Element Perturbation Approach to Fluid/Rotor Interaction in Turbomachinery Elements. Part 2: Application

**E. A. Baskharone**
Associate Professor.
Mem. ASME

**S. J. Hensel**[1]
Mem. ASME

Department of Mechanical Engineering,
Texas A&M University,
College Station, Texas 77843

*A newly devised perturbation model for the fluid-induced vibration of turbomachinery rotating elements is used to compute the rotordynamic coefficients of an annular seal. First, the finite element-based solution of the flow field in the centered-rotor operation mode is verified and its grid dependency tested for different seal configurations. The rotordynamic behavior of a hydraulic seal with a clearance gap depth/length ratio of 0.01, as a representative case, is then analyzed under a cylindrical type of rotor whirl and several running speeds. The direct and cross-coupled rotordynamic coefficients dictating the rotor instability mechanism in this case are compared to experimental and analytical data, and the outcome is favorable. The numerical results are also used to discuss the validity of a common assumption in existing computational models in regard to the circumferential distribution of the perturbed flow variables in the eccentric rotor operation mode.*

## Introduction

Fluid-induced vibration of turbomachinery rotating components is often a result of today's high performance demands. These, among others, include excessively tight clearances, high speeds, and highly loaded blades in the primary-flow passages. While these design trends intendingly maximize the overall efficiency, they may also lead to forced vibration of the rotating components. This potentially dangerous situation can also be the result of fluid/solid interaction mechanisms in secondary-flow passages such as seals, dampers and bearings. Of these, the problem of seal rotordynamics has been the focus of extensive research in recent years.

Although the primary function of seals is leakage control, they evidently influence the overall stability of turbomachines. While nonsmooth seals, of the grooved, labyrinth and honeycomb types (Diewald and Nordmann, 1988; Childs and Scharrer, 1987; Childs, 1988) are known to produce minimum leakage, it is not established with certainty that they provide better rotordynamic characteristics when compared to smooth untapered seals. It is established, however, that the instability in all cases are dependent upon such parameters as the clearance depth (Childs and Scharrer, 1987), the flow preswirl (Childs, 1988) and other geometry-related variables. The latter includes the taper angle, in the case of an annular seal (Nelson, 1984) and whether the seal is of the "look-through" or the stepped type (Scharrer, 1988) in the class of labyrinth seals.

Recent advances in the seal rotordynamics area have established the computational fluid dynamics tool as a strong modeling foundation. The first and foremost contribution in this field was that by Dietzen and Nordmann (1987), where a finite-difference formulation of Navier-Stokes equations was used in conjunction with a perturbation model to compute the rotordynamic coefficients of incompressible-flow annular seals (Fig. 1). The significance of that study lies in the departure it advocated from the bulk-flow model (Childs, 1983) in which details of the rotor-to-housing flow field were significantly simplified. A common assumption in the study by Dietzen and Nordmann (1987), as well as that of Childs (1983), has involved a single-harmonic sinusoidal variation of the flow properties in the tangential direction.

It is the purpose of this paper to validate a comprehensive finite element-based perturbation model which the authors have recently devised (Baskharone and Hensel, 1991). The model conceptually deviates from the traditional perturbation analyses (Dietzen and Nordmann, 1987; Childs, 1983) in that the perturbation equations emerge from the flow-governing equations in their discrete, finite-element form as opposed to the differential form in all existing models. The perturbation in the flow field, in this case, is physically perceived as a result of virtual distortions in an assembly of finite elements that is occupying the rotor-to-housing gap. The computational approach, as such, makes it potentially possible to analyze different rotor vibration modes which may not necessarily involve a uniform rotor eccentricity (which leads to a cylindrical rotor whirl), as well as imparts the versatility and adaptability of the finite-element method to this class of engineering applications.

In view of the substantial versatility of the current model,

[1]Graduate Research Assistant, currently a Senior Engineer at Westinghouse Savannah River Laboratory, Aiken, South Carolina.

Contributed by the Fluids Engineering Division for publication in the JOURNAL OF FLUIDS ENGINEERING. Manuscript received by the Fluids Engineering Division March 27, 1990.

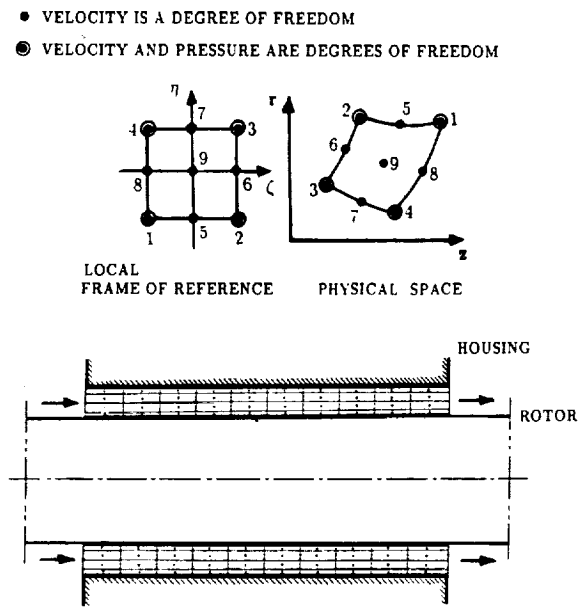


**Fig. 1 Finite-element discretization model of the centered-rotor clearance gap**

it may appear that cylindrically whirling rotors of annular seals do not represent a sufficiently challenging problem, owing to the extensive amount of existing data that virtually covers all aspects of this problem. However, it is precisely the availability of these data that led to selecting this sample case. As demonstrated by Baskharone and Hensel (1991), the new perturbation model offers a conceptual deviation from all existing fluid-induced vibration models. Although the originality here is indeed rotordynamics-related, it is also the application of the finite-element technique to such excessively narrow gaps with a considerable magnitude of flow turbulence and inertia domination, that is hardly verified in the literature. Since analysis of the zeroth-order and perturbed flow fields are both based on this technique, the availability of experimental data to verify the finite-element flow solution was a primary criterion in the selection process. As a result, the numerical investigation in this paper asserts, among others, the finite-element method as a reliable means of securing the narrow-gap zeroth-order flow solution, with which the perturbation analysis is initiated. The investigation, therefore, goes beyond the objective of simply validating the final outcome of the perturbation model.

## Centered-Rotor Flow Field

The axisymmetric flow analysis corresponding to this rotor position provides the zeroth-order solution in the perturbation model (Baskharone and Hensel, 1991). Presented here, however, is an assessment of the stability, smoothness and accuracy aspects of the numerical solution as strongly tied to the level of nonlinearity in the flow equations, the latter being implied by the Reynolds number, and the manner in which the flow turbulence and near-wall flow structure are analyzed. One of two example cases under investigation is a hydraulic annular seal with the following dimensions and operating conditions:

Rotor radius ($a$) = 31.0 mm

Clearance ($s$) = 0.294 mm

Length ($L$) = 200.0 mm

Through-Flow Reynolds number ($R_e$) = $10^4$

Tangential Reynolds number ($R_{e,\omega}$) = $2.5 \times 10^4$

where the through-flow Reynolds number is based on the inlet through-flow velocity and the tangential Reynolds number is based on the circumferential velocity of the rotor surface, with the characteristic length being the seal clearance in both cases. Experimental measurements concerning this seal configuration were reported by Yamada (1962) in the form of a seal "resistance" parameter ($\lambda$), which is defined as follows:

$$\lambda = \frac{\Delta p}{\rho V_{z_i}^2} \tag{1}$$

where:

$\Delta p$ is the static pressure drop across the seal,
$\rho$ is the fluid density,
$V_{z_i}$ is the seal-inlet through-flow velocity.

**Turbulence Closure and Near-Wall Flow Zone.** An algebraic eddy viscosity model by Baldwin and Lomax (1978) is used to simulate the flow turbulent behavior. According to this model, the effective kinematic viscosity is viewed as composed of two, molecular and eddy, components as follows:

$$\nu_e = \nu_l + \nu_t \tag{2}$$

In calculating the eddy component, $\nu_t$, the procedure assumes the presence of two, inner and outer, layers. In the inner layer, the Prandtl-van Driest formulation yields the following expression:

$$\nu_{t,i} = l^2 |\omega'| \tag{3}$$

where the subscript $i$ refers to the inner layer. The mixing length $l$ in expression (3) is defined as follows:

$$l = \kappa y \left[ 1 - \exp\left( \frac{-y^+}{A^+} \right) \right], \quad y^+ = \frac{\sqrt{\rho_w \tau_w}}{\mu_w} y$$

where:

$y$ is the distance normal to the nearest wall
$\tau_w$ is the wall shear stress
$\omega'$ is the local vorticity

The model switches from Van Driest formulation to that of the outer region at the smallest value of $y$ for which the inner and outer values of the eddy kinematic viscosity are equal. The formulation for the outer layer is given by:

$$\nu_{t,o} = KC_{cp} F_{\max} y_{\max} F_{KLEB} \tag{4}$$

where:

## Nomenclature

$a$ = rotor radius
$b$ = housing radius
$C, c$ = direct and cross-coupled damping coefficients
$K, k$ = direct and cross-coupled stiffness coefficients
$L$ = seal length
$l$ = mixing length
$M, m$ = direct and cross-coupled inertia coefficients
$p$ = static pressure
Re = Reynolds number
$s$ = clearance gap width
$y$ = distance from the wall
$\beta$ = grid refinement factor
$\lambda$ = dimensionless seal resistance (defined in Eq. (1))
$\mu$ = viscosity coefficient
$\nu$ = kinematic viscosity coefficient
$\rho$ = density
$\tau$ = shear stress
$\Omega$ = whirl frequency
$\omega$ = shaft running speed
$\omega'$ = vorticity

**Subscripts**

$i$ = seal inlet station
$R$ = relative flow property
$r$ = radial component
$w$ = value at the wall
$z$ = axial component
$\theta$ = tangential component

$$F_{max} = y_{max}|\omega'|\left[1-\exp\left(\frac{-y^+}{A^+}\right)\right]; \text{ and}$$

$$F_{KLEB} = \left[1+5.5\left(C_{KLEB}\frac{y}{y_{max}}\right)^6\right]^{-1}$$

with $y_{max}$ referring to the value of $y$ at which $F_{max}$ occurs. The various constants in Baldwin-Lomax model are as follows:

$$A^+ = 26,\ \kappa = 0.4,\ K = 0.0168,\ C_{cp} = 1.6; \text{ and } C_{KLEB} = 0.3$$

It is important to point out that in applying this turbulence model, which was devised for two-dimensional flow applications, the vorticity and wall shear stress calculations were modified in such a way that the tangential velocity component is taken into account. This was necessary since the flow in the rotor-to-housing passage is generally that of the swirling type.

The authors experience with the foregoing turbulence closure during the course of this study has proven that, regardless of any "practical" level of mesh refinement near solid boundary segments, accurate values of the near-wall eddy viscosity were unachievable at high Reynolds numbers. The focus then was on the annular seal described above, for which the flow resistance, as measured by the static pressure drop across the seal, was persistently overestimated. Further investigation revealed that the high velocity gradients in the near-wall zone were improperly depicted. The situation was conclusively remedied by utilizing the universal law of the wall concept in computing the wall shear stress "$\tau_w$" appearing in the expression of the dimensionless distance $y^+$ above.

Computation of the wall shear stress, that is associated with a typical node "$i$" (Fig. 2), is based on the near-wall zone treatment proposed by Benim and Zinser (1985). The assumption here is that the universal law of the wall at any wall location is extendible, across the wall element width, to the grid node "$j$" (Fig. 2) at this axial location. Referring to the distance of node "$j$" from the wall by $y_{min}$, the following expression for the wall shear stress is then obtained:

$$\tau_w = \begin{cases} \dfrac{\nu_l \rho V_{min}}{y_{min}} & \text{for } y^+_{min} < 11.6 \\ \dfrac{\kappa C_D^{1/4} \rho V_{min} k_{min}^{1/2}}{\ln\left(E C_D^{1/4} y_{min} \dfrac{k_{min}^{1/2}}{\nu_l}\right)} & \text{for } y^+_{min} \geq 11.6 \end{cases} \quad (5)$$

where: $k_{min} = \dfrac{\tau_w}{\rho C_D^{1/2}}$, $C_D = 0.09$, $\kappa = 0.4$, $E = 9.0$

with $V_{min}$ referring to the magnitude of velocity, with the tangential component taken into account, at the interior node and $\nu_l$ being the molecular coefficient of kinematic viscosity. Referring to Eq. (5) above, note that the outcome of this equation in the case where $y^+_{min} \geq 11.6$ is a recursive relationship since $\tau_w$ now appears on both sides of the equation. An iterative procedure is executed, in this case, to compute $\tau_w$. Noteworthy is also the fact that the node "$j$" (Fig. 2) in the Benim and Zinser model is replaced by the corner node "$k$" which is consistent with their choice being a four-noded bilinear finite element. In reality, however, neither one of these nodes would be sufficiently close to the wall, in view of the steep velocity gradient in this region. An alternate choice of this near-wall point was, in this case, adopted as part of the accuracy enhancement process discussed next.

Numerical implementation of the preceding turbulence closure, including the near-wall model, is achieved with the aid of an array of points that is different from the primary set of computational nodes. Figure 2 shows an enlarged segment of the computational domain near a solid wall, in which the primary nodes in the finite-element discretization model are identified by hollow circles, while the points used in the eddy viscosity computations at the typical node "$i$" are solid circles.

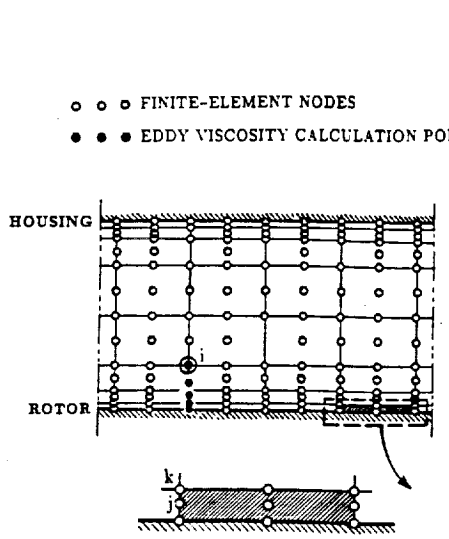


**Fig. 2 Refinement of the near-wall region for accurate prediction of the eddy viscosity**

The objective here was twofold; to estimate the cut-off location between the inner and outer layer with sufficient accuracy, and to capture the steep gradients of the flow variables near the solid wall. A substantial enhancement of the solution was, as a result, observed during the preliminary testing phase. This, for the major part, was due to the excellent accuracy with which the wall shear stress was computed, for it was generally possible to compute the stress at a point where the dimensionless wall coordinate ($y^+$) was acceptably small.

A modification to the Baldwin and Lomax turbulence closure was made in the current study to accommodate the angular motion of the rotor surface. Referring to the definition of the inner-layer kinematic eddy viscosity (Eq. (3)), and considering the case in which the layer is attached to this rotating surface, the vorticity and wall shear stress were both defined on the basis of the relative velocity ($\mathbf{V}_R$) as opposed to the absolute velocity ($\mathbf{V}$), where:

$$\mathbf{V}_R = \mathbf{V} - \omega a \mathbf{e}_\theta \quad (7)$$

where:

$\omega$ is the rotor spinning speed

$a$ is the rotor radius

$\mathbf{e}_\theta$ is the unit vector in the positive tangential direction

In this case, the absolute vorticity ($\omega'_R$) is expressible in terms of the absolute velocity ($\omega'$) as follows:

$$\omega'_R = \omega' - 2\omega \quad (8)$$

Calculation of the eddy viscosity in the outer layer (Eq. (4)) as pertaining to the rotating surface was consistently performed using the relative flow properties.

**Introduction to the Upwinding Technique.** Adoption of the conventional Galerkin's method in deriving the finite-element equivalent of the flow governing equations was, perhaps expectedly, unsuccessful. This was a result of the high Reynolds number which caused the flow field to be inertia-dominated. Surprisingly, the "wiggles" appearing in the streamwise pressure distribution in this case were not entirely eliminated even when full upwinding of the equations of motion, in the manner devised by Heinrich and Zienkiewicz (1977), was implemented. In fact, the large magnitude of false numerical diffusion that was imparted to the flow field in this case also made it practically impossible to achieve a numerical solution in the neighborhood of the experimental data. The situation was further worsened by the large aspect ratio of the rotor-to-housing gap (defined as the gap length/clearance ratio) which, in turn, produced high aspect-ratio finite elements. This had an adverse numerical effect, especially near the rotor and housing surfaces where the need for high resolution of the flow structure led to excessively narrow elements in this region.

Corrective measures included deviation from the full up-

winding strategy and optimization of the elemental aspect ratio. First, in implementing the weighted-residual method (Zienkiewicz, 1971), terms in the error functions which result from the momentum equations were weighed differently in the process of deriving the finite element equations. In this case, the weight functions proposed by Heinrich and Zienkiewicz (1977), being applicable to the current axisymmetric flow problem, were used in conjunction with only the convection terms in the momentum equations. On the other hand, the element shape functions were used with all other terms. This is consistent with the well-known practice in the area of finite-difference modeling, where backward differencing is exclusively utilized when approximating the convection terms. Optimization of the element aspect ratio, on the other hand, contributed to the smoothness of the flow variables as will be discussed in the grid dependency section of the numerical results.

**Grid Dependency and Accuracy Assessment.** Sensitivity of the numerical solution to the size of the finite-element discretization model, and the level of field resolution it provides, was first investigated. In all cases considered, the number of cross-flow stations between the seal inlet and exit stations was fixed at 48, while the number of grid lines between the inner and outer walls, referred to as $N_r$, was varied from 7 to 11. The latter family of grid lines was constructed with varying increments in the radial direction. To better quantify this variation, the growth of the increments from either wall to the mean radius was made to be of the geometric sequence type with a common ratio "$\beta$." Illustrated in Fig. 3 is the geometrical effects of varying "$\beta$" from 1.0, which yields equal increments, to a value of 1.5 for the case where $N_r$ is fixed at 11. Note the drastic change in the width of the wall elements as a result.

Shown in Fig. 4 is a comparison between the computed seal resistance "$\lambda$," corresponding to different discretization patterns, and the experimental value of Yamada (1962). Examination of this figure reveals that the accuracy of the seal resistance, which is largely influenced by the precision of the computed eddy viscosity, is generally improved by refining the finite-element grid near the walls, be that the result of increasing "$N_r$" or "$\beta$." It was in view of these results, that an optimum grid with $N_r = 9$ and $\beta = 1.5$ was permanently fixed thereafter.

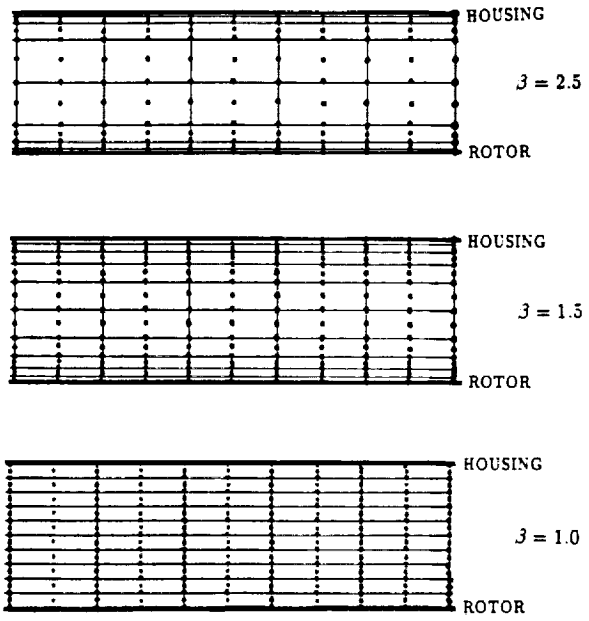


**Fig. 3 Geometrical effects of varying the refinement factor ($\beta$) on the finite-element discretization model**

Accuracy of the centered-rotor flow field was further investigated, with the emphasis being on the cross-flow velocity profiles through the seal. Evaluation of the finite-element solution in this case was made in light of the flow measurements of Morrison et al. (1988) for an annular seal with a gap width/length ratio of 0.034. Development of the through-flow and tangential velocity profiles along this seal were measured by Morrison et al. under a high preswirl/inlet through-flow velocity ratio of 4.2, and a Reynolds number, based on the clearance width and inlet velocity, of 13,280. Figure 5 shows the set of measured through-flow and tangential velocity profiles at non-dimensional axial length ratios of 25, 50, and 75 percent, together with the computed profiles for comparison. As seen in the figure, the computed velocities seem to depict the experimental profiles with reasonable accuracy. Note that the peak point of the through-flow velocity profiles, particularly in the computed profiles, corresponds to radii which are higher than the mean radius due to the radial shifting of the flow particles as a result of the high circumferential velocity which, in turn, is caused by the high rotational speed of the

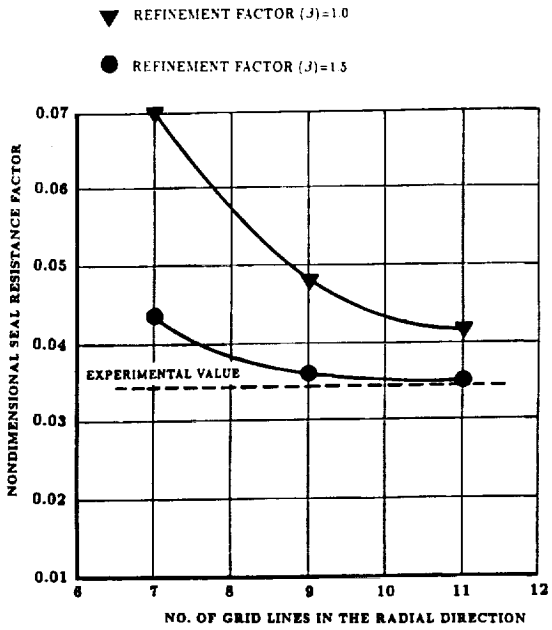


**Fig. 4 Seal resistance as a function of the finite-element model size and near-wall refinement**

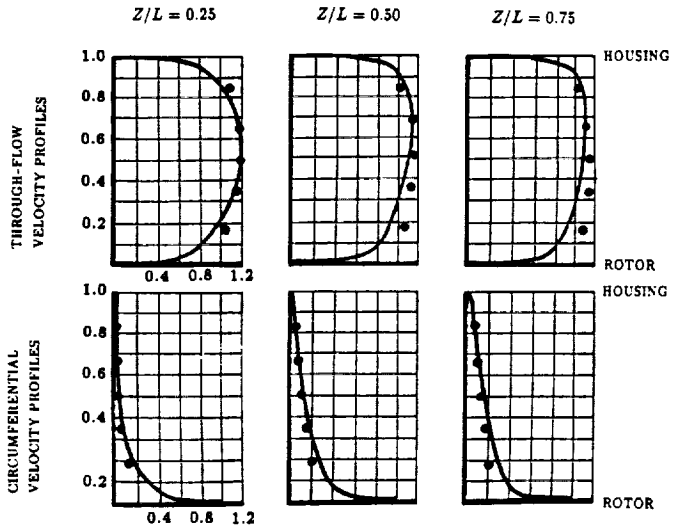


**Fig. 5 Comparison of the through-flow and tangential velocity profiles at three axial locations with experimental data (experimental data in solid circles)**

seal inner wall. Development of the computed tangential velocity along the seal in this figure seems to also be in close agreement with the flow measurements.

## Perturbation Analysis and Rotordynamic Coefficients

The newly devised perturbation analysis (Baskharone and Hensel, 1991) was applied to a representative case of annular seal for which experimental and analytical rotordynamic data exist (Dietzen and Nordmann, 1987). Under focus here was the variation of the direct and cross-coupled stiffness, damping and inertia coefficients ($K$, $k$, $C$, $c$, $M$, and $m$) of the fluid/rotor interaction system. Of these, only the stiffness and damping coefficients were reported by Dietzen and Nordmann (1987), and are used in the present study for verification purposes. The analytical data by Dietzen and Nordmann (1987) is the outcome of a traditional finite difference-based perturbation analysis in which sinusoidal variations of the field variables around the circumference were assumed, as opposed to circumferential variations that are totally unrestricted in the current model.

Of particular interest in assessing the new perturbation model were the stability-related rotordynamic coefficients of which experimental and analytical data were reported by Dietzen and Nordmann (1987) for a typical hydraulic seal. These are the cross-coupled stiffness and direct damping coefficients "$k$" and "$C$," respectively, which dictate the fluid-exerted tangential force and, subsequently, the rotor whirl. The seal under investigation had a clearance/length ratio of 0.0085, a rotor radius of 23.5 mm, and a Reynold's number (based on the clearance and inlet through-flow velocity) of 4700. Operating speeds of 2000, 4000, and 6000 rpm were considered, together with inlet preswirl/through-flow velocity ratios 0.04, 0.10 and 0.17, respectively.

The three-dimensional grid used to analyze the distorted clearance gap (Baskharone and Hensel, 1991) was first optimized. In this case, the number of tangential stations "$N_\theta$" in this gap (Fig. 6) was varied, while maintaining the axial and radial station counts, as well as the near-wall refinement level, unchanged. Figure 6 shows the variation of the error in the computed force derivatives, $\partial F_x/\partial\epsilon$ and $\partial F_y/\partial\epsilon$, where "$\epsilon$" is the rotor virtual eccentricity, as a result. The error in this figure is defined as the dimensionless difference between the force derivative and that corresponding to an $N_\theta$ value of 12, and the force derivatives are those associated with a zero whirl frequency. Based on the asymptotic shape of both curves in Fig. 6, the number of tangential stations was chosen to be 12. As a result, the RAM and CPU time consumption, regardless of the whirl frequency magnitude, were roughly 1220 K. bytes and 12 minutes, respectively, on the SX2 supercomputer, per each whirl frequency.

Shown in Fig. 7 is a comparison of the computed rotordynamic coefficients with those reported by Dietzen and Nordmann (1987). The latter data set contained measurements of the direct and cross-coupled stiffness coefficients, but only the direct damping coefficient. Also contained in this set were the numerical results obtained by Dietzen and Nordmann, for all four of the stiffness and damping coefficients, using a traditional perturbation analysis in which the finite-difference method was utilized. As seen in this figure, the computed results are generally in close agreement with the experimental and analytical data as far as the cross-coupled stiffness and direct damping coefficients are concerned. These two coefficients, as discussed earlier, are representative of the fluid-induced tangential force perturbation and, as such, dominate the mechanism of rotor instability. The cross-coupled stiffness coefficient "$k$" is, by reference to Fig. 7, positive, therefore destabilizing, and increases with the rotor speed. The direct damping coefficient "$C$," on the other hand, provides a stabilizing effect which, according to the computed results, increases slightly with the operating speed. Examination of Fig. 7 reveals, however, that the predicted values of the direct stiffness coefficient "$K$" and cross-coupled damping coefficient "$c$" are significantly different from those computed by Dietzen and Nordmann (1987). This, for the major part, is caused by differences in the unperturbed flow fields including, in particular, the radial profiles of the flow properties along the seal axis as explained next.

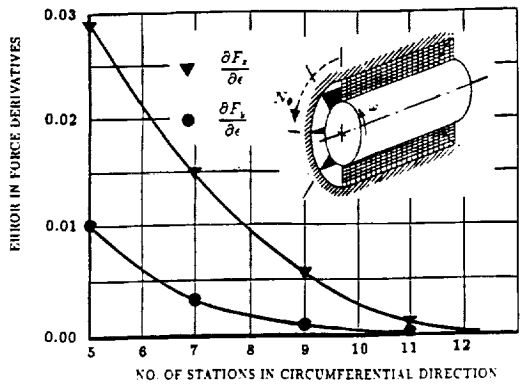


**Fig. 6 Sensitivity of the force derivatives to the number of grid planes around the circumference**

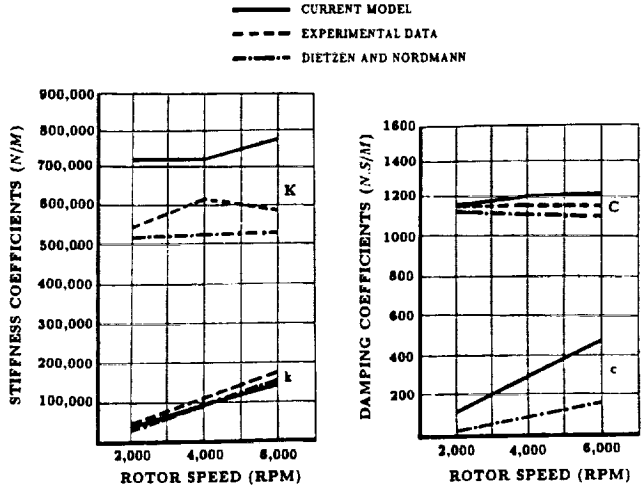


**Fig. 7 Comparison of the direct and cross-coupled rotordynamic coefficients with experimental and analytical data**

Evolution of the direct stiffness and cross-coupled damping coefficients in Fig. 7 can be traced back (Baskharone and Hensel, 1991) to a single source, namely the radial component of the fluid reaction force on the rotor. As reported by Hensel (1990) for the same seal, this force component is highly sensitive to the inlet through-flow velocity profile including, in particular, the inlet boundary layer thickness. For instance, Hensel reported an average reduction of nearly 21 percent in the direct stiffness coefficient "$K$" as a result of arbitrarily reducing the inlet boundary layer thickness, on both the rotor and housing surfaces, from 15 percent of the clearance width to 7.5 percent, which is the current value, with the cross-coupled stiffness and direct damping coefficients remaining practically unchanged. Such sensitivity would naturally be anticipated in seals, such as the present, where the axial length is too small to permit a fully developed flow even at the exit station. It is therefore true that the computed values of "$K$" in Fig. 7 are primarily dependent on the inlet boundary layer thickness assumption which, in turn, was necessary since no measured thickness was available. On the other hand, there is no clear evidence that this assumption had any significant effect on the trend of "$K$" with the rotor speed in Fig. 7. Nevertheless, it should be noted, in reference to this figure, that the experimentally-determined peak of "$K$" at a rotor speed of 4000 rpm is as absent in the

results of Dietzen and Nordmann (1987) as it is in the current results despite the major difference in simulating the flow turbulence in both studies.

**Versatility Assessment of the Current Perturbation Model.** Thorough examination of the current numerical results for the simple annular seal under consideration appeared, as anticipated, to confirm the validity of the single-wave sinusoidal forms of flow perturbations around the circumference. The flow variable under focus was the rotor-surface pressure perturbation ($\partial p_i/\partial \epsilon$) at the middle seal section which, through use of the computed nodal pressures, was cast in the following Fourier series form:

$$\frac{\partial p_i}{\partial \epsilon} = a_0 + \sum_n a_n \cos(n\theta) + \sum_n b_n \sin(n\theta) \tag{9}$$

where the subscript "$i$" refers to the inner (or rotor) radius and "$\theta$" is the angular coordinate. The number of sine and cosine waves "$n$" in expression (9) was arbitrarily set equal to five. The ratios ($a_n/a_1$) and ($b_n/b_1$) were then computed. All of these ratios came to be less than 0.5 percent for $2 \leq n \leq 5$ regardless of the whirl frequency/spinning speed ratio. This simply means that the common form of field variable perturbation, namely:

$$\mathcal{P} = \mathcal{P}_c \cos\theta + \mathcal{P}_s \sin\theta \tag{10}$$

where $\mathcal{P}$ stands for the perturbation of any flow variable, is seemingly as accurate as can be. This functional form is recognizably a built-in assumption in any existing perturbation model in this rotordynamics area (e.g., Dietzen and Nordmann, 1987; Childs, 1983).

Complex clearance gaps and/or vibration modes, however, are where approximations of the type indicated above may become inapplicable. Consider, for instance, the problem of a shrouded pump impeller (e.g., Baskharone and Hensel, 1989) where the rotor, being the shrouded impeller in this case, undergoes a conical type of whirl as a result of an angular eccentricity of the rotor axis. As indicated by the authors (Baskharone and Hensel, 1991), it is this problem configuration to which the virtual finite-element distortion concept, being the foundation of the current perturbation model, is uniquely applicable. In this case, deformations of the finite elements, due to the angular rotor eccentricity, will give rise to differential changes in the rotor surface pressure which, in the end, produce fluid-exerted moments $M_x$ and $M_y$ around the center of conical whirl. Future application of the current analysis to this type of rotor eccentricity may indeed make it possible to assess the validity of the simple sinusoidal distribution (indicated above) under such circumstances. The authors suspect that such simple distribution would probably be unrealistic in the tooth-to-tooth gap of the labyrinth seal which may very well be part of the leakage passage (e.g., Baskharone and Hensel, 1989), as well as other subdomains where flow separation and recirculation occur. Stated differently, it is in critical subdomains, such as these, that the coefficients "$a_n$" and "$b_n$" in expression (9) may not be necessarily zero for $n > 1$ as is generally assumed to be the case in virtually all existing perturbation models of fluid-rotor interaction.

## Concluding Remarks

The intention in this paper was to verify a new and categorically different methodology in the area of fluid-induced vibration, as well as validate its fluid mechanics foundation. Both tasks were successfully accomplished using representative annular seal configurations. The direct and cross-coupled rotordynamic coefficients, which comprise the ultimate goal of the study, were in close agreement with available experimental and analytical data, particularly those which are directly linked to the rotor instability. While the strategy in the current perturbation model was clearly different from all existing perturbation models in this field, an effort to assess the versatility of the new model, by comparison, was made and the fundamental differences identified. Since limitations on the rotor-to-housing clearance gap in the model are practically nonexisting, it is presently the plan to apply the model to shrouded impellers of the Space Shuttle Main Engine turbopumps for which the destabilizing forces are developed in the shroud-to-housing secondary-flow gap. Release of the computer code, as part of an upcoming NASA contractor report, will take place upon completion of this final research phase.

## Acknowledgment

This study was funded by NASA-Marshall Space Flight Center (Huntsville, Alabama), contract no. NAS8-37821, NASA monitor: James Cannon. Partial funding was also provided by the Houston Advanced Research Center (The Woodlands, Texas), grant no. 88-025.

## References

Baldwin, B. S., and Lomax, H., 1978, "Thin Layer Approximation and Algebraic Model for Separated Turbulent Flows," AIAA Paper No. 78-257.

Baskharone, E. A., and Hensel, S. J., 1989, "A New Model for Leakage Prediction in Shrouded-Impeller Turbopumps," ASME JOURNAL OF FLUIDS ENGINEERING, Vol. 111, pp. 118-123.

Baskharone, E. A., and Hensel, S. J., 1991, "A Finite-Element Perturbation Approach to Fluid/Rotor Interaction in Turbomachinery Elements. Part 1: Theory," ASME JOURNAL OF FLUIDS ENGINEERING, published in this issue, pp. 353-361.

Benim, A. C., and Zinser, W., 1985, "Investigation of the Finite Element Analysis of Confined Turbulent Flows Using a $k$-$\epsilon$ Model of Turbulence," *Computer Methods in Applied Mechanics and Engineering*, Vol. 51, pp. 507-523.

Childs, D. W., 1983, "Finite Length Solutions for Rotordynamic Coefficients of Turbulent Annular Seals," ASME *Journal of Lubrication Technology*, Vol. 105, pp. 437-445.

Childs, D. W., and Scharrer, J. K., 1987, "Theory Versus Experiment for the Rotordynamic Coefficients of Labyrinth Gas Seals: Part II-A Comparison to Experiment," *ASME Rotating Machinery Dynamics*, Vol. 2, pp. 427-434.

Childs, D. W., 1988, "Annular Honeycomb Seals: Test Results for Leakage and Rotordynamic Coefficients; Comparison to Labyrinth and Smooth Configurations," *Proceedings of the Fifth Workshop on Rotordynamic Instability Problems in High-Performance Turbomachinery*, Texas A&M University.

Dietzen, F. J., and Nordmann, R., 1987, "Calculating Rotordynamic Coefficients of Seals by Finite Difference Techniques," ASME *Journal of Tribology*, Vol. 109, pp. 388-394.

Diewald, W., and Nordmann, R., 1988, "Influence of Different Types of Seals on the Stability Behavior of Turbopumps," *Proceedings of the Fifth Workshop on Rotordynamic Instability Problems in High-Performance Turbomachinery*, Texas A&M University.

Heinrich, J. C., and Zienkiewicz, O. C., 1977, "Quadratic Finite Element Schemes for Two-Dimensional Convective-Transport Problems," *Int. J. Num. Meth. Eng.*, Vol. 11, pp. 1831-1844.

Hensel, S. J., 1990, "A New Method for Determining Rotordynamic Forces on Liquid Annular Seals," Ph.D. dissertation, Texas A&M University.

Morrison, G. L., Johnson, M. C., and Tatterson, G. B., 1988, "3-D Laser Anemometer Measurements in an Annular Seal," ASME Paper No. 88-GT-64.

Nelson, C. C., 1984, "Analysis for Leakage and Rotordynamic Coefficients of Surface Roughened Tapered Annular Seals," *Proceedings of the Third Workshop on Rotordynamic Instability Problems in High-Performance Turbomachinery*, Texas A&M University.

Scharrer, J. K., 1988, "Rotordynamic Coefficients for Stepped Labyrinth Gas Seals," *Proceedings of the Third Workshop on Rotordynamic Instability Problems in High-Performance Turbomachinery*, Texas A&M University.

Yamada, Y., 1962, "Resistance of Flow Through an Annulus with an Inner Rotating Surface," *Bulletin of JSME*, Vol. 5, No. 18, pp. 302-310.

Zienkiewicz, O. C., 1971, *The Finite Element Method in Engineering Science*, McGraw-Hill.

**PAPER# 3**

*Int. J. Mech. Sci.* Vol. 33, No. 2, pp. 151–167, 1991
Printed in Great Britain.

0020-7403/91 $3.00 + .00


# MOMENT COEFFICIENTS OF INCOMPRESSIBLE-FLOW SEALS WITH CONICALLY WHIRLING ROTORS

E. A. BASKHARONE and S. J. HENSEL†
Mechanical Engineering Department, Texas A&M University, College Station, TX 77843, U.S.A.

(*Received* 7 *May* 1990; *and in revised form* 13 *September* 1990)

**Abstract**—A computational model is developed to investigate the dynamic behavior of a rotor that is in contact with a fluid, to infinitesimally small disturbance modes. The rotor here is that of an annular seal, commonly used in turbomachinery applications, with an incompressible flow in the annular clearance gap. Under consideration is an angular excitation of the rotor axis, coupled with a whirling motion around the housing centerline at a finite whirl frequency. The fluid response in this case is quantified in the form of direct and cross-coupled moment coefficients, which constitute a measure of the stiffness, damping and inertia effects of the rotor/fluid interaction. Uniqueness of the computational model stems from the manner in which the rotor eccentricity is physically perceived and subsequently incorporated. It is first established that the fluid reaction components are the result of infinitesimally small deformations of varied magnitudes that are experienced by an assembly of finite elements in the rotor-to-housing gap as the gap becomes distorted due to the rotor virtual eccentricity. The idea is then cast into a perturbation model in which the perturbation equations emerge from the flow-governing equations in their discrete finite-element form, as opposed to the differential form, which is traditionally the case. The computational model is potentially applicable to a wide range of rotor-to-housing pasage configurations where ellipticity of the passage flow field is too significant to ignore. The numerical results are compared to those obtained through an existing bulk-flow model which is particularly suited for the leakage passage in annular seals and other similarly simple passage configurations.

## 1. INTRODUCTION

Seals are conceptually leakage control devices which are extensively used in turbomachines to minimize the secondary flow rate in clearance gaps. Of these the straight type (Fig. 1) is

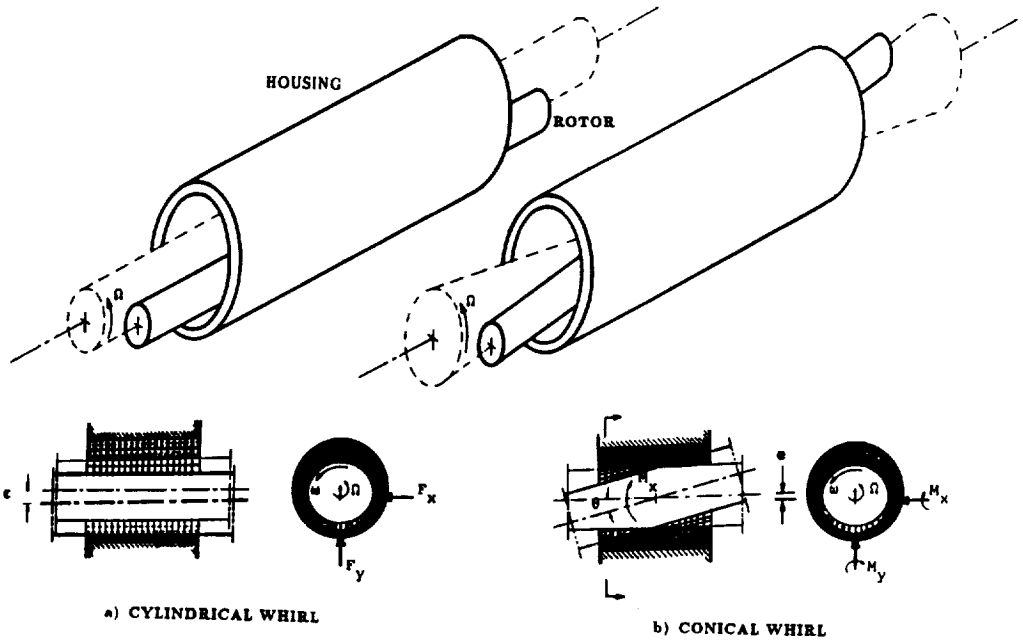


FIG. 1. Cylindrical and conical whirl of an annular seal rotor.

†Currently with Westinghouse Savannah River Laboratory, Aiken, South Carolina, U.S.A.

often utilized in shrouded-impeller turbopumps to reduce leakage over the impeller front face. However, it has long been recognized (e.g. Black [1]) that the seal rotordynamic characteristics also have a primary influence on the stability of the entire turbomachine and are, therefore, crucial in the life estimation process. This motivated several researchers to compute [2–5] and measure [5, 6] the stiffness, damping and inertia coefficients resulting from the fluid/rotor interaction. Despite the difference in methodology among computational analysts in this area, the definite majority of numerical models existing today are those concerned with the force coefficients associated with cylindrical whirl of the rotor axis (Fig. 1a).

The study by Childs [3] was the first and remains the only analytical attempt to quantify the moment-related coefficients in annular seals. This was a perturbation analysis based on the Hirs' bulk-flow model [7] where the rotor tilting motion was coupled with the rotor whirl around the centered position (Fig. 1b). Childs' conclusions were later validated by Kanemori and Iwatsubo [6] for a long seal where the fluid-induced moments would naturally be of predominant influence on the seal dynamic behavior. The experimental study by Kanemori and Iwatsubo was, nevertheless, incomplete for it was only concerned with the fluid-exerted moment resulting from a uniform lateral eccentricity (cylindrical whirl). Figure 2 illustrates this type of rotor excitation which, considering the axial gradient of the rotor surface pressure, indeed leads to tilting moments, especially in long seals. The impact of these moments becomes negligible as the seal length is made smaller, a case that is best represented by the so-called neck ring seal. Figure 3 shows this seal as part of the secondary flow passage in a pump stage that is similar to the booster impeller stage of the Space Shuttle Main Engine oxidizer turbopump.

The current computational study deals with the direct effects of an angular eccentricity that is simultaneously coupled with a whirling motion of the rotor at a finite whirl frequency $\Omega$ as depicted in Fig. 4. The analysis is based on, and intendingly advocates, what may be referred to as the virtually distorted finite element concept. Aimed at the direct and cross-coupled moment coefficients of the seal, the computational model is particularly applicable to short seals with length/diameter ratios that are generally less than unity.

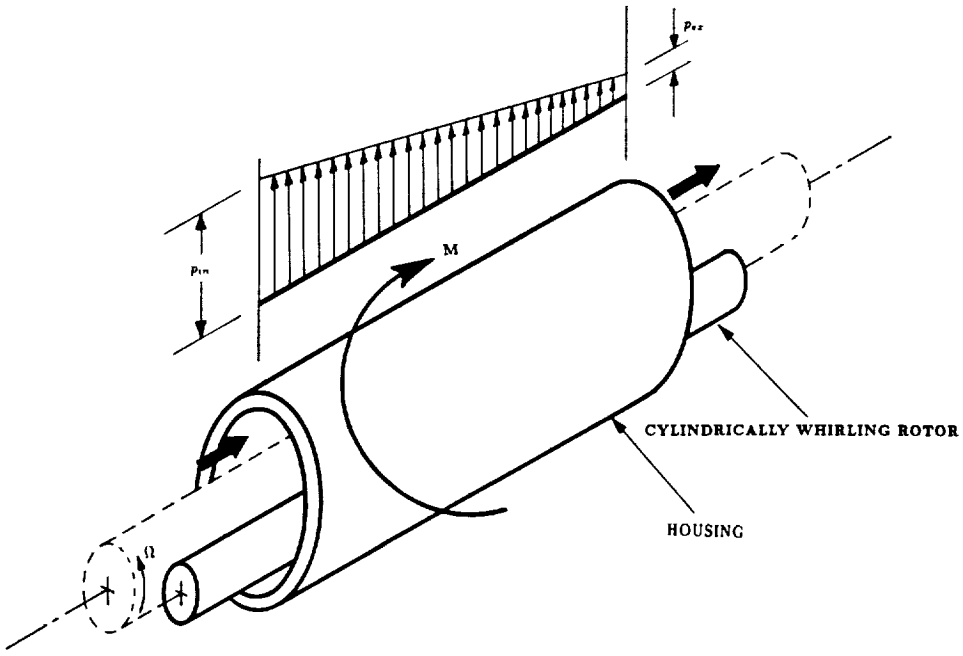


FIG. 2. Fluid-exerted moments in long seals as a result of the pressure differential across the rotor.

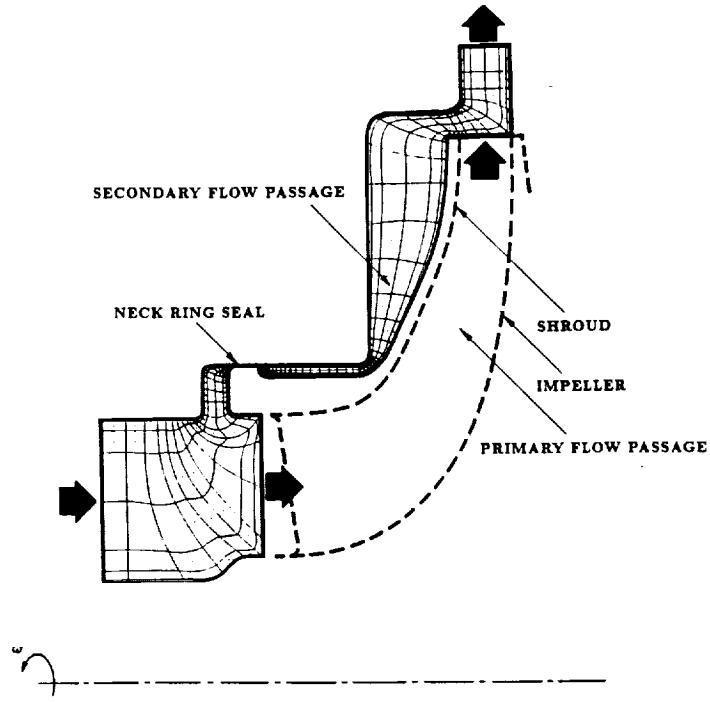


FIG. 3. Neck ring seal as part of the secondary passage in shrouded-impeller pumps.

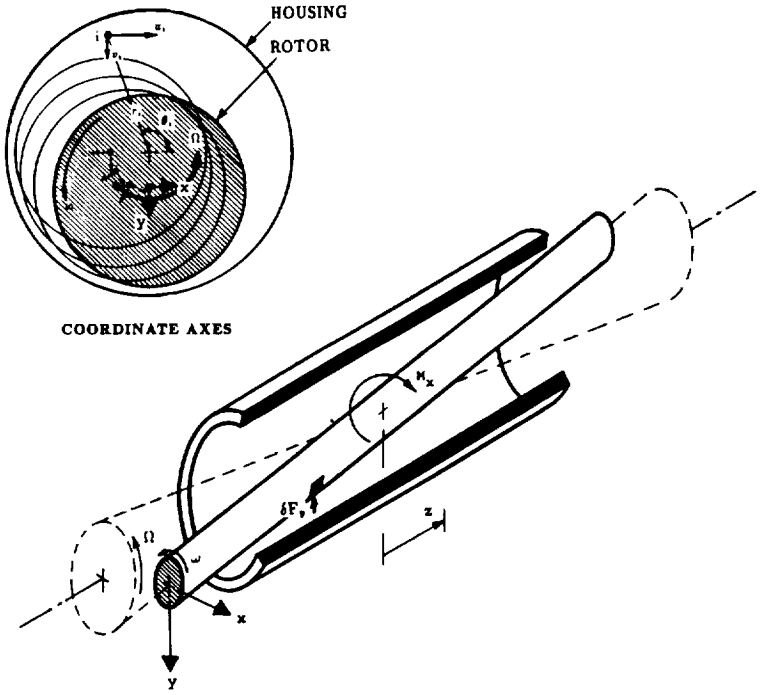


FIG. 4. Fluid-induced moments on a conically whirling rotor and definition of the coordinate axes.

## 2. ANALYSIS

*Components of fluid/rotor interaction*

Figure 4 shows a whirling rotor which is experiencing an infinitesimally small angular eccentricity $\theta$ around the center of tilting motion. Referring to the whirl frequency by $\Omega$, the eccentricity can generally be resolved at any given time $t$ into two angular displacement

components around the $x$ and $y$ axes as follows:

$$\theta_x = \frac{e}{z}\cos(\Omega t), \quad \theta_y = \frac{e}{z}\sin(\Omega t) \tag{1}$$

with $z$ being the distance from the center of tilting motion (Fig. 4). The fluid reaction, in this case, is in the form of differential moments $\delta M_x$ and $\delta M_y$ around the $x$ and $y$ axes, for which the following linearized relationship [2–5] applies:

$$-\begin{Bmatrix}\delta M_x \\ \delta M_y\end{Bmatrix} = \begin{bmatrix}\bar{K} & \bar{k} \\ -\bar{k} & \bar{K}\end{bmatrix}\begin{Bmatrix}\theta_x \\ \theta_y\end{Bmatrix} + \begin{bmatrix}\bar{C} & \bar{c} \\ -\bar{c} & \bar{C}\end{bmatrix}\begin{Bmatrix}\dot{\theta}_x \\ \dot{\theta}_y\end{Bmatrix} + \begin{bmatrix}\bar{M} & \bar{m} \\ -\bar{m} & \bar{M}\end{bmatrix}\begin{Bmatrix}\ddot{\theta}_x \\ \ddot{\theta}_y\end{Bmatrix}, \tag{2}$$

where $\theta_x$ and $\theta_y$ are the components of angular displacements of the rotor axis around the $x$ and $y$ axes, respectively. The direct ($\bar{K}$, $\bar{C}$, $\bar{M}$) and cross-coupled ($\bar{k}$, $\bar{c}$, $\bar{m}$) rotordynamic coefficients, in the square matrices above, are the seal stiffness, damping and inertia coefficients under an angular rotor excitation. The differential moments $\delta M_x$ and $\delta M_y$ in equation (2) represent the fluid reaction to this excitation, where:

$$\delta M_x = \int_z z\delta F_y; \quad \text{and} \tag{3}$$

$$\delta M_y = \int_z z\delta F_x \tag{4}$$

with $\delta F_x$ and $\delta F_y$ being the differential changes in the forces exerted on the rotor due to the infinitesimally small shift in pressure on the rotor surface as a result of the angular eccentricity (Fig. 4). With no lack of generality, consider the special location of the displaced rotor axis in a plane that is at a distance $z$ from the center of the tilting motion as shown in Fig. 1(b). Using equation (1) in this case yields the following expressions for the angular location, velocity and acceleration of the rotor axis:

$$\theta_x = \frac{e}{z} = \theta, \quad \theta_y = 0 \tag{5}$$

$$\dot{\theta}_x = 0, \quad \dot{\theta}_y = \frac{\dot{e}}{z} = \Omega\theta \tag{6}$$

$$\ddot{\theta}_x = \frac{\ddot{e}}{z} = -\Omega^2\theta, \quad \ddot{\theta}_y = 0. \tag{7}$$

Use of expressions (5)–(7) in the matrix equation (2) gives rise to the following two equations:

$$\frac{\partial M_x}{\partial\theta} = \lim_{\theta\to 0}\left(\frac{\delta M_x}{\theta}\right) = -\bar{K} - \Omega\bar{c} + \Omega^2\bar{M} \tag{8}$$

$$\frac{\partial M_y}{\partial\theta} = \lim_{\theta\to 0}\left(\frac{\delta M_y}{\theta}\right) = \bar{k} - \Omega\bar{C} + \Omega^2\bar{m}. \tag{9}$$

Determination of the stiffness, damping and inertia coefficients in equations (8) and (9) requires computation of $\partial M_x/\partial\theta$ and $\partial M_y/\partial\theta$ at three or more different values of the whirl frequency $\Omega$. Interpolation of these two derivatives as quadratic functions of $\Omega$, using curve fitting techniques, leads to the evaluation of $\bar{K}$, $\bar{k}$, $\bar{C}$, . . . etc. by simply equating corresponding terms on both sides of equations (8) and (9).

The procedure to determine $\partial M_x/\partial\theta$ and $\partial M_y/\partial\theta$ above is initiated by securing a finite-element solution of the undisturbed flow field in the rotor-to-housing annular gap for the centered-rotor operation mode. Next, a virtual angular eccentricity $\theta$ (Fig. 1b) is introduced. As a result, the finite-element nodal points undergo virtual lateral displacements of different magnitudes depending on the spatial location of each node (Fig. 1b). Analysis of the perturbed set of finite-element equations under such virtual distortion yields, among other variables, the rate at which the rotor surface pressure varies with the angular eccentricity

(i.e. $\partial p/\partial\theta$). The coefficients $\partial M_x/\partial\theta$ and $\partial M_y/\partial\theta$ are, in the end, determined by integration along the rotor axis.

*Zeroth-order flow field*

The undisplaced rotor flow problem is defined in a frame of reference that is attached to the rotor (Fig. 4) and is whirling around the housing centerline at the rate of $\Omega$. It may appear at this point that selection of these rotating axes serves no purpose other than complicating the flow-governing equations. However the reader is reminded that this selection leads to a steady relative flow field (as viewed in the rotating frame of reference) once the rotor displacement occurs. Prior to this displacement, the coordinate axes are of the simply rotating type (Fig. 5) and the relative flow field (referred to as the zeroth-order flow field) is also steady.

Definition of the coordinate axes in the manner described above, is not intended to imply the need to solve the flow-governing equations in the physically distorted clearance gap (e.g. Dietzen and Nordmann [4]). The fact, however, is that this choice, despite the complex and three-dimensional flow equations it produces (as will be seen next), makes it systematic to develop the perturbation model as it ensures consistency of the unperturbed and perturbed flow fields, of which only the earlier is physically axisymmetric. Note that this consistency requirement can alternately be ensured by solving the simple axisymmetric flow field in the undistorted passage, and then casting this "zeroth-order" solution in the frame of reference defined above [8]. This procedure was actually implemented during execution of the computer code for the substantial reduction in the core and CPU time consumption it provides.

Viewed in the preceding frame of reference, the swirling flow in the rotor-to-housing gap is assumed adiabatic, incompressible and generally turbulent. The momentum and mass conservation equation can therefore be expressed in the rotating frame of reference (noting that $\Omega$ in Fig. 5 is negative) as follows:

$$\hat{u}\frac{\partial u}{\partial x}+\hat{v}\frac{\partial u}{\partial y}+\hat{w}\frac{\partial u}{\partial z}+2\Omega v-\Omega^2 x=-\frac{1}{\rho}\frac{\partial p}{\partial x}+\nu_e\nabla^2 u$$
$$+2\frac{\partial \nu_t}{\partial x}\frac{\partial u}{\partial x}+\frac{\partial \nu_t}{\partial y}\left(\frac{\partial u}{\partial y}+\frac{\partial v}{\partial x}\right)+\frac{\partial \nu_t}{\partial z}\left(\frac{\partial u}{\partial z}+\frac{\partial w}{\partial x}\right) \tag{10}$$

$$\hat{u}\frac{\partial v}{\partial x}+\hat{v}\frac{\partial v}{\partial y}+\hat{w}\frac{\partial v}{\partial z}-2\Omega u-\Omega^2 y=-\frac{1}{\rho}\frac{\partial p}{\partial y}+\nu_e\nabla^2 v$$
$$+2\frac{\partial \nu_t}{\partial y}\frac{\partial v}{\partial y}+\frac{\partial \nu_t}{\partial x}\left(\frac{\partial u}{\partial y}+\frac{\partial v}{\partial x}\right)+\frac{\partial \nu_t}{\partial z}\left(\frac{\partial v}{\partial z}+\frac{\partial w}{\partial y}\right) \tag{11}$$

$$\hat{u}\frac{\partial w}{\partial x}+\hat{v}\frac{\partial w}{\partial y}+\hat{w}\frac{\partial w}{\partial z}=-\frac{1}{\rho}\frac{\partial p}{\partial z}+\nu_e\nabla^2 w+2\frac{\partial \nu_t}{\partial z}\frac{\partial w}{\partial z}+\frac{\partial \nu_t}{\partial x}\left(\frac{\partial u}{\partial z}+\frac{\partial w}{\partial x}\right) \tag{12}$$

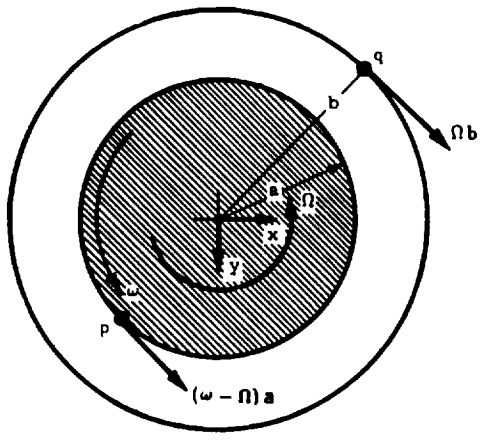


FIG. 5. Definition of the rotating axes in the undisturbed-rotor operation mode.

$$\frac{\partial u}{\partial x} + \frac{\partial v}{\partial y} + \frac{\partial w}{\partial z} = 0, \tag{13}$$

where $u$, $v$, $w$ are the relative velocity components, $p$ is the static pressure, $\Omega$ is the rotational frequency of the coordinate axes (to be set equal to the whirl frequency as the rotor enters its disturbed operation mode) and $\nu_l$, $\nu_t$, $\nu_e$ are the molecular, eddy and effective components of kinematic viscosity coefficients, respectively, where $\nu_e = \nu_l + \nu_t$, with the symbol ($\hat{}$) designating values that are carried over from a previous iteration or an initial guess for the purpose of successively linearizing the momentum equations. As seen, the whirl frequency $\Omega$ is part of these equations, which is a result of including the centrifugal and Coriolis acceleration effects produced by the axes rotational motion.

Simulation of the flow turbulence is based on the algebraic eddy-viscosity turbulence model by Baldwin and Lomax [9]. However, an adjustment in this vorticity-based model was implemented whereby the relative, as opposed to the absolute, vorticity was used to calculate the mixing length in the fluid layer that is adjacent to the rotor surface. Equally important in implementing the model was the analysis of the near-wall zone which was conceptually based on the Benim and Zinser approach [10].

*Boundary conditions*

Referring to the computational domain in Fig. 6, appropriate boundary conditions are needed over all boundary segments as a result of uncompromising the flow ellipticity in the current flow model. These include known profiles of inlet velocity components and zero streamwise diffusion of the exit velocity vector. The latter replaces a zero velocity gradient exit condition which would imply a fully developed flow that may or may not prevail at the exit station depending on the seal length. The last category of boundary conditions concerns the rotor and housing surfaces, and is created by the rotation of the coordinate axes. Referring to Fig. 5, the housing surface, to an observer in the rotating frame of reference, will no longer appear stationary, but will rather possess a relative velocity component $\Omega b$ as indicated in the figure, where $b$ is the housing radius. Considering the case of what would amount to forward whirl (as the rotor axis becomes eccentric), the rotor surface will appear to the same observer as rotating at an angular speed that is less than the rotor operating speed $\omega$ by the amount $\Omega$. The rotor surface velocity in this case is $(\omega - \Omega)a$, where $a$ is the rotor radius.

*Finite-element formulation*

Numerical solution of the centered-rotor flow field is based on the Petrov–Galerkin weighted-residual principle in which the weight functions are so chosen to incorporate the upwinding concept. An effective tool in alleviating spurious pressure modes, this concept has been advocated by many analysts in handling highly convective flows, such as the present. The concept is equally opposed by others due to the false "numerical" diffusion it imparts to the finite element equations. The desire to minimize this false diffusion in the current flow model led to selecting a mixture of the weight functions devised by Heinrich and Zienkiewicz [11] and those used in the conventional Galerkin method in such a way that upwinding is applied only to the nonlinear convection terms on the left-hand side of the momentum equations (10)–(12).

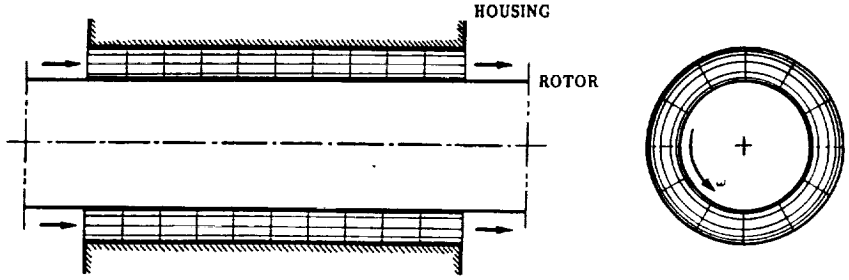


FIG. 6. Finite-element discretization model (drawing not to scale).

The finite-element model is constructed with the 20-node quadratic element in Fig. 7 as the discretization unit. The procedure is initiated by defining the element shape and the Cartesian-to-local system mapping relations. Within a typical element (Fig. 7), let the spatial coordinate conversion be defined, in terms of the nodal values, as follows:

$$x = \sum_{i=1}^{20} N_i x_i, \quad y = \sum_{i=1}^{20} N_i y_i, \quad z = \sum_{i=1}^{20} N_i z_i, \tag{14}$$

where $N_i$ are quadratic "shape" functions [12] of the local coordinates $\zeta$, $\eta$ and $\xi$. Conversion of the spatial derivatives is, in this case, defined as follows:

$$\begin{Bmatrix} \frac{\partial}{\partial x} \\ \frac{\partial}{\partial y} \\ \frac{\partial}{\partial z} \end{Bmatrix} = [T] \begin{Bmatrix} \frac{\partial}{\partial \zeta} \\ \frac{\partial}{\partial \eta} \\ \frac{\partial}{\partial \xi} \end{Bmatrix}, \tag{15}$$

where the components of the matrix $[T]$ are as follows:

$$T_{11} = \frac{1}{|J|}\left( \sum_{i=1}^{20} \frac{\partial N_i}{\partial \eta} y_i \sum_{i=1}^{20} \frac{\partial N_i}{\partial \xi} z_i - \sum_{i=1}^{20} \frac{\partial N_i}{\partial \eta} z_i \sum_{i=1}^{20} \frac{\partial N_i}{\partial \xi} y_i \right)$$

$$T_{12} = \frac{1}{|J|}\left( \sum_{i=1}^{20} \frac{\partial N_i}{\partial \xi} y_i \sum_{i=1}^{20} \frac{\partial N_i}{\partial \zeta} z_i - \sum_{i=1}^{20} \frac{\partial N_i}{\partial \zeta} y_i \sum_{i=1}^{20} \frac{\partial N_i}{\partial \xi} z_i \right)$$

$$T_{13} = \frac{1}{|J|}\left( \sum_{i=1}^{20} \frac{\partial N_i}{\partial \zeta} y_i \sum_{i=1}^{20} \frac{\partial N_i}{\partial \eta} z_i - \sum_{i=1}^{20} \frac{\partial N_i}{\partial \eta} y_i \sum_{i=1}^{20} \frac{\partial N_i}{\partial \xi} z_i \right)$$

$$T_{21} = \frac{1}{|J|}\left( \sum_{i=1}^{20} \frac{\partial N_i}{\partial \xi} x_i \sum_{i=1}^{20} \frac{\partial N_i}{\partial \eta} z_i - \sum_{i=1}^{20} \frac{\partial N_i}{\partial \eta} x_i \sum_{i=1}^{20} \frac{\partial N_i}{\partial \xi} z_i \right)$$

$$T_{22} = \frac{1}{|J|}\left( \sum_{i=1}^{20} \frac{\partial N_i}{\partial \zeta} x_i \sum_{i=1}^{20} \frac{\partial N_i}{\partial \xi} z_i - \sum_{i=1}^{20} \frac{\partial N_i}{\partial \xi} x_i \sum_{i=1}^{20} \frac{\partial N_i}{\partial \zeta} z_i \right)$$

$$T_{23} = \frac{1}{|J|}\left( \sum_{i=1}^{20} \frac{\partial N_i}{\partial \eta} x_i \sum_{i=1}^{20} \frac{\partial N_i}{\partial \zeta} z_i - \sum_{i=1}^{20} \frac{\partial N_i}{\partial \zeta} x_i \sum_{i=1}^{20} \frac{\partial N_i}{\partial \eta} z_i \right)$$

$$T_{31} = \frac{1}{|J|}\left( \sum_{i=1}^{20} \frac{\partial N_i}{\partial \eta} x_i \sum_{i=1}^{20} \frac{\partial N_i}{\partial \xi} y_i - \sum_{i=1}^{20} \frac{\partial N_i}{\partial \xi} x_i \sum_{i=1}^{20} \frac{\partial N_i}{\partial \eta} y_i \right)$$

$$T_{32} = \frac{1}{|J|}\left( \sum_{i=1}^{20} \frac{\partial N_i}{\partial \xi} x_i \sum_{i=1}^{20} \frac{\partial N_i}{\partial \zeta} y_i - \sum_{i=1}^{20} \frac{\partial N_i}{\partial \zeta} x_i \sum_{i=1}^{20} \frac{\partial N_i}{\partial \xi} y_i \right)$$

$$T_{33} = \frac{1}{|J|}\left( \sum_{i=1}^{20} \frac{\partial N_i}{\partial \zeta} x_i \sum_{i=1}^{20} \frac{\partial N_i}{\partial \eta} y_i - \sum_{i=1}^{20} \frac{\partial N_i}{\partial \eta} x_i \sum_{i=1}^{20} \frac{\partial N_i}{\partial \zeta} y_i \right)$$

with $|J|$ being the Jacobian of transformation.

Next, the flow variables are interpolated within the typical element in a similar fashion. Guided by the Ladyshenskaya–Babuska–Brezzi compatibility requirements [13], as applied to the current problem, the velocity components and pressure are expressed as follows:

$$u = \sum_{i=1}^{20} N_i u_i, \quad v = \sum_{i=1}^{20} N_i v_i, \quad w = \sum_{i=1}^{20} N_i w_i, \quad p = \sum_{k=1}^{8} M_k p_k, \tag{16}$$

where the interpolants $M_k$ appearing in the pressure expression are the linear shape functions associated with the finite element corner nodes [12].

The error functions produced by the unperturbed flow governing equations as a result of the interpolation expressions above, are then made orthogonal to a special set of weight functions $W_i$ throughout the finite element. In constructing these functions, the so-called error consistency criterion of Hood and Taylor [14] is implemented, whereby the element

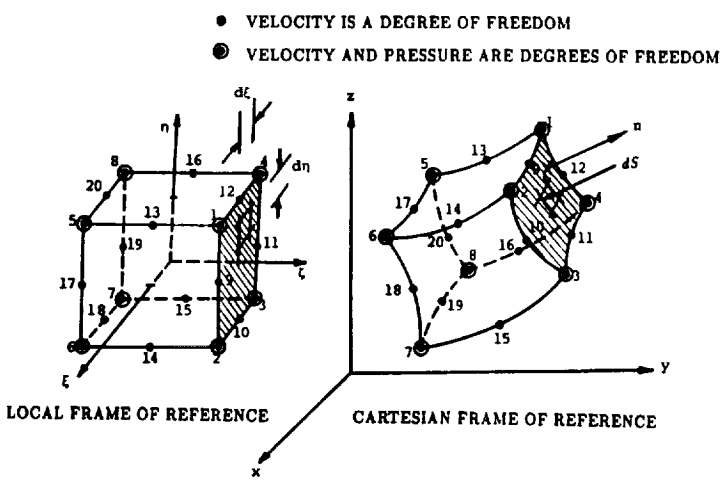


FIG. 7. Quadrilateral isoparametric finite element used for field discretization.

linear shape functions, $M_i$, are used in conjunction with the continuity equation. The weight functions used with the momentum equations, on the other hand, are of the upwind form $W_i$ described by Heinrich and Zienkiewicz [11] when applied to the convection terms, and are identical to the element quadratic shape functions $N_i$ for all other terms.

The orthogonality conditions, stated above, constitute the elemental set of eqations, which can be written as follows:

$$[a_1]\{u\} + [a_2]\{v\} + [a_3]\{w\} + [a_4]\{p\} = \{b_1\} \tag{17}$$

$$[a_5]\{u\} + [a_6]\{v\} + [a_7]\{w\} + [a_8]\{p\} = \{b_2\} \tag{18}$$

$$[a_9]\{u\} + [a_{10}]\{v\} + [a_{11}]\{w\} + [a_{12}]\{p\} = \{b_3\} \tag{19}$$

$$[a_{13}]\{u\} + [a_{14}]\{v\} + [a_{15}]\{w\} = 0, \tag{20}$$

where

$$a_1)_{i,j} = \int_{V^{(e)}} \{\hat{v}_e[\mathbf{F}(N_i)\mathbf{F}(N_j) + \mathbf{G}(N_i)\mathbf{G}(N_j) + \mathbf{H}(N_i)\mathbf{H}(N_j)]$$
$$- W_i[\mathbf{G}(\hat{v}_t)\mathbf{G}(N_j) + \mathbf{H}(\hat{v}_t)\mathbf{H}(N_j) + 2\mathbf{F}(\hat{v}_t)\mathbf{F}(N_j)]$$
$$+ W_i[\hat{u}\mathbf{F}(N_j) + \hat{v}\mathbf{G}(N_j) + \hat{w}\mathbf{H}(N_j)]\}\,dV$$

$$a_2)_{i,j} = \int_{V^{(e)}} - N_i[\mathbf{G}(\hat{v}_t)\mathbf{F}(N_j) - 2\Omega N_j]\,dV$$

$$a_3)_{i,j} = \int_{V^{(e)}} - W_i\mathbf{H}(\hat{v}_t)\mathbf{F}(N_j)\,dV$$

$$a_4)_{i,k} = \int_{V^{(e)}} \frac{1}{\rho} N_i\mathbf{F}(M_k)\,dV$$

$$a_5)_{i,j} = \int_{V^{(e)}} - N_i[\mathbf{F}(\hat{v}_t)\mathbf{G}(N_j) + 2\Omega N_j]\,dV$$

$$a_6)_{i,j} = \int_{V^{(e)}} \{\hat{v}_e[\mathbf{F}(N_i)\mathbf{F}(N_j) + \mathbf{G}(N_i)\mathbf{G}(N_j) + \mathbf{H}(N_i)\mathbf{H}(N_j)]$$
$$- W_i[\mathbf{F}(\hat{v}_t)\mathbf{F}(N_j) + \mathbf{H}(\hat{v}_t)\mathbf{H}(N_j) + 2\mathbf{G}(\hat{v}_t)\mathbf{G}(N_j)]$$
$$+ W_i[\hat{u}\mathbf{F}(N_j) + \hat{v}\mathbf{G}(N_j) + \hat{w}\mathbf{H}(N_j)]\}\,dV$$

$$a_7)_{i,j} = \int_{V^{(e)}} -N_i \mathbf{H}(\hat{v}_t)\mathbf{G}(N_j)\mathrm{d}V$$

$$a_8)_{i,k} = \int_{V^{(e)}} \frac{1}{\rho} N_i \mathbf{G}(M_k)\mathrm{d}V$$

$$a_9)_{i,j} = \int_{V^{(e)}} -N_i \mathbf{F}(\hat{v}_t)\mathbf{H}(N_j)\mathrm{d}V$$

$$a_{10})_{i,j} = \int_{V^{(e)}} -N_i \mathbf{G}(\hat{v}_t)\mathbf{H}(N_j)\mathrm{d}V$$

$$\begin{aligned} a_{11})_{i,j} = \int_{V^{(e)}} \{&\hat{v}_e[\mathbf{F}(N_i)\mathbf{F}(N_j) + \mathbf{G}(N_i)\mathbf{G}(N_j) + \mathbf{H}(N_i)\mathbf{H}(N_j)] \\ &- W_i[\mathbf{F}(\hat{v}_t)\mathbf{F}(N_j) + \mathbf{G}(\hat{v}_t)\mathbf{G}(N_j) + 2\mathbf{H}(\hat{v}_t)\mathbf{H}(N_j)] \\ &+ W_i[\hat{u}\mathbf{F}(N_j) + \hat{v}\mathbf{G}(N_j) + \hat{w}\mathbf{H}(N_j)]\}\,\mathrm{d}V \end{aligned}$$

$$a_{12})_{i,k} = \int_{V^{(e)}} \frac{1}{\rho} N_i \mathbf{H}(M_k)\mathrm{d}V$$

$$a_{13})_{k,j} = \int_{V^{(e)}} M_k \mathbf{F}(N_j)\mathrm{d}V$$

$$a_{14})_{k,j} = \int_{V^{(e)}} M_k \mathbf{G}(N_j)\mathrm{d}V$$

$$a_{15})_{k,j} = \int_{V^{(e)}} M_k \mathbf{H}(N_j)\mathrm{d}V$$

$$b_1)_i = \int_{S^{(e)}} \hat{v}_e N_i(\vec{n}\cdot\nabla u)\mathrm{d}S + \Omega^2 \int_{V^{(e)}} N_i\left(\sum_{l=1}^{20} N_l x_l\right)\mathrm{d}V$$

$$b_2)_i = \int_{S^{(e)}} \hat{v}_e N_i(\vec{n}\cdot\nabla v)\mathrm{d}S + \Omega^2 \int_{V^{(e)}} N_i\left(\sum_{l=1}^{20} N_l y_l\right)\mathrm{d}V$$

$$b_3)_i = \int_{S^{(e)}} \hat{v}_e N_i(\vec{n}\cdot\nabla w)\mathrm{d}S,$$

where $i = 1, 2, \ldots, 20$; $j = 1, 2, \ldots, 20$; $k = 1, 2, \ldots, 8$; the superscript ($\hat{}$) refers to a value that is known from a previous iteration or an initial guess, $\mathrm{d}S$ is the differential element of surface area (Fig. 7) and $\vec{n}$ is the local unit vector normal to the boundary. Also, the volume differential $\mathrm{d}V$ and the operators **F**, **G** and **H** are defined as follows:

$$\mathrm{d}V = |J|\mathrm{d}\zeta\mathrm{d}\eta\mathrm{d}\xi$$

$$\mathbf{F} = T_{11}\frac{\partial}{\partial\zeta} + T_{12}\frac{\partial}{\partial\eta} + T_{13}\frac{\partial}{\partial\xi} \tag{21}$$

$$\mathbf{G} = T_{21}\frac{\partial}{\partial\zeta} + T_{22}\frac{\partial}{\partial\eta} + T_{23}\frac{\partial}{\partial\xi} \tag{22}$$

$$\mathbf{H} = T_{31}\frac{\partial}{\partial\zeta} + T_{32}\frac{\partial}{\partial\eta} + T_{33}\frac{\partial}{\partial\xi}. \tag{23}$$

It should be pointed out that expanding the finit element equations in terms of the operators **F**, **G** and **H**, defined above, is consistent with, and indeed simplifies, the procedure leading to the perturbed version of these equations, as will be seen later in this section.

Equations (17)–(20) can be rewritten in the following compact form:

$$[a]\{\phi\} = \{b\}, \tag{24}$$

where the vector $\{\phi\}$ contains the nodal values of velocity components and static pressure

that are associated with the typical finite element. The global form of the elemental set of equations (24) is obtained by assembling all finite element contributions, and introducing the various boundary conditions, at which point the equations are expressible in the following form:

$$[A]\{\Phi\} = \{B\}. \tag{25}$$

*Perturbation model*

Referring to equations (8) and (9), determination of the rotordynamic coefficients reduces to the fundamental problem of computing the rate at which fluid-exerted moments in the clearance gap are developed with respect to an infinitesimally small angular eccentricity of the rotor axis. This is the problem under focus in this section.

The current model is centered around the manner in which the finite-element equations (25) are altered as a result of the rotor virtual angular eccentricity $\theta$ which leads to the rotor conical whirl depicted in Fig. 1b. Referring to this figure, this infinitesimally small eccentricity will create a linearly varying displacement, $e$, of the rotor axis where:

$$e = \theta z \tag{26}$$

with $z$ being the distance from the center of the tilting motion. Under such lateral displacement, each finite element will, as a result of virtual distortion, yield a perturbed set of equations. Let the assembled form of these equations, by reference to (25), be as follows:

$$([A] + \theta[\bar{A}])(\{\Phi\} + \{\delta\Phi\}) = (\{B\} + \theta\{\bar{B}\}). \tag{27}$$

Subtracting (25) from (27), the following expression for $\delta\Phi$ is obtained:

$$\{\delta\Phi\} = \theta[A]^{-1}(\{\bar{B}\} - [\bar{A}]\{\Phi\}) \tag{28}$$

or,

$$\frac{\partial\{\Phi\}}{\partial\theta} = \lim_{\theta\to 0}\left(\frac{\delta\Phi}{\theta}\right) = [A]^{-1}(\{\bar{B}\} - [\bar{A}]\{\Phi\}). \tag{29}$$

Equation (29) implies that two new arrays, namely the matrix $[\bar{A}]$ and the vector $\{\bar{B}\}$, are needed to compute the rate at which the flow variables (namely the velocity components and pressure) vary with respect to the rotor angular eccentricity $\theta$. These arrays are primarily a result of finite elements distortion effects that are associated with the rotor displaced position (Fig. 8). The arrays $[\bar{A}]$ and $\{\bar{B}\}$ are derived next as part of the procedure

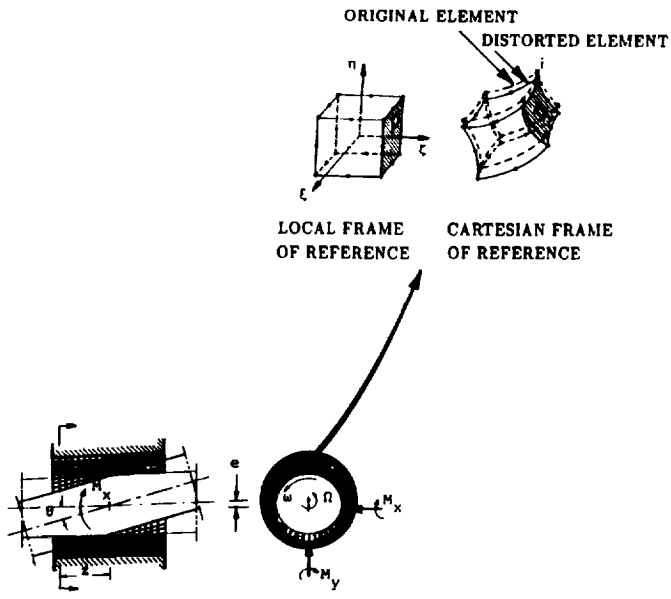


FIG. 8. Destruction of the flow axisymmetry as a result of the rotor eccentricity.

to compute the rotordynamic coefficients. To do this, a typical distorted element will first be analysed, and the elemental contributions $[\bar{a}]$ and $\{\bar{b}\}$ derived. The global arrays $[\bar{A}]$ and $\{\bar{B}\}$ can subsequently be obtained by assembling $[\bar{a}]$ and $\{\bar{b}\}$ among all finite elements.

*Analysis of a distorted finite element in the whirling frame of reference.* Consider a distorted finite element in the clearance gap that corresponds to the displaced rotor operation mode (Fig. 8). A typical node $i$ of this element will now be displaced by an amount that is a function of the local value of the rotor lateral displacement (which is a function of the axial coordinate) and the node location in the cross-flow plane. Referred to the axes in their displaced location, the new nodal coordinates are:

$$X_i = x_i, \quad Y_i = y_i + \lambda_i\theta \quad \text{and} \quad Z_i = z_i. \tag{30}$$

The quantity $\lambda_i$ attains its maximum value on the housing (where it is equal to $-z_i$) and vanishes for nodes on the rotor. The reason is that the housing, to an observer in the whirling frame of reference, is the surface that undergoes the virtual displacement (note the positive direction of the $y$-axis in Fig. 8). The local-to-Cartesian transformation Jacobian $|J|$ can correspondingly be written for a distorted finite element as $|J_1|$ where:

$$|J_1| = |J| + \theta|\bar{J}| \tag{31}$$

in which the Jacobian $|J|$ is that of the undistorted element, and $|\bar{J}|$ is as follows:

$$|\bar{J}| = \begin{vmatrix} \sum_{i=1}^{20} \frac{\partial N_i}{\partial \zeta} x_i & \sum_{i=1}^{20} \frac{\partial N_i}{\partial \zeta} \lambda_i & \sum_{i=1}^{20} \frac{\partial N_i}{\partial \zeta} z_i \\ \sum_{i=1}^{20} \frac{\partial N_i}{\partial \eta} x_i & \sum_{i=1}^{20} \frac{\partial N_i}{\partial \eta} \lambda_i & \sum_{i=1}^{20} \frac{\partial N_i}{\partial \eta} z_i \\ \sum_{i=1}^{20} \frac{\partial N_i}{\partial \xi} x_i & \sum_{i=1}^{20} \frac{\partial N_i}{\partial \xi} \lambda_i & \sum_{i=1}^{20} \frac{\partial N_i}{\partial \xi} z_i \end{vmatrix}.$$

A new spatial derivative operator, that is equivalent to that in equation (10) can now be derived as follows:

$$\begin{Bmatrix} \frac{\partial}{\partial x} \\ \frac{\partial}{\partial y} \\ \frac{\partial}{\partial z} \end{Bmatrix} = ([T] + \theta[P]) \begin{Bmatrix} \frac{\partial}{\partial \zeta} \\ \frac{\partial}{\partial \eta} \\ \frac{\partial}{\partial \xi} \end{Bmatrix}, \tag{32}$$

where the matrix $[T]$ is as described in equation (15) while the matrix $[P]$ is defined as follows:

$$P_{11} = \frac{1}{|J|}\left( \sum_{i=1}^{20} \frac{\partial N_i}{\partial \eta} \lambda_i \sum_{i=1}^{20} \frac{\partial N_i}{\partial \xi} z_i - \sum_{i=1}^{20} \frac{\partial N_i}{\partial \xi} \lambda_i \sum_{i=1}^{20} \frac{\partial N_i}{\partial \eta} z_i \right) - \frac{|\bar{J}|}{|J|^2} T_{11}$$

$$P_{12} = \frac{1}{|J|}\left( \sum_{i=1}^{20} \frac{\partial N_i}{\partial \xi} \lambda_i \sum_{i=1}^{20} \frac{\partial N_i}{\partial \zeta} z_i - \sum_{i=1}^{20} \frac{\partial N_i}{\partial \zeta} \lambda_i \sum_{i=1}^{20} \frac{\partial N_i}{\partial \xi} z_i \right) - \frac{|\bar{J}|}{|J|^2} T_{12}$$

$$P_{13} = \frac{1}{|J|}\left( \sum_{i=1}^{20} \frac{\partial N_i}{\partial \zeta} \lambda_i \sum_{i=1}^{20} \frac{\partial N_i}{\partial \eta} z_i - \sum_{i=1}^{20} \frac{\partial N_i}{\partial \eta} \lambda_i \sum_{i=1}^{20} \frac{\partial N_i}{\partial \zeta} z_i \right) - \frac{|\bar{J}|}{|J|^2} T_{13}$$

$$P_{21} = -\frac{|\bar{J}|}{|J|^2} T_{21}$$

$$P_{22} = -\frac{|\bar{J}|}{|J|^2} T_{22}$$

$$P_{23} = -\frac{|\bar{J}|}{|J|^2} T_{23}$$

$$P_{31}=\frac{1}{|J|}\left(\sum_{i=1}^{20}\frac{\partial N_i}{\partial\eta}x_i\sum_{i=1}^{20}\frac{\partial N_i}{\partial\xi}\lambda_i-\sum_{i=1}^{20}\frac{\partial N_i}{\partial\xi}x_i\sum_{i=1}^{20}\frac{\partial N_i}{\partial\eta}\lambda_i\right)-\frac{|\bar{J}|}{|J|^2}T_{31}$$

$$P_{32}=\frac{1}{|J|}\left(\sum_{i=1}^{20}\frac{\partial N_i}{\partial\xi}x_i\sum_{i=1}^{20}\frac{\partial N_i}{\partial\zeta}\lambda_i-\sum_{i=1}^{20}\frac{\partial N_i}{\partial\zeta}x_i\sum_{i=1}^{20}\frac{\partial N_i}{\partial\xi}\lambda_i\right)-\frac{|\bar{J}|}{|J|^2}T_{32}$$

$$P_{33}=\frac{1}{|J|}\left(\sum_{i=1}^{20}\frac{\partial N_i}{\partial\zeta}x_i\sum_{i=1}^{20}\frac{\partial N_i}{\partial\eta}\lambda_i-\sum_{i=1}^{20}\frac{\partial N_i}{\partial\eta}x_i\sum_{i=1}^{20}\frac{\partial N_i}{\partial\zeta}\lambda_i\right)-\frac{|\bar{J}|}{|J|^2}T_{33}.$$

Substituting expressions (31) and (32) into the flow equations (10)–(13) and re-applying Galerkin's weighted-residual procedure, the distorted element equations can be written (upon separation of terms containing $\theta$) as follows:

$$([a]+\theta[\bar{a}])(\{\phi\}+\{\delta\phi\})=(\{b\}+\theta\{\bar{b}\}), \tag{33}$$

where the matrix $[\bar{a}]$ and vector $\{\bar{b}\}$ result from the distortion in the element shape. The vector $\{\delta\phi\}$ in this case contains the differential changes in the nodal values of velocity components and pressure that are created by the virtual eccentricity.

Noting that the matrix $[\bar{a}]$ is similar in construction to $[a]$ in equation (24), the former can consistently be viewed as composed of submatrices $[\bar{a}_1]$–$[\bar{a}_{15}]$, which correspond to those in equations (17)–(20), and are defined as follows:

$$\begin{aligned}\bar{a}_1)_{i,j}=a_1^*)_{i,j}+\int_{V^{(e)}}\{&\hat{v}_e[\mathbf{F}(N_i)\mathbf{I}(N_j)+\mathbf{I}(N_i)\mathbf{F}(N_j)+\mathbf{G}(N_i)\mathbf{J}(N_j)+\mathbf{J}(N_i)\mathbf{G}(N_j)\\&+\mathbf{H}(N_i)\mathbf{K}(N_j)+\mathbf{K}(N_i)\mathbf{H}(N_j)]-N_i[\mathbf{G}(\hat{v}_t)\mathbf{J}(N_j)+\mathbf{J}(\hat{v}_t)\mathbf{G}(N_j)\\&+\mathbf{H}(\hat{v}_t)\mathbf{K}(N_j)+\mathbf{K}(\hat{v}_t)\mathbf{H}(N_j)\\&+2\mathbf{F}(\hat{v}_t)\mathbf{I}(N_j)+2\mathbf{I}(\hat{v}_t)\mathbf{F}(N_j)]+N_i[\hat{u}\mathbf{I}(N_j)+\hat{v}\mathbf{J}(N_j)+\hat{w}\mathbf{K}(N_j)]\}\,\mathrm{d}V\end{aligned}$$

$$\bar{a}_2)_{i,j}=a_2^*)_{i,j}-\int_{V^{(e)}}N_i[\mathbf{G}(\hat{v}_t)\mathbf{I}(N_j)+\mathbf{J}(\hat{v}_t)\mathbf{F}(N_j)]\mathrm{d}V$$

$$\bar{a}_3)_{i,j}=a_3^*)_{i,j}-\int_{V^{(e)}}N_i[\mathbf{H}(\hat{v}_t)\mathbf{I}(N_j)+\mathbf{K}(\hat{v}_t)\mathbf{F}(N_j)]\mathrm{d}V$$

$$\bar{a}_4)_{i,k}=a_4^*)_{i,k}+\int_{V^{(e)}}\frac{1}{\rho}N_i\mathbf{I}(M_k)\mathrm{d}V$$

$$\bar{a}_5)_{i,j}=a_5^*)_{i,j}-\int_{V^{(e)}}N_i[\mathbf{F}(\hat{v}_t)\mathbf{J}(N_j)+\mathbf{I}(\hat{v}_t)\mathbf{G}(N_j)]\mathrm{d}V$$

$$\begin{aligned}\bar{a}_6)_{i,j}=a_6^*)_{i,j}+\int_{V^{(e)}}\{&\hat{v}_e[\mathbf{F}(N_i)\mathbf{I}(N_j)+\mathbf{I}(N_i)\mathbf{F}(N_j)+\mathbf{G}(N_i)\mathbf{J}(N_j)+\mathbf{J}(N_i)\mathbf{G}(N_i)\\&+\mathbf{H}(N_i)\mathbf{K}(N_j)+\mathbf{K}(N_i)\mathbf{H}(N_j)]-N_i[\mathbf{F}(\hat{v}_t)\mathbf{I}(N_j)+\mathbf{I}(\hat{v}_t)\mathbf{F}(N_j)\\&+\mathbf{H}(\hat{v}_t)\mathbf{K}(N_j)+\mathbf{K}(\hat{v}_t)\mathbf{H}(N_j)+2\mathbf{G}(\hat{v}_t)\mathbf{J}(N_j)+2\mathbf{J}(\hat{v}_t)\mathbf{G}(N_j)]\\&+N_i[\hat{u}\mathbf{I}(N_j)+\hat{v}\mathbf{J}(N_j)+\hat{w}\mathbf{K}(N_j)]\}\,\mathrm{d}V\end{aligned}$$

$$\bar{a}_7)_{i,j}=a_7^*)_{i,j}-\int_{V^{(e)}}N_i[\mathbf{H}(\hat{v}_t)\mathbf{J}(N_j)+\mathbf{K}(\hat{v}_t)\mathbf{G}(N_j)]\mathrm{d}V$$

$$\bar{a}_8)_{i,k}=a_8^*)_{i,k}-\int_{V^{(e)}}\frac{1}{\rho}N_i\mathbf{J}(M_k)\mathrm{d}V$$

$$\bar{a}_9)_{i,j}=a_9^*)_{i,j}-\int_{V^{(e)}}N_i[\mathbf{F}(\hat{v}_t)\mathbf{K}(N_j)+\mathbf{I}(\hat{v}_t)\mathbf{H}(N_j)]\mathrm{d}V$$

$$\bar{a}_{10})_{i,j}=a_{10}^*)_{i,j}-\int_{V^{(e)}}N_i[\mathbf{G}(\hat{v}_t)\mathbf{K}(N_j)+\mathbf{J}(\hat{v}_t)\mathbf{H}(N_j)]\mathrm{d}V$$

$$\bar{a}_{11})_{i,j} = a^*_{11})_{i,j} + \int_{V^{(e)}} \{\hat{v}_e[\mathbf{F}(N_i)\mathbf{I}(N_j) + \mathbf{I}(N_i)\mathbf{F}(N_j) + \mathbf{G}(N_i)\mathbf{J}(N_j) + \mathbf{J}(N_i)\mathbf{G}(N_j) + \mathbf{H}(N_i)\mathbf{K}(N_j) + \mathbf{K}(N_i)\mathbf{H}(N_j)] - N_i[\mathbf{F}(\hat{v}_t)\mathbf{I}(N_j) + \mathbf{I}(\hat{v}_t)\mathbf{F}(N_j) + \mathbf{G}(\hat{v}_t)\mathbf{J}(N_j) + \mathbf{J}(\hat{v}_t)\mathbf{G}(N_j) + 2\mathbf{H}(\hat{v}_t)\mathbf{K}(N_j) + 2\mathbf{K}(\hat{v}_t)\mathbf{H}(N_j) + N_i[\hat{u}\mathbf{I}(N_j) + \hat{v}\mathbf{J}(N_j) + \hat{w}\mathbf{K}(N_j)]\}\mathrm{d}V$$

$$\bar{a}_{12})_{i,k} = a^*_{12})_{i,k} + \int_{V^{(e)}} \frac{1}{\rho} N_i \mathbf{K}(M_k)\mathrm{d}V$$

$$\bar{a}_{13})_{k,j} = a^*_{13})_{k,j} + \int_{V^{(e)}} M_k \mathbf{I}(N_j)\mathrm{d}V$$

$$\bar{a}_{14})_{k,j} = a^*_{14})_{k,j} + \int_{V^{(e)}} M_k \mathbf{J}(N_j)\mathrm{d}V$$

$$\bar{a}_{15})_{k,j} = a^*_{15})_{k,j} + \int_{V^{(e)}} M_k \mathbf{K}(N_j)\mathrm{d}V.$$

In these expressions, a variable with an asterisk has the same form as that in equations (17)–(20), with the exception that the Jacobian $|J|$ is now replaced by $|\bar{J}|$ as defined in equation (31), also $\mathrm{d}V = |J|\mathrm{d}\zeta\mathrm{d}\eta\mathrm{d}\xi$. The vector $\{\bar{b}\}$ in equation (33) can similarly be defined by the subvectors $\{\bar{b}_1\}$, $\{\bar{b}_2\}$ and $\{\bar{b}_3\}$, in consistency with equations (17)–(20), as follows:

$$\bar{b}_1)_i = \Omega^2 \int_{V^{(e)}} N_i \left( \sum_{l=1}^{20} N_l x_l \right) |\bar{J}|\mathrm{d}\zeta\mathrm{d}\eta\mathrm{d}\xi$$

$$\bar{b}_2)_i = \Omega^2 \int_{V^{(e)}} N_i \left( \sum_{l=1}^{20} N_l y_l \right) |\bar{J}|\mathrm{d}\zeta\mathrm{d}\eta\mathrm{d}\xi - \Omega^2 \int_{V^{(e)}} N_i \left( \sum_{l=1}^{20} N_l \lambda_l \right)\mathrm{d}V$$

$$\bar{b}_3)_i = 0,$$

where $i$ and $j$ vary from 1–20, while $k$ varies from 1–8. With the operators **F**, **G** and **H** being those defined by equations (21)–(23), the new operators **I**, **J** and **K** are defined as follows:

$$\mathbf{I} = P_{11}\frac{\partial}{\partial\zeta} + P_{12}\frac{\partial}{\partial\eta} + P_{13}\frac{\partial}{\partial\xi} \tag{34}$$

$$\mathbf{J} = P_{21}\frac{\partial}{\partial\zeta} + P_{22}\frac{\partial}{\partial\eta} + P_{23}\frac{\partial}{\partial\xi} \tag{35}$$

$$\mathbf{K} = P_{31}\frac{\partial}{\partial\zeta} + P_{32}\frac{\partial}{\partial\eta} + P_{33}\frac{\partial}{\partial\xi} \tag{36}$$

with the matrix $[P]$ being that defined earlier in this section.

*Calculation of the rotordynamic coefficients.* Equation (29) can be rewritten in the following detailed form:

$$\frac{\partial\Phi}{\partial\theta} \equiv \frac{\partial}{\partial\theta}\begin{Bmatrix}\{U\}\\ \{V\}\\ \{W\}\\ \{P\}\end{Bmatrix} = [A]^{-1}(\{\bar{B}\} - [\bar{A}]\{\Phi\}), \tag{37}$$

where $\{U\}$, $\{V\}$, $\{W\}$ and $\{P\}$ are vectors containing the nodal values of the velocity components and pressure, respectively, with the overbars signifying quantities that are associated with the perturbation in the rotor-to-housing flow field. Of all the pressure nodal values in the vector $\{P\}$ above, define a subvector $\{\mathscr{P}\}$ as composed of the pressure values at the rotor surface nodes, i.e.

$$\{\mathscr{P}\} = \{p_i, i = 1, N_s\} \subset \{P\} \tag{38}$$

where $N_s$ is the total number of corner nodes existing on the rotor surface. It is true, in this case, that $\{\partial\mathscr{P}/\partial\theta\} = \{(\partial p/\partial\theta)_i, i = 1, N_s\}$ is but a subvector of the already computed global vector $\{\partial\Phi/\partial\theta\}$ in equation (37) and is, therefore, known at this computational step.

Next, consider a finite element face "s" that exists on the rotor surface (Fig. 9). The pressure derivative $p_{,\theta}^{(s)}$ over this surface element can now be interpolated in terms of the known pressure derivatives at the four corner nodes as follows:

$$p_{,\theta}^{(s)} = \sum_{i=1}^{4} M_i(1, \eta, \xi)\left(\frac{\partial p}{\partial\theta}\right)_i. \tag{39}$$

Once integrated over the proper differential segment of the rotor surface, the function $p_{,\varepsilon}$ (above) yields a differential force which in turn, can be resolved in the $x$ and $y$ directions. Taking the moments of these forces around the center of tilting motion in Fig. 2 and summing the result over all finite elements sharing faces with the rotor surface, the rate (with respect to $\theta$) at which the fluid reaction moments are exerted can be expressed as follows:

$$\frac{\partial M_x}{\partial\theta} = \sum_{i=1}^{N_s}\int_{-1}^{+1}\int_{-1}^{+1} zn_y(\eta, \xi)p_{,\theta}(\eta, \xi)G(\eta, \xi)\,d\eta\,d\xi \tag{40}$$

$$\frac{\partial M_y}{\partial\theta} = \sum_{i=1}^{N_s}\int_{-1}^{+1}\int_{-1}^{+1} zn_x(\eta, \xi)p_{,\theta}(\eta, \xi)G(\eta, \xi)\,d\eta\,d\xi, \tag{41}$$

where $n_x$ and $n_y$ are the components of the local unit vector that is normal to the rotor surface. Also, the parameter $G(\eta, \xi)$ is a Jacobian-like function for Cartesian-to-local area transformation, and was previously derived by Baskharone [15] as follows:

$$G(\eta, \xi) = \left[\left(\frac{\partial y}{\partial\eta}\frac{\partial z}{\partial\xi} - \frac{\partial y}{\partial\xi}\frac{\partial z}{\partial\eta}\right)^2 + \left(\frac{\partial x}{\partial\xi}\frac{\partial z}{\partial\eta} - \frac{\partial x}{\partial\eta}\frac{\partial z}{\partial\xi}\right)^2 + \left(\frac{\partial x}{\partial\eta}\frac{\partial y}{\partial\xi} - \frac{\partial x}{\partial\xi}\frac{\partial y}{\partial\eta}\right)^2\right]^{1/2},$$

where the derivatives on the right-hand side are evaluated using the interpolation expressions (16) for a $\zeta$ value of 1.0 (Fig. 9).

At this point, the requirements for computing the moment coefficients ($\bar{K}$, $\bar{k}$, $\bar{C}$, $\bar{c}$, $\bar{M}$, $\bar{m}$) are, by reference to equations (8) and (9), complete. The process, as described earlier, consists of computing the two moment derivatives in equations (40) and (41) at three or more whirl frequencies $\Omega$ to create a quadratic function of $\partial M_x/\partial\theta$ and $\partial M_y/\partial\theta$ in $\Omega$. Substitution in equations (8) and (9) finally leads to the moment coefficients $\bar{K}$, $\bar{k}$, $\bar{C}$, . . . by inspection.

## 3. RESULTS AND DISCUSSION

A hydraulic annular seal with a clearance/length ratio of 0.0085 was selected for the purpose of verifying the current computational model. The force coefficients of this seal were determined by Dietzen and Nordmann [2], and later verified by Hensel [8]. This seal has a rotor radius of 23.5 mm and a Reynolds number (based on the clearance and inlet through-flow velocity) of 4700. Operating speeds of 2000, 4000 and 6000 rpm were

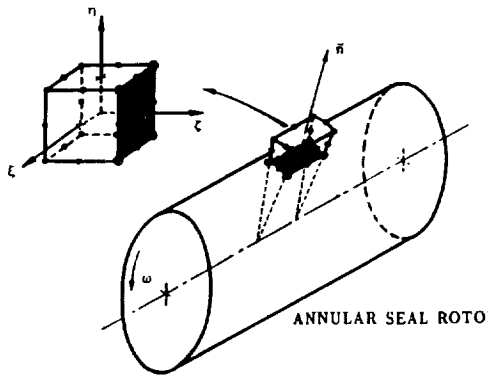


FIG. 9. Integration of the pressure forces on the rotor surface.

considered in this case, together with preswirl/inlet velocity ratios of 0.04, 0.10 and 0.17, respectively.

Shown in Fig. 10 is an assessment of the zeroth-order undisplaced-rotor flow solution under the operating conditions cited above. Compared in this figure is the computed nondimensional pressure drop across the seal, to that obtained through Yamada's experimental correlation [16]. This correlation is probably the most accurate empirical means of determining the seal resistance in terms of the seal geometry, rotor speed and preswirl ratio. As seen in Fig. 10, the computed pressure drop is in good agreement with Yamada's predictions as the average deviation between the two data sets in the seal operation range is approximately 5%.

The computed rotordynamic coefficients are compared to those obtained through Childs' bulk flow analysis [3] for the same seal configuration and operating conditions. Worth noting here is the fact that Childs' simplified model has reportedly been successful [6] when applied to simple clearance gaps where zones of flow separation and recirculation, such as those in labyrinth seals, are non-existing. Absence of these complications provides an environment where Childs' idealization of the clearance gap flow, including parabolized flow equations and unsimulated shear stresses away from solid walls, would have a minimum impact on the numerical solution. Note that the current computational model is conceptually capable of handling such flow complications since the model is based on a totally elliptic flow field in the clearance gap. However, it is felt that the algebraic turbulence closure in the current analysis may not be appropriate for seal configurations which are inherently associated with massive flow separation and recirculation (e.g. the labyrinth seal category). Under such circumstances, a two-equation turbulence closure (e.g. Benim and Zinser [10]) would provide a more accurate means of modeling the flow field.

Figure 11 shows a comparison between the computed moment coefficients and those obtained through Childs' bulk-flow model [3]. These are the direct ($\bar{K}$, $\bar{C}$) and cross-coupled ($\bar{k}$, $\bar{c}$) stiffness and damping coefficients defined in equation (2). The direct inertia coefficient ($\bar{M}$) in this equation was extremely small in the two sets of results, making the magnitudes of this coefficient comparable to the numerical errors in both computer codes. On the other hand, it is known [6] that straight annular seals, such as the present, are categorically incapable of displaying any cross-coupled inertia coefficient ($\bar{m}$) whatsoever.

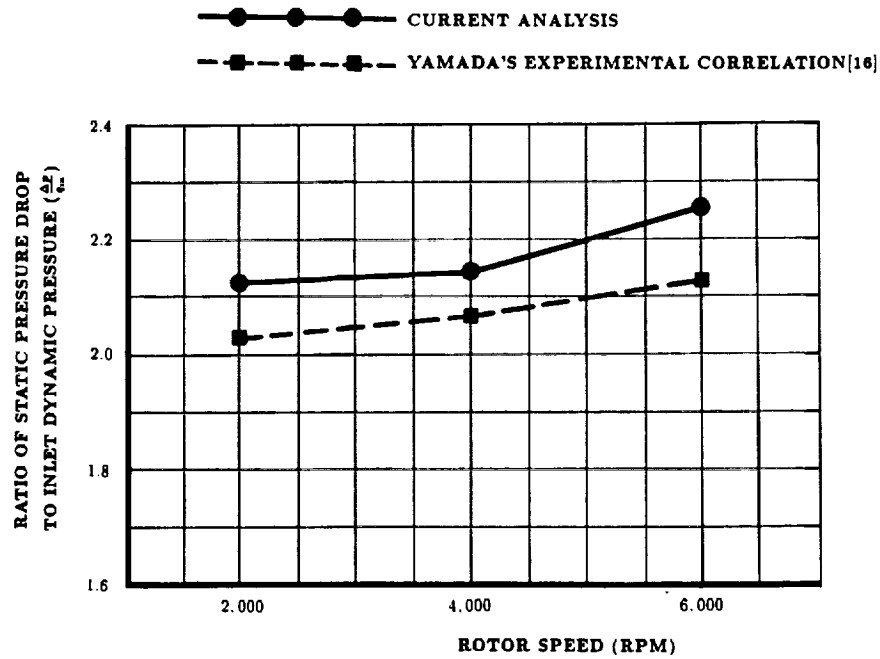


FIG. 10. Comparison of the computed seal pressure drop with that obtained through Yamada's experimental correlation formula.

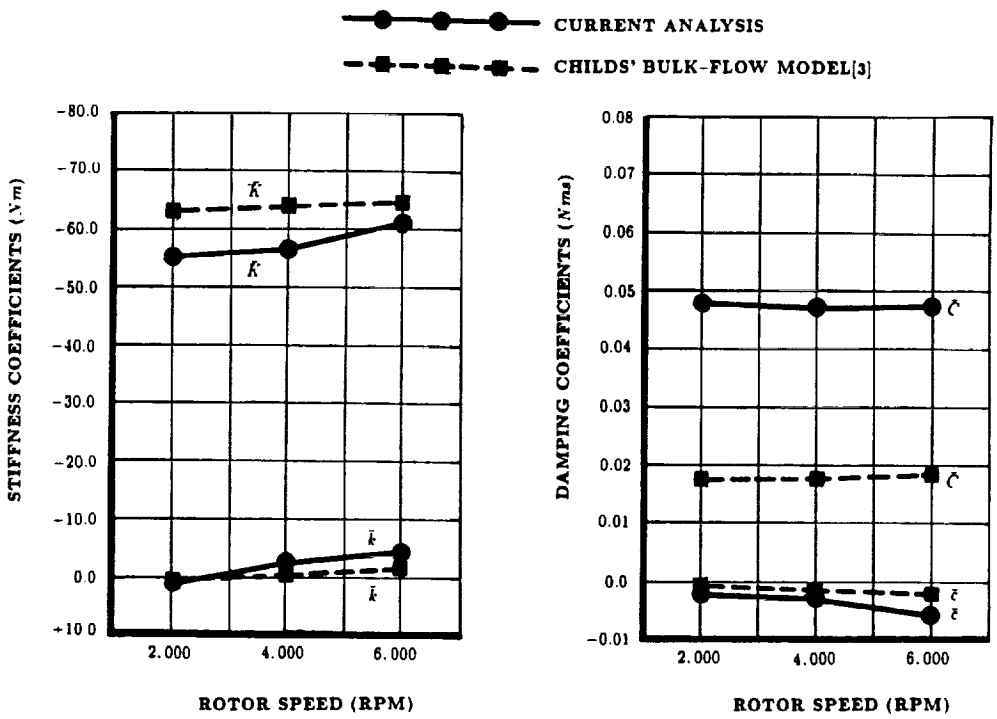


FIG. 11. Comparison of the computed moment coefficients with those computed through Childs' bulk flow model.

Interpretation of the numerical results in Fig. 11 is made by reference to the rotor components of motion illustrated in Fig. 1 and the moment derivatives in equation (9). It is seen in the figure that conical whirl, which is the instability mechanism under consideration, is created and sustained by the moment component $M_y$, and that a positive value of $\partial M_y/\partial\theta$ indeed creates an aggrevating, as opposed to restoring, effect in the case of forward whirl (where the rotor whirl is in the same direction as the spinning speed $\omega$), which is the case depicted in Fig. 1b. With this in mind, equation (9) suggests that such destabilizing effect would be created by positive and large magnitudes of $\bar{k}$, and would diminish at sufficiently large and positive magnitudes of $\bar{C}$. Examination of the results in Fig. 11, in light of this discussion, reveals that the seal under consideration becomes more stable as the rotor speed $\omega$ is increased. This seems to consistently be the case in the speed range under consideration in spite of the deviation between, in particular, the $\bar{C}$ values computed in the current study and those resulting from the bulk-flow analysis. Otherwise, it is worth noting that the trends of the other rotordynamic coefficients are similar in both sets of results and that the direct stiffness coefficients, in particular, are in good agreement. Importance of the latter observation stems from the fact that the two computational modes are vastly different in the aspects of strategy and numerical details.

## 4. CONCLUDING REMARKS

The analysis outlined in this paper provides a detailed look at the rotor/fluid interaction in seals as the rotor operation experiences a conical type of whirl. This unstable operation can be initiated by a rotor misalignment, as is frequently the case in turbomachinery applications, or by rotor self excitation. Regardless of the instability origin, it is crucial to identify the sources and magnitudes of the destabilizing moments for the purpose of suppressing this type of fluid-induced vibration.

Applicability of the current finite element-based model is illustrated through a sample case involving a straight annular seal to which a simpler bulk-flow model was also applied. Comparison of the numerical results in this case led to favorable conclusions, especially in

the category of stiffness coefficients. Yet the authors realize that the power of the new model would be most appreciated as the model is applied to more complex secondary passages in turbomachines, such as that in Fig. 3, where the flow field in the rotor-to-housing gap is significantly more complex by comparison. Extension of the model to these and other traditionally difficult configurations is currently under consideration.

*Acknowledgement*—This study was funded by NASA-Marshall Space Flight Center (Huntsville, Alabama), Contract no. NAS8-37821, NASA monitor: James Cannon. Funding was also provided by Houston Advanced Research Center (The Woodlands, Texas), Grant No. 88-025.

## REFERENCES

1. H. F. BLACK, Effects of hydraulic forces in annular pressure seals on the vibrations of centrifugal pump rotors. *Mech. Engng Sci.* **11**, 206 (1969).
2. F. J. DIETZEN and R. NORDMANN, Calculation of rotordynamic coefficients of seals by finite difference techniques. *J. Tribol.* **109** (July 1987).
3. D. W. CHILDS, Rotordynamic moment coefficients for finite-length turbulent seals. *Proc. Int. Conf. Rotordynamic Problems in Power Plants*, Rome, Italy, pp. 371–378 (Sept. 1982).
4. F. J. DIETZEN and R. NORDMANN, A 3-dimensional finite-difference method for calculating the dynamic coefficients of seals. Presented at the Workshop on Rotordynamic Instability in High Performance Turbomachinery, Texas A & M University (1988).
5. D. CHILDS and C. H. KIM, Analysis and testing for rotordynamic coefficients of turbulent annular seals with different homogeneous surface roughness treatment for rotor and stator elements. *J. Tribol.* **107**, 296 (July 1985).
6. Y. KANEMORI and T. IWATSUBO, Experimental study of dynamic fluid forces and moments for a long annular seal, Machinery dynamics—applications and vibration control problems. ASME Publication No. DE-Vol. 18-2, pp. 141–147 (1989).
7. G. G. HIRS, A bulk-flow theory for turbulence in lubricant film. *J. Lubric. Tech.* 137 (1973).
8. S. J. HENSEL, A new method for determining rotordynamic forces on rotating mechanical components. Ph.D. Dissertation, Texas A & M University (1990).
9. B. S. BALDWIN and H. LOMAX, Thin layer approximation and algebraic model for separated turbulent flows. AIAA Paper No. 78-257 (January 1978).
10. A. C. BENIM and W. ZINSER, Investigation into the finite element analysis of confined turbulent flows using a $k$–$\varepsilon$ model of turbulence. *Comput. Meth. appl. Mech. Engng* **51**, 507 (1985).
11. J. C. HEINRICH and O. C. ZIENKIEWICZ, Quadratic finite element schemes for two-dimensional convective-transport problems. *Int. J. Numer. Meth. Engng* **11**, 1831 (1977).
12. O. C. ZIENKWICZ, *The Finite Element Method in Engineering Science*. McGraw-Hill, New York (1971).
13. G. F. CAREY and J. T. ODEN, *Finite Elements: Fluid Mechanics, The Texas Finite Element Series Vol. IV*. Prentice-Hall, New York (1986).
14. P. HOOD and C. TAYLOR, Navier–Stokes equations using mixed interpolation. *Proc. Int. Symp. Finite Element Methods in Flow Problems*, University of Wales, Swansea, United Kingdom (January 1974).
15. E. BASKHARONE, A new approach in turbomachinery flow analysis using the finite element method. Ph.D. Dissertation, University of Cincinnati, Ohio (1979).
16. Y. YAMADA, Resistance of a flow through an annulus with an inner rotating cylinder. *Bull. JSME* **5**, 301 (1962).

**PAPER# 4**

# Interrelated Rotordynamic Effects of Cylindrical and Conical Whirl of Annular Seal Rotors

**E. A. Baskharone**
Associate Professor.
Mem. ASME

**S. J. Hensel**[1]
Mem. ASME

Department of Mechanical Engineering,
Texas A&M University,
College Station, Texas 77843

*A comprehensive approach for computing the dynamic coefficients of an annular seal is presented. The coefficients are partly those associated with a uniform lateral eccentricity mode of the rotor (known as the cylindrical whirl mode) and with an angular eccentricity (which gives rise to a conical whirl type). The rotor excitation effects in both cases are treated as interrelated by recognizing the fluid-exerted moments resulting from the lateral eccentricity and the net fluid force resulting from the angular eccentricity. In all cases, the rotor is assumed to undergo a whirling motion around the housing centerline. The computational procedure is a finite-element perturbation model in which the zeroth-order undisplaced-rotor flow solution in the clearance gap is obtained through a Petrov-Galerkin approach. Next, the rotor translational and angular eccentricities, considered to be infinitesimally small, are perceived to cause virtual distortions of varied magnitudes in the finite element assembly which occupies the clearance gap. Perturbations in the flow variables including, in particular, the rotor surface pressure, are then obtained by expanding the finite-element equations in terms of the rotor eccentricity components. The fluid-exerted forces and moments are in this case computed by integration over the rotor surface, and the full matrix of rotordynamic coefficients, in the end, obtained. The computational model is verified against a bulk-flow model for a sample case involving a straight annular seal. Choice of this sample model for validation was made on the basis that no other existing model has yet been expanded to account for the mutual interaction between the cylindrical and conical rotor whirl, which is under focus in this study.*

## Introduction

Annual seals of the type used in turbomachines are known to have a significant impact on the rotordynamic behavior of the entire engine. Much of the research effort in the turbomachinery community has therefore been focused on creating computational tools to predict the stiffness, damping and inertia coefficients of these seals (e.g., Childs, 1982a; Childs, 1982b; Childs and Kim, 1985; Nelson, 1985; Dietzen and Nordmann, 1988; and Tam et al., 1988). Simultaneously, several investigators (e.g., Childs and Kim, 1985; Childs and Kim, 1988 as well as Kanemori and Iwatsubo, 1989) have successfully measured these coefficients over a range of operating conditions.

Perhaps the most widely used model of seal rotordynamics today is the Childs' bulk-flow model for its simplicity and flexibility. This model was progressively modified to include the effects of fluid prerotation (Childs, 1982a), surface roughness (Childs and Kim, 1985) and seal taper (Nelson, 1985). The model was also adapted to handle the case of conical rotor whirl (Childs, 1982b) which results from a tilting (angular) eccentricity of the rotor axis. The model is therefore exclusively capable of predicting the mutual interaction effects of cylindrical and conical whirl, namely the fluid-exerted moments associated with a uniform lateral eccentricity of the rotor axis, and the fluid forces associated with a tilting eccentricity of the axis. This is the problem under focus in the current study (Fig.1), except that the present analysis is much more detailed and applies to virtually any leakage passage configuration that may give rise to a highly complex flow behavior (Fig. 2). Shortcomings of the bulk-flow model, by comparison, emerge from a parabolized leakage flow assumption, which would be inapplicable should flow separation and recirculation occur, and unsimulated fluid stresses away from the rotor and housing surfaces.

Recently, successful attempts to utilize sophisticated computational fluid dynamics techniques to the seal rotordynamics problem have been published. These are best represented by the study of Dietzen et al. (1987), in which a traditional perturbation approach to the problem was undertaken, where the zeroth-order flow field was computed by solving the time-averaged Navier-Stokes equations, together with a two-equation turbulence closure, in the clearance gap. However, this

[1]Graduate Research Assistant, currently a Senior Engineer at Westinghouse Savannah River Laboratory, Aiken, South Carolina.

Contributed by the Tribology Division for publication in the JOURNAL OF TRIBOLOGY. Manuscript received by the Tribology Division June 25, 1990; revised manuscript received November 12, 1990. Associate Editor: K. E. Rouch.

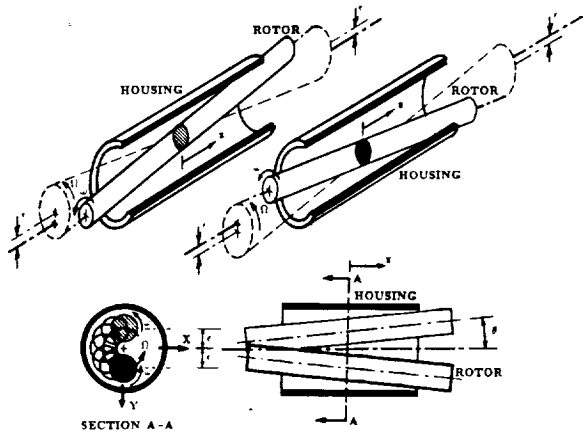


**Fig. 1 Translational and angular rotor eccentricities in annular seals**

computational model, as well as other similar models, have not yet been applied to any rotor eccentricity mechanisms other than the simple uniform displacement, under which the rotor whirl is strictly cylindrical. Other existing detailed models include those by Dietzen et al. (1988) and Tam et al. (1988) where the flow is instead analyzed in the physically distorted rotor-to-housing passage. These are highly accurate models which further advocate the use of rigorous flow computational techniques in predicting the fluid/rotor interaction effects. However, such models would be hampered the most by geometrical complications should the rotor tilting eccentricity be superimposed on the uniform lateral displacement.

A common feature in all existing perturbation models of the problem is that the perturbation equations (which emerge from the flow-governing equations in their differential form) contain the clearance gap width. This would imply that the computational domain is necessarily bound by the rotor surface, being the inner boundary, and the housing surface as the outer boundary, and that this condition will have to be valid at all axial locations. The deficiency here is that a general leakage passage, such as that in Fig. 2, which is naturally connected to the primary flow passage at both ends to facilitate primary/secondary flow interaction in real turbomachines (Baskharone and Hensel, 1989) would not constitute an acceptable computational domain for any of the existing perturbation analyses. The current perturbation model, on the other hand, utilize what may be referred to as the "virtually distorted finite element" technique, whereby the perturbation equations are derived from the discrete finite-element equations associated with the finite elements occupying the flow domain. The latter includes, but is not restricted to, the annular passage within which the rotor whirl occurs.

The assumptions made in the present analysis give rise to specific applicability limitations which are typical in perturbation models of the fluid/structure interaction phenomenon. For instance, the analysis is inherently inapplicable to large eccentricities of the rotor axis (Fig. 3). Moreover it is assumed that the clearance-gap flow field, relative to a whirling frame of reference that is attached to the rotor (Fig. 4), is steady at all times. This, in effect, rules out seal configurations where the rotor and/or the housing are longitudinally or spirally grooved. It also precludes situations where the relative flow field in the clearance gap is influenced by time-dependent boundary conditions at the flow inlet and exit stations. Nevertheless, the current model embraces the seal category where the rotor or the housing surface is circumferentially grooved (e.g., labyrinth seals) and tolerates a pre-existing rotor eccentricity, which is normally a result of misalignment.

## Analysis

The rotor virtual eccentricity under focus is shown in Fig. 1. This consists of a uniform lateral eccentricity "$\epsilon$" on which an angular displacement "$\theta$" is superimposed. These infinitesimally small deviations, from the centered-rotor position, are simultaneously accompanied by a rotor whirl at a finite

## Nomenclature

$[A],[a]$ = global and elemental matrices of influence coefficients in the finite element equations
$\{B\},\{b\}$ = global and elemental load vectors in the finite element equations
$C,c$ = direct and cross-coupled damping coefficients
$F$ = force
$\mathbf{F,G,H,I,J,K}$ = linear operators defined in Appendices I and II
$K,k$ = direct and cross-coupled stiffness coefficients
$M,m$ = direct and cross-coupled inertia coefficients
$M_i(\zeta,\eta,\xi)$ = linear shape function that is associated with the $i$th corner node of a finite element
$N_i(\zeta,\eta,\xi)$ = quadratic shape function that is associated with the $i$th corner or midside node of a finite element
$\mathbf{n}$ = outward normal unit vector
$p$ = static pressure
$S$ = area
$t$ = time
$u,v,w$ = velocity components in the cartesian frame of reference
$V$ = volume
$W_i$ = weight function in the Petrov-Galerkin weighted-residual analysis
$X,Y$ = $x$ and $y$ components of the rotor lateral eccentricity
$X_i,Y_i,Z_i$ = nodal coordinates in the whirling frame of reference
$x,y$ = cartesian coordinates in the stationary frame of reference
$\epsilon$ = lateral eccentricity of the rotor axis
$\zeta,\eta,\xi$ = coordinates in the element local frame of reference (Fig. 4)
$\nu$ = kinematic viscosity
$\rho$ = density
$\theta$ = angular eccentricity of the rotor axis
$\{\Phi\},\{\phi\}$ = global and elemental vector of unknown velocity components and pressure
$\Omega$ = whirl frequency
$\omega$ = rotor operating speed

**Subscripts**

$i,j,k$ = nodal numbers in the finite element model

**Superscripts**

$(e)$ = a typical finite element

**Other Symbols**

overbar = perturbation in a quantity due to the rotor eccentricity
$(\hat{\ })$ = a quantity that is known from a previous iteration or an initial guess

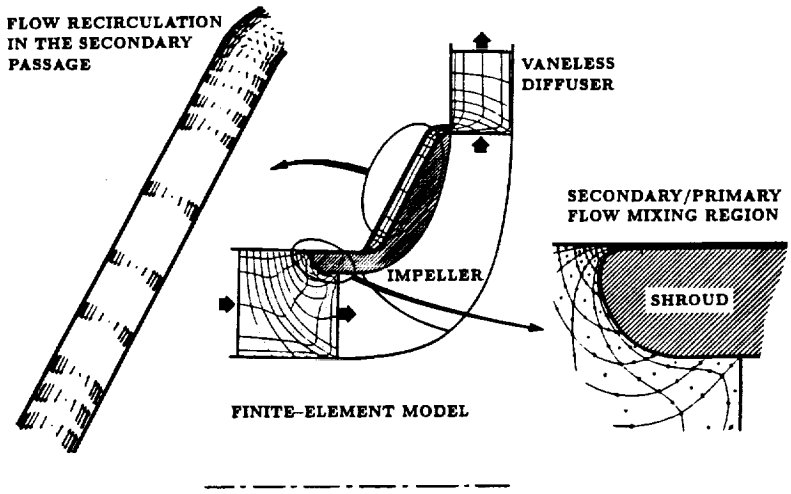


**Fig. 2 Generalization of the fluid/rotor interaction problem: Definition of the computational domain and example of the flow behavior in the shroud-to-housing passage of a centrifugal pump**

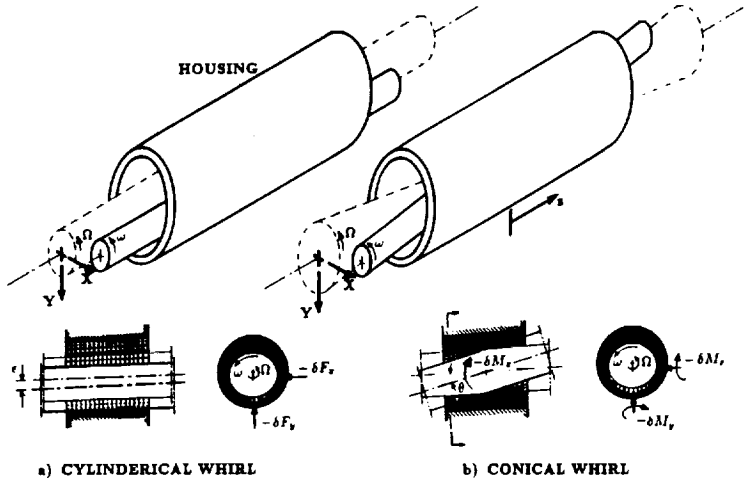


**Fig. 3 Cylinderical and conical whirl components of the rotor eccentric motion**

frequency Ω (Fig. 1).The fluid reaction in this case is in the form of forces and moments in the "$x$" and "$y$" directions, which can be related to the displacement components of the whirling rotor (Childs, 1982b) as follows:

$$-\begin{Bmatrix}\delta F_x\\ \delta F_y\\ \delta M_y\\ \delta M_x\end{Bmatrix}=\begin{bmatrix}K & k & K_{\epsilon\theta} & -k_{\epsilon\theta}\\ -k & K & -k_{\epsilon\theta} & -K_{\epsilon\theta}\\ K_{\theta\epsilon} & k_{\theta\epsilon} & K_\theta & -k_\theta\\ k_{\theta\epsilon} & -K_{\theta\epsilon} & k_\theta & K_\theta\end{bmatrix}\begin{Bmatrix}X\\ Y\\ \theta_y\\ \theta_x\end{Bmatrix}$$
$$+\begin{bmatrix}C & c & C_{\epsilon\theta} & -c_{\epsilon\theta}\\ -c & C & -c_{\epsilon\theta} & -C_{\epsilon\theta}\\ C_{\theta\epsilon} & c_{\theta\epsilon} & C_\theta & -c_\theta\\ c_{\theta\epsilon} & -C_{\theta\epsilon} & c_\theta & C_\theta\end{bmatrix}\begin{Bmatrix}\dot X\\ \dot Y\\ \dot\theta_y\\ \dot\theta_x\end{Bmatrix}$$
$$+\begin{bmatrix}M & m & M_{\epsilon\theta} & -m_{\epsilon\theta}\\ -m & M & -m_{\epsilon\theta} & -M_{\epsilon\theta}\\ M_{\theta\epsilon} & m_{\theta\epsilon} & M_\theta & -m_\theta\\ m_{\theta\epsilon} & -M_{\theta\epsilon} & m_\theta & M_\theta\end{bmatrix}\begin{Bmatrix}\ddot X\\ \ddot Y\\ \ddot\theta_y\\ \ddot\theta_x\end{Bmatrix} \quad (1)$$

where the symbols $(K,k)$, $(C,c)$, and $(M,m)$ are the direct and cross-coupled stiffness, damping and inertia coefficients of the fluid/rotor system, respectively. A single subscript of these coefficients implies force-displacement or moment-tilt types of relationship, while double subscripts tie fluid-exerted moments to rotor displacements and forces to rotor tilting angles. Note that a rotor eccentricity, be that linear or angular, in the $x$-direction (for instance) will generally produce a restoring (or aggravating) fluid reaction in the $y$-direction. Also note that straight annular seals are incapable of displaying any cross-coupled inertia coefficients, i.e.

$$m=m_\theta=m_{\epsilon\theta}=m_{\theta\epsilon}=0 \quad (2)$$

The procedure to compute the rotordynamic coefficients in the matrix equation (1) is initiated by expressing the local radius ($\delta$) of the rotor axis orbit (Fig. 1) as follows:

$$\delta=\epsilon+\epsilon_\theta \quad (3)$$

where:

$$\epsilon_\theta=\theta z \quad (4)$$

with $\epsilon_\theta$ being the lateral eccentricity due to the rotor tilting motion. Motion of the rotor axis in Fig. 1 can be decoupled into the cylindrical and conical whirl modes depicted in Fig. 3. Referred to the frame of reference in Fig. 3, the lateral displacement components "$X$" and "$Y$" of the tilting motion center can be written for the whirling axis at any given time "$t$" as follows:

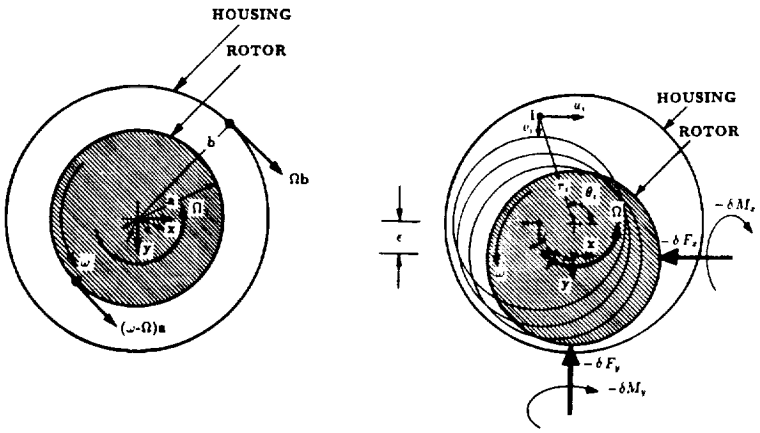


**Fig. 4 Lateral motion of the coordinate axes before and after the rotor eccentricity**

$$X=\epsilon\cos(\Omega t),\ Y=\epsilon\sin(\Omega t) \tag{5}$$

Similarly, the angular displacement can be expressed in terms of the whirl frequency (Fig. 2(*b*) as follows:

$$\theta_x=\frac{\epsilon_z}{z}\cos(\Omega t),\ \theta_y=\frac{\epsilon_z}{z}\sin(\Omega t) \tag{6}$$

With no lack of generality, consider the special location of the displaced rotor axis where $X=0$ and $\theta_y = 0$ (as shown in Fig. 3). Using expressions (5) and (6) above, the linear and angular magnitudes of the rotor axis position, velocity and acceleration of the rotor axis at the axial location "$z$" can then be written as follows:

$$X=0,\ Y=\epsilon \tag{7}$$

$$\dot{X}=\Omega\epsilon,\ \dot{Y}=0 \tag{8}$$

$$\ddot{X}=0,\ \ddot{Y}=-\Omega^2\epsilon \tag{9}$$

$$\theta_x=\theta,\ \theta_y=0 \tag{10}$$

$$\dot{\theta}_x=0,\ \dot{\theta}_y=\Omega\theta \tag{11}$$

$$\ddot{\theta}_x=-\Omega^2\theta,\ \ddot{\theta}_y=0 \tag{12}$$

Substituting (7) through (12) in (1), and taking the limit as the rotor eccentricity components tend to zero, the following equations are achieved:

$$\frac{\partial F_x}{\partial\epsilon}=-k-\Omega C \tag{13}$$

$$\frac{\partial F_y}{\partial\epsilon}=-K+\Omega c+\Omega^2 M \tag{14}$$

$$\frac{\partial F_x}{\partial\theta}=k_{e\theta}-\Omega C_{e\theta}+\Omega^2 M_{e\theta} \tag{15}$$

$$\frac{\partial F_y}{\partial\theta}=K_{e\theta}+\Omega c_{e\theta} \tag{16}$$

$$\frac{\partial M_y}{\partial\epsilon}=-k_{\theta\epsilon}-\Omega C_{\theta\epsilon} \tag{17}$$

$$\frac{\partial M_x}{\partial\epsilon}=K_{\theta\epsilon}-\Omega c_{\theta\epsilon}-\Omega^2 M_{\theta\epsilon} \tag{18}$$

$$\frac{\partial M_y}{\partial\theta}=k_\theta-\Omega C_\theta \tag{19}$$

$$\frac{\partial M_x}{\partial\theta}=-K_\theta-\Omega c_\theta+\Omega^2 M_\theta \tag{20}$$

in which the cross-coupled inertia coefficients were set equal to zero (equation (2)).

Determination of the rotordynamic coefficients in the different matrices of equation (1) now reduces to computing the derivatives on the left-hand side of equations (13) through (20) at a minimum of three whirl frequencies. Interpolation of these derivatives as parabolic expressions of $\Omega$, using curve fitting techniques, leads to these coefficients by simply equating the different terms in these expressions to the right-hand sides of equations (13) through (20). With this in mind, the remainder of this section is therefore centered around computing the derivatives appearing on the left-handed side of equations (13) through (20) as the ultimate goal of the finite-element perturbation model. This model, as seen next, is initiated by solving the zeroth-order flow field in the undisplaced-rotor clearance gap.

**Centered-Rotor Flow Field.** This zeroth-order flow problem is defined in a frame of reference that is attached to the rotor and is rotating (Fig. 4(*a*)) at the rate of $\Omega$. Although the axes rotation here may appear as serving no purpose at this stage, it ensures compatibility of the unperturbed and perturbed flow fields, with the rotor eccentricity effects being the only difference. As seen in Fig. 4(*b*), definition of the axes in this manner eliminates the time dependency of the perturbed flow field once the rotor undergoes the eccentric operation mode. In this case, the coordinate axes become of the rotating-translating (or simply whirling) type (Fig. 4(*b*)), with the magnitude of $\Omega$ being set equal to the rotor whirl frequency. However, the term $\Omega$ is viewed as an arbitrary rotational frequency of the coordinate axes in formulating the undisplaced-rotor flow problem (which is under consideration at this point).

Denoting the relative velocity components in the rotating frame of reference (of which the origin is fixed, Fig. 4(*a*)) by $u$, $v$, and $w$, the momentum and mass conservation equation in the undistorted clearance gap are:

$$\hat{u}\frac{\partial u}{\partial x}+\hat{v}\frac{\partial u}{\partial y}+\hat{w}\frac{\partial u}{\partial z}+2\Omega v-\Omega^2 x=-\frac{1}{\rho}\frac{\partial p}{\partial x}+\nu_e\nabla^2 u+2\frac{\partial\nu_t}{\partial x}\frac{\partial u}{\partial x}+\frac{\partial\nu_t}{\partial y}\left(\frac{\partial u}{\partial y}+\frac{\partial v}{\partial x}\right)+\frac{\partial\nu_t}{\partial z}\left(\frac{\partial u}{\partial z}+\frac{\partial w}{\partial x}\right) \tag{21}$$

$$\hat{u}\frac{\partial v}{\partial x}+\hat{v}\frac{\partial v}{\partial y}+\hat{w}\frac{\partial v}{\partial z}-2\Omega u-\Omega^2 y=-\frac{1}{\rho}\frac{\partial p}{\partial y}+\nu_e\nabla^2 v+2\frac{\partial\nu_t}{\partial y}\frac{\partial v}{\partial y}+\frac{\partial\nu_t}{\partial x}\left(\frac{\partial u}{\partial y}+\frac{\partial v}{\partial x}\right)+\frac{\partial\nu_t}{\partial z}\left(\frac{\partial v}{\partial z}+\frac{\partial w}{\partial y}\right) \tag{22}$$

$$\hat{u}\frac{\partial w}{\partial x}+\hat{v}\frac{\partial w}{\partial y}+\hat{w}\frac{\partial w}{\partial z}=-\frac{1}{\rho}\frac{\partial p}{\partial z}+\nu_e\nabla^2 w+2\frac{\partial \nu_t}{\partial z}\frac{\partial w}{\partial z}+\frac{\partial \nu_t}{\partial x}\left(\frac{\partial u}{\partial z}+\frac{\partial w}{\partial x}\right) \quad (23)$$

$$\frac{\partial u}{\partial x}+\frac{\partial v}{\partial y}+\frac{\partial w}{\partial z}=0 \quad (24)$$

where:

| | |
|---|---|
| $u,v,w$ | are the relative velocity components. |
| $p$ | is the static pressure. |
| $\Omega$ | is the rotational frequency of the coordinate axes (to be set equal to the whirl frequency as the rotor enters its disturbed operation mode) |
| $\nu_l,\nu_t,\nu_e$ | are the molecular, eddy and effective components of kinematic viscosity coefficients, respectively, where $\nu_e=\nu_l+\nu_t$ |

with the symbol ( $\hat{}$ ) designating values that are carried over from a previous iteration or an initial guess for the purpose of successively linearizing the momentum equations. As seen, the whirl frequency $\Omega$ is part of these equations, which is a result of including the centrifugal and Coriolis acceleration effects produced by the axes rotational motion.

Simulation of the flow turbulence is based on the algebraic eddy-viscosity turbulence model by Baldwin and Lomax (1978). However, an adjustment in this vorticity-based model was implemented whereby the relative, as opposed to the absolute, vorticity was used to calculate the mixing length in the fluid layer that is adjacent to the rotor surface. Equally important in implementing the model was the analysis of the near-wall zone which was based on the approach by Benim and Zinser (1985).

## Boundary Conditions

These include known profiles of the inlet velocity components and zero streamwise diffusion of the exit velocity vector. The latter boundary condition is achieved by equating to zero the second streamwise derivatives of all velocity components. This condition is consistent with the foundation of the boundary layer theory, provided that the boundary layer remains attached to the rotor and housing surfaces as the exit station is approached. Note that the traditional zero velocity-gradient exit condition would be less accurate by comparison, for it implies a fully developed flow that may or may not prevail at the exit station depending on the seal length.

The last category of boundary conditions concerns the rotor and housing surfaces, and is largely influenced by the rotation of the coordinates axes. Referring to Fig. 4(*a*), the housing surface, to an observer in the rotating frame of reference, will no longer appear stationary, but will rather possess a relative velocity component $\Omega b$ as indicated in the Figure, where "$b$" is the housing radius. Furthermore, the rotor surface will appear to the same observer as rotating at an angular speed that is less than the rotor operating speed $\omega$ by the amount $\Omega$. The rotor surface velocity in this case is $(\omega-\Omega)a$, where "$a$" is the rotor radius.

**Finite-Element Formulation.** Numerical solution of the centered-rotor flow field is based on the Petrov-Galerkin weighted-residual principle in which the weight functions are so chosen to incorporate the upwinding concept. An effective tool in alleviating spurious pressure modes, this concept has been advocated by many analysts in handling highly convective flows, such as the present. The concept is equally opposed by others due to the false "numerical" diffusion it imparts to the finite element equations. The desire to minimize this false diffusion in the current flow model led to selecting a mixture of the weight functions devised by Heinrich and Zienkiewicz (1977) and those used in the conventional Galerkin method in such a way that upwinding is applied only to the nonlinear convection terms on the left-hand side of the momentum equations (21) through (23). Note that excessively narrow and long clearance gaps in typical annular seals would naturally lead to finite elements with unavoidably large aspect ratios, especially near the walls, due to the special refinement of elements that is required across the boundary layer. Nevertheless, utilization of the preceding upwinding technique gave rise to a sufficiently accurate flow field for elemental aspect ratios of as large as 196 in the immediate vicinity of the rotor and housing surfaces.

The finite-element model is constructed with the twenty-node quadratic element in Fig. 5 as the discretization unit. The procedure is initiated by defining the element shape and the cartesian-to-local system mapping relations. Within a typical element, let the spatial coordinate conversion be defined, in terms of the nodal values, as follows:

$$x=\sum_{i=1}^{20}N_i x_i,\quad y=\sum_{i=1}^{20}N_i y_i,\quad z=\sum_{i=1}^{20}N_i z_i \quad (25)$$

where $N_i$ are quadratic "shape" functions (Zienkiewicz, 1971) of the local coordinates $\zeta$, $\eta$ and $\xi$ (Fig. 5). Conversion of the spatial derivatives is, in this case, defined as follows:

$$\begin{Bmatrix}\frac{\partial}{\partial x}\\ \frac{\partial}{\partial y}\\ \frac{\partial}{\partial z}\end{Bmatrix}=[T]\begin{Bmatrix}\frac{\partial}{\partial \zeta}\\ \frac{\partial}{\partial \eta}\\ \frac{\partial}{\partial \xi}\end{Bmatrix} \quad (26)$$

where the components of the matrix $[T]$ are as follows:

$$T_{11}=\frac{1}{|J|}\left(\sum_{i=1}^{20}\frac{\partial N_i}{\partial \eta}y_i\sum_{i=1}^{20}\frac{\partial N_i}{\partial \xi}z_i-\sum_{i=1}^{20}\frac{\partial N_i}{\partial \eta}z_i\sum_{i=1}^{20}\frac{\partial N_i}{\partial \xi}y_i\right)$$

$$T_{12}=\frac{1}{|J|}\left(\sum_{i=1}^{20}\frac{\partial N_i}{\partial \xi}y_i\sum_{i=1}^{20}\frac{\partial N_i}{\partial \zeta}z_i-\sum_{i=1}^{20}\frac{\partial N_i}{\partial \zeta}y_i\sum_{i=1}^{20}\frac{\partial N_i}{\partial \xi}z_i\right)$$

$$T_{13}=\frac{1}{|J|}\left(\sum_{i=1}^{20}\frac{\partial N_i}{\partial \zeta}y_i\sum_{i=1}^{20}\frac{\partial N_i}{\partial \eta}z_i-\sum_{i=1}^{20}\frac{\partial N_i}{\partial \eta}y_i\sum_{i=1}^{20}\frac{\partial N_i}{\partial \zeta}z_i\right)$$

$$T_{21}=\frac{1}{|J|}\left(\sum_{i=1}^{20}\frac{\partial N_i}{\partial \xi}x_i\sum_{i=1}^{20}\frac{\partial N_i}{\partial \eta}z_i-\sum_{i=1}^{20}\frac{\partial N_i}{\partial \eta}x_i\sum_{i=1}^{20}\frac{\partial N_i}{\partial \xi}z_i\right)$$

$$T_{22}=\frac{1}{|J|}\left(\sum_{i=1}^{20}\frac{\partial N_i}{\partial \zeta}x_i\sum_{i=1}^{20}\frac{\partial N_i}{\partial \xi}z_i-\sum_{i=1}^{20}\frac{\partial N_i}{\partial \xi}x_i\sum_{i=1}^{20}\frac{\partial N_i}{\partial \zeta}z_i\right) \quad (27)$$

$$T_{23}=\frac{1}{|J|}\left(\sum_{i=1}^{20}\frac{\partial N_i}{\partial \eta}x_i\sum_{i=1}^{20}\frac{\partial N_i}{\partial \zeta}z_i-\sum_{i=1}^{20}\frac{\partial N_i}{\partial \zeta}x_i\sum_{i=1}^{20}\frac{\partial N_i}{\partial \eta}z_i\right)$$

$$T_{31}=\frac{1}{|J|}\left(\sum_{i=1}^{20}\frac{\partial N_i}{\partial \eta}x_i\sum_{i=1}^{20}\frac{\partial N_i}{\partial \xi}y_i-\sum_{i=1}^{20}\frac{\partial N_i}{\partial \xi}x_i\sum_{i=1}^{20}\frac{\partial N_i}{\partial \eta}y_i\right)$$

$$T_{32}=\frac{1}{|J|}\left(\sum_{i=1}^{20}\frac{\partial N_i}{\partial \xi}x_i\sum_{i=1}^{20}\frac{\partial N_i}{\partial \zeta}y_i-\sum_{i=1}^{20}\frac{\partial N_i}{\partial \zeta}x_i\sum_{i=1}^{20}\frac{\partial N_i}{\partial \xi}y_i\right)$$

$$T_{33}=\frac{1}{|J|}\left(\sum_{i=1}^{20}\frac{\partial N_i}{\partial \zeta}x_i\sum_{i=1}^{20}\frac{\partial N_i}{\partial \eta}y_i-\sum_{i=1}^{20}\frac{\partial N_i}{\partial \eta}x_i\sum_{i=1}^{20}\frac{\partial N_i}{\partial \zeta}y_i\right)$$

with $|J|$ being the Jacobian of transformation.

Next, the flow variables are interpolated within the typical element (Fig. 5) in a similar fashion. Guided by the Ladyshenskaya-Babuska-Brezzi compatibility requirements (Carey and Oden, 1986), as applied to the current problem, the velocity components and pressure are expressed as follows:

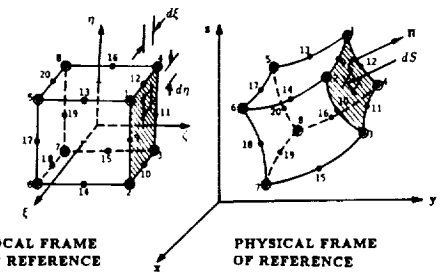


**Fig. 5 Quadrilateral curve-sided isoparametric finite element for analyzing the rotor-to-housing flow field**

$$u=\sum_{i=1}^{20}N_iu_i,\ v=\sum_{i=1}^{20}N_iv_i,\ w=\sum_{i=1}^{20}N_iw_i,\ p=\sum_{k=1}^{8}M_kpk \quad (28)$$

where the interpolants "$M_k$" appearing in the pressure expression are the linear shape functions associated with the finite element corner nodes (Zienkiewicz, 1971).

The error functions produced by the unperturbed flow governing equations, as a result of the interpolation expressions above, are then made orthogonal to a special set of weight functions $W_i$ throughout the finite element. In constructing these functions, the so-called error consistency criterion of Hood and Taylor (1974) is implemented, whereby the element linear shape functions, $M_i$, are used in conjunction with the continuity equation. The weight functions used with the momentum equations, on the other hand, are of the upwind form described by Heinrich and Zienkiewicz (1977) when applied to the convection terms, and are identical to the element quadratic shape functions "$N_i$" for all other terms.

The orthogonality conditions, stated above, constitute the elemental set of equations, which can be written as follows:

$$[a_1]\{u\}+[a_2]\{v\}+[a_3]\{w\}+[a_4]\{p\}=\{b_1\} \quad (29)$$

$$[a_5]\{u\}+[a_6]\{v\}+[a_7]\{w\}+[a_8]\{p\}=\{b_2\} \quad (30)$$

$$[a_9]\{u\}+[a_{10}]\{v\}+[a_{11}]\{w\}+[a_{12}]\{p\}=\{b_3\} \quad (31)$$

$$[a_{13}]\{u\}+[a_{14}]\{v\}+[a_{15}]\{w\}=0 \quad (32)$$

where the vectors $\{u\}$, $\{v\}$, $\{w\}$, and $\{p\}$ contain the nodal values of the velocity components and static pressure, associated with the finite element. The coefficient matrices $[a_1]$ through $[a_{15}]$ and the right-hand side vectors $\{b_1\}$ through $\{b_3\}$ are all defined in Appendix I. Equations (17) through (20) can be rewritten in the following compact form:

$$[a]\{\phi\}=\{b\} \quad (33)$$

where the vector $\{\phi\}$ contains the nodal values of velocity components and static pressure associated with the typical finite element. The global form of the elemental set of equations (33) is obtained by assembling all finite element contributions, and introducing the various boundary conditions, at which point the equations are expressible in the following form:

$$[A]\{\Phi\}=\{B\} \quad (34)$$

where the global vector $\{\Phi\}$ contains all nodal values of the velocity components and pressure prior to the rotor excitation. These unperturbed flow variables constitute an axisymmetric flow field for a perfectly centered rotor, which is the special case under consideration in the current study. However, should a rotor misalignment (including a fixed tilt) be the case, the unperturbed flow field described by equation (34) would generally be three-dimensional and should be modeled as such.

**Perturbation Model.** Referring to equations (13) through (20), determination of the rotordynamic coefficients reduces to the fundamental problem of computing the rate at which the fluid-exerted forces and moments in the clearance gap are developed with respect to a compound (translational and tilting) eccentricity of the rotor axis. This problem is analyzed next.

The current computational model is centered around the manner in which the finite-element equations (34) are altered as a result of the rotor virtual eccentricity depicted in Fig. 1. Since the rotordynamic coefficient are (by reference to equations (13) through (20)) dependent on partial derivatives of the rotor displacement components "$\epsilon$" and "$\theta$", it is legitimate to treat the fluid response to each component separately. Referring to Fig. 3 in this case, let "$e$" symbolize the rotor axis eccentricity, where:

$$e=\begin{cases}\epsilon & \text{for translational motion}\\ \theta z & \text{for tilting motion}\end{cases} \quad (35)$$

with $z$ being the distance from the center of the tilting motion. Under such displacement, each finite element will, as a result of virtual distortion (Fig. 6), yield a perturbed set of equations. Let the assembled form of these equations, by reference to (34), be as follows:

$$([A]+e[\bar{A}])(\{\Phi\}+\{\delta\Phi\})=(\{B\}+e\{\bar{B}\}) \quad (36)$$

Subtracting (34) from (36), the following expression for "$\delta\Phi$" is obtained:

$$\{\delta\Phi\}=e[A]^{-1}(\{\bar{B}\}-[\bar{A}]\{\Phi\}) \quad (37)$$

or,

$$\frac{\partial\{\Phi\}}{\partial e}=\lim_{e\to 0}\left(\frac{\partial\Phi}{e}\right)=[A]^{-1}(\{\bar{B}\}-[\bar{A}]\{\Phi\}) \quad (38)$$

The general equation (38) implies that two new arrays, namely the matrix $[\bar{A}]$ and the vector $\{\bar{B}\}$, are needed to compute the rate at which the flow variables (namely the velocity components and pressure) vary with respect to the rotor eccentricity "$e$." These arrays are primarily a result of finite elements distortion effects that are associated with the rotor displaced position (Fig. 6). The arrays $[\bar{A}]$ and $\{\bar{B}\}$ are derived next as part of the procedure to compute the rotordynamic coefficients. To do this, a typical distorted element will first be analyzed, and the elemental contributions $[\bar{a}]$ and $\{\bar{b}\}$ derived. The global arrays $[\bar{A}]$ and $\{\bar{B}\}$ can subsequently be obtained by assembling $[\bar{a}]$ and $\{\bar{b}\}$ among all finite elements.

*Analysis of a Distorted Finite Element.* Consider the distortion experienced by the typical finite element shown in Fig. 6. As seen, the distortion is caused by virtual displacements of the element nodes as a result of the rotor eccentricity. Recalling that the axes are attached to the whirling rotor, it is those nodes on the housing that will be displaced the most, while the rotor surface nodes remain stationary.

With "$e$" signifying the linear or angular eccentricity (expression 35), let the new coordinates of a typical node "$i$" (Fig. 6) be $(X_i, Y_i, Z_i)$, where:

$$X_i=x_i,\ Y_i=y_i+\lambda_i e \text{ and } Z_i=z_i \quad (39)$$

where in general:

$$\lambda_i=\lambda_i(x_i, y_i, z_i) \quad (40)$$

Dependency of $\lambda_i$ on the in-plane position of the node "$i$" (i.e., $x_i$ and $y_i$) is clear by reference to Fig. 3. However, it is only the purely conical whirl in this figure where $\lambda_i$ is additionally dependent on "$z_i$." For instance, $\lambda_i=-z_i$ for nodes on the housing surface under this type of whirl (note the positive direction of the $y$-axis in Fig. 6).

Let the new local-to-cartesian transformation Jacobian $|J_1|$ be related to the undistorted-element Jacobian $|J|$ as follows:

$$|J_1|=|J|+e|\bar{J}| \quad (41)$$

The determinant $|J|$ can be derived using the coordinate re-

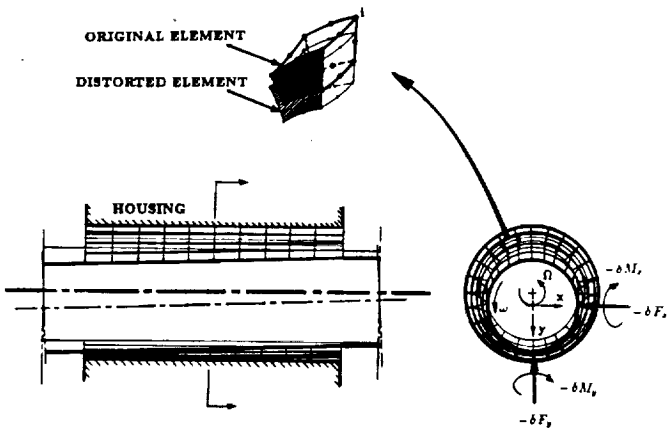


**Fig. 6 Deformation of the finite elements in the roto-to-housing gap as a result of the rotor eccentricity**

lationships (expression 39) and ignoring high-order terms of "$e$" as follows:

$$|\bar{J}| = \begin{vmatrix} \sum_{i=1}^{20}\frac{\partial N_i}{\partial \zeta}x_i & \sum_{i=1}^{20}\frac{\partial N_i}{\partial \zeta}\lambda_i & \sum_{i=1}^{20}\frac{\partial N_i}{\partial \zeta}z_i \\ \sum_{i=1}^{20}\frac{\partial N_i}{\partial \eta}x_i & \sum_{i=1}^{20}\frac{\partial N_i}{\partial \eta}\lambda_i & \sum_{i=1}^{20}\frac{\partial N_i}{\partial \eta}z_i \\ \sum_{i=1}^{20}\frac{\partial N_i}{\partial \xi}x_i & \sum_{i=1}^{20}\frac{\partial N_i}{\partial \xi}\lambda_i & \sum_{i=1}^{20}\frac{\partial N_i}{\partial \xi}z_i \end{vmatrix} \tag{42}$$

A new spatial derivative conversion relationship, that is equivalent to equation (26) can now be derived as follows:

$$\begin{Bmatrix} \frac{\partial}{\partial x} \\ \frac{\partial}{\partial y} \\ \frac{\partial}{\partial z} \end{Bmatrix} = ([T]+e[P]) \begin{Bmatrix} \frac{\partial}{\partial \zeta} \\ \frac{\partial}{\partial \eta} \\ \frac{\partial}{\partial \xi} \end{Bmatrix} \tag{43}$$

where the matrix $[T]$ is as described in equation (27) while the matrix $[P]$ is defined as follows:

$$P_{11}=\frac{1}{|J|}\left(\sum_{i=1}^{20}\frac{\partial N_i}{\partial \eta}\lambda_i\sum_{i=1}^{20}\frac{\partial N_i}{\partial \xi}z_i-\sum_{i=1}^{20}\frac{\partial N_i}{\partial \xi}\lambda_i\sum_{i=1}^{20}\frac{\partial N_i}{\partial \eta}z_i\right)-\frac{|\bar{J}|}{|J|^2}T_{11}$$

$$P_{12}=\frac{1}{|J|}\left(\sum_{i=1}^{20}\frac{\partial N_i}{\partial \xi}\lambda_i\sum_{i=1}^{20}\frac{\partial N_i}{\partial \zeta}z_i-\sum_{i=1}^{20}\frac{\partial N_i}{\partial \zeta}\lambda_i\sum_{i=1}^{20}\frac{\partial N_i}{\partial \xi}z_i\right)-\frac{|\bar{J}|}{|J|^2}T_{12}$$

$$P_{13}=\frac{1}{|J|}\left(\sum_{i=1}^{20}\frac{\partial N_i}{\partial \zeta}\lambda_i\sum_{i=1}^{20}\frac{\partial N_i}{\partial \eta}z_i-\sum_{i=1}^{20}\frac{\partial N_i}{\partial \eta}\lambda_i\sum_{i=1}^{20}\frac{\partial N_i}{\partial \zeta}z_i\right)-\frac{|\bar{J}|}{|J|^2}T_{13}$$

$$P_{21}=-\frac{|\bar{J}|}{|J|^2}T_{21}$$

$$P_{22}=-\frac{|\bar{J}|}{|J|^2}T_{22} \tag{44}$$

$$P_{23}=-\frac{|\bar{J}|}{|J|^2}T_{23}$$

$$P_{31}=\frac{1}{|J|}\left(\sum_{i=1}^{20}\frac{\partial N_i}{\partial \eta}x_i\sum_{i=1}^{20}\frac{\partial N_i}{\partial \xi}\lambda_i-\sum_{i=1}^{20}\frac{\partial N_i}{\partial \xi}x_i\sum_{i=1}^{20}\frac{\partial N_i}{\partial \eta}\lambda_i\right)-\frac{|\bar{J}|}{|J|^2}T_{31}$$

$$P_{32}=\frac{1}{|J|}\left(\sum_{i=1}^{20}\frac{\partial N_i}{\partial \xi}x_i\sum_{i=1}^{20}\frac{\partial N_i}{\partial \zeta}\lambda_i-\sum_{i=1}^{20}\frac{\partial N_i}{\partial \zeta}x_i\sum_{i=1}^{20}\frac{\partial N_i}{\partial \xi}\lambda_i\right)-\frac{|\bar{J}|}{|J|^2}T_{32}$$

$$P_{33}=\frac{1}{|J|}\left(\sum_{i=1}^{20}\frac{\partial N_i}{\partial \zeta}x_i\sum_{i=1}^{20}\frac{\partial N_i}{\partial \eta}\lambda_i-\sum_{i=1}^{20}\frac{\partial N_i}{\partial \eta}x_i\sum_{i=1}^{20}\frac{\partial N_i}{\partial \zeta}\lambda_i\right)-\frac{|\bar{J}|}{|J|^2}T_{33}$$

Substituting expressions (41) and (43) into the flow equations (21) through (24) and reapplying the weighted-residual procedure, the distorted element equations can be written (upon separation of terms containing $e$) as follows:

$$([a]+e[\bar{a}])(\{\phi\}+\{\delta\phi\})=(\{b\}+e\{\bar{b}\}) \tag{45}$$

where the matrix $[\bar{a}]$ and vector $\{\bar{b}\}$ result from the distortion in the element shape. The vector $\{\delta\phi\}$ in this case contains the differential changes in the nodal values of velocity components and pressure that are created by the virtual eccentricity.

Noting that the matrix $[\bar{a}]$ is similar in construction to $[a]$ in equation (33), the former can consistently be viewed as composed of submatrices $[\bar{a}_1]$ through $[\bar{a}_{15}]$, which are compatible with those in Appendix I for the undistorted finite element. These new matrices are defined in Appendix II. The vector $\{\bar{b}\}$ is substructured in a similar manner, and is also defined in Appendix II. Finally, the global arrays $[\bar{A}]$ and $\{\bar{B}\}$ appearing in equation (38) are attained by assembling $[\bar{a}]$ and $\{\bar{b}\}$ among all finite elements.

*Calculation of the Rotordynamic Coefficients.* Equation (38) can be rewritten in the following detailed form:

$$\frac{\partial \Phi}{\partial e}=\frac{\partial}{\partial e}\begin{Bmatrix}\{U\}\\ \{V\}\\ \{W\}\\ \{P\}\end{Bmatrix}=[A]^{-1}(\{\bar{B}\}-[\bar{A}]\{\Phi\}) \tag{46}$$

where $\{U\}$, $\{V\}$, $\{W\}$, and $\{P\}$ are global vectors containing the nodal values of the velocity components and pressure, respectively, with the overbars signifying quantities that are associated with the perturbation in the rotor-to-housing flow field. Of all the pressure nodal values in the vector $\{P\}$ above, define a subvector $\{\mathcal{P}\}$ as composed of the pressure values at the rotor surface nodes, i.e.,

$$\{\mathcal{P}\}=\{p_i,\ i=1,N_s\}\subset\{P\} \tag{47}$$

where $N_s$ is the total number of corner nodes existing on the rotor surface. Note that $\left\{\frac{\partial \mathcal{P}}{\partial e}\right\}=\left(\left\{\frac{\partial p}{\partial e}\right\}_i,\ i=1,N_s\right\}$ is but a subvector of the already computed global vector $\left\{\frac{\partial \Phi}{\partial e}\right\}$ in equation (46) and is, therefore, known at this computational step.

Next, consider a finite element face "$s$" that exists on the rotor surface (Fig. 7). The pressure derivative $p_{,e}^{(s)}$ over this surface element can now be interpolated in terms of the known pressure derivatives at the four corner nodes as follows:

$$p_{,e}^{(s)}=\sum_{i=1}^{4}M_i(1,\eta,\xi)\left(\frac{\partial p}{\partial e}\right)_i \tag{48}$$

Once integrated over the proper differential segments of the rotor surface, the function $p_{,e}^{(s)}$ (above) yields a differential force which, in turn, can be resolved in the "$x$" and "$y$" directions. Furthermore, taking the moments of these forces around the center of tilting motion in Fig. 3($b$) and summing the result over all finite elements sharing faces with the rotor surface, the rate (with respect to "$e$") at which the fluid reaction moments are exerted can be attained. The different derivatives in equations (13) through (20) are then obtained by appropriately replacing $e$ with $\epsilon$ or $\theta z$ (equation (35)) as follows:

$$\frac{\partial F_x}{\partial \epsilon}=\sum_{i=1}^{N_s}\int_{-1}^{+1}\int_{-1}^{+1}n_x(\eta,\xi)p_{,\epsilon}(\eta,\xi)G(\eta,\xi)d\eta d\xi \tag{49}$$

$$\frac{\partial F_y}{\partial \epsilon}=\sum_{i=1}^{N_s}\int_{-1}^{+1}\int_{-1}^{+1}n_y(\eta,\xi)p_{,\epsilon}(\eta,\xi)G(\eta,\xi)d\eta d\xi \tag{50}$$

$$\frac{\partial M_y}{\partial \epsilon}=\sum_{i=1}^{N_s}\int_{-1}^{+1}\int_{-1}^{+1}zn_x(\eta,\xi)p_{,\epsilon}(\eta,\xi)G(\eta,\xi)d\eta d\xi \tag{51}$$

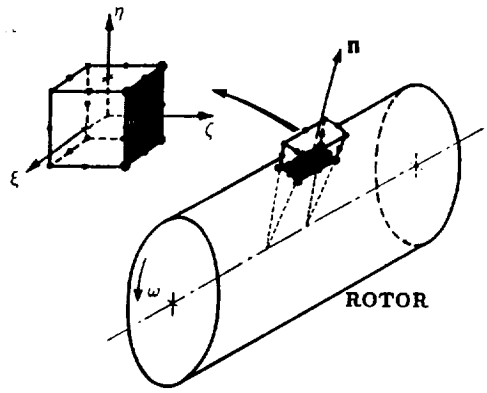


Fig. 7 Integration of the pressure forces on the rotor surface

$$\frac{\partial M_x}{\partial \epsilon} = \sum_{i=1}^{N_s} \int_{-1}^{+1} \int_{-1}^{+1} z n_y(\eta,\xi) p_{,\epsilon}(\eta,\xi) G(\eta,\xi) d\eta d\xi \tag{52}$$

$$\frac{\partial F_x}{\partial \theta} = \sum_{i=1}^{N_s} \int_{-1}^{+1} \int_{-1}^{+1} z n_x(\eta,\xi) p_{,\theta}(\eta,\xi) G(\eta,\xi) d\eta d\xi \tag{53}$$

$$\frac{\partial F_y}{\partial \theta} = \sum_{i=1}^{N_s} \int_{-1}^{+1} \int_{-1}^{+1} z n_y(\eta,\xi) p_{,\theta}(\eta,\xi) G(\eta,\xi) d\eta d\xi \tag{54}$$

$$\frac{\partial M_y}{\partial \theta} = \sum_{i=1}^{N_s} \int_{-1}^{+1} \int_{-1}^{+1} z n_x(\eta,\xi) p_{,\theta}(\eta,\xi) G(\eta,\xi) d\eta d\xi \tag{55}$$

$$\frac{\partial M_x}{\partial \theta} = \sum_{i=1}^{N_s} \int_{-1}^{+1} \int_{-1}^{+1} z n_y(\eta,\xi) p_{,\theta}(\eta,\xi) G(\eta,\xi) d\eta d\xi \tag{56}$$

where $n_x$ and $n_y$ are the components of the local unit vector that is normal to the rotor surface. Also, the parameter $G(\eta,\xi)$ is a Jacobian-like function for cartesian-to-local area transformation, and was previously derived by Baskharone (1979) as follows:

$$G(\eta,\xi) = \left[ \left( \frac{\partial y}{\partial \eta}\frac{\partial z}{\partial \xi} - \frac{\partial y}{\partial \xi}\frac{\partial z}{\partial \eta} \right)^2 + \left( \frac{\partial x}{\partial \xi}\frac{\partial z}{\partial \eta} - \frac{\partial x}{\partial \eta}\frac{\partial z}{\partial \xi} \right)^2 + \left( \frac{\partial x}{\partial \eta}\frac{\partial y}{\partial \xi} - \frac{\partial x}{\partial \xi}\frac{\partial y}{\partial \eta} \right)^2 \right]^{\frac{1}{2}}$$

where the derivatives on the right-hand side are evaluated using the interpolation expressions (25) for a "$\zeta$" value of 1.0 (Fig. 7). As seen, the first four derivatives (equations (49) through (52)) are the outcome of a cylindrical whirl problem (Fig. 3(*a*)) where $e = \epsilon$, while the remaining derivatives are associated with the conical whirl problem, in which case $e = \theta z$. (Fig. 3(*b*)).

At this point, the requirements for computing the rotordynamic coefficients in equation (1) are, by reference to equations (13) through (20), complete. The process, as described earlier, consists of computing the force and moment derivatives in equations (49) through (56) at three or more whirl frequencies. Substitution in equations (13) through (20) finally leads to the different rotordynamic coefficients by inspection.

## Results and Discussion

A hydraulic annular seal with a clearance/length ratio of 0.0085 was selected for the purpose of verifying the current computational model. The force coefficients of this seal were determined by Dietzen and Nordmann (1987), and later verified by Hensel (1990). This seal has a rotor radius of 23.5 mm and a Reynolds number (based on the clearance and inlet throughflow velocity) of 4700. Operating speeds of 2000, 4000, and 6000 rpm were considered in this case, together with preswirl/inlet velocity ratios of 0.04, 0.10, and 0.17, respectively. The zeroth-order flow solution corresponding to each set of operating conditions required an average of 3.5 hours of CPU time on the VAX 8800 mainframe. Execution of the pertubation analysis, on the other hand, consumed nearly 12 minutes of CPU time on the NEC SX2 Supercomputer for each whirl frequency of the rotor axis.

An early version of the current analysis was tested by Hensel (1990) using the same annular seal described above, and the results compared to experimental and analytical data. Missing in these results, however, were the rotordynamic coefficients linking the effects of translational and tilting rotor eccentricies to one another since the computational model, then, did not account for such effects. Presentation and assessment of these coefficients are therefore the focus of this section.

Shown in Fig. 8 is a comparison between the computed values of the moment coefficients. $K_{\theta\epsilon}$, $k_{\theta\epsilon}$, $C_{\theta\epsilon}$, and $c_{\theta\epsilon}$ associated with the rotor cylindrical whirl, and those obtained through Child's bulk flow model. Of these, the cross-coupled stiffness and direct damping coefficients $k_{\theta\epsilon}$ and $C_{\theta\epsilon}$ represent the moments around the $y$-axis (Fig. 2) which arise from the rotor cylindrical whirl. These moments suppress (or aggravate) the rotor whirling motion and are therefore of particular interest. As seen, the trends of these two coefficients with the rotor spinning speed are basically similar in both sets of results. However, the bulk-flow model seems to produce magnitudes that are significantly smaller than those produced by the current analysis.

Figure 9 is intended to support, in a general sense, the impression that the bulk-flow model tends to underpredict the coefficients $k_{\theta\epsilon}$ and $C_{\theta\epsilon}$ discussed above. The comparison in this figure is between the results of applying this model (Childs, 1982b) and the experimental measurement by Kanemori and Iwatsubo (1989) for a hydraulic annular seal with a clearance/length ratio of 0.002 and a length/inner diameter ratio of 3.0. The rotordynamic coefficients in this figure were obtained by interpolation at a fixed overall pressure drop of 100 k. Pa. Examination of Fig. 9 reveals that this model is constantly and significantly underpredicting both coefficients. It should be pointed out here that conversion of the experimental data by Kanemori and Iwatsubo (1989) into the form shown in Fig. 9 may have involved some interpolation errors, and that the differences (in dimensions and operating conditions) between the tested seal and the current, indeed present another source of uncertainty. Nevertheless, the differences between our computed magnitudes of $k_{\theta\epsilon}$ and $C_{\theta\epsilon}$ (Fig. 8) and those produced by the simple bulk-flow model, seem to be consistent with the experimental findings.

The rotordynamic coefficients $K_{\epsilon\theta}$, $k_{\epsilon\theta}$, $C_{\epsilon\theta}$, and $c_{\epsilon\theta}$ in Fig. 10 represent the fluid-exerted forces on the rotor as a result of conical whirl. Again, the cross-coupled stiffness and direct damping coefficients ($k_{\epsilon\theta}$ and $C_{\epsilon\theta}$) give rise to aggravating and restoring forces, respectively, in the event where $k_{\epsilon\theta}$ is negative which is the case here. Aside from the moderate agreement between the computed values of $K_{\epsilon\theta}$ and $c_{\epsilon\theta}$ and those obtained through the bulk-flow model, it is seen that the respective values of $k_{\epsilon\theta}$ and $C_{\epsilon\theta}$ are far apart. In fact, our results indicate that the rotor is comparatively much more stable, as far as this conical-to-cylinderical whirl conversion is concerned. Unfortunately, there is no experimental or analytical data covering this aspect of rotor eccentric motion that can be used to favor a set of numerical results over the other, as the case was in discussing the counterparts of these coefficients earlier in this section.

## Concluding Remarks

The perturbation model presented in this paper is a quite general tool that embraces the most general mode of rotor eccentric motion and lends itself to a challenging category of fluid/rotor interaction problems, yet to be explored. This is where the seal is part of a secondary (or leakage) passage which,

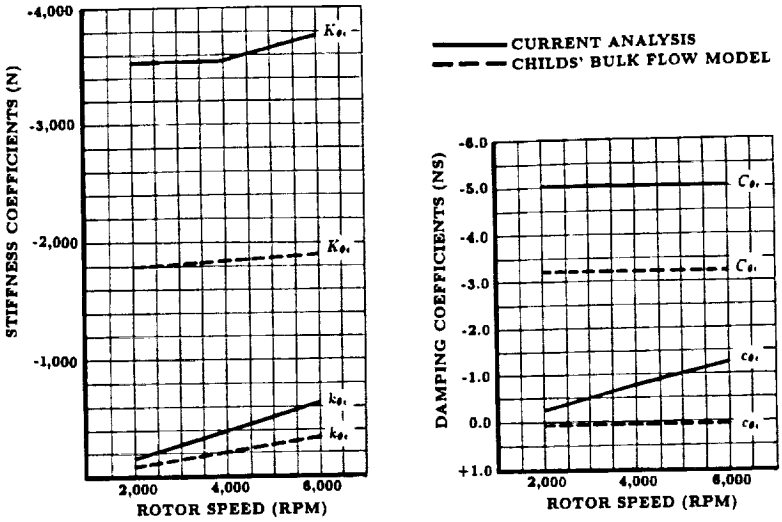


**Fig. 8 Moment coefficients due to the rotor translational eccentricity and comparison with Childs' bulk-flow model results**

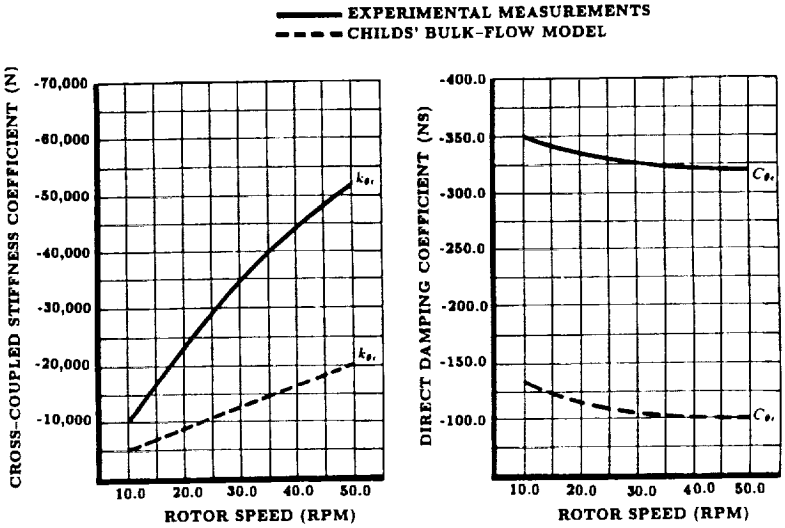


**Fig. 9 Comparison of Childs' bulk-flow model results with the experimental data of Kanemori and Iwatsubo (1989)**

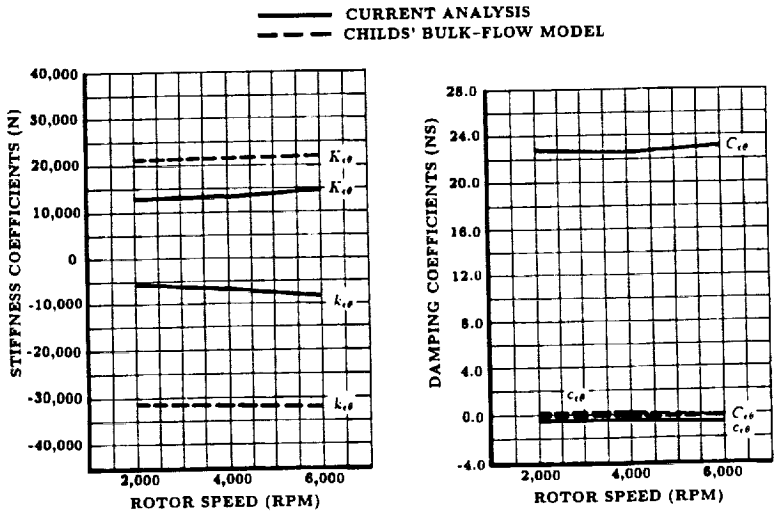


**Fig. 10 Force coefficients due to the rotor angular eccentricity and comparison with Childs' bulk-flow model results**

in turn, is connected to the primary flow passage at both ends in a manner that permits the mutual interaction between the two flow fields (Fig. 2). The authors are not aware of any existing perturbation analysis that is conceptually applicable in this case for the simple fact that existing analyses address the problem where the gap between the whirling body and the housing extends between the flow inlet and exit stations, with the gap width being part of the flow-governing equations. This restriction is totally alleviated in the current model since the virtually-distorted finite element concept, on which the computational model is based, would in this case be utilized exclusively in subdomains which interface with the whirling rotor surface. The difficulty, however, in investigating such a problem stems from the need to use a large size finite-element model (Fig. 2) as the computational domain is unavoidably complex from a geometrical standpoint. Efforts are currently made by the authors to minimize the computational resources needed in this case towards a sufficiently accurate numerical solution.

Current analysis of the coupled cylindrical/conical whirl effects in annular seals is preceded only by simplified models which do not fully account for the flow details in the annular passage. The analysis yields the direct and cross-coupled stiffness and damping coefficients linking each whirling motion to the other. Comparison of the results with those obtained through Childs' bulk-flow model revealed that the latter model generally underpredicts the rotordynamic coefficients under focus in this study. Experimental evidence, however, suggests that the current results are more accurate by comparison.

## Acknowledgment

This research was funded by NASA-Marshall Space Flight Center, Huntsville, Alabama, Contract No. NAS8-37821, NASA Technical Monitor: James Cannon. Partial funding was also provided by Houston Advanced Research Center, The Woodlands, Texas, Grant No. 88-025. The authors wish to thank Professor Dara Childs, Director of the Texas A&M Turbomachinery Laboratory, for making his bulk-flow analysis code available to them and for his genuine interest in this study.

## References

Baldwin, B. S., and Lomax, H., 1978, "Thin Layer Approximation and Algebraic Model for Separated Turbulent Flows," AIAA Paper No. 78-257.

Baskharone, E. A., 1979, "A New Approach in Turbomachinery Flow Analysis Using the Finite Element Method," Ph.D. dissertation, University of Cincinnati, Ohio.

Baskharone, E. A., and Hansel, S. J., 1989, "A New Model for Leakage Prediction in Shrouded-Impeller Turbopumps," ASME *Journal of Fluids Engineering*, Vol. 111, pp. 118-123.

Benim, A. C., and Zinser, W., 1985, "Investigation into the Finite Element analysis of Confined Turbulent Flows Using a $k$-$\epsilon$ Model of Turbulence," *Computer Methods in Applied Mechanics and Engineering*, Vol. 51, pp. 507-523.

Carey, G. F., and Oden, J. T., 1986, "Finite Elements: Fluid Mechanics," The Texas Finite Element Series, Vol. IV, Prentice-Hall Inc.

Childs, D. W., 1982a, "Finite-Length Solutions for Rotordynamic Coefficients of Turbulent Annular Seals," ASME Paper No. 82-Lub-42.

Childs, D. W., 1982b, "Rotordynamic Moment Coefficients for Finite-Length Turbulent Seals," *Proceedings of the International Conference on Rotordynamic Problems in Power Plants*, Rome, Italy, pp. 371-378.

Childs, D., and Kim, C-H., 1985, "Analysis and Testing for Rotordynamic Coefficients of Turbulent Annular Seals with Different Directionally Homogeneous Surface Roughness Treatment for Rotor and Stator Elements," ASME JOURNAL OF TRIBOLOGY, Vol. 108, pp. 296-306.

Childs, D., and Kim, C-H., 1988, "Annular Honeycomb Seals: Test Results for Leakage and Rotordynamic Coefficients; Comparison to Labyrinth and Smooth Configurations," *Proceedings of the Workshop on Rotordynamic Instability in High-Performance Turbomachinery*, Texas A&M University.

Dietzen, F. J., and Nordmann, R., 1987, "Calculation of Rotordynamic Coefficients of Seals by Finite Difference Techniques," ASME JOURNAL OF TRIBOLOGY, Vol. 109.

Dietzen, F. J., and Nordmann, R., 1988, "A 3-Dimensional Finite-Difference Method for Calculating the Dynamic Coefficients of Seals," *Proceedings of the Workshop on Rotordynamic Instability in High Performance Turbomachinery*, Texas A&M University.

Heinrich, J. C., and Zienkiewicz, O. C., 1977, "Quadratic Finite Element Schemes for Two-Dimensional Convective-Transport Problems," *Int. J. Num. Meth. Eng.*, Vol. 11, pp. 1831-1844.

Hensel, S. J., 1990, "A New Method for Determining Rotordynamic Forces on Rotating Mechanical Components," Ph.D. dissertation, Texas A&M University.

Hood, P. and Taylor, C., 1974, "Navier-Stokes Equations Using Mixed Interpolation," *Proceedings of the International Symposium on Finite Element Methods in Flow Problems*, University of Wales, Swansea, United Kingdom.

Kanemori, Y. and Iwatsubo, T., 1989, "Experimental Study of Dynamic Fluid Forces and Moments for a Long Annular Seals," *Machinery Dynamics-Applications and Vibration Control Problems*, (ASME Publication No. DE-Vol. 18-2), pp. 141-147.

Nelson, C. C., 1985, "Rotordynamic Coefficients for Compressible Flow in Tapered Annular Seals," ASME JOURNAL OF TRIBOLOGY, Vol. 107.

Tam, L. T., Przekwas, A. J., Muszynska, A., Hendricks, R. C., Braun, M. J., and Mullen, R. L., 1988, "Numerical and Analytical Study of Fluid Dynamic Forces in Seals and Bearings," ASME *Journal of Vibration, Acoustics, Stress and Reliability in Design*, Vol. 110, pp. 315-325.

Zienkiewicz, O. C., 1971, *The Finite Element Method in Engineering Science*, McGraw-Hill, New York.

## APPENDIX I

### Coefficient Matrices of an Undistorted Finite Element

Define the differential operators **F**, **G**, and **H** such that:

$$\mathbf{F} = T_{11}\frac{\partial}{\partial\zeta} + T_{12}\frac{\partial}{\partial\eta} + T_{13}\frac{\partial}{\partial\xi}$$

$$\mathbf{G} = T_{21}\frac{\partial}{\partial\zeta} + T_{22}\frac{\partial}{\partial\eta} + T_{23}\frac{\partial}{\partial\xi}$$

$$\mathbf{H} = T_{31}\frac{\partial}{\partial\zeta} + T_{32}\frac{\partial}{\partial\eta} + T_{33}\frac{\partial}{\partial\xi}$$

where the coefficients $T_{11}$, $T_{12}$,...etc. are as defined by the set of expressions (27). The different coefficient arrays in the equations associated with a typical finite element (equations (29) through (32)) can now be expressed in terms of these operators as follows:

$$a_1)_{i,j} = \int_{V(e)} \{\hat{\nu}_e[\mathbf{F}(N_i)\mathbf{F}(N_j) + \mathbf{G}(N_i)\mathbf{G}(N_j) + \mathbf{H}(N_i)\mathbf{H}(N_j)] - W_i[\mathbf{G}(\hat{\nu}_t)\mathbf{G}(N_j) + \mathbf{H}(\hat{\nu}_t)\mathbf{H}(N_j) + 2\mathbf{F}(\hat{\nu}_t)\mathbf{F}(N_j)] + W_i[\hat{u}\mathbf{F}(N_j) + \hat{v}\mathbf{G}(N_j) + \hat{w}\mathbf{H}(N_j)]\}dV$$

$$a_2)_{i,j} = \int_{V(e)} -N_i[\mathbf{G}(\hat{\nu}_t)\mathbf{F}(N_j) - 2\Omega N_j]dV$$

$$a_3)_{i,j} = \int_{V(e)} -W_i\mathbf{H}(\hat{\nu}_t)\mathbf{F}(N_j)dV$$

$$a_4)_{i,k} = \int_{V(e)} \frac{1}{\rho} N_i\mathbf{F}(M_k)dV$$

$$a_5)_{i,j} = \int_{V(e)} -N_i[\mathbf{F}(\hat{\nu}_t)\mathbf{G}(N_j) + 2\Omega N_j]dV$$

$$a_6)_{i,j} = \int_{V(e)} \{\hat{\nu}_e[\mathbf{F}(N_i)\mathbf{F}(N_j) + \mathbf{G}(N_i)\mathbf{G}(N_j) + \mathbf{H}(N_i)\mathbf{H}(N_j)] - W_i[\mathbf{F}(\hat{\nu}_t)\mathbf{F}(N_j) + \mathbf{H}(\hat{\nu}_t)\mathbf{H}(N_j) + 2\mathbf{G}(\hat{\nu}_t)\mathbf{G}(N_j)] + W_i[\hat{u}\mathbf{F}(N_j) + \hat{v}\mathbf{G}(N_j) + \hat{w}\mathbf{H}(N_j)]\}dV$$

$$a_7)_{i,j} = \int_{V(e)} -N_i\mathbf{H}(\hat{\nu}_t)\mathbf{G}(N_j)dV$$

$$a_8)_{i,k} = \int_{V(e)} \frac{1}{\rho} N_i\mathbf{G}(M_k)dV$$

$$a_9)_{i,j} = \int_{V(e)} -N_i\mathbf{F}(\hat{\nu}_t)\mathbf{H}(N_j)dV$$

$$a_{10})_{i,j} = \int_{V(e)} -N_i\mathbf{G}(\hat{\nu}_t)\mathbf{H}(N_j)dV$$

$$a_{11})_{i,j} = \int_{V(e)} \{\hat{\nu}_e[\mathbf{F}(N_i)\mathbf{F}(N_j) + \mathbf{G}(N_i)\mathbf{G}(N_j) + \mathbf{H}(N_i)\mathbf{H}(N_j)] - W_i[\mathbf{F}(\hat{\nu}_t)\mathbf{F}(N_j) + \mathbf{G}(\hat{\nu}_t)\mathbf{G}(N_j) + 2\mathbf{H}(\hat{\nu}_t)\mathbf{H}(N_j)] + W_i[\hat{u}\mathbf{F}(N_j) + \hat{v}\mathbf{G}(N_j) + \hat{w}\mathbf{H}(N_j)]\}dV$$

$$a_{12})_{i,k} = \int_{V(e)} \frac{1}{\rho} N_i \mathbf{H}(M_k) dV$$

$$a_{13})_{k,j} = \int_{V(e)} M_k \mathbf{F}(N_j) dV$$

$$a_{14})_{k,j} = \int_{V(e)} M_k \mathbf{G}(N_j) dV$$

$$a_{15})_{k,j} = \int_{V(e)} M_k \mathbf{H}(N_j) dV$$

$$b_1)_i = \int_{S(e)} \hat{\nu}_e N_i (\mathbf{n} \cdot \nabla u) dS + \Omega^2 \int_{V(e)} N_i \left( \sum_{l=1}^{20} N_l x_l \right) dV$$

$$b_2)_i = \int_{S(e)} \hat{\nu}_e N_i (\mathbf{n} \cdot \nabla v) dS + \Omega^2 \int_{V(e)} N_i \left( \sum_{l=1}^{20} N_l y_l \right) dV$$

$$b_3)_i = \int_{S(e)} \hat{\nu}_e N_i (\mathbf{n} \cdot \nabla w) dS$$

where $i = 1,2,\ldots,20$, $j = 1,2,\ldots,20$, $k = 1,2,\ldots,8$, the symbol $\hat{\ }$ refers to a value that is known from a previous iteration or an initial guess, $dS$ is the differential element of surface area (Fig. 5) and $\mathbf{n}$ is the local unit vector normal to the boundary. Also, the volume differential $dV$ is as follows:

$$dV = |\mathbf{J}| d\zeta d\eta d\xi$$

where $|\mathbf{J}|$ is the Jacobian of transformation from the local to the cartesian frame of reference (Fig. 5) for the undistorted finite element.

## APPENDIX II

### Perturbed Set of Finite Element Equations

Referring to equation (45), the matrix $[\tilde{a}]$ and vector $\{\tilde{b}\}$ associated with the distorted element in Fig. 6 is broken up into smaller arrays $[\tilde{a}_1]$ through $[\tilde{a}_{15}]$ and $\{\tilde{b}_1\}$ through $\{\tilde{b}_3\}$. These arrays are similar in construction to those defined in Appendix I (for the undistorted element), and can be expressed as follows:

$$\begin{aligned}\tilde{a}_1)_{i,j} = a_1^*)_{i,j} + \int_{V(e)} \{ &\hat{\nu}_e [\mathbf{F}(N_i)\mathbf{I}(N_j) + \mathbf{I}(N_i)\mathbf{F}(N_j) \\ &+ \mathbf{G}(N_i)\mathbf{J}(N_j) + \mathbf{J}(N_i)\mathbf{G}(N_j) + \mathbf{H}(N_i)\mathbf{K}(N_j) + \mathbf{K}(N_i)\mathbf{H}(N_j)] \\ &- N_i [\mathbf{G}(\hat{\nu}_t)\mathbf{J}(N_j) + \mathbf{J}(\hat{\nu}_t)\mathbf{G}(N_j) + \mathbf{H}(\hat{\nu}_t)\mathbf{K}(N_j) + \mathbf{K}(\hat{\nu}_t)\mathbf{H}(N_j) \\ &+ 2\mathbf{F}(\hat{\nu}_t)\mathbf{I}(N_j) + 2\mathbf{I}(\hat{\nu}_t)\mathbf{F}(N_j)] + N_i [\hat{u}\mathbf{I}(N_j) + \hat{v}\mathbf{J}(N_j) + \hat{w}\mathbf{K}(N_j)] \} dV\end{aligned}$$

$$\tilde{a}_2)_{i,j} = a_2^*)_{i,j} - \int_{V(e)} N_i [\mathbf{G}(\hat{\nu}_t)\mathbf{I}(N_j) + \mathbf{J}(\hat{\nu}_t)\mathbf{F}(N_j)] dV$$

$$\tilde{a}_3)_{i,j} = a_3^*)_{i,j} - \int_{V(e)} N_i [\mathbf{H}(\hat{\nu}_t)\mathbf{I}(N_j) + \mathbf{K}(\hat{\nu}_t)\mathbf{F}(N_j)] dV$$

$$\tilde{a}_4)_{i,k} = a_4^*)_{i,k} + \int_{V(e)\rho} \frac{1}{\rho} N_i \mathbf{I}(M_k) dV$$

$$\tilde{a}_5)_{i,j} = a_5^*)_{i,j} - \int_{V(e)} N_i [\mathbf{F}(\hat{\nu}_t)\mathbf{J}(N_j) + \mathbf{I}(\hat{\nu}_t)\mathbf{G}(N_j)] dV$$

$$\begin{aligned}\tilde{a}_6)_{i,j} = a_6^*)_{i,j} + \int_{V(e)} \{ &\hat{\nu}_e [\mathbf{F}(N_i)\mathbf{I}(N_j) + \mathbf{I}(N_i)\mathbf{F}(N_j) \\ &+ \mathbf{G}(N_i)\mathbf{J}(N_j) + \mathbf{J}(N_i)\mathbf{G}(N_j) + \mathbf{H}(N_i)\mathbf{K}(N_j) + \mathbf{K}(N_i)\mathbf{H}(N_j)] \\ &- N_i [\mathbf{F}(\hat{\nu}_t)\mathbf{I}(N_j) + \mathbf{I}(\hat{\nu}_t)\mathbf{F}(N_j) + \mathbf{H}(\hat{\nu}_t)\mathbf{K}(N_j) + \mathbf{K}(\hat{\nu}_t)\mathbf{H}(N_j) + 2\mathbf{G}(\hat{\nu}_t) \\ &\times \mathbf{J}(N_j) + 2\mathbf{J}(\hat{\nu}_t)\mathbf{G}(N_j)] + N_i [\hat{u}\mathbf{I}(N_j) + \hat{v}\mathbf{J}(N_j) + \hat{w}\mathbf{K}(N_j)] \} dV\end{aligned}$$

$$\tilde{a}_7)_{i,j} = a_7^*)_{i,j} - \int_{V(e)} N_i [\mathbf{H}(\hat{\nu}_t)\mathbf{J}(N_j) + \mathbf{K}(\hat{\nu}_t)\mathbf{G}(N_j)] dV$$

$$\tilde{a}_8)_{i,j} = a_8^*)_{i,j} - \int_{V(e)\rho} \frac{1}{\rho} N_i \mathbf{J}(M_k) dV$$

$$\tilde{a}_9)_{i,j} = a_9^*)_{i,j} - \int_{V(e)} N_i [\mathbf{F}(\hat{\nu}_t)\mathbf{K}(N_j) + \mathbf{I}(\hat{\nu}_t)\mathbf{H}(N_j)] dV$$

$$\tilde{a}_{10})_{i,j} = a_{10}^*)_{i,j} - \int_{V(e)} N_i [\mathbf{G}(\hat{\nu}_t)\mathbf{K}(N_j) + \mathbf{J}(\hat{\nu}_t)\mathbf{H}(N_j)] dV$$

$$\begin{aligned}\tilde{a}_{11})_{i,j} = a_{11}^*)_{i,j} + \int_{V(e)} \{ &\hat{\nu}_e [\mathbf{F}(N_i)\mathbf{I}(N_j) + \mathbf{I}(N_i)\mathbf{F}(N_j) + \mathbf{G}(N_i)\mathbf{J}(N_j) \\ &+ \mathbf{J}(N_i)\mathbf{G}(N_j) + \mathbf{H}(N_i)\mathbf{K}(N_j) + \mathbf{K}(N_i)\mathbf{H}(N_j)] - N_i [\mathbf{F}(\hat{\nu}_t)\mathbf{I}(N_j) \\ &+ \mathbf{I}(\hat{\nu}_t)\mathbf{F}(N_j) + \mathbf{G}(\hat{\nu}_t)\mathbf{J}(N_j) + \mathbf{J}(\hat{\nu}_t)\mathbf{G}(N_j) + 2\mathbf{H}(\hat{\nu}_t)\mathbf{K}(N_j) \\ &+ 2\mathbf{K}(\hat{\nu}_t)\mathbf{H}(N_j) + N_i [\hat{u}\mathbf{I}(N_j) + \hat{v}\mathbf{J}(N_j) + \hat{w}\mathbf{K}(N_j)] \} dV\end{aligned}$$

$$\tilde{a}_{12})_{i,k} = a_{12}^*)_{i,k} + \int_{V(e)\rho} \frac{1}{\rho} N_i \mathbf{K}(M_k) dV$$

$$\tilde{a}_{13})_{k,j} = a_{13}^*)_{k,j} + \int_{V(e)} M_k \mathbf{I}(N_j) dV$$

$$\tilde{a}_{14})_{k,j} = a_{14}^*)_{k,j} + \int_{V(e)} M_k \mathbf{J}(N_j) dV$$

$$\tilde{a}_{15})_{k,j} = a_{15}^*)_{k,j} + \int_{V(e)} M_k \mathbf{K}(N_j) dV$$

$$\tilde{b}_1)_i = \Omega^2 \int_{-1}^{+1} \int_{-1}^{+1} \int_{-1}^{+1} N_i \left( \sum_{l=1}^{20} N_l x_l \right) |\tilde{\mathbf{J}}| d\zeta d\eta d\xi$$

$$\tilde{b}_2)_i = \Omega^2 \int_{-1}^{+1} \int_{-1}^{+1} \int_{-1}^{+1} N_i \left( \sum_{l=1}^{20} N_l y_l \right) |\tilde{\mathbf{J}}| d\zeta d\eta d\xi - \Omega^2 \int_{V(e)} N_i \left( \sum_{l=1}^{20} N_l \lambda_l \right) dV$$

$$\tilde{b}_3)_i = 0$$

In these expressions, a variable with an asterisk has the same form as that in Appendix I, with the exception that the Jacobian $|\mathbf{J}|$ is now replaced by $|\tilde{\mathbf{J}}|$ as defined in equation (41) where $i$ and $j$ vary from 1 to 20, while $k$ varies from 1 to 8. With the operators $\mathbf{F}$, $\mathbf{G}$, and $\mathbf{H}$ being those defined in Appendix I, the new operators $\mathbf{I}$, $\mathbf{J}$, and $\mathbf{K}$ are defined as follows:

$$\mathbf{I} = P_{11} \frac{\partial}{\partial \zeta} + P_{12} \frac{\partial}{\partial \eta} + P_{13} \frac{\partial}{\partial \xi}$$

$$\mathbf{J} = P_{21} \frac{\partial}{\partial \zeta} + P_{22} \frac{\partial}{\partial \eta} + P_{23} \frac{\partial}{\partial \xi}$$

$$\mathbf{K} = P_{31} \frac{\partial}{\partial \zeta} + P_{32} \frac{\partial}{\partial \eta} + P_{33} \frac{\partial}{\partial \xi}$$

with the matrix $[P]$ being that defined by the set of expressions (44). The volume differential "dV" is the same as defined in Appendix I for the undistorted finite element.

**PAPER# 5**

These are the page proofs of a paper
which will appear in the December issue
of the ASME Journal of Fluids Engineering

# Flow Field in the Secondary, Seal-Containing Passages of Centrifugal Pumps[1]

**E. A. Baskharone**
Associate Professor.
Mem. ASME

**S. J. Hensel**[2]
Graduate Research Assistant.
Mem. ASME

Department of Mechanical Engineering.
Texas A&M University.
College Station. Texas 77843

*This paper illustrates the impact of seal configuration on the through-flow leakage in centrifugal pumps with shrouded impellers. The flow model is based on the Petrov-Galerkin finite element method, and the computational domain permits the primary/secondary flow interaction at both ends of the clearance gap. The model is applied to a hydraulic pump with two different seal configurations for the purpose of comparison. The computed results show a strong dependency of the leakage flow percentage and swirl-velocity retention on the overall shape of the shroud-to-housing passage including, in particular, the seal geometry. The results are generally consistent with documented observations and measurements in similar pump stages. From a rotordynamic standpoint, the current computational model conceptually provides the centered-rotor "zeroth-order" flow field for existing perturbation models of fluid/rotor interaction. The flow model is applied to two different secondary passage configurations of a centrifugal pump, and the results used in interpreting existing rotordynamic data concerning the same passage configurations.*

## Introduction

Leakage flow in the shroud-to-housing gap of centrifugal pumps has significant performance and rotor-integrity consequences. First, it is the leakage flow rate, as determined by the through-flow velocity component, which is typically a major source of the stage losses. The swirl velocity component, on the other hand, is perhaps the single most predominant destabilizing contributor to the impeller rotordynamic behavior. Control of the through-flow velocity in the clearance gap is often achieved through utilization of a tight-clearance seal. Suppression of the flow swirl, however, requires careful design of the leakage passage and/or the use of such devices as the so-called swirl "brakes" (e.g., Childs et al., 1991) or straightening grooves/ribs in the inner housing surface (e.g., Ohashi, 1988). Unfortunately, an efficient leakage control device, such as the labyrinth seal, may itself trigger an instability problem of fluid-induced vibration (Childs and Elrod, 1988). In the current study, two seal configurations, comprising part of the shroud-to-housing passage in a centrifugal pump, are analyzed for comparison. In both cases, the impeller geometry and the pump operating conditions are identical.

The current computational tool is an expanded version of a finite-element model which was previously proposed by the authors (Baskharone and Hensel, 1989), where the mere idea of including primary-flow segments in the computational domain definition was introduced. This was a means of avoiding the need for what would otherwise be unrealistic boundary conditions at the primary/secondary flow interface. The model, initially based on a laminar flow assumption, has since been upgraded by recognizing such aspects as turbulence and inertia domination of the flow field.

The outcome of the current study is tightly linked to the rotordynamic stability analysis of shrouded pump impellers. This is true in the sense that the numerical results can essentially be utilized as the "zeroth-order" flow field in existing perturbation models (e.g., Baskharone and Hensel, 1991a) for computing the stiffness, damping and inertia coefficients of the fluid/shroud interaction forces, as the impeller axis undergoes a whirling motion around the housing centerline. Accuracy of these rotordynamic coefficients was reported by Baskharone and Hensel (1991a) to be a strong function of the centered-impeller flow solution, which is under investigation here.

## Analysis

Figure 1 shows the primary and secondary flow passages in a typical pump stage, and the computational domain under consideration. The latter includes two primary-flow segments, which render the domain to a double/entry, double/departure flow region. Also shown in Fig. 1 are the major features of the finite element model in which a biquadratic curve-sided element (Fig. 2) is used as the discretization unit.

Definition of the computational domain in the manner shown in Fig. 1 is hardly traditional. Inclusion of two primary flow

[1]This research was funded by NASA-Marshall Space Flight Center (Huntsville, Alabama), Contract No. NAS8-37821, technical monitor: James Cannon.

[2]Currently with Westinghouse Savannah River Laboratory, Aiken, South Carolina,.

Contributed by the Fluids Engineering Division for publication in the JOURNAL OF FLUIDS ENGINEERING. Manuscript received by the Fluids Engineering Division August 10, 1992; revised manuscript received December 30, 1992. Associate Technical Editor: N. A. Cumpsty.

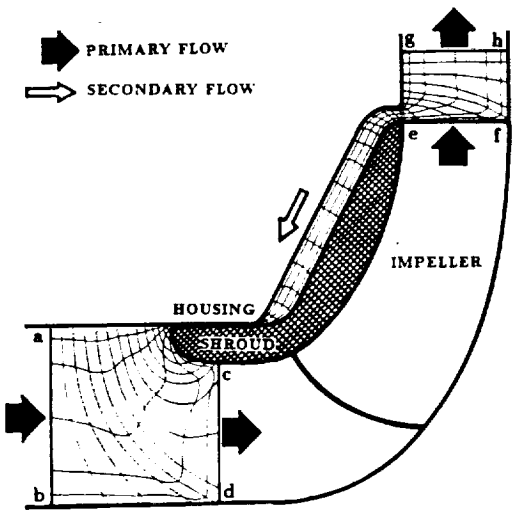


Fig. 1 Definition of the computational domain in a typical centrifugal pump

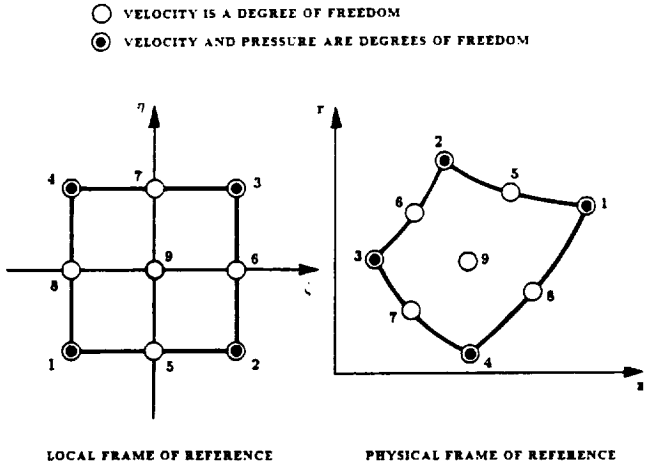


Fig. 2 Biquadratic nine-noded finite element of the Lagrangian type

segments in this domain is aimed at facilitating, to a reasonable level, the primary/secondary flow interaction effects at both ends of the secondary passage, without resorting to a much larger numerical model, had the impeller subdomain been added. Existing computational models, by comparison, treats the secondary passage as totally isolated from the primary-flow passage (e.g., Childs, 1989). As seen in Fig. 1, inclusion of the primary-flow passages (labeled a-b-d-c and e-f-h-g) clearly alleviates the need to specify what would otherwise be grossly simplified boundary conditions at the two primary/secondary flow interaction locations at both ends of the secondary-flow passage.

It might appear, at first, that the current flow problem is solvable using one of the existing commercial flow codes. However the very nature of the computational domain, as a multiple entry/departure flow region, and some of the corresponding boundary conditions (discussed later in this section) are too nontraditional for such codes.

**Flow-Governing Equations.** The momentum and mass conservation laws governing the swirling axisymmetric flow of the incompressible fluid in Fig. 1 can be expressed as follows:

$$V_r\frac{\partial V_r}{\partial r}+V_z\frac{\partial V_r}{\partial z}-\frac{V_\theta^2}{r}=-\frac{1}{\rho}\frac{\partial p}{\partial r}+\nabla\cdot(\nu_{\text{eff}}\nabla V_r)+\frac{\partial \nu_t}{\partial r}\frac{\partial V_r}{\partial r}-\frac{\nu_{\text{eff}}}{r^2}V_r+\frac{\partial \nu_t}{\partial z}\frac{\partial V_z}{\partial r} \quad (1)$$

$$V_r\frac{\partial V_\theta}{\partial r}+V_z\frac{\partial V_\theta}{\partial z}+\frac{V_rV_\theta}{r}=\nabla\cdot(\nu_{\text{eff}}\nabla V_\theta)-\left[\frac{1}{r}\frac{\partial \nu_t}{\partial r}+\frac{\nu_{\text{eff}}}{r^2}\right]V_\theta \quad (2)$$

$$V_r\frac{\partial V_z}{\partial r}+V_z\frac{\partial V_z}{\partial z}=-\frac{1}{\rho}\frac{\partial p}{\partial z}+\nabla\cdot(\nu_{\text{eff}}\nabla V_z)+\frac{\partial \nu_t}{\partial z}\frac{\partial V_z}{\partial z}+\frac{\partial \nu_t}{\partial r}\frac{\partial V_r}{\partial z} \quad (3)$$

$$\frac{\partial V_r}{\partial r}+\frac{\partial V_z}{\partial z}+\frac{V_r}{r}=0 \quad (4)$$

where:

$V_r$, $V_\theta$, and $V_z$ are the $r$, $\theta$, and $z$ velocity components
$p$ = is the static pressure,
$\rho$ = is the flow density,
$\nu_t$ and $\nu_{\text{eff}}$ = are the eddy and effective kinematic viscosity coefficients, respectively.

**Turbulence Model.** The turbulence closure in this study is that devised by Baldwin and Lomax (1978), together with an enhanced version of the near-wall zone treatment proposed by Benim and Zinser (1985). First, the effective kinematic viscosity $\nu_{\text{eff}}$, in Eqs. (1) through (3), is cast in terms of the molecular and eddy components, $\nu_l$ and $\nu_t$. In calculating the eddy component, $\nu_t$, the procedure assumes the presence of two, inner and outer, layers. In the inner layer, the Prandtl-Van Driest formulation yields the following expression:

$$\nu_{t,i}=l^2|\omega| \quad (5)$$

where the subscript $i$ refers to the inner layer, and the symbol $\omega$ stands for the local vorticity. The mixing length, $l$, in expression (5) is defined as follows:

## Nomenclature

$A$ = finite element area in the meridional plane
$K$, $k$ = constants in the turbulence closure
$L$ = length along the finite element boundary
$l$ = mixing length
$M_i(\zeta, \eta)$ = linear shape function associated with the $i$th corner node of a finite element
$N_i(\zeta, \eta)$ = quadratic shape function associated with the $i$th corner, midside or interior node of a finite element
$p$ = static pressure
$U_t$ = tip speed of the pump impeller
$\mathbf{V}$ = absolute velocity vector
$V_z$, $V_\theta$, $V_r$ = absolute velocity components in the cylindrical frame of reference
$\mathbf{W}$ = relative velocity vector
$W_i$ = weight function in the Petrov-Galerkin weighted-residual analysis
$z$, $r$ = coordinates in the meridional plane
$\zeta$, $\eta$ = coordinates in the element local frame of reference
$\nu$ = kinematic viscosity
$\rho$ = density
$\tau_w$ = wall shear stress
$\{\Phi\}$, $\{\phi\}$ = global and element vector of unknown velocity components and pressure
$\Omega$ = impeller spinning speed
$\omega$ = vorticity

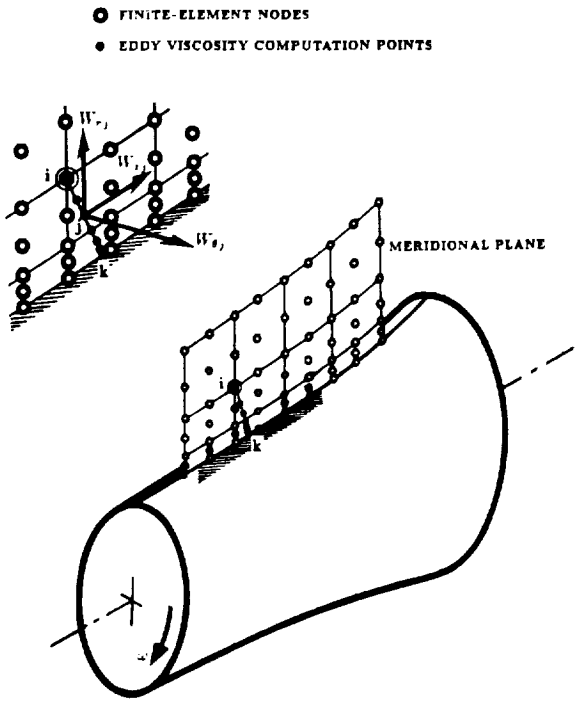


**Fig. 3 Near-wall refinement for accurate prediction of the eddy viscosity**

$$l = ky\left[1 - \exp\left(\frac{-y^+}{A^+}\right)\right], \quad y^+ = \frac{\sqrt{\rho_\omega \tau_\omega}}{\mu_\omega} y; \text{ and} \tag{6}$$

where:

$y$ = the distance normal to the nearest wall,
$A^+$ = the sublayer thickness,
$\tau_\omega$ = the wall shear stress

The model switches from Van Driest formulation to that of the outer region at the smallest value of $y$ for which the inner and outer values of the eddy kinematic viscosity are equal. The formulation for the outer layer is given by:

$$\nu_{t,o} = KC_{cp} F_{max} y_{max} F_{KLEB} \tag{7}$$

where:

$$F_{max} = y_{max} |\omega| \left[1 - \exp\left(\frac{-y^+}{A^+}\right)\right]; \text{ and}$$

$$F_{KLEB} = \left[1 + 5.5\left(C_{KLEB}\frac{y}{y_{max}}\right)^6\right]^{-1}$$

with $y_{max}$ referring to the value of $y$ at which $F_{max}$ occurs. The various constants in Baldwin-Lomax model are as follows:

$A^+ = 26$, $k = 0.4$, $K = 0.0168$, $C_{cp} = 1.6$; and $C_{KLEB} = 0.3$

A modification to the Baldwin and Lomax turbulence closure was made in the current study to accommodate the angular motion of the shroud surface (Fig. 1). Referring to the definition of the inner-layer kinematic eddy viscosity, and considering the case in which the layer is attached to this rotating surface, the vorticity and wall shear stress were both defined on the basis of the relative velocity (**W**) as opposed to the absolute velocity (**V**), where:

$$\mathbf{W} = \mathbf{V} - \Omega r \mathbf{e}_\theta \tag{8}$$

where:

$\Omega$ = the rotor spinning speed
$r$ = the local radius
$\mathbf{e}_\theta$ = the unit vector in the positive tangential direction

In this case, the relative vorticity ($\omega_R$) is expressible in terms of the absolute vorticity ($\omega$) as follows:

$$\omega_R = \omega - 2\Omega \tag{9}$$

Calculation of the eddy viscosity in the outer layer (Eq. (7)), as pertaining to the rotating surface, was consistently performed using the relative flow properties.

Computation of the wall shear stress, $\tau_w$, is based on the near-wall zone treatment proposed by Benim and Zinser (1985). The assumption here is that the universal law of the wall at any wall location is extendible to an interior computational node that is closest to the wall at this location (Fig. 3). Referring to this minimum distance from the wall by $y_{min}$, the following expression for the wall shear stress is then obtained:

$$\tau_w = \begin{cases} \dfrac{\nu_l \rho W_{min}}{y_{min}} & \text{for } y^+_{min} < 11.6 \\ \dfrac{\kappa C_D^{1/4} \rho W_{min} k_{min}^{1/2}}{\ln\left(EC_D^{1/4} y_{min} \dfrac{k_{min}^{1/2}}{\nu_l}\right)} & \text{for } y^+_{min} \geq 11.6 \end{cases} \tag{10}$$

where:

$$k_{min} = \frac{\tau_w}{\rho C_D^{1/2}}, \quad C_D = 0.09, \quad \kappa = 0.4, \quad E = 9.0$$

The symbol $W_{min}$ in expression (10) refers to the interior-node velocity relative to the wall for a rotating wall segment, and is identical to the absolute velocity otherwise (Fig. 3). Note that the outcome of this equation in the case where $y^+_{min} \geq 11.6$ is a recursive relationship since the wall shear stress $\tau_w$ now appears on both sides of the equation. An iterative procedure is executed, in this case, to compute $\tau_w$.

Enhancement of the accuracy of the preceding turbulence closure, including the near-wall model, is achieved with the aid of an array of points that is different from the primary set of computational nodes in the finite-element model. This is in contrast to the model by Benim and Zinser, where the flow properties at the finite-element node closest to the wall were used to calculate the wall shear stress. Figure 3 shows an enlarged segment of the computational domain near a generally rotating wall, in which the primary nodes in the finite-element discretization model are identified by hollow circles, while the points used in the eddy viscosity computations at the typical node "*i*" are solid circles. The objective here was twofold; to estimate the cut-off location between the inner and outer layer with sufficient accuracy, and to capture the steep gradients of the flow variables near the solid wall.

**Boundary Conditions.** Referring to the flow-permeable boundary segments in Fig. 1, the boundary conditions over these segments are as follows:

(*i*) *Stage Inlet Station.* This is the boundary segment a-b in Fig. 1, which is located sufficiently far upstream from the impeller. Fully developed flow is assumed at this location, giving rise to the following boundary condition:

$$\frac{\partial V_r}{\partial z} = \frac{\partial V_\theta}{\partial z} = \frac{\partial V_z}{\partial z} = 0$$

In addition, the stage-inlet static pressure is specified at the node midway between the endwalls on this station.

(*ii*) *Impeller Inlet and Exit Stations.* These are labeled c-d and e-f in Fig. 1. Fixed profiles of the velocity components, corresponding to the stage operating conditions, are imposed over these boundary segments. Note that the operating conditions here involve the primary impeller passage, and do not include the secondary mass flow rate.

(*iii*) *Stage Exit Station.* The flow behavior at this station (designated g-h in Fig. 1) is viewed as predominantly confined to satisfying the mass and angular momentum conservation equations in a global sense. In their derivative forms, these can be expressed as follows:

$$\frac{\partial V_r}{\partial r} = -\frac{V_r}{r} \text{ and } \frac{\partial V_\theta}{\partial r} = -\frac{V_\theta}{r}$$

These two boundary conditions are linear and are, therefore, introduced non-iteratively in the numerical solution process. Moreover, a zero normal derivative of $V_z$ is imposed over this station, and the stage-exit static pressure is specified at the computational node midway between the endwalls on this station.

As for the solid boundary segments in Fig. 1, namely those of the housing and shroud as well as the hub surface segment b-d, the no-slip boundary condition applies as follows:

$$V_r = 0,\ V_z = 0 \text{ and } V_\theta = C$$

where $C$ is equal to $(\Omega r)$ and zero for rotating and nonrotating boundary segments, respectively.

**Finite-Element Formulation.** A special version of the Petrov-Galerkin weighted residual method is used to derive the finite-element form of the flow-governing equations. The current approach ensures upwinding of the convection terms in the momentum equations while preserving the elliptic nature of the diffusion terms. This, for a simple orthogonal grid, would be equivalent to backward-differencing the convection terms and central-differencing the diffusion terms in the conventional finite difference analyses of inertia-dominated flows. Successful implementation of this strategy, within a finite-element context, was achieved by Hughes (1978) for only simple (linear and bi-linear) finite-element configurations by modifying the integration algorithm in the process of deriving the element equations. This effectively eliminated the "wiggles" in the streamwise pressure variation which are typically associated with the conventional Galerkin's weighted residual approach when applied to high Reynolds number flows, such as the present. Expansion of essentially the same concept to a highly accurate biquadratic element, is employed in the current model, by selecting the weight functions on a term-by-term basis.

The characteristic features of the finite element discretization model in the current study are shown in Fig. 1. The discretization unit, which is a nine-noded curve-sided finite element of the Lagrangian type (Zienkiewicz, 1971) is separately shown in Fig. 2 in both the local and physical frames of reference. Within a typical element $(e)$, let the spatial coordinates be interpolated as follows:

$$z^{(e)} = \sum_{i=1}^{9} N_i(\zeta, \eta) z_i, \quad r^{(e)} = \sum_{i=1}^{9} N_i(\zeta, \eta) r_i$$

where $N_i$ are quadratic "shape" functions associated with the element corner, midside and interior nodes. Next, the flow variables are interpolated throughout the element in a similar fashion. Guided by the Ladyshenskaya-babuska-brezzi compatibility requirements (Carey and Oden, 1986) for the problem at hand, the velocity components and pressure are expressed as follows:

$$V_z^{(e)} = \sum_{i=1}^{9} N_i(\zeta, \eta) V_{z,i}, \quad V_r^{(e)} = \sum_{i=1}^{9} N_i(\zeta, \eta) V_{r,i}$$

$$V_\theta^{(e)} = \sum_{i=1}^{9} N_i(\zeta, \eta) V_{\theta,i}, \quad p^{(e)} = \sum_{k=1}^{4} M_k(\zeta, \eta) p_k$$

where $M_k$ are the linear shape functions associated with the element corner nodes.

According to the weighted residual method, the error functions produced by Eqs. (1) through (4) as a result of substituting the interpolation expressions, above, are then made orthogonal to a special set of weight functions over the finite element subdomain. In constructing the latter set of functions, the so-called error consistency criterion of Hood and Taylor (1974) was implemented, whereby the element shape functions, $M_k$ were used in conjunction with the continuity equation. On the other hand, quadratic functions which include the element shape functions "$N_i$" and a set of derived functions "$W_i$" were used in conjunction with the momentum equations in such a way to ensure full upwinding of the convection terms. Of these, the functions "$W_i$" were previously defined by Heinrich and Zienkiewicz (1977) in terms of the shape functions and some upwinding constants which depend on the element geometry and local velocity direction.

With the weight functions now defined, derivation of the finite-element equivalent to Eqs. (1) through (4) is straightforward. The process requires linearization of these equations, using known values for the velocity components and eddy viscosity, and use of Gauss divergence theorem. The final form of these equations for the typical element $(e)$ is as follows:

$$\left[\int_{A^{(e)}}\int\left\{\hat{\nu}_{\text{eff}}\left(\frac{\partial N_i}{\partial r}\frac{\partial N_j}{\partial r}+\frac{\partial N_i}{\partial z}\frac{\partial N_j}{\partial z}\right)+W_i\left(\hat{V}_r\frac{\partial N_j}{\partial r}+\hat{V}_z\frac{\partial N_j}{\partial z}\right)-N_i\frac{\partial \hat{\nu}_t}{\partial r}\frac{\partial N_j}{\partial r}+\frac{\hat{\nu}_{\text{eff}}}{r^2}N_iN_j\right\}rdA\right]V_{r,j}$$
$$-\left[\int_{A^{(e)}}\int\frac{\hat{V}_\theta}{r}N_iN_j rdA\right]V_{\theta,j}-\left[\int_{A^{(e)}}\int N_i\frac{\partial \hat{\nu}_t}{\partial z}\frac{\partial N_j}{\partial r}rdA\right]V_{z,j}$$
$$+\left[\int_{A^{(e)}}\int\frac{1}{\rho}N_i\frac{\partial M_k}{\partial r}rdA\right]p_k=\oint_{L^{(e)}}\hat{\nu}_{\text{eff}}N_i\,(\vec{n}\cdot\nabla V_r)dL \tag{11}$$

$$\left[\int_{A^{(e)}}\int\left\{\hat{\nu}_{\text{eff}}\left(\frac{\partial N_i}{\partial r}\frac{\partial N_j}{\partial r}+\frac{\partial N_i}{\partial z}\frac{\partial N_j}{\partial z}\right)+W_i\left(\hat{V}_r\frac{\partial N_j}{\partial r}+\hat{V}_z\frac{\partial N_j}{\partial z}\right)+\left(\frac{1}{r}\frac{\partial \hat{\nu}_t}{\partial r}+\frac{\hat{\nu}_{\text{eff}}}{r^2}+\frac{\hat{V}_r}{r}\right)N_iN_j\right\}rdA\right]V_{\theta,j}$$
$$=\oint_{L^{(e)}}\nu_{\text{eff}}rN_i(\vec{n}\cdot\nabla V_\theta)dL \tag{12}$$

$$-\left[\int_{A^{(e)}}\int N_i\frac{\partial \hat{\nu}_t}{\partial r}\frac{\partial N_j}{\partial z}rdA\right]V_{r,j}+\left[\int_{A^{(e)}}\int\left\{\hat{\nu}_{\text{eff}}\left(\frac{\partial N_i}{\partial r}\frac{\partial N_j}{\partial r}+\frac{\partial N_i}{\partial z}\frac{\partial N_j}{\partial z}\right)+W_i\left(\hat{V}_r\frac{\partial N_j}{\partial r}+\hat{V}_z\frac{\partial N_j}{\partial z}\right)+N_i\frac{\partial \hat{\nu}_t}{\partial z}\frac{\partial N_j}{\partial z}\right\}rdA\right]V_{z,j}$$
$$+\left[\int_{A^{(e)}}\int\frac{1}{\rho}N_i\frac{\partial M_k}{\partial r}rdA\right]p_k=\oint_{L^{(e)}}\nu_{\text{eff}}rN_i(\vec{n}\cdot\nabla V_z)dL \tag{13}$$

$$\left[\int_{A^{(e)}}\int\left(M_k\frac{\partial N_j}{\partial r}+\frac{1}{r}M_kN_j\right)rdA\right]V_{r,j}+\left[\int_{A^{(e)}}\int M_k\frac{\partial N_j}{\partial z}rdA\right]V_{z,j}=0 \tag{14}$$

In these equations, the subscripts "$i$" and "$j$" vary from 1 to 9, while "$k$" varies from 1 to 4. Also the symbol $\hat{(\ )}$ in these equations signifies a value that is known from a previous iteration or an initial guess. The global set of equations is achieved by assembling Eqs. (11) through (14) among all elements, for the current iterative step, and the result is a system of linear algebraic equations in the flow nodal variables.

## Results and Discussion

Two secondary-flow passage configurations, corresponding to the same impeller geometry and operating conditions, were chosen for comparison. These are shown in Fig. 4, and feature a conventional wear-ring and a face seal as part of the secondary passage. The pump, which was the focus of rotordynamic testing by Sulzer Bros. (Bolleter et al., 1989), has the

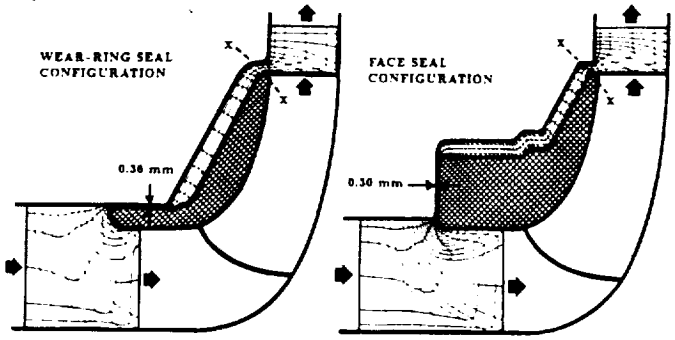


Fig. 4 Sulzer Bros.' wear ring and face-seal pump configurations (Bolleter et al., 1989)

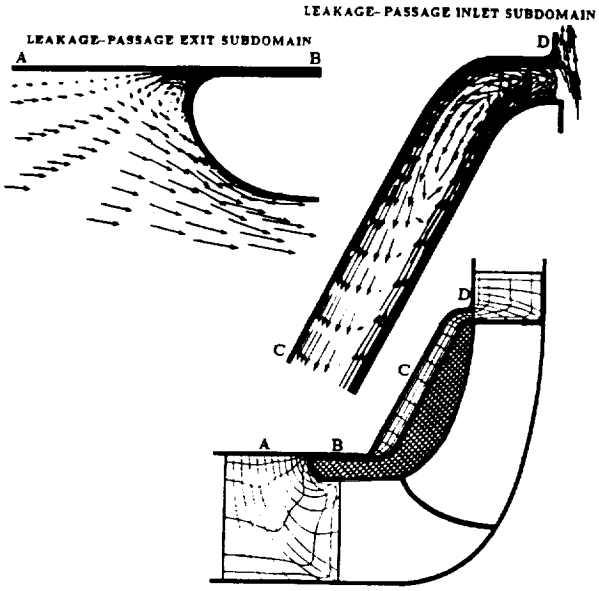


Fig. 5 Meridional velocity vector plot for the wear ring-seal pump configuration

following characteristics and design-point operating conditions.

Impeller tip radius = 17.5 cm
Impeller speed = 2000 rpm
Working medium is water at 30°C
Volumetric flow rate = 130 l/s
Total head = 68 m
Reynolds' number (based on the tip speed and radius) = $8.02 \times 10^6$

In creating the finite-element models in Fig. 4, a total of thirteen computational nodes were placed on each cross-flow grid line in the seal region. These nodes were closely spaced near the walls in anticipation of large velocity gradients there. In an early numerical experimentation phase of the study, this finite-element grid was proven to provide a good flow resolution and rule out any significant grid dependency of the computed flow field.

Figure 5 shows a plot of the computed meridional velocity component for the conventional wear-ring seal configuration. This component, together with the corresponding swirl velocity and static pressure (Figs. 6 and 7) constitute the flow solution corresponding to the current model. Examination of Fig. 5 reveals that the shroud-to-housing flow is experiencing a pronounced recirculatory motion in the secondary-passage segment leading to the wear-ring seal. This is a result of the tendency of the fluid particles adjacent to the shroud to migrate radially outwards due to the centrifugal force caused by the shroud rotation, on one hand, and the tendency of those particles near the housing to proceed radially inwards as a result of the static pressure differential across the passage, on the other.

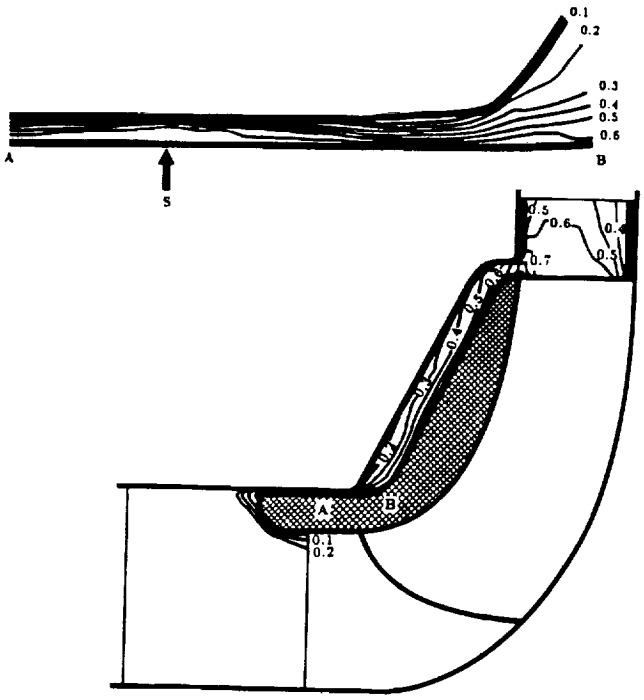


Fig. 6 Contour plot of the nondimensional swirl velocity for the wear ring-seal pump configuration

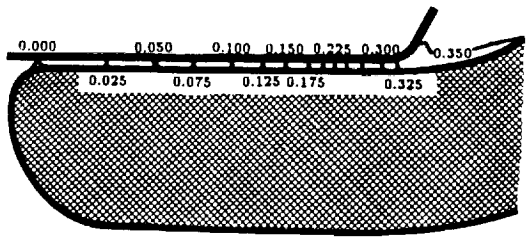


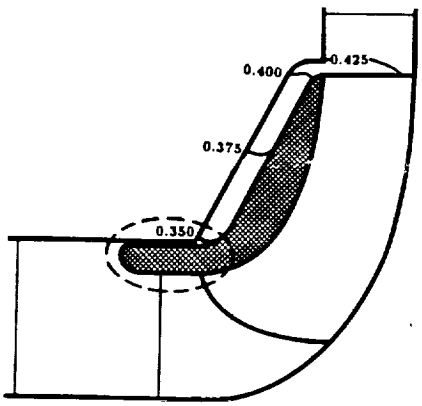


Fig. 7 Contour plot of the nondimensional static pressure for the wear ring-seal pump configuration

Contours of the swirl velocity component and static pressure associated with the secondary flow field are shown in Figs. 6 and 7, respectively. The swirl velocity values in Fig. 6 are nondimensionalized using the impeller tip speed $U_t$, and the nondimensional pressure ($\bar{p}$) in Fig. 7 is defined as follows:

$$\bar{p} = \frac{(p - p_i)}{\rho U_t^2}$$

with $p$ and $p_i$ referring to the local and stage-inlet pressures,

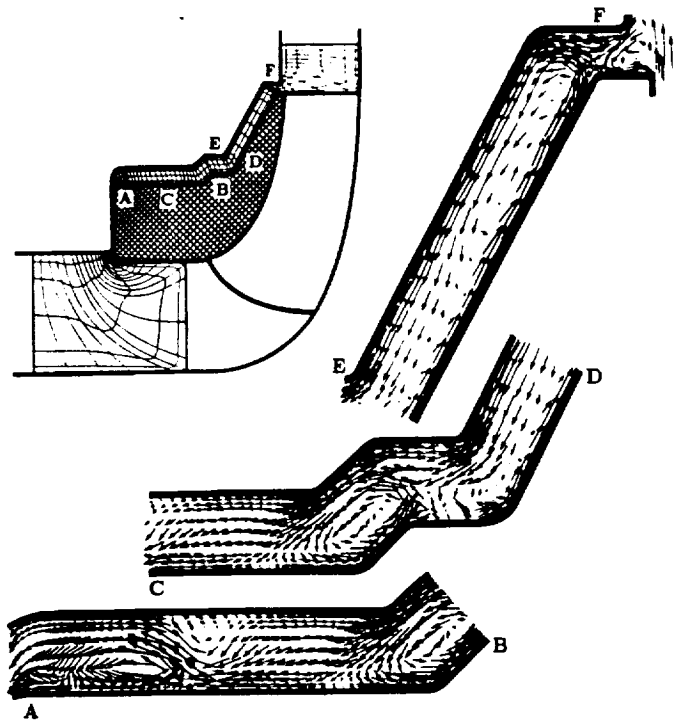


Fig. 8 Meridional velocity plot for the face-seal pump configuration

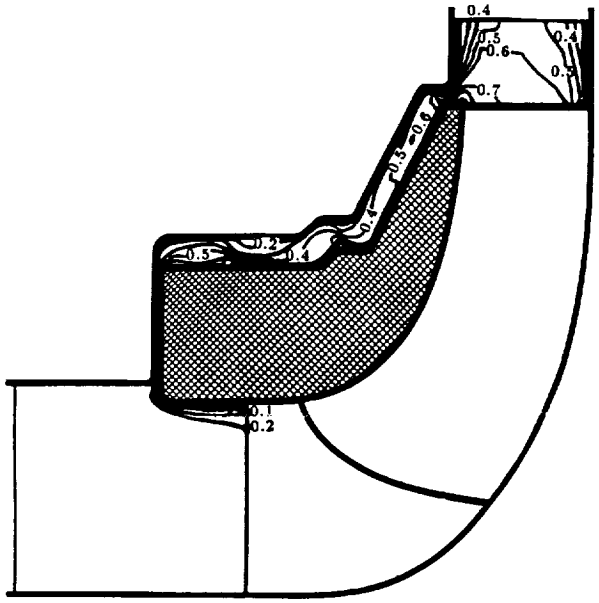


Fig. 9 Contour plot of the nondimensional swirl velocity for the face-seal pump configuration

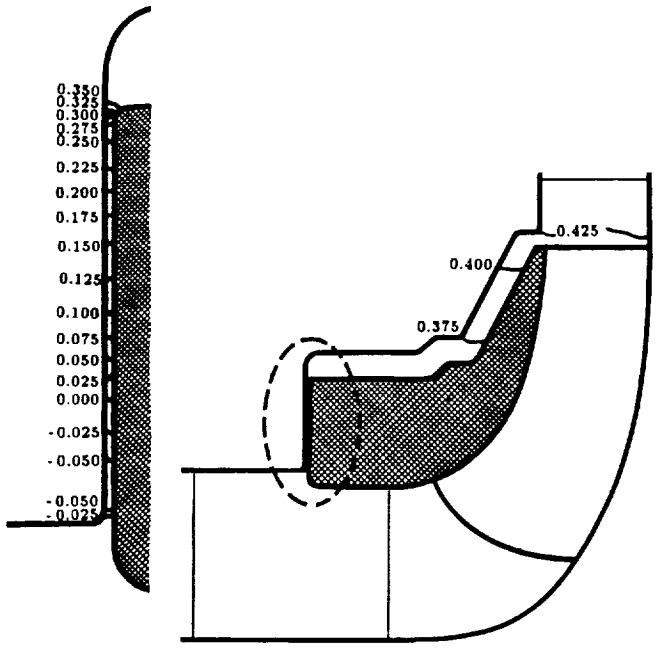


Fig. 10 Contour plot of the nondimensional static pressure for the face-seal pump configuration

respectively. Also shown in Fig. 7 is a magnified view of the wear-ring seal where the major part of the pressure differential, across the leakage passage, takes place.

The meridional and swirl velocity components, along with the static pressure obtained for the face-seal pump configurations are shown in Figs. 8 through 10. Again, the meridional velocity vectors, in Fig. 8, indicate a strong recirculatory motion in virtually all segments of the secondary passage. Reasoning of this flow behavior was discussed earlier. However, a unique, and perhaps peculiar, flow structure is seen to exist in the horizontal segment of the leakage passage in Fig. 8, where radial shifting of the flow trajectories and vortex breakdown takes place. It is apparent, however, that the magnitude of the pressure gradient in this low-radius region exceeds that of the centrifugal force. This seems to weaken the flow recirculation in this leakage-passage segment, confining it to the shroud side of the leakage passage.

There is a rather modest amount of experimental data to validate the computed flow field in Figs. 5 through 10. First, it was indicated by Sulzer Bros. that the average swirl velocity component at the leakage-passage inlet station was measured, for the face-seal pump configuration under the above-mentioned operating conditions, to be approximately 0.5 of the impeller tip speed (Childs, 1989). With the current finite-element model, the average value of this velocity component was computed to be 0.526 of the tip speed. Note that the shroud-to-housing swirl velocity profile, which gave rise to this average value, is not specified a priori, but is rather part of the finite-element flow solution (Fig. 9). This advantage, as indicated earlier, is a result of including primary flow segments in the computational domain definition (Fig. 4). Further experimental observations which are consistent with the computed flow field in this study concern the recirculatory pattern of the meridional flow (Fig. 8), and were qualitatively reported by Guelich et al. (1989).

Rigorous verification of the seal friction resistance was not quite attainable. This was particularly the case for the face-seal configuration, which is rather an uncommon seal type. Indeed the only "vaguely" similar problem in literature is that of a rotating disk in a stationary chamber (e.g., Daily and Nece, 1960) or in open space (e.g., Uzkan and Lipstein, 1986). Such studies were focused on the pumping of secondary, often cooling, flow over the face of what is typically a bladed-rotor disk between the shaft and the disk tip radius. The flow direction in this case would naturally be radially outwards, in contrast to that of the face seal flow (Fig. 4), which is predominantly driven by a strong inward pressure decline. Validation of the wear-ring seal results, on the other hand, may appear possible in light of such experimental correlations as those of Yamada (1962). The fact, however, is that Yamada's study did not account for the seal-inlet preswirl velocity which, by reference to Fig. 6, is hardly confined to a thin layer adjacent to the rotor, nor did the study address the complex flow pattern at the end of the shroud-to-housing gap leading to the seal segment (Fig. 4). In fact, the combination of these two real

flow effects lead to an early, but localized, flow separation over the shroud surface at the point marked "S" in Fig. 6, a situation that was not encountered in Yamada's study, where only simple isolated annular seals were tested.

Fortunately, the authors were recently able to validate the current computational model, including the turbulence closure, for a straight annular seal using Yamada's experimental data (Baskharone and Hensel, 1991). The seal under consideration had a clearance/length ratio of 0.034, and a Reynolds' number (based on the clearance width and inlet through-flow velocity) of 13,280. The computed seal resistance for this seal was reported to be in excellent agreement with Yamada's experimental data. Furthermore, the agreement between the computed profiles of through-flow and tangential velocity components and those of Morrison et al. (1988) was equally favorable.

Performance assessment of the two secondary-flow passages (Fig. 4), in light of the numerical results, involves their effectiveness as leakage suppressants and swirl dissipators. In order to determine the leakage control capacity of each passage, the mass flux was integrated at the passage inlet station. The results indicated that the leakage-flow rates in the wear-ring and face-seal pump configurations were 0.0011 and 0.0038 $m^3/s$, respectively. These represent 0.85 and 2.92 percent of the primary flow rate, and illustrate the relative superiority of the wear-ring seal configuration, as a leakage-control device over the face-seal alternative. This, in part, is due to the highly favorable streamwise pressure gradient across the face seal as a result of the substantial radius diminishment, between the seal inlet and exit station, which lessens the boundary layer build-up over the solid walls and eliminates the likelihood of any flow separation. On the other hand, the tendency of the fluid particles to migrate radially outwards near the constant-radius shroud surface, in the case of the wear-ring seal, added to the complex flow structure in the passage leading to the seal, create an environment for an early flow separation over the shroud surface (location "S" in Fig. 6). Despite the rapid flow reattachment, in this case, the recirculation region, following the separation point, has the effect of enhancing the seal frictional resistance and, therefore, the sealing effectiveness of the wear-ring seal configuration by comparison. Another contributing factor behind the wear-ring effectiveness, as a leakage-control device, is the existence of a substantial recirculation zone at the seal-exit station (Fig. 5), with practically no comparable seal-exit flow behavior in the case of the face-seal configuration (Fig. 8). As for the swirl velocity dissipation across the secondary passage, examination of Figs. 6 and 9 reveals that the "kink" in the secondary passage of the face-seal pump configuration (Fig. 9), is causing a sudden and measurable reduction in the swirl velocity in the axial passage segment, with no equivalent swirl velocity reduction mechanism in the wear-ring seal pump configuration. More importantly, the average swirl velocity component at the secondary passage inlet station (designated x-x in Fig. 4) was found to be as low as 0.526 of the impeller tip speed for the face-seal pump configuration, as opposed to 0.812 for its counterpart. Worth noting is the fact that the choice of station x-x in Fig. 4 is consistent with that of Childs (1989), as a meaningful parameter in interpreting the rotordynamic behavior of the same pump configurations in Fig. 4. Although these swirl characteristics of the face-seal pump configuration are not quantitatively convertible into a rotordynamic stability-related factor, it is established (Childs et al., 1991) that swirl suppression at the secondary passage inlet station is among the most effective tools for shrouded-impeller rotordynamic stability enhancement. This, in view of the current results, would imply that the face-seal pump configuration provides a less destabilizing effect. The conclusion here is consistent with the experimental findings of Bolleter et al. (1989), who reported comparable direct-damping coefficients for the fluid/shroud interaction system, but a significantly lower cross-coupled stiffness coefficient for the face-seal pump configuration. Since unstable operation of the impeller (in the form of a whirling motion) is triggered by low direct damping and/or high cross-coupled stiffness, the experimental measurements suggest that the face-seal pump configuration results in a more stable impeller operation, which is what the numerical results seem to imply.

## Concluding Remarks

The finite-element model of the pump secondary flow in this paper is a versatile tool for predicting the leakage-suppression and rotordynamic-stability characteristics of viable secondary-passage designs. The model accuracy stems from the manner in which the computational domain is defined to permit the typically strong primary/secondary flow interaction. Simulation of the flow turbulence and recognition of the inertia domination in formulating the problem makes the model applicable to a wide range of real-life operating conditions. The model was applied to two representative configurations of seal-containing secondary passages in an existing centrifugal pump stage for code verification and seal-performance assessment purposes. The results are consistent with experimental measurements concerning the same pump, and documented observations in similar secondary-passage configurations. The computed flow field in the current study constitutes the so-called "zeroth-order" flow solution in existing perturbation models of the fluid-induced vibration of shrouded pump impellers. This explains the desire for an accurate flow field in the secondary passage, since the output of such perturbation models would naturally be a strong function of the flow behavior prior to the impeller excitation.

## Acknowledgment

This study was funded by NASA-Marshall Space Flight Center (Huntsville, AL), contract no. NAS8-37821, technical monitor: James Cannon. Partial funding was also provided by the Texas A&M Turbomachinery Research Consortium.

## References

Baldwin, B. S., and Lomax, H., 1978, "Thin Layer Approximation and Algebraic Model for Separated Turbulent Flows," AIAA Paper No. 78-257.

Baskharone, E. A., and Hensel, S. J., 1989, "A New Model for Leakage Prediction in Shrouded-Impeller Turbopumps," ASME JOURNAL OF FLUIDS ENGINEERING, Vol. 111, pp. 118–123.

Baskharone, E. A., and Hensel, S. J., 1991, "A Finite-Element Perturbation Approach to Fluid/Rotor Interaction in Turbomachinery Elements. Part 1: Theory," ASME JOURNAL OF FLUIDS ENGINEERING, Vol. 113, No. 3, pp. 353–361.

Baskharone, E. A., and Hensel, S. J., 1991, "A Finite-Element Perturbation Approach to Fluid/Rotor Interaction in Turbomachinery Elements. Part 2: Application," ASME JOURNAL OF FLUIDS ENGINEERING, Vol. 113, No. 3, pp. 362–367.

Benim, A. C., and Zinser, W., 1985, "Investigation into the Finite Element Analysis of Confined Turbulent Flows Using a $k-\epsilon$ Model of Turbulence," *Computer Methods in Applied Mechanics and Engineering*, Vol. 51, pp. 507–523.

Bolleter, U., Leibundgut, E., and Sturchler, R., 1989, "Hydraulic Interaction and Excitation Forces of High Head Pump Impellers," Presented at the Third Joint ASCE/ASME Mechanics Conference, University of California, La Jolla, CA.

Carey, G. F., and Oden, J. T., 1986, "Finite Elements: Fluids Mechanics," *The Texas Finite Element Series*, Vol. IV, Prentice-Hall.

Childs, D. W., 1989, "Fluid-Structure Interaction Forces at Pump-Impeller-Shroud Surfaces for Rotordynamic Calculations," SSME *Journal of Vibration, Stress and Reliability in Design*, Vol. 111, pp. 216–225.

Childs, D. W., Baskharone, E., and Ramsey, C., 1991, "Test Results for Rotordynamic Coefficients of the SSME HPOTP Turbine Interstage Seal With Two Swirl Brakes," ASME *Journal of Tribology*, Vol. 113, No. 3.

Childs, D., and Elrod, D., 1988, "Annular Honeycomb Seals: Test Results for Leakage and Rotordynamic Coefficients, Comparisons to Labyrinth and

Smooth Configurations," NASA Conference Publication 3026, Rotordynamic Instability Problems in High-Performance Turbomachinery, pp. 143-159.

Daily, W., and Nece, R. E., 1960, "Chamber Dimension Effects on Induced Flow and Frictional Resistance of Enclosed Rotating Disks," ASME *Journal of Basic Engineering*, Vol. 82, No. 1, pp. 217-231.

Guelich, J., Florjancic, D., and Pace, S. E., 1989, "Influence of Flow Between Impeller and Casing on Part-Load Performance of Centrifugal Pumps," *Rotating Machinery Dynamics*, ASME Publication DE-Vol. 2, pp. 227-235.

Heinrich, J. C., and Zienkiewicz, O. C., 1977, "Quadratic Finite Element Schemes for Two-Dimensional Convective-Transport Problems," *Int. J. Num. Meth. Eng.*, Vol. 11, pp. 1831-1844.

Hood, P., and Taylor, C., 1974, "Navier-Stokes Equations Using Mixed Interpolation," *Proceedings of the International Symposium on Finite Element Methods in Flow Problems*, University of Wales, Swansea, United Kingdom.

Hughes, T. J. R., 1978, "A Simple Scheme for Developing 'Upwind' Finite Elements," *Int. J. Num. Meth. Engg.*, Vol. 12, pp. 1359-1365.

Morrison, G. L., Johnson, M. C., and Tatterson, G. B., 1988, "3-D Laser Anemometer Measurements in an Annular Seal," ASME Paper No. 88-GT-64.

Ohashi, H., Sakurai, A., and Nishima, J., 1988, "Influence of Impeller and Diffuser Geometries on the Lateral Fluid Forces of Whirling Centrifugal Impeller," NASA CP-3026, pp. 285-306.

Uzkan, T., and Lipstein, N. J., 1986, "Effects of Honeycomb Shaped Walls on the Flow Regime Between a Rotating Disk and a Stationary Wall," ASME Paper No. 86-GT-161.

Yamada, Y., 1962, "Resistance of Flow Through an Annulus with an Inner Rotating Surface," *Bulletin of JSME*, Vol. 5, pp. 302-310.

Zienkiewicz, O. C., 1971, *The Finite Element Method in Engineering Science*, McGraw-Hill, New York, NY.

# APPENDIX 2

## PAPERS CURRENTLY UNDER REVIEW

PAPER# 1

A Paper Entitled:

# Rotordynamic Effects of the Shroud–to–Housing Leakage Flow in Centrifugal Pumps

(currently under review for publication in the ASME J. of Fluids Engineering)

# Rotordynamic Effects of the Shroud–to–Housing Leakage Flow in Centrifugal Pumps [1]

**E.A. Baskharone [2] , A.S. Daniel [3] and S.J. Hensel [4]**

Department of Mechanical Engineering
Texas A&M University
College Station, Texas 77843

The fluid/shroud interaction forces acting on a pump impeller that is precessing around the housing centerline, are computed and the rotordynamic coefficients deduced. The numerical procedure utilized is an upgraded version of a finite–element–based perturbation model, initially devised for simple see–through annular seals. The computational model accounts for the complex flow structure in the shroud–to–housing secondary flow passage, which includes a tight–clearance face seal. The model also facilitates the mutual interaction between the primary and secondary flows near the impeller inlet and discharge stations. The numerical results are compared to existing experimental data, as well as the results of a simpler and widely used numerical model. Sources of discrepancies between the numerical results are identified, and a comprehensive assessment made in light of the experimental data.

1 This research was funded by NASA–Marshall Space Flight Center, Huntsville, Alabama, Contract No. NAS8–37821 (technical monitor: James Cannon), and the Texas A&M Turbomachinery Research Consortium.

2 Associate Professor, Mem. ASME.

3 Graduate Research Assistant.

4 Graduate Research Assistant, currently with Westinghouse Savannah River Laboratory, Aiken, South Carolina, Mem. ASME.

## Introduction

Frequent mechanical failure of turbomachinery rotating components, due to fluid–induced vibration, has been reported over the past two decades. The most common instability mechanism in this case is one where the impeller whirls around the housing centerline at a subsynchronous whirl frequency (e.g. Childs and Moyer, 1985). Serious efforts are now being devoted to the development of reliable predective tools for capturing the dynamics of fluid–encompassed rotors and testing ways to enhance the fluid restoring forces.

Rotordynamic forces on shrouded pump impellers have particularly been the subject of an increasing number of experimental and numerical investigations. Of the experimental studies, those by Bolleter et al. (1989) and Guinzburg (1992) are perhaps the most comprehensive. In both cases, the fluid–exerted forces were reported to have a more or less parabolic dependency on the impeller whirl frequency. This dependency was approximated with a least–square fit to obtain the direct and cross–coupled stiffness, damping and inertia coefficients of the fluid/shroud system.

Perhaps the simplest, and most popular, numerical tool in this area is the bulk–flow model devised by Childs (1983). This model was later upgraded (Childs, 1989) and used to compute the rotordynamic coefficients of two leakage–passage configurations, both corresponding to the same impeller geometry and operating conditions. Results of this study were compared to the experimental data by Bolleter et al. (1989). More detailed models of the fluid/rotor interaction problem have also been reported by Tam et al. (1988) as well as Dietzen and Nordmann (1988). However, attention in these two studies was focused on simple annular seals and journal bearings.

The current study is the first such attempt, known to the authors, where a full–scale unsplit secondary passage of a pump stage is under investigation within a framework which tolerates such real flow effects as separation and recirculation. The study is an extension of the model previously

published by Baskharone and Hensel (1991a) for a simple untapered annular seal. The idea of utilizing segments of the primary flow passage in defining the computational domain (Fig. 1) was first outlined (also by Baskharone and Hensel, 1989) as a means of facilitating the primary/secondary flow interaction effects. However, the published analysis, then, merely presented the idea, but treated the secondary flow as strictly laminar and, as a result, had no appreciable engineering value. The current study is, therefore, one which expands previously devised ideas, by the authors, and applies the outcome to a traditionally complex problem for which an equally detailed solution is simply non-existing.

## Analysis

Fig. 1 shows a schematic of a hydraulic pump stage, with a face seal as a leakage-control device. Shown on the same Figure is the computational domain for solving the centered-rotor (zeroth-order) flow-governing equations. In addition to the secondary shroud-to-housing flow passage, the selected domain also includes two primary-flow segments, which are naturally connected to the secondary passage near the impeller inlet and discharge stations. The objective here is to alleviate the need for specifying, assuming, or iteratively obtaining the secondary-passage inlet flow conditions. Of these common choices, Childs, for instance, has reportedly utilized the iterative approach, whereby the secondary passage was isolated, and the flow solution iteratively obtained under the condition that the streamwise pressure differential, across the passage, is identical to that across the impeller (Childs, 1989). Such approach is understandably appropriate, considering that the secondary flow in this case is treated as one layer with no cross-flow gradients taken into account. However, this and any other equivalent simplifications would fall between insufficient and inadequate in the current detailed flow model where inlet and exit velocity profiles will also have to be prescribed, should the passage be isolated. Contouring the computational domain in the manner seen in Fig. 1 has the effect of converting the the secondary passage inlet and exit flow conditions

into internal variables to be part of the numerical solution. Note that the passage inlet and exit swirl profiles, which have a predominant effect on the impeller stability, are included among these variables.

Fig. 2 shows the finite-element discretization model which was created for the centered-rotor operation mode. The model is composed of non-overlapping nine-noded bi-quadratic elements of the Lagrangian type (Zienkiewich, 1971). These elements are generally curve-sided, a feature which had a highly favorable effect in matching the domain boundaries. Intensity of the finite elements are, by reference to Fig. 2, much higher in regions where pronounced gradients of the flow thermophysical properties are anticipated.

**Flow-governing Equations.** In order to eliminate the flow field time-dependency, that is imparted by the impeller whirling motion (Fig. 3), the flow conservation laws are cast in a frame of reference that is attached to the rotor, being the impeller-shroud assembly, and whirls with it. The time-avaraged flow equations, now expressed in terms of relative velocity components, include such terms as the Coriolis and centripetal acceleration components. These equations, as well as their finite-element equivalent, were previously published by Baskharone and Hensel (1991b). The published model also contained a modified version of Baldwin and Lomax turbulence closure (1978).

**Boundary Conditions.** Referring to the flow-permeable boundary segments in Fig. 1, the boundary conditions over these segments are as follows:

*i*) Stage Inlet Station: This is the boundary segment a-b in Fig. 1, which is located sufficiently far upstream from the impeller. Fully developed flow is assumed at this location, giving rise to the following boundary condition:

$$\frac{\partial V_r}{\partial z} = \frac{\partial V_\theta}{\partial z} = \frac{\partial V_z}{\partial z} = 0$$

In addition, the stage–inlet static pressure is specified at the node midway between the endwalls on this station.

*ii*) Impeller Inlet and Exit Stations: These are labled c–d and e–f in Fig. 1. Fixed profiles of the velocity components, corresponding to the stage operating conditions, are imposed over these boundary segments. Note that the operating conditions here involve the primary impeller passage, and do not include the secondary mass flow rate.

*iii*) Stage Exit Station: The flow behavior at this station (designated g–h in Fig. 1) is viewed as predominantly confined to satisfying the mass and angular momentum conservation equations in a global sense. In their derivative forms, These can be expressed as follows:

$$\frac{\partial V_r}{\partial r} = -\frac{V_r}{r} \quad and \quad \frac{\partial V_\theta}{\partial r} = -\frac{V_\theta}{r}$$

These two boundary conditions are linear and are, therefore, introduced non–iteratively in the numerical solution process. Moreover, a zero normal derivative of $V_z$ is imposed over this station, and the stage–exit static pressure is specified at the computational node midway between the endwalls on this station.

As for the solid boundary segments in Fig. 1, namely those of the housing and shroud as well as the hub surface segment b–d, the no–slip boundary condition applies as follows:

$$V_r = 0, \quad V_z = 0 \quad and \quad V_\theta = C$$

where C is equal to $(\Omega r)$ and zero for rotating and non–rotating boundary segments, respectively.

**Perturbation Model.** As the impeller enters the whirling motion depicted in Fig. 3, the flow properties including, in particular, the shroud pressure distribution, assume non–axisymmetric

patterns. The current perturbation model perceives such deviation, from that of the centered-impeller, as the result of infinitesimally small distortions in the finite-element grid due to the eccentricity "$\epsilon$" of the impeller axis of rotation (Fig. 3). Expansion of the flow-governing equations, in their finite-element form, as functions of "$\epsilon$" is then carried out and, in the end, gives rise to the differential changes of the flow variables. Of these differential changes, those associated with the shroud pressure distribution are then isolated and integrated over the entire shroud surface. The result, in this case, is the rate, with respect to $\epsilon$ at which the fluid reaction forces (restoring or aggravating) are exerted on the shroud. The fluid/shroud interaction forces are then analyzed at various whirl frequencies to determine the stiffness, damping and inertia coefficients with which the fluid contributes to the shroud whirling motion.

Aside from the different geometry and boundary conditions in the current study, the perturbation model just described is virtually identical to that by Baskharone and Hensel (1991) where the much simpler case of a straight annular seal was analyzed. Note that both of virtual eccentricity "$\epsilon$" and the whirl frequency "$\Omega$", do affect the differential changes in boundary conditions in the process of expanding the finite-element equations.

**Results and Discussion**

A typical pump stage, designed and tested by Sulzer Bros. Inc. (Switzerland), was chosen for the current study. This is schematically shown in Fig. 1, and has been previously selected for rotordynamic analysis by Childs (1989). The stage dimensions and operating conditions were reported by Bolleter et al. (1989) as follows:

Impeller tip radius = 17.5 cm

Impeller speed = 2000 rpm

Working medium is water at $30°C$

Volumetric flow rate = 130 $l/s$

Total head = 68 m Reynolds' number (based on the tip speed and radius) = $8.02 \times 10^6$

Figures 4, 5 and 6 present the most significant features of the centered–impeller flow structure in the secondary passage. The complexity of this flow field is most apparent in Fig. 4, which is a vector plot of the meridional velocity component in the shroud–to–housing passage. The flow pattern in this Figure is characterized by massive separation and recirculation zones in virtually all segments of the passage. This characteristic is the result of the flow tendency to migrate radially outwards near the "spinning" shroud (due to the locally high centrifugal force and the flow viscosity), which is opposed by the tendency to proceed radially inwards near the housing (due to the static pressure differential across the flow passage). Such flow behavior is generally consistent with experimental observation (e.g. Guelich et al., 1987), but was never part of a rotordynamic analysis to the authors' best knowledge. Equally important are the swirl velocity profiles in Figs. 5 and 6 at the leakage–passage and the seal flow inlet stations (Figs. 5 and 6, respectively). This is due to the well–established fact that the flow swirl in the leakage passage acts as a major destabilizing factor. Examination of the cross-flow swirl velocity distributions in Figs. 5 and 6 reveals significantly large boundary layer thicknesses at the solid walls, with a rather narrow "core flow" region as the flow passage contracts just upstream of the face seal (Fig. 6). The relatively small value of the swirl velocity in Fig. 6 is a natural outcome of the "no–slip" condition which prevails at the shroud surface which is relatively small at this radial location by comparison.

Prior to the full–scale execution of our perturbation model, a grid–dependency study was conducted. The independent variable here was the number of computational planes in the circumferential direction (Fig. 3), whereby the fluid–exerted forces at an arbitrarily fixed whirl–frequency ratio ($\Omega/\omega$) of 0.3, were monitored. Results of this numerical experimentation phase are shown in

Fig. 7 in the form of tangential and radial components of the net shroud force. The Figure clearly shows that the force trends begin to level out for a circumferential plane count of 9. As a result, the impeller rotordynamic analysis was conducted in its entirety using this value in a compromise between the precision of the numerical results, on one hand, and the consumption of computational resources, on the other.

Results of the perturbation analysis, as fluid–exerted forces on the shroud, are shown in Fig. 8 for a range of whirl frequency ratio ($\Omega/\omega$) between -1.25 and +1.25. The fluid–exerted forces in this Figure, as well as Fig. 8, are non–dimensionalized in the same manner proposed by Bolleter et al. (1989), namely:

$$\bar{F}_r = \frac{\frac{\partial F_r}{\partial \epsilon}}{\pi {r_t}^2 \rho b_t \omega^2}$$

$$\bar{F}_t = \frac{\frac{\partial F_t}{\partial \epsilon}}{\pi {r_t}^2 \rho b_t \omega^2}$$

where $\epsilon$ is the orbit radius of the impeller axis (Fig. 3), $r_t$ is the impeller tip radius, $b_t$ is the impeller–tip endwall spacing, $\rho$ is the fluid density, and $\omega$ is the running speed. Reproduced on the same Figure are the experimental measurements of Bolleter et al. (1989), and the forces computed by Childs (1989) using a bulk–flow perturbation model. Of these, Childs' results are shown for pre–imposed inlet swirl values of 0.5 and 0.6 of the impeller tip speed. The reader is reminded that this ratio, in the current computational procedure, is treated as unknown to be produced in the solution of the zeroth–order flow field, and that our computed average value is, by reference to Fig. 6, 0.526 of the impeller tip speed. As seen in Fig. 8, the bulk–flow model produces rather sharp force fluctuations, initially thought of a resonance–like, for the elevated inlet swirl ratio of 0.6, within a narrow range of whirl–frequency ratio of 0.3. These fluctuations are neither confirmed by

the current results or the experimental data. The fact that such drastic change in the force trends corresponds to modest changes in the inlet swirl ratio, by comparison to the smooth flow trends obtained for a swirl ratio of 0.5 (Fig. 8), was equally surprising. However, the point should be made that the seal–inlet swirl velocity in Childs' study was significantly higher than (roughly double) the computed value in the current study (Fig. 6). Knowing that the seal–inlet swirl velocity deviation, between the two numerical studies, grows even wider as the leakage–passage inlet swirl velocity is elevated, it would perhaps be natural to expect the type of disagreement between the two sets of results in Fig. 8.

Next, the direct and cross–coupled stiffness, damping and inertia (added mass) coefficients of the fluid/shroud interaction were computed. The computational procedure here is essentially equivalent to that previously outlined by Baskharone and Hensel (1991a) for an annular seal problem. The calculated rotordynamic coefficients are shown in Table 1 versus the experimental results of Bolleter et al. (1989) and the numerical results of the bulk–flow model (Childs, 1989). Of these the results by Childs correspond to an externally–prescribed leakage–passage inlet swirl ratio of 0.5 which, by reference to Fig. 8, gives rise to smooth trends of the fluid reaction force components. Referring to Table 1, it seems that the bulk–flow model significantly underestimates the direct stiffness and cross–coupled inertia coefficients, particularly the latter. Otherwise, the rotordynamic coefficients produced by the two perturbation analyses appear to be of comparable magnitudes.

In appraising the current numerical results in Table 1, the fact should be emphasized that a significantly better agreement with the experimental data was not initially anticipated. Despite our success in facilitating (to a reasonable extent) the primary/secondary flow interaction within the pump stage (Fig. 1), it is the intolerance of our perturbation model to the force contributions of the impeller primary flow which led to such modest expectations in the first place. Nevertheless, the fact remains that our finite–element–based perturbation model, including the relatively rigorous

| | CURRENT PERTURBATION MODEL | SULZER BROS. EXP. DATA (Bolleter et al. 1989) | BULK-FLOW MODEL (Childs, 1989) INLET SWIRL RATIO = 0.5 |
|---|---|---|---|
| K (MN/m) | -0.268 | -0.500 | -0.042 |
| k (MN/m) | 0.165 | 0.600 | 0.288 |
| C (Ns/m) | 1640.8 | 2570 | 2020 |
| c (Ns/m) | 2916.3 | 7610 | 2290 |
| M (kg) | 5.034 | 29.6 | 8.96 |
| m (kg) | 3.035 | 10.800 | -0.009 |

Table 1 Comparison of the impeller rotordynamic coefficients with experimental and numerical data

flow analysis on which it is founded, is by no means less accurate than any existing perturbation model known to the authors.

## Concluding Remarks

A perturbation model, originally devised for simple annular seals, has been upgraded and applied to the problem of fluid/shroud interaction in a typical pump stage. The computed rotordynamic coefficients are compared to existing experimental and numerical data. The current results seem closer to the experimental values for those coefficients where a substantial disagreement, with the existing numerical data, occurs. A primary source of discrapencies between the newly–computed sets of rotordynamic parameters and their numerical counterparts (Childs, 1989) was identified to be the seal–inlet swirl velocity magnitude. In the current analysis, this key variable is part of the zeroth–order (centered–impeller) flow solution and, as such, is a function of not only the pump operating conditions but also the manner in which the leakage passage is naturally connected to the seal segment of the secondary passage. The authors believe that the value of the current perturbation model would be enhanced by integrating the impeller primary flow passage into the computational domain. Such upgrade, which is major in nature, is currently under consideration.

## Acknowledgment

This study was funded by NASA–Marshall Space Flight Center (Huntsville, Alabama), contract no. NAS8–37821, technical monitor: James Cannon. The study was also sponsored by the Texas A&M Turbomachinery Research Consortium.

## References

Baldwin, B.S. and Lomax, H., 1978, "Thin Layer Approximation and Algebraic Model for Separated Turbulent Flows", AIAA Paper No. 78-257.

Baskharone, E.A. and Hensel, S.J., 1989, "A New Model for Leakage Prediction in Shrouded–Impeller Turbopumps," ASME J. of Fluids Engineering, Vol. 111, pp. 118–123.

Baskharone, E.A. and Hensel, S.J. , 1991a, "A Finite–Element Perturbation Approach to Fluid/Rotor Interaction in Turbomachinery Elements. Part 1: Theory," ASME J. of Fluids Engineering, Vol. 113, No. 3, pp. 353–361.

Baskharone, E.A. and Hensel, S.J. , 1991b, "A Finite–Element Perturbation Approach to Fluid/Rotor Interaction in Turbomachinery Elements. Part 1: Application," ASME J. of Fluids Engineering, Vol. 113, No. 3, pp. 362–367.

Bolleter, U., Leibundgut, E. and Sturchler, R., 1989, "Hydraulic Interaction and Excitation Forces of High Head Pump Impellers," presented at the Third Joint ASCE/ASME Mechanics Conference, University of California, La Jolla, California.

Childs, D.W., 1983, "Finite Length Solutions for Rotordynamic Coefficients of Turbulent Annular Seals," ASME J. of Lubrication Technology, Vol. 105, pp. 437–445.

Childs, D.W. and Moyer, D., 1985, "Vibration Characteristics of the High Pressure Oxygen Turbopump of the Space Shuttle Main Engine," ASME J. of Engineering for Gas Turbine and Power, Vol. 107, pp. 152–159.

Childs, D.W., 1989, "Fluid–Structure Interaction Forces at Pump–Impeller–Shroud Surfaces for Rotordynamic Calculations," ASME J. of Vibration, Stress and Reliability in Design, Vol. 111, pp. 216–225.

Dietzen, F.J. and Nordmann, R., 1988, "Calculating Rotordynamic Coefficients of Seals by Finite Difference Techniques," ASME J. of Tribology, Vol. 109, pp. 388–394.

Guelich, J., Florjancic, D. and Pace, S.E., 1989, "Influence of Flow Between Impeller and Casing on Part–Load Performance of Centrifugal Pumps," Rotating Machinery Dynamics, ASME Publication DE–Vol.2, pp.

Guinzburg, A., 1992, "Rotordynamic Forces Generated by Discharge-to-Suction Leakage Flows in Centrifugal Pumps," Ph.D. Dissertation, California Institute of Technology, Pasadena, California.

Tam, L.T., Prezkwas, A.J., Muszynska, A., Hendricks, R.C., Braun, M.J. and Mullen, R.L., 1988, "Numerical and Analytical Study of Fluid Dynamic Forces in Seals and Bearings," ASME J. of Vibration, Acoustics, Stress, and Reliability in Design, Vol. 110, pp. 315-325.

Zienkiewicz, O.C., 1971, "The Finite Element Method in Engineering Science", McGraw-Hill.

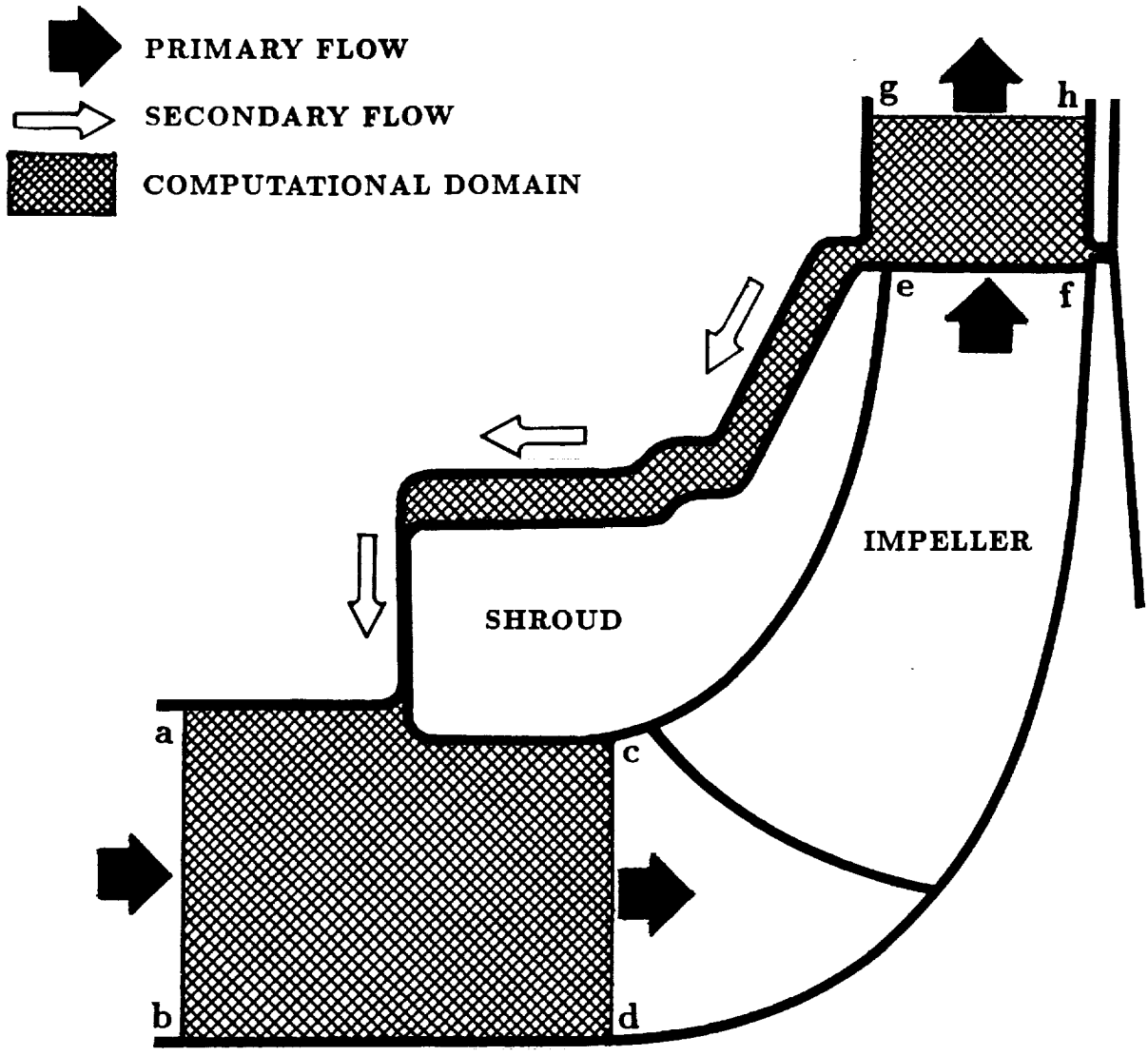


Fig. 1 Definition of the computational domain

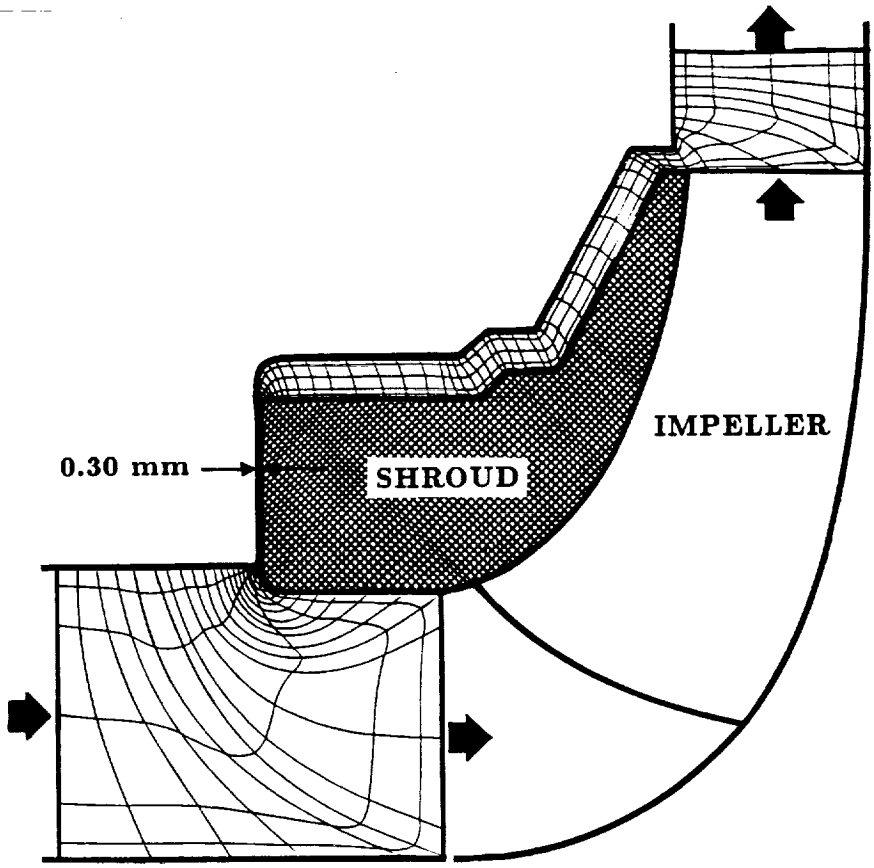


Fig. 2 Finite–element discretization model for the centered–impeller operation mode

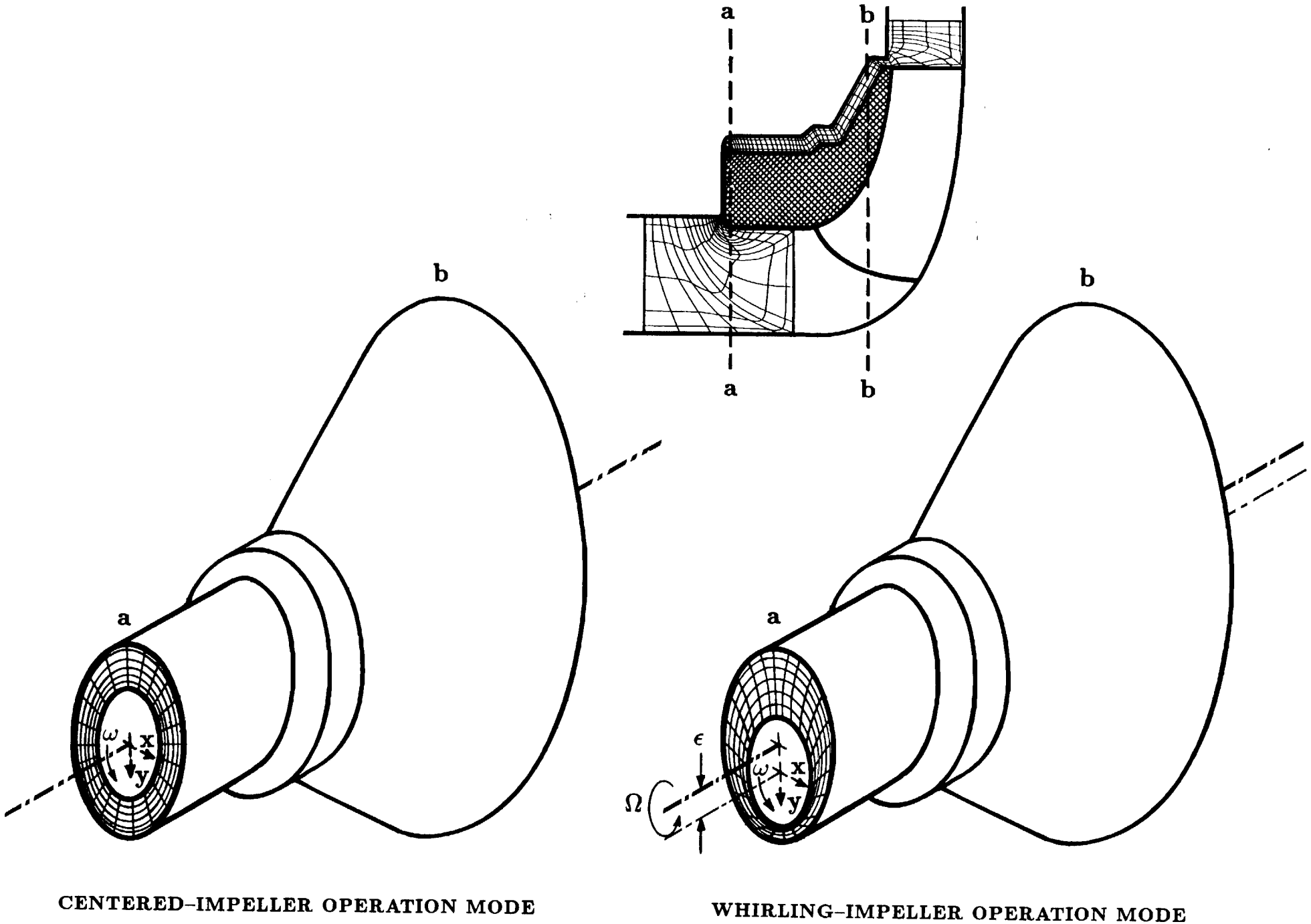


CENTERED–IMPELLER OPERATION MODE

WHIRLING–IMPELLER OPERATION MODE

**Fig. 3 Distortion of the shroud–to–housing finite element assembly due to the impeller whirl**

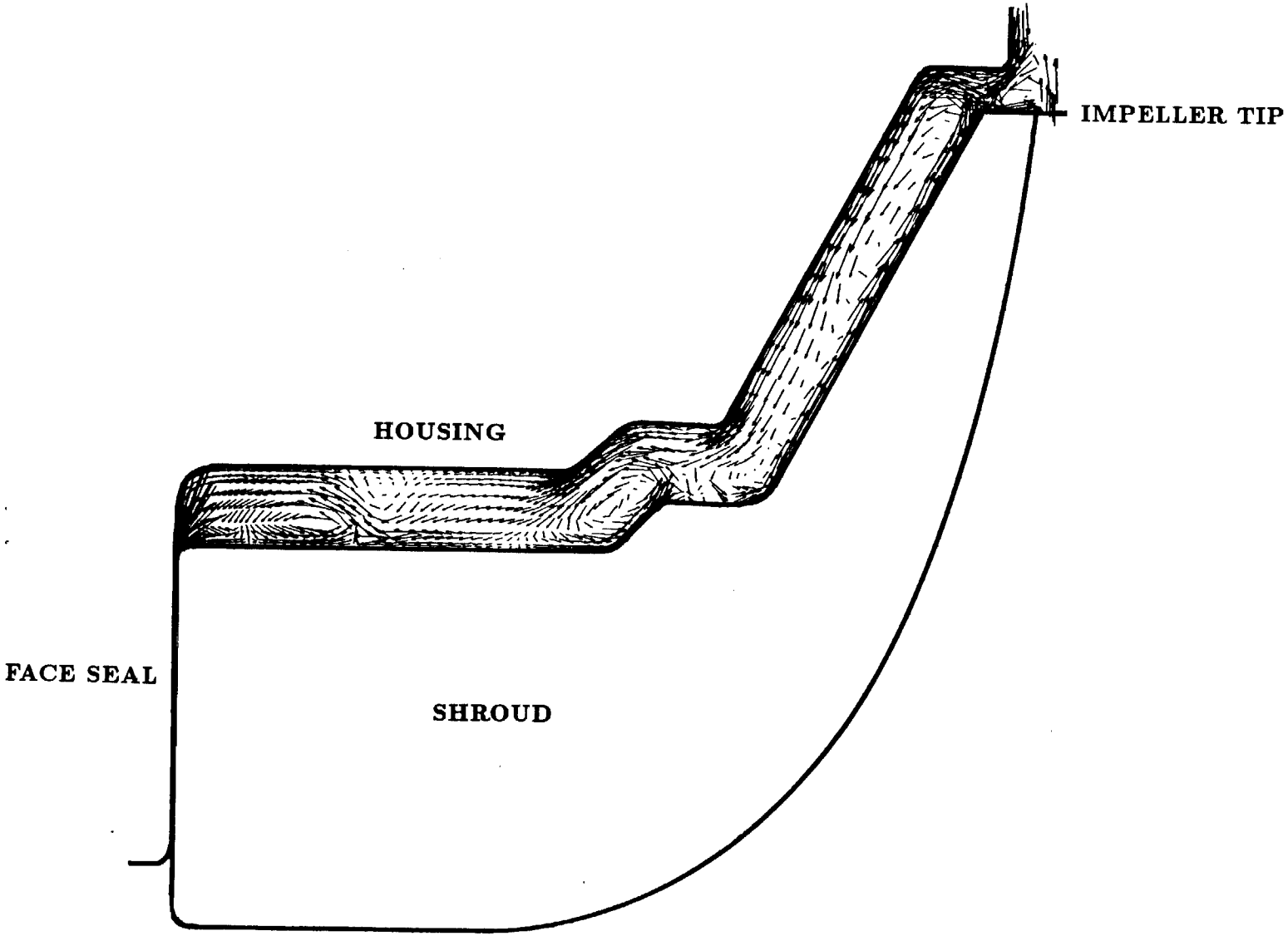


Fig. 4 Vector plot of meridional velocity component for the centered–impeller operation mode

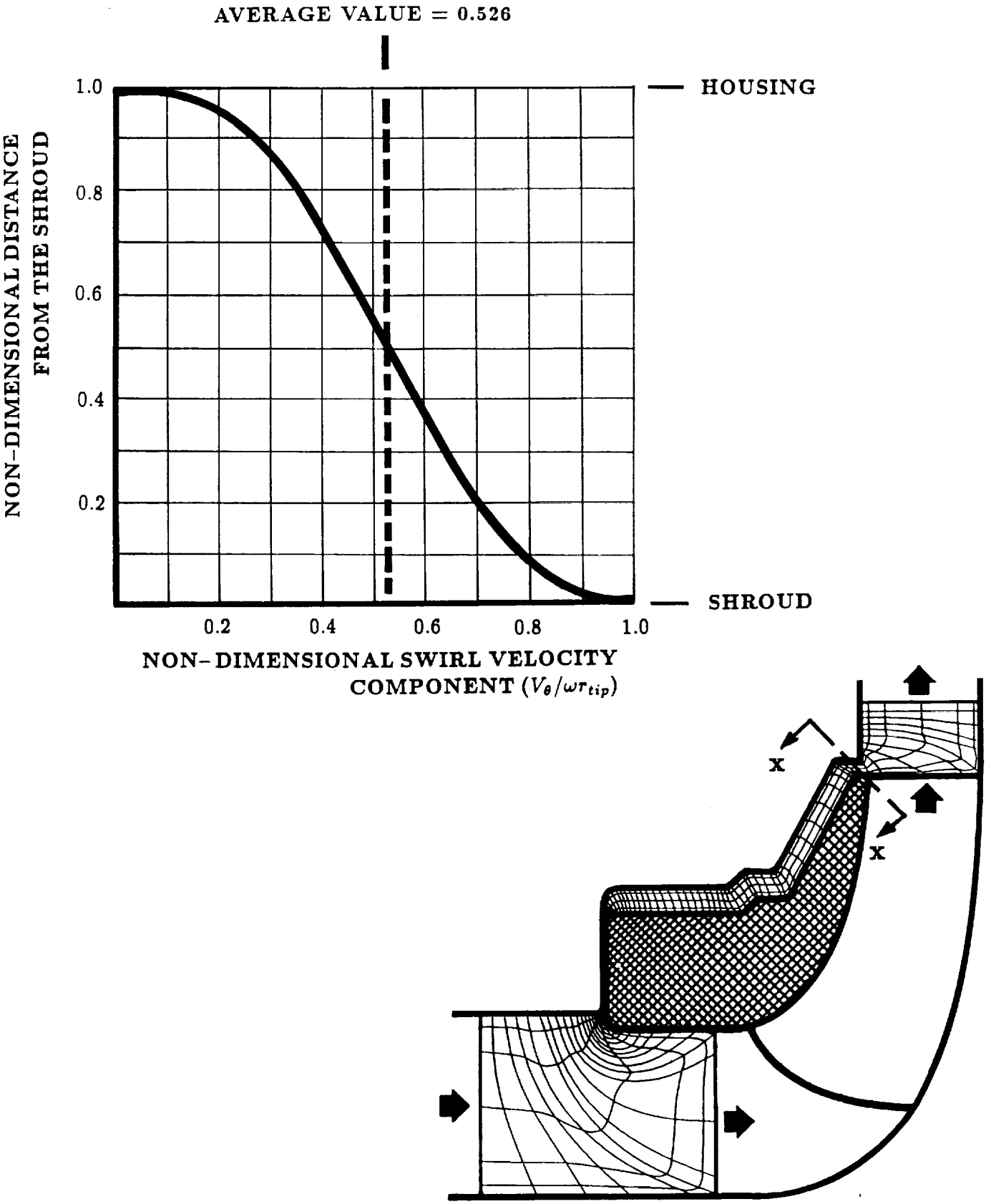


Fig. 5 Distribution of the non-dimensional swirl velocity component at the leakage-passage inlet station

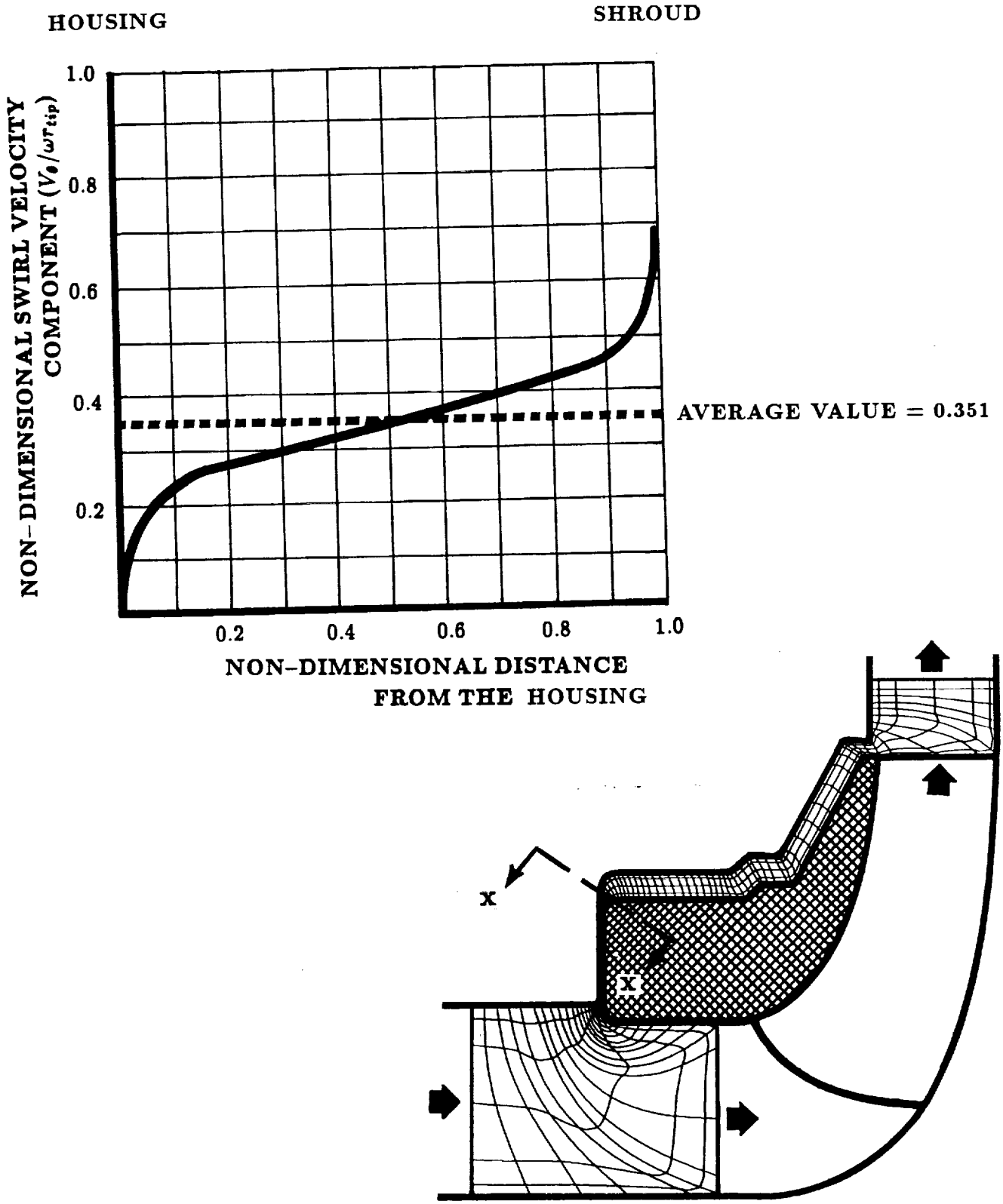


Fig. 6 Distribution of the non-dimensional swirl velocity component at the face-seal inlet station

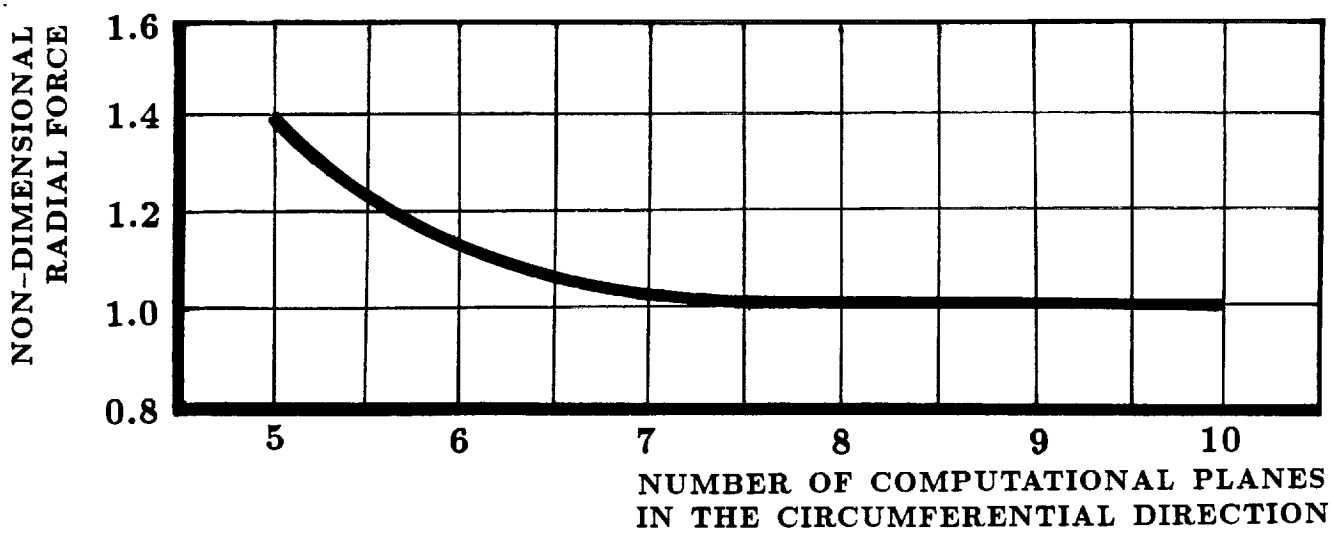


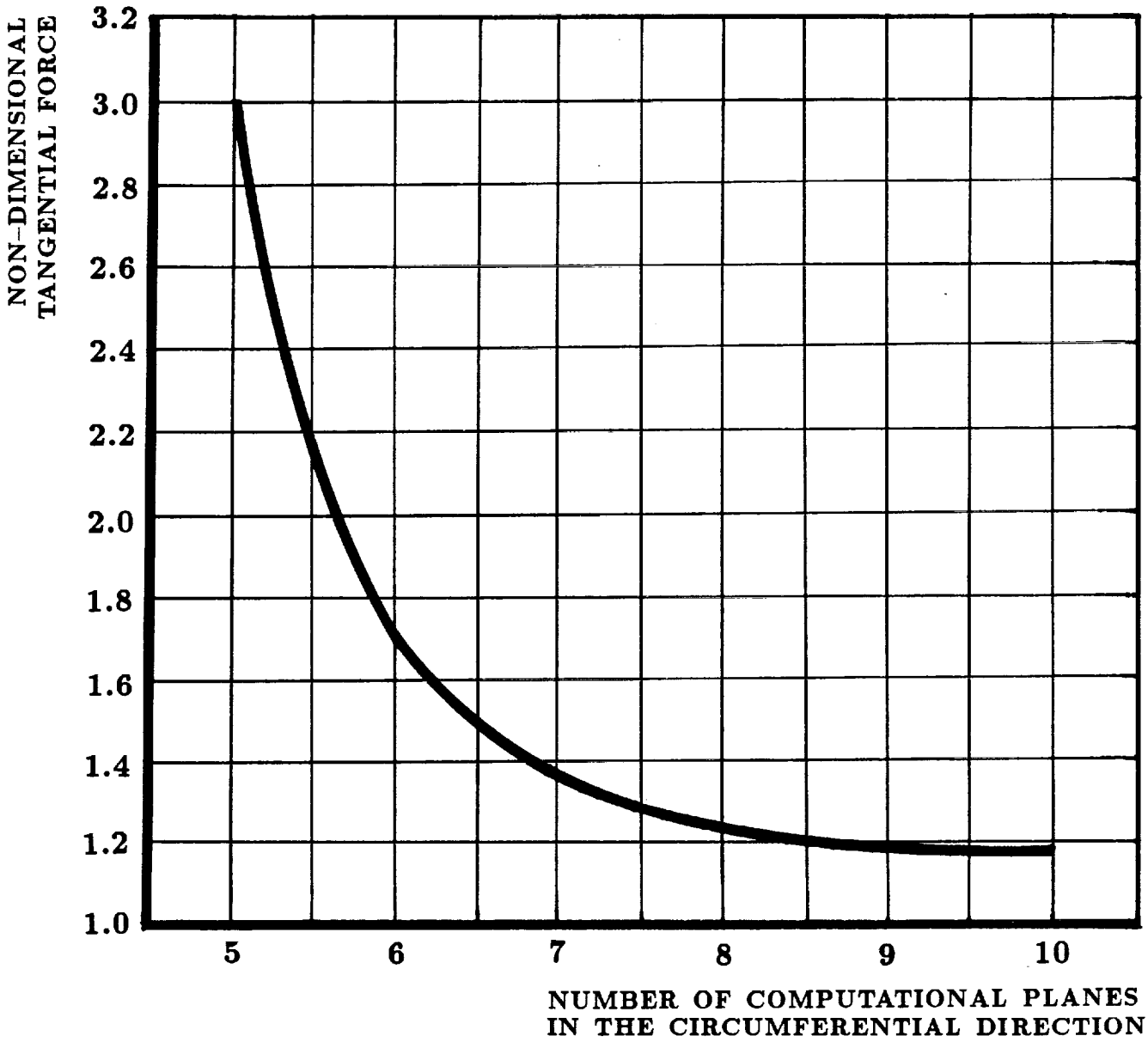


Fig. 7 Dependency of the fluid-exerted forces on the grid resolution in the circumferential direction

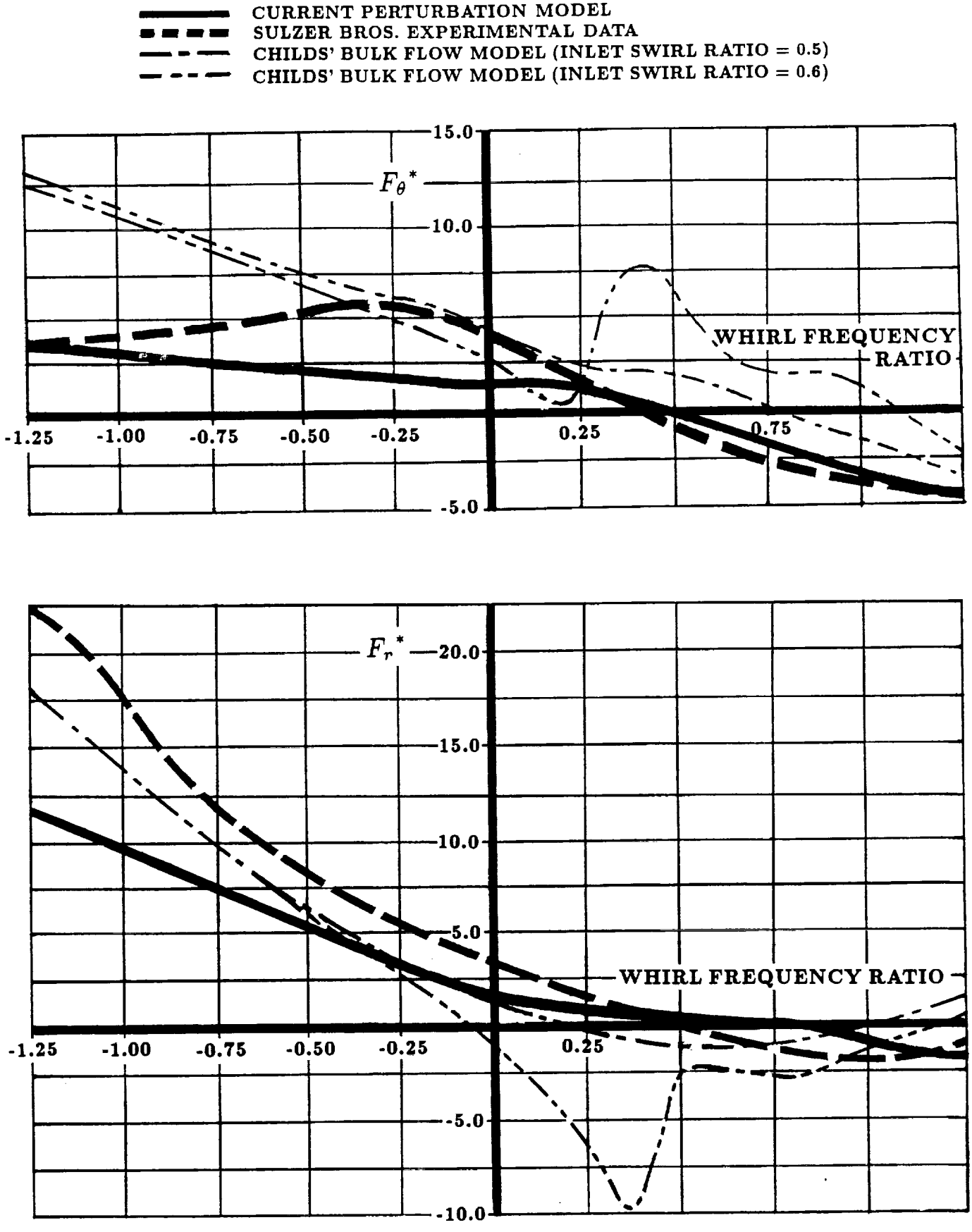


**Fig. 8 Comparison of the shroud forces with experimental and numerical data**

PAPER# 2

A Paper Entitled:

# Stability Assessment of Incompressible–flow Labyrinth Seals in Turbomachinery Applications

(currently under review for publication in the AIAA J. of Propulsion and Power)

# Stability Assessment of Incompressible–Flow Labyrinth Seals in Turbomachinery Applications *

E.A. Baskharone ** and A. Ghali ***
Department of Mechanical Engineering
Texas A&M University
College Station, Texas 77843

## ABSTRACT

A detailed finite–element–based perturbation analysis, initially developed for straight annular seals, is extended to the labyrinth seal rotordynamics problem. This particular seal category is frequently used in turbopumps, such as those of the Space Shuttle Main Engine, for its effectiveness as a leakage control device. The same seal configuration is also known to produce a net destabilizing force, which stems from the fluid/rotor interaction. The general objective here is to assess the effect of a design parameter, namely the number of tooth–to–tooth chambers, on the seal relative stability. To this end, two representative cases of teeth–on–rotor labyrinth seals are selected for the purpose of comparison. The chosen seals share the same tooth–to–tooth chamber geometry, but are composed of one and five such chambers. The centered–rotor flow solution corresponding to each seal version is first obtained, and relevant flow characteristics in each case outlined. This "zeroth–order" flow solution is next used as input to the perturbation model, with the outcome being the fluid–exerted forces on the rotor as the latter whirls around the housing centerline. These forces are then analyzed to determine the direct and cross–coupled stiffness, damping and inertia coefficients of the fluid/rotor interaction. The computed rotordynamic coefficients are compared to an existing set of experimental measurements concerning the same two seal configurations. The final outcome of the study is consistent with the general belief that labyrinth seals impart a rotordynamically destabilizing effect. In terms of relative stability, however, the five–chamber seal configuration offers less of this destabilizing effect, by comparison.

* This research was funded by NASA–Marshall Space Flight Center (Huntsville, Alabama), Contract No. NAS8–37821 (technical monitor: James Cannon) and the Texas A&M Turbomachinery Research Consortium.

** Associate Professor, Mem. AIAA.

*** Graduate Research Assistant.

## NOMENCLATURE

$C$ = direct damping coefficient of the fluid/rotor interaction

$c$ = cross-coupled damping coefficient

$F_r$ = radial component of the fluid-induced force

$F_r^* = \partial F_r / \partial \epsilon$

$F_\theta$ = tangential component of the fluid-induced force

$F_\theta^* = \partial F_\theta / \partial \epsilon$

$f$ = whirl frequency ratio

$h$ = seal clearance

$K$ = Direct stiffness coefficient of the fluid/rotor interaction

$k$ = cross-coupled stiffness coefficient

$p$ = static pressure

$p_i$ = seal-inlet static pressure

$r$ = radius

$r_i$ = inner radius of the labyrinth seal

$V_z$ = axial velocity component

$V_\theta$ = tangential velocity component

$\epsilon$ = lateral eccentricity of the rotor axis

$\rho$ = density

$\Omega$ = whirl frequency

$\omega$ = rotor operating speed

# INTRODUCTION

Labyrinth seals are generally regarded as efficient leakage–control devices in turbomachinery applications (Fig. 1). Since leakage flow is considered on of the primary loss mechanisms, and subsequently performance degradation, in turbomachines, much of the numerical studies on seals have been focused on this particular seal category. Among those are the computational leakage models by Stoff (1980), Rhode et al. (1984) for incompressible flow applications. Compressible–flow labyrinth seal models, for gas turbine applications, have also been devised [e.g. Wittig et al. (1987) and, more recently, Rhode and Hibbs (1992)].

Experimental measurements and flow visualization studies in labyrinth seals have also been reported in the literature. Examples of these include the LDA measurements by Wittig et al. (1987), the flow visualization study by Iwatsubo and Kawai (1984), and the discharge coefficient measurements by Wittig et al. (1987). The complexity of the flow structure in labyrinth seals has also encouraged researchers to devise, and continually update, empirical correlations (e.g. Zimmermann and Wolff, 1987).

Despite the performance improvements attained through the utilization of labyrinth seals, serious fluid–induced vibrations have been attributed to them by many rotordynamicists. Among those, Alford (1965) was the first to point out the destabilizing effects of labyrinth seals. Iwatsubo and Kawai (1984) later reported significantly poor direct damping coefficients for a hydraulic labyrinth seal under a matrix of different operating conditions. In a comparative study involving several seal categories, Childs and Elrod (1988) also concluded that the flow swirl at the labyrinth seal inlet station would make a bad rotordynamic situation even worse, and that an effective swirl brake would be required in this case.

Recent theoretical developments in this area have generally been either too simplified to account for real flow effects in labyrinth seals, or so tailored as to handle simple geometries and/or

uniform lateral eccentricity of the whirling rotor. Under the first category are the "one-volume" models by Iwatsubo (1980) and that by Childs and Scharrer (1984). To the author's knowledge, the first attempt to apply rigorous computational fluid dynamics tools, within the framework of a perturbation approach, was that by Nordmann and Weiser (1988). This finite difference-based model is based on the transformation of the entire rotor-to-housing computational domain to a fictitious frame of reference whereby the rotor eccentricity (assumed uniform along the seal axis) is eliminated. Despite the apparent generality and complex nature of this approach, the method is practically limited to rectangular tooth-to-tooth chambers, and is concepually incapable of addressing rotor excitations in the form of conical whirl, which would be of serious consequences for long seals with appreciable streamwise pressure differential.

The current perturbation model is a versatile predictive tool, which is based on what we generically termed the "virtually" deformable finite-element concept. Theoretical details of this model were documented by Baskharone and Hensel (1991a), and a sample case of a straight annular seal successfully analyzed (Baskharone and Hensel, 1991b). Versatility of this model was also demonstrated by analyzing, as interrelated, the cylindrical and conical whirl of a straight annular seal rotor (Baskharone and Hensel, 1991c). The present study illustrates another versatility aspect of the perturbation model, namely that of the seal geometry arbitrariness. The study addresses both the traditional difficulty of analyzing the flow past a sequence of high aspect-ratio cavities, normally found in labyrinth seals, as well as the task of classifying, as restoring or aggravating, the fluid reaction forces due to excitations of the rotor axis (Fig. 2).

## COMPUTATIONAL DEVELOPMENT

**Zeroth-Order Flow Field.** The perturbation procedure is initiated by computing this "zeroth-order" flow field, which is clearly axisymmetric. Details of the flow-governing equations,

turbulence closure, and finite–element formulation of this relatively simple problem were all discussed by Baskharone and Hensel (1991b), where a test case involving a straight annular seal was comprehensively covered. Comparison of the computed through–flow and swirl velocity profiles in the rotor–to–housing passage with the experimental data previously reported by Morrison et al. (1991), was also presented, and the agreement between the two sets of data was encouraging.

**Perturbation Analysis.** The centered–rotor flow solution, referenced above, was used in the current study as input to the perturbation analysis phase of the computational procedure. Devised by Baskharone and Hensel (1991a), the perturbation model here is based on what was generically termed the "virtually" deformable finite element concept, where the perturbed flow equations emerge from expansion of the finite–element equations in terms of the rotor eccentricity $\epsilon$. Since no circumferential pattern is pre–imposed on the perturbations of the flow properties, the problem at this point shifts to the fully three–dimensional type, as the rotor eccentricity destroys the flow axisymmetry (Fig. 2). Simultaneously, the flow problem is cast in a rotating–translating frame of reference, which is attached to the whirling rotor at all times (Fig. 2) in order to eliminate the time dependency of the flow field in this case.

## RESULTS AND DISCUSSION

Two labyrinth seals, composed of the same tooth–to–tooth chamber geometry, but different in the number of chambers were selected for this study. These one and five–chamber hydraulic seals were the subject of a flow visualization study and rotordynamic testing by Iwatsubo and Kawai (1984). In both cases, a seal–inlet pressure and rotor speed of 147 KPa and 3.7 Hz were arbitrarily chosen from the experimental matrix of operating conditions. The finite–element model created

for the two seal configurations are shown in Figs. 3 and 4, respectively. The discretization unit in these two Figures is a bi-quadratic curve-sided element of the Lagrangian type. The process of generating finite-element grids, such as these, was largely automated and the level of near-wall refinement in the preprocessing segment of the computational procedure was made totally arbitrary. This capability made it possible to conduct a preliminary numerical "experimentation" study of grid optimization for the centered-rotor (axisymmetric) flow solution. The finite-element grids in Fig. 3 and 4 are the outcome of this early study, where a careful compromise was made between the numerical accuracy, on one hand, and the consumption of computational resources, on the other.

**Centered-Rotor Flow Field.** Figures 5 through 7 show the centered-rotor flow solution for the one-chamber seal configuration. This solution constitutes the zeroth-order flow field in the current perturbation analysis. First, the meridional flow behavior is shown in Fig. 5, with enlarged segments of the computational domain to clarify the flow recirculation within the tooth-to-tooth chamber and the vorticity breakdown in the dump region downstream from the chamber. The flow pattern in this Figure was qualitatively compared to that resulting from a flow visualization study by Iwatsubo and Kawai (1984), and the major features of the computed flow pattern were found to be consistent with the experimental findings.

The swirl velocity contours, throughout the computational domain, are shown in Fig. 6. The swirl velocity ($V_\theta$) in this Figure is non-dimensionalized using the average inlet through-flow velocity component ($V_{zi}$). Note that The Figure shows no inlet preswirl, which is consistent with Iwatsubo's seal-inlet conditions. Also note the swirl-velocity boundary layer profile development over the rotor surface. As seen in the Figure, the swirl velocity near the housing surface appears in the tooth-to-tooth chamber region, and steadily declines, over the housing, away from the chamber, up to the location where the flow recirculation zone, downstream from the second tooth (Fig. 5) ends.

Fig. 7 shows a contour plot of the static pressure ($\bar{p}$), with an enlarged view of the tooth-to-tooth seal chamber. The non-dimensional pressure ($\bar{p}$) in this Figure is defined as follows:

$$\bar{p} = \frac{(p - p_i)}{\rho {V_{zi}}^2}$$

where p and $p_i$ are the local and seal-inlet static pressures, respectively, $\rho$ is the fluid density, and $V_{zi}$ is the average through-flow velocity at the seal inlet station. Note that the upstream side of the second tooth is exposed to a rather high pressure near the housing, despite the fact that the center of the low-pressure island is closer to the that tooth.

The centered-rotor flow field corresponding to the five-chamber seal configuration is shown in Figs. 8 through 10, with particular emphasis on the flow structure in the first and last chambers. Examination of Fig. 8 reveals that the center of the cavity recirculatory motion gradually moves from the cavity center towards the tooth pressure side as the flow progresses from one cavity to the next. The most significant difference between the swirl velocity distribution in Fig. 9 and that of the single-chamber seal (Fig. 6) is the continuous rise in the magnitude of this velocity component in the through-flow direction, by comparison. This characteristic simply means that the five-chamber seal gives rise to "elongated" flow trajectories over the last few chambers. One would expect, as a result, a substantial total pressure differential across these chambers, which is consistent with the known fact that the leakage-suppression capability of labyrinth seals is drastically enhanced by increasing the number of tooth-to-tooth chambers. As for the static pressure distribution in Fig. 10, it seems that the largest pressure increments occur across the first and last chambers.

**Grid Dependency.**

As would naturally be anticipated, the perturbed flow resolution is dependent on the grid resolution which, as the domain three-dimensionality prevails, translates into the number of computational stations in the circumferential direction (Fig. 2). Investigation of this dependency was

carried out by varying this number and repeatedly computing the fluid-exerted forces on the rotor for an arbitrarily chosen whirl frequency "$\Omega$" that is identical to the operating speed "$\omega$". Results of this preliminary step are shown in Fig. 11, where the fluid force components $F_r^*$ and $F_\theta^*$ are obtained by integrating the rotor-surface pressure forces, upon resolution in the radial and tangential directions, over all of the contributing finite element boundaries.

The force trends in Fig. 11 suggest that the radial force are more sensitive to the tangential grid resolution by comparison. The Figure also shows that changes in the force magnitudes becomes acceptably small as the tangential computational-station count approaches 11. Given the fact that $F_r$ itself varies by as low as 2.7% by increasing the number of these computational stations from 10 to 11, and in an attempt to maintain a "manageable" CPU time consumption, the number was fixed at 11 thereafter.

**Fluid-Induced Forces and Rotordynamic Coefficients.** The trends of the fluid-exerted forces are shown in Fig. 12 for the five-chamber seal configuration over a range of the rotor whirl frequency between -200% and 200%, with the negative values representing backward whirl. The reassuring feature of the radial and tangential force trends in this Figure is that each of them is more or less parabolic, a commonly known characteristics of seals in general. Of the two components in Fig. 12, the tangential force is exlusively responsible for aggravating or suppressing the rotor whirling motion. With this in mind, the impression one would have, by examining Fig. 12, is that of rotordynamic instability in the range of positive (forward) rotor whirl frequency between zero and 20% of the rotor speed, judging by the positive tangential force in this range.

The computed fluid-exerted forces were then used to compute the rotordynamic coefficients of the fluid/rotor interaction, in the manner previously outlined by Baskharone and Hensel (1991a).

The results of this computational step are contained in Tables 1 and 2 for the one- and five-chamber seal configurations, respectively. Reproduced in these tables are also the experimental measurements by Iwatsubo and Kawai (1984) for comparison. Perhaps the most alarming values in these two tables is the poor value of the direct damping coefficient "C" in both cases. In fact, the negative value of this coefficient, for the single-chamber seal configuration, implies a highly destabilizing effect of this seal, particularly in view of the positive (also destabilizing) value of the cross-coupled stiffness coefficient "k" in this case.

A useful parameter in quantifying the relative rotordynamic stability of general fluid-encompassed rotors is the so-called whirl frequency ratio "f", where:

$$f = \frac{k}{\omega C}$$

This is the ratio of the destabilizing-to-stabilizing forces acting on the rotor. A given seal would have a stabilizing influence for a whirl frequency ratio "f" below 1.0 (Scharrer, 1988).Application of this criterion to the five-chamber seal configuration leads to the conclusion that this particular seal imparts rotordynamic stability to the shaft (in a global sense), for it gives rise to a whirl frequency ratio of approximately 0.22. However, the "relative stability" criterion, above, is inapplicable to the single-chamber seal configuration. This is due to the negative value of the direct damping coefficient in this case. Such characteristic simply renders the seal unstable regardless of the magnitude of the cross-coupled stiffness coefficient, should the latter be positive.

## CONCLUDING REMARKS

The objective of this study was twofold; to demonstrate the applicability of a categorically new perturbation model to the traditionally complex problem of labyrinth-seal rotordynamics, and

to assess the stability effects of multiple-chamber seal configurations. Of these, the latter task is largely design-related, and is currently receiving an increasing amount of attention, owing to documented fluid-induced vibration problems in the Space Shuttle Main Engine turbopumps, for which labyrinth seals are primarily blamed. An intermediate outcome of the current study, namely the centered-rotor flow field, is equally suggestive from a design standpoint. This is true in the sense that knowledge of the flow pattern, for this operation mode, provides a means of predicting the seal effectiveness as a leakage-control device.

## ACKNOWLEDGMENT

This study was funded by NASA-Marshall Space Flight Center (Huntsville, Alabama), contract no. NAS8-37821, technical monitor: James Cannon. Partial funding was also provided by the Texas A&M Turbomachinery Research Consortium.

## REFERENCES

Alford, J.S., 1965, "Protecting Turbomachinery From Self-Excited Rotor Whirl," J. of Engineering for Power (ASME Trans.), pp. 333-344.

Baskharone, E.A. and Hensel, S.J., 1991a, "A Finite-Element Perturbation Approach to Fluid/Rotor Interaction in Turbomachinery Elements. Part 1: Theory," J. of Fluids Engineering (ASME Trans.), Vol.113, No. 3, pp. 362-367.

Baskharone, E.A. and Hensel, S.J., 1991b, "A Finite-Element Perturbation Approach to Fluid/Rotor Interaction in Turbomachinery Elements. Part 2: Application," J. of Fluids Engineering (ASME Trans.), Vol.113, No. 3, pp. 353-361.

Baskharone, E.A. and Hensel S.J., 1991c, "Interrelated Rotordynamic Effects of Cylindrical and Conical Whirl of Annular Seal Rotors," J. of Tribology (ASME Trans.), Vol. 113, No. 3, pp. 470–480.

Childs, D. and Elrod D., 1988, "Annular Honeycomb Seals: Test Results for Leakage and Rotordynamic Coefficients; Comparisons to Labyrinth and Smooth Configurations," NASA Conference Publication 3026, Rotordynamic Instability Problems in High–Performance Turbomachinery, pp. 143–159.

Childs D. and Scharrer J., 1984, "An Iwatsubo–Based Solution for Labyrinth Seals, Comparison with Experimental Results," NASA Conference Publication 2338, Rotordynamic Instability Problems in High Performance Turbomachinery.

Iwatsubo, T., 1980, "Evaluation of Instability Forces of Labyrinth Seals in Turbines or Compressors," NASA Conference Publication 2133, Rotordynamic Instability Problems in High–Performance Turbomachinery, pp. 139–167.

Iwatsubo, T. and Kawai R., 1984, "Analysis of Dynamic Characteristics of Fluid Force Induced By Labyrinth Seal," NASA Conference Publication 2338, Rotordynamic Instability in High–Performance Turbomachinery, pp. 211–234.

Nordmann, R. and Weiser P., 1988, "Rotordynamic Coefficients For Labyrinth Seals Calculated By Means Of a Finite Difference Technique," NASA Conference Publication 3026, Rotordynamic Instability in High–Performance Turbomachinery, pp. 161–175.

Rhode, D.L. and Hibbs, R.I., 1992, "New Model for Flow Over Open Cavities. Part II: Assessment for Seal Leakage," AIAA J. of Propulsion and Power, Vol. 8, No. 2, pp. 398–402.

Rhode, D.L., Demko, J.A., Morrison, G.L., Traegner, U.K. and Sobolik, S.R., 1984, "On the Prediction of Incompressible Flow in Labyrinth Seals," J. of Fluids Engineering (ASME Trans.), Vol. 108, pp. 19–25.

Scharrer. J.K., 1988, "Rotordynamic Coefficients for Stepped Labyrinth Seals," NASA CP-3026, pp. 177-195.

Stoff, H., 1980, "Incompressible Flow in a Labyrinth Seal," J. of Fluid Mechanics, Vol. 100, pp. 817-829.

Wittig, S., Schelling, U., Kim, S. and Jacobsen, K., 1987, "Numerical Predictions and Measurements of Discharge Coefficients in Labyrinth Seals," ASME Paper 87-GT-188.

Zimmermann H. and Wolff, K.H., 1987, "Comparison Between Empirical and Numerical Labyrinth Flow Correlations," ASME Paper 87-GT-86.

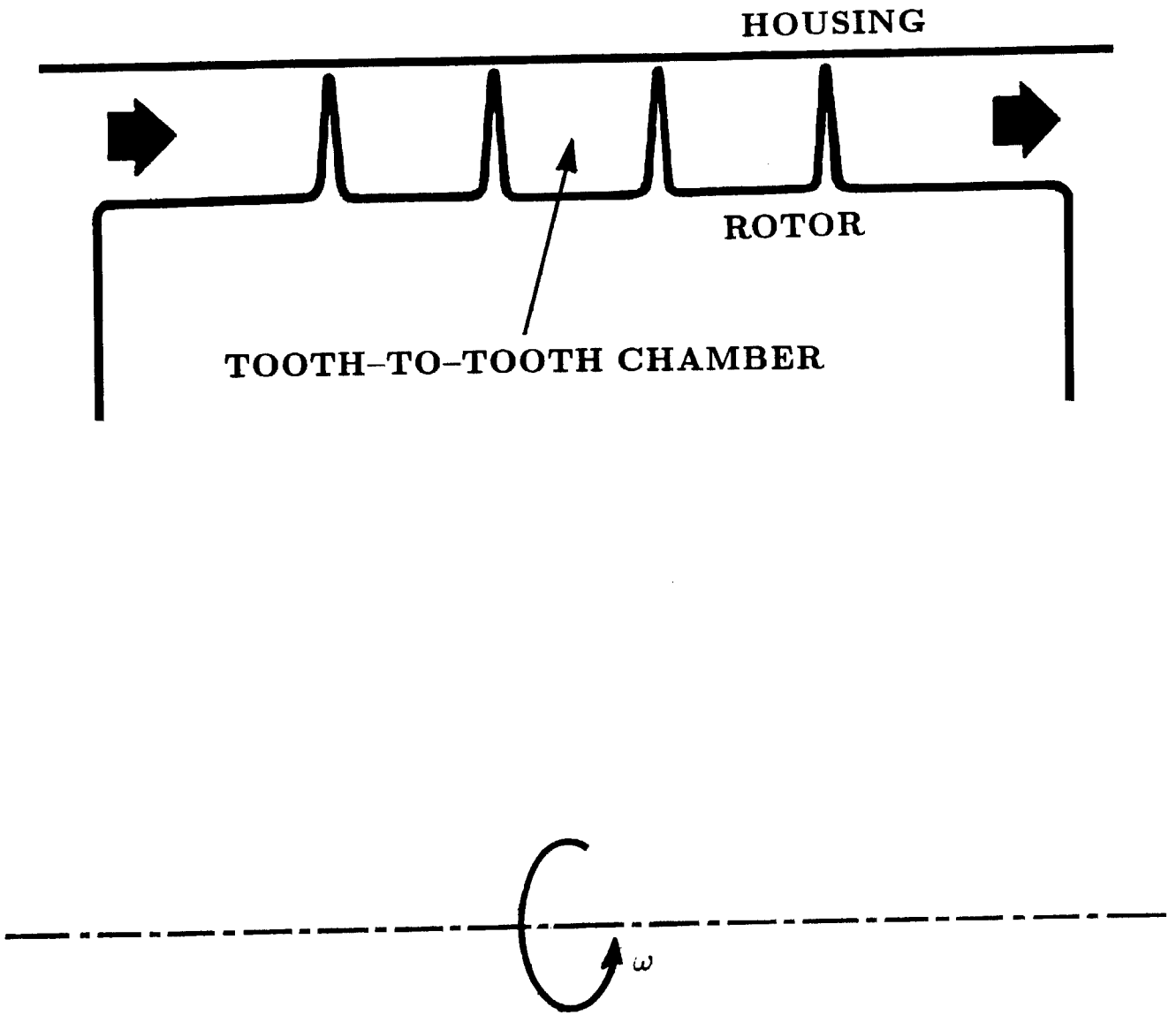


Fig. 1 Schematic of a typical labyrinth seal

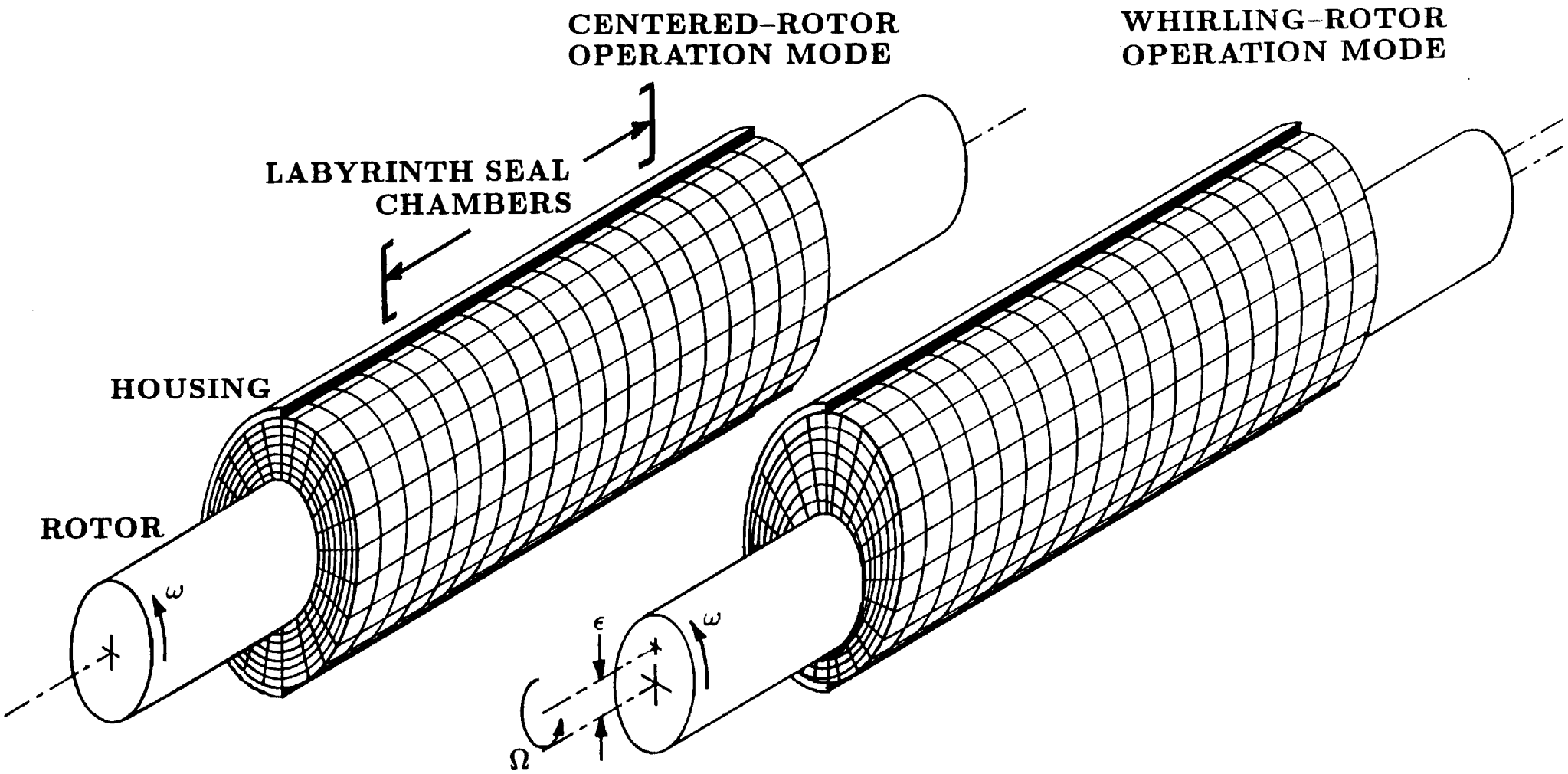


**Fig. 2 Distortion of the rotor–to–housing finite element assembly as a result of the rotor eccentricity**

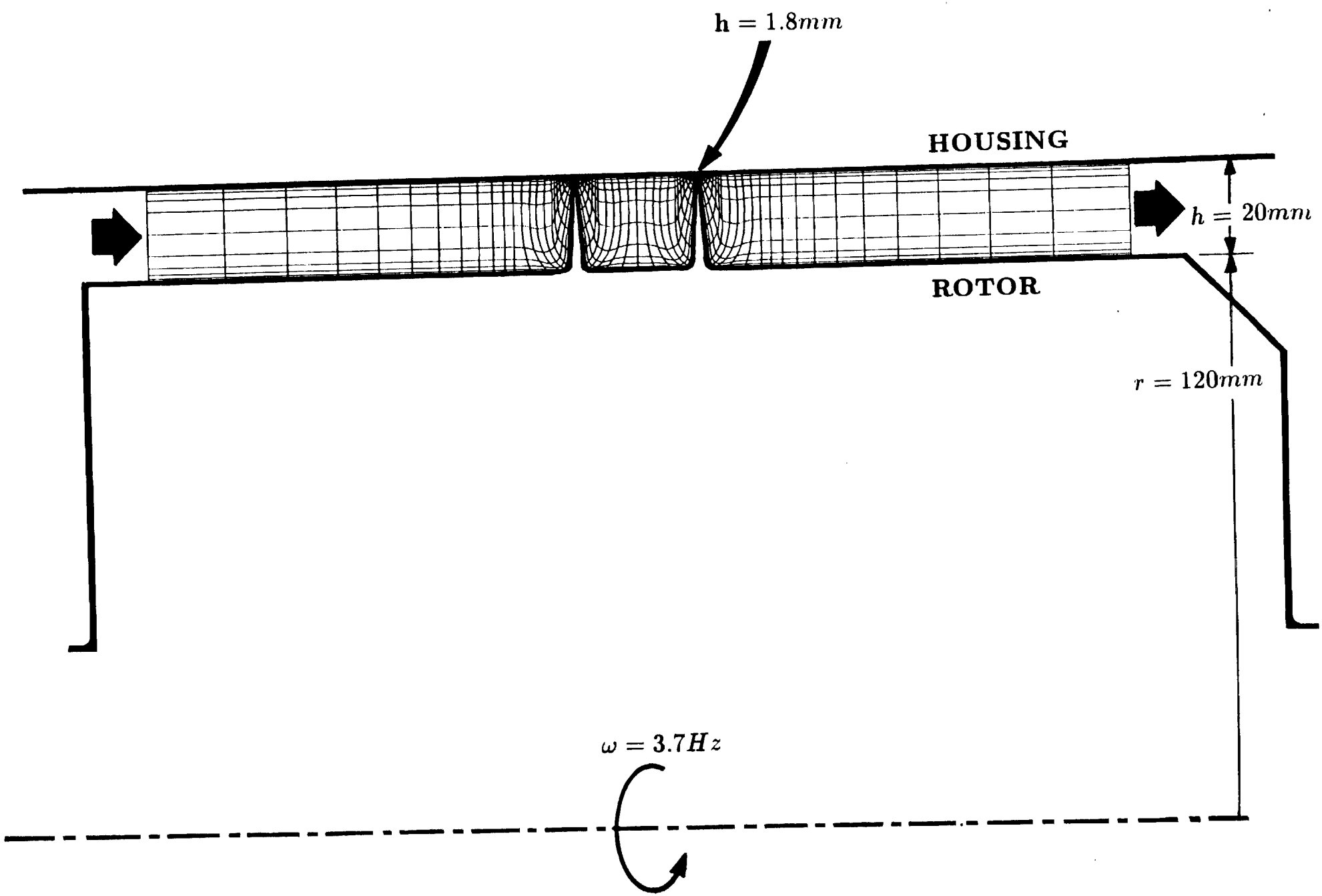


**Fig. 3 Finite–element model of the single–chamber seal configuration**

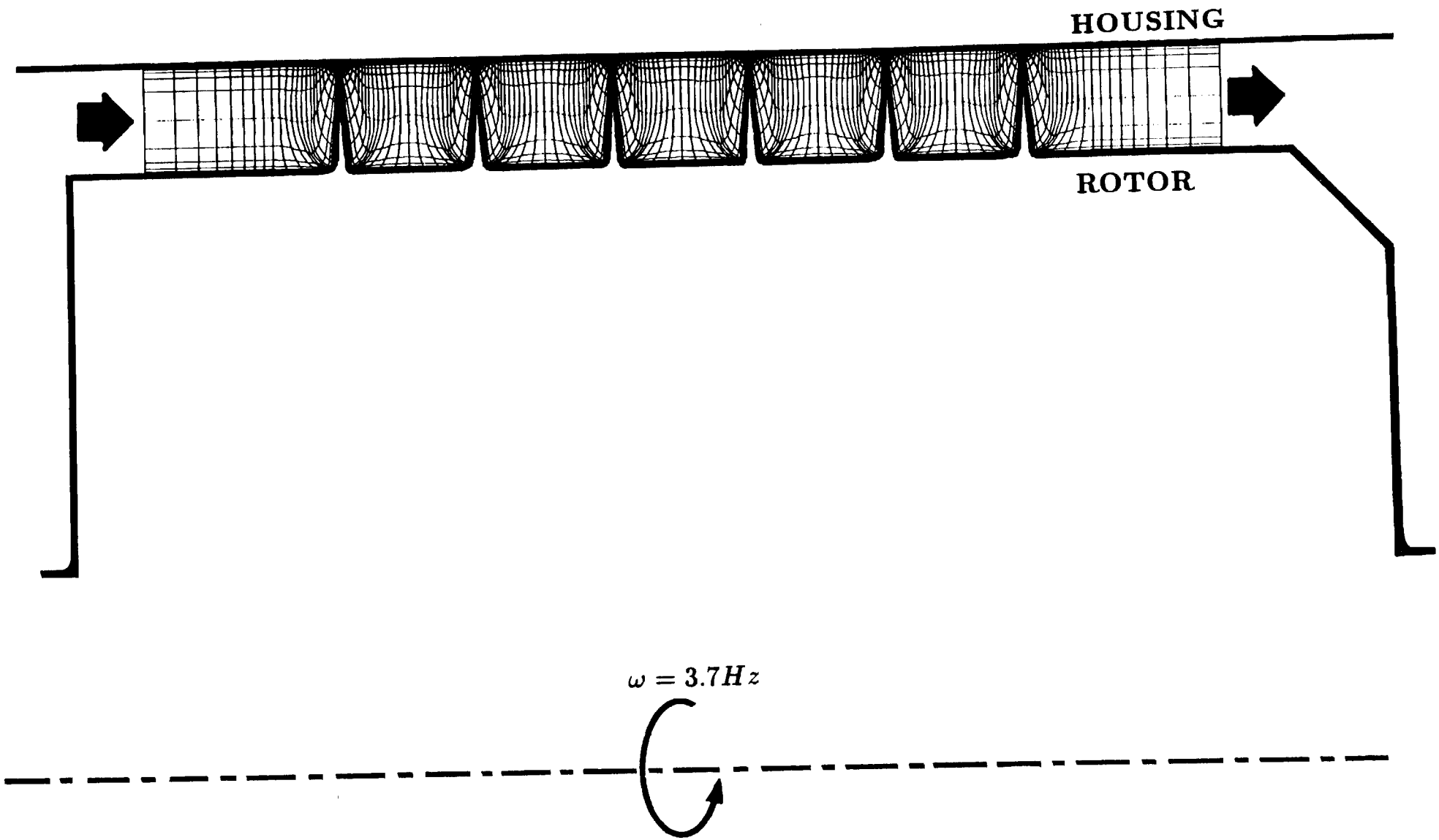


**Fig. 4 Finite–element model of the five–chamber seal configuration**

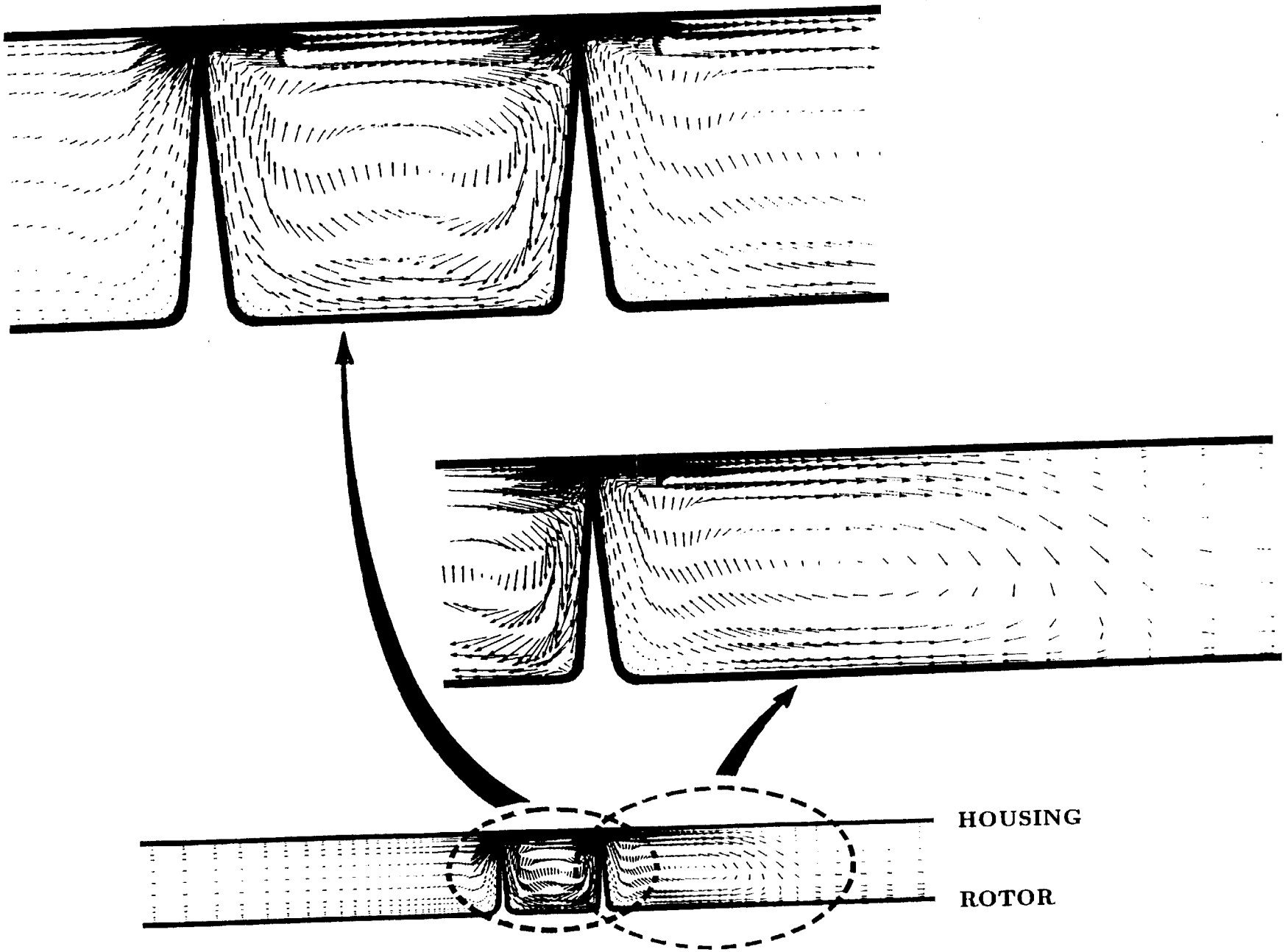


Fig. 5 Vector plot of the meridional velocity component for the centered-rotor operation mode of the single-chamber seal configuration

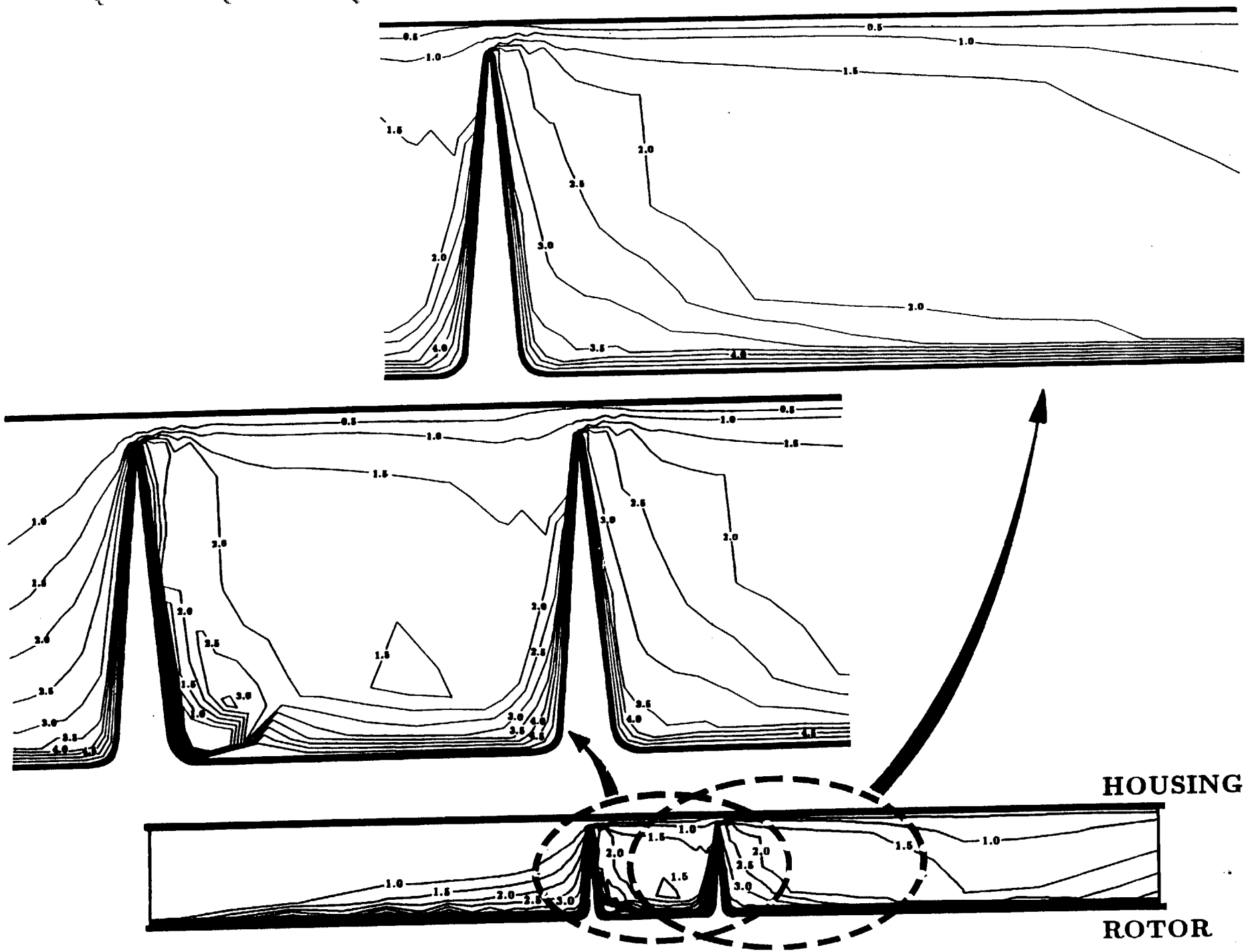


Fig. 6 Contour plot of the swirl velocity component for the centered–rotor operation mode of the single–chamber seal configuration

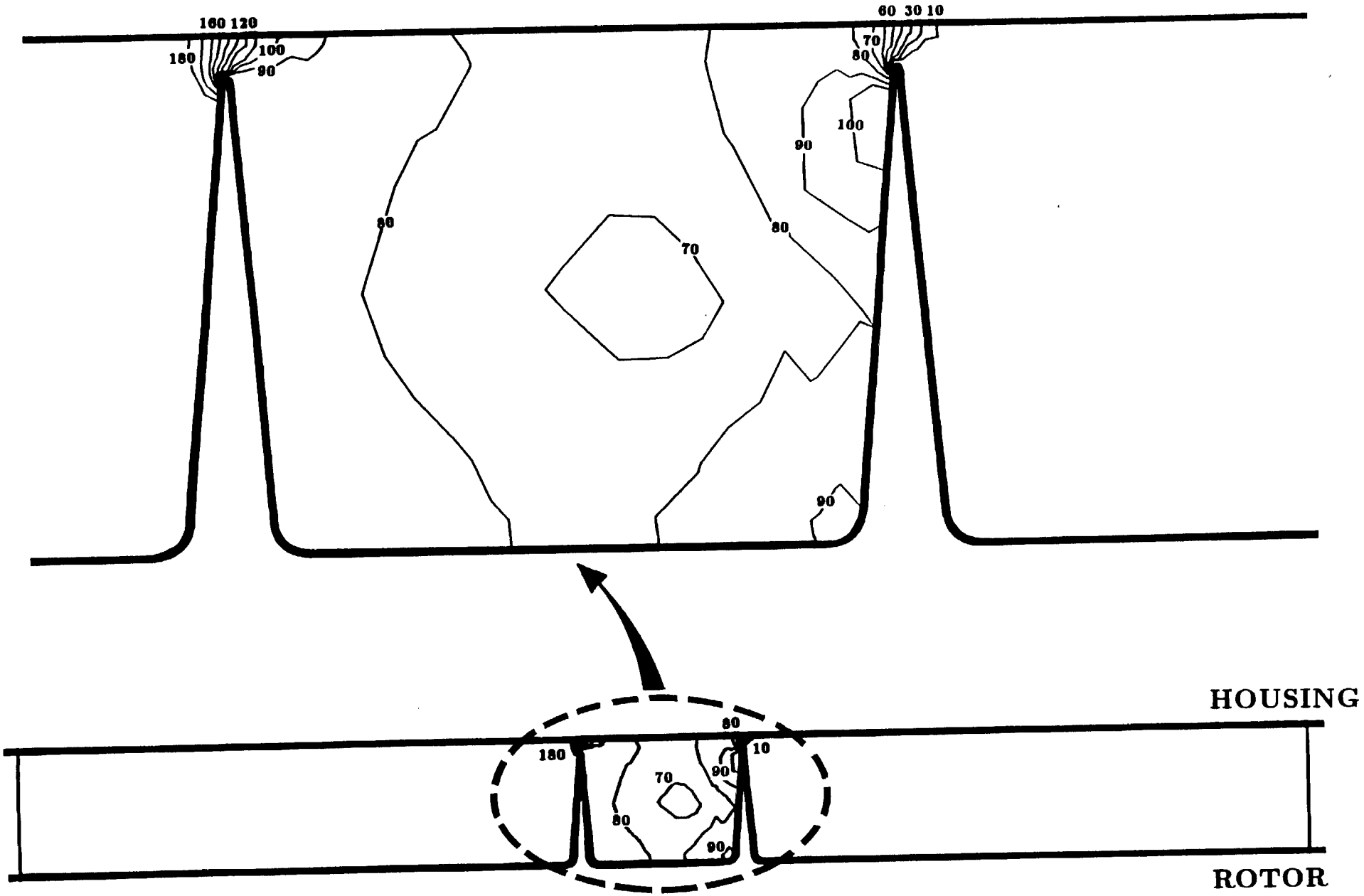


**Fig. 7 Contour plot of the static pressure for the centered–rotor operation mode of the single–chamber seal configuration**

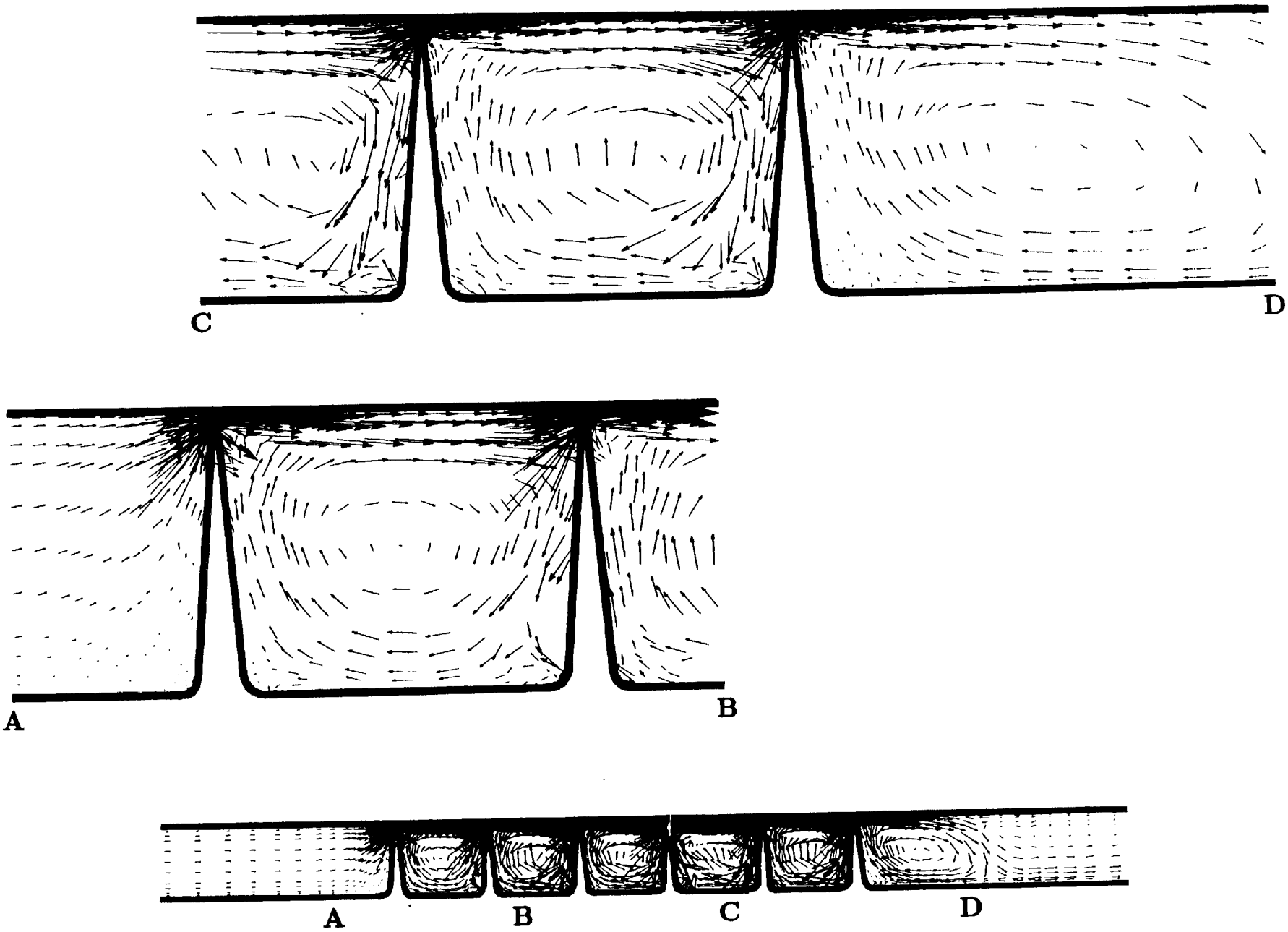


**Fig. 8 Vector plot of the meridional velocity component for the centered-rotor operation mode of the five-chamber seal configuration**

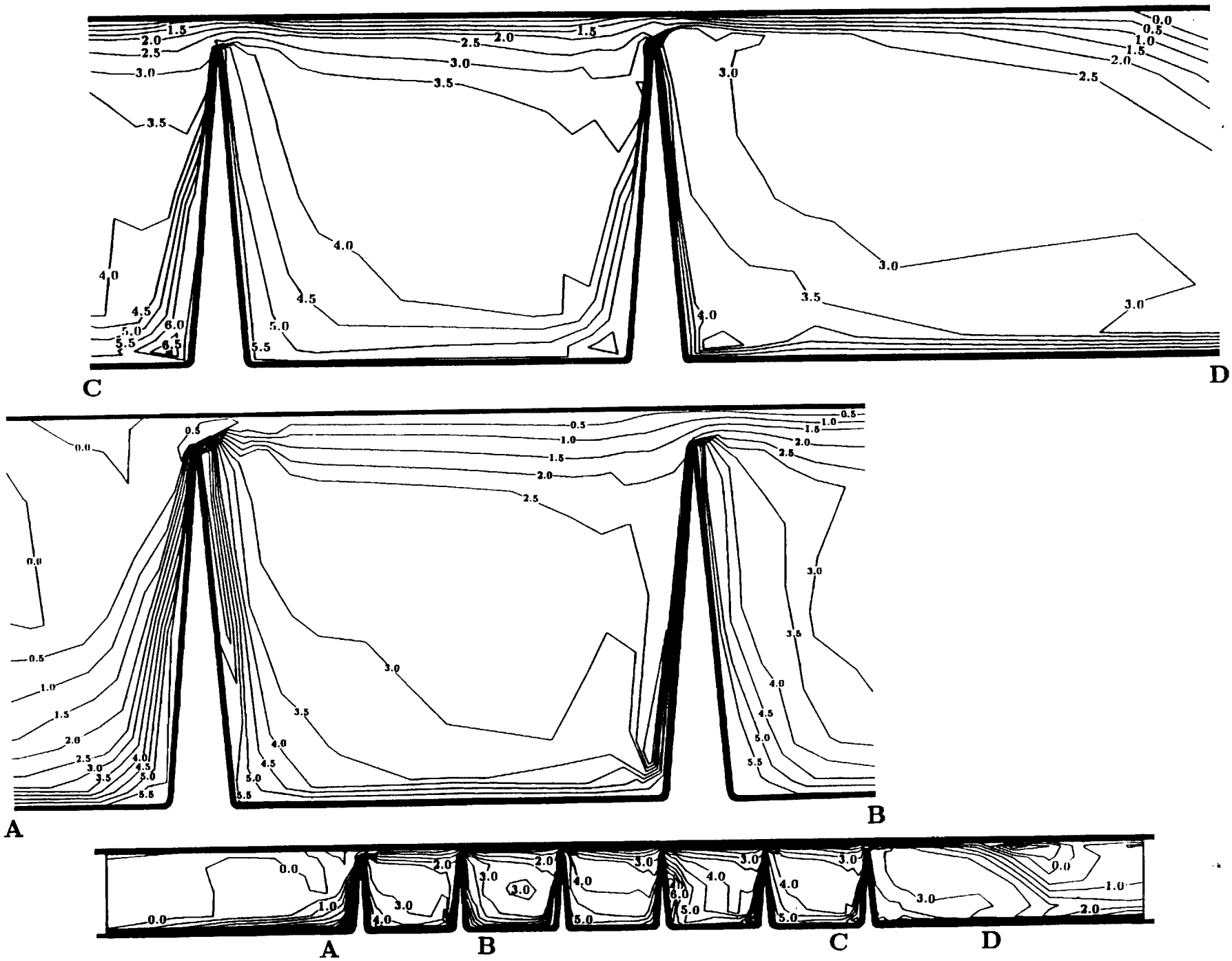


Fig. 9 Contour plot of the swirl velocity component for the centered-rotor operation mode of the five-chamber seal configuration

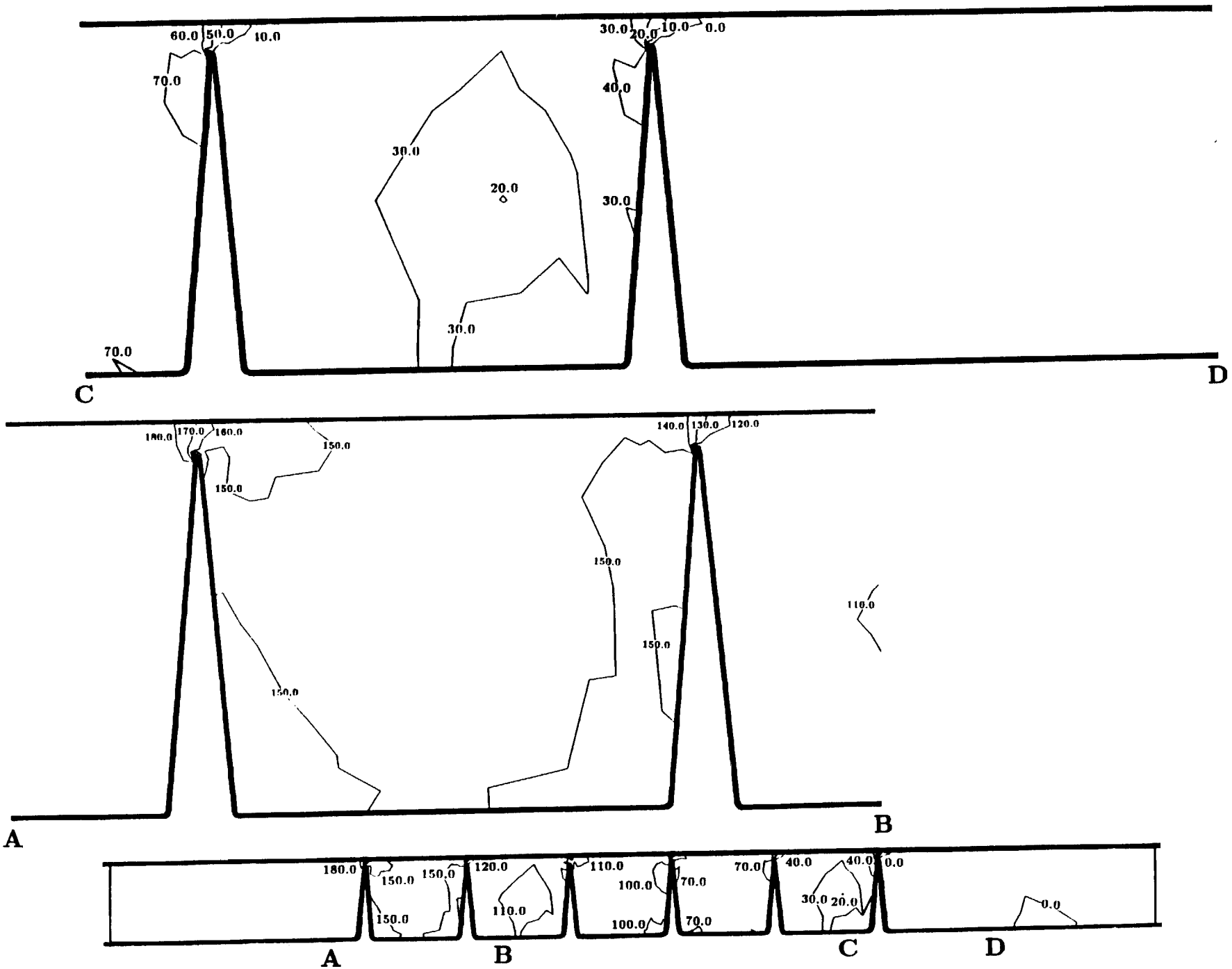


**Fig. 10 Contour plot of the static pressure for the centered–rotor operation mode of the five–chamber seal configuration**

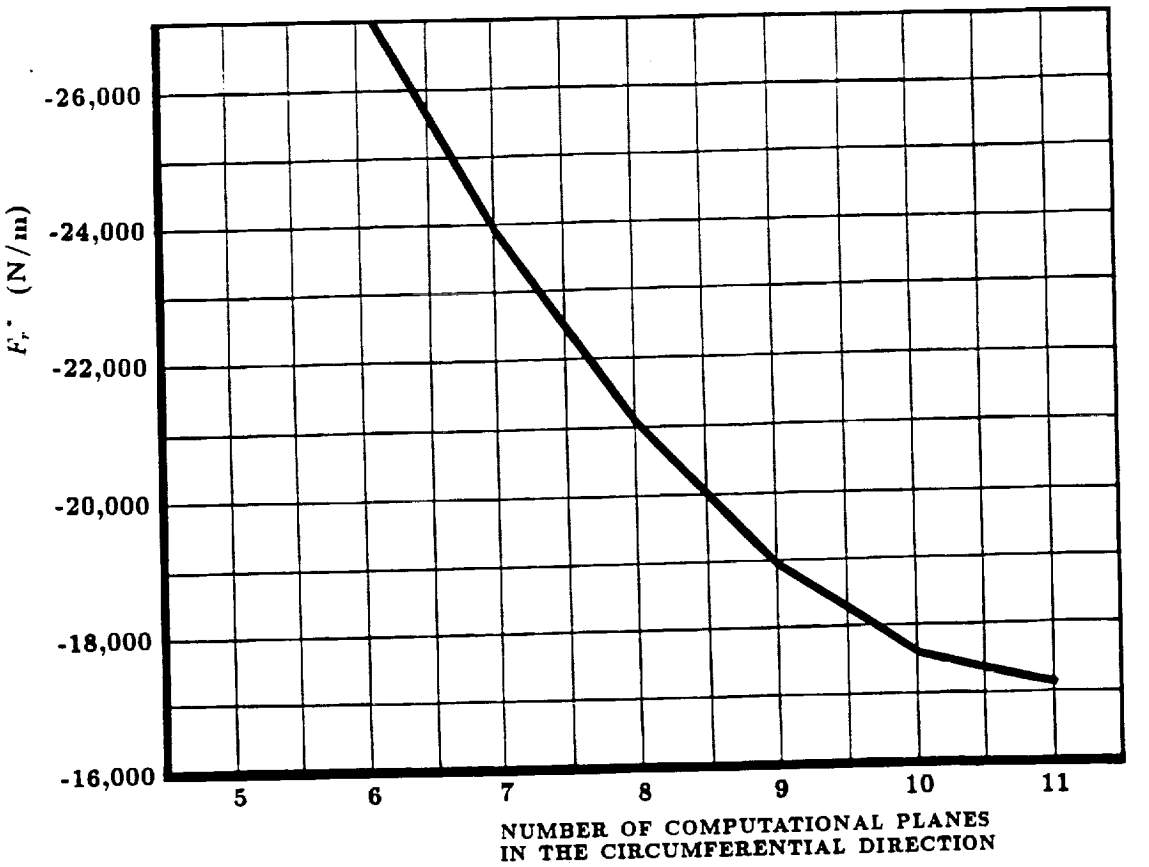


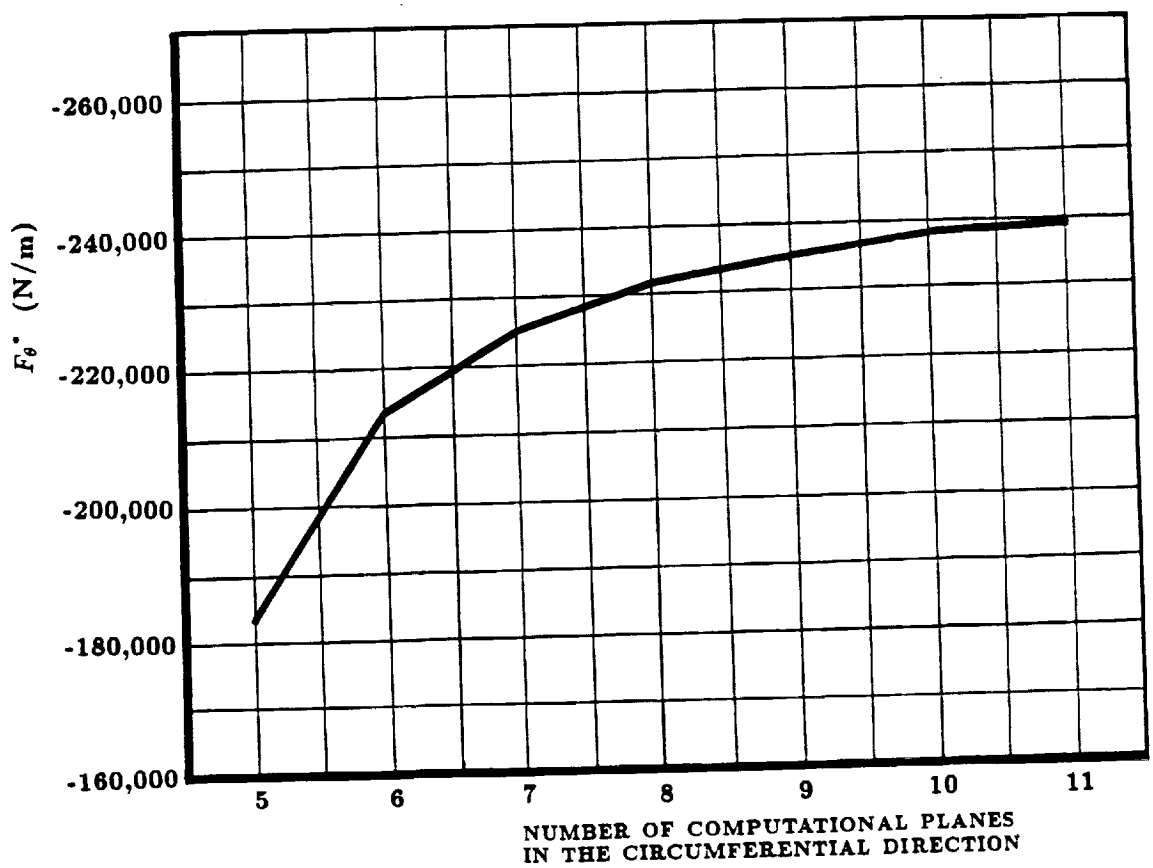


**Fig. 11 Dependency of the fluid–exerted forces on the grid resolution in the circumferential direction for the case of synchronous whirl ($\Omega/\omega = 1.0$)**

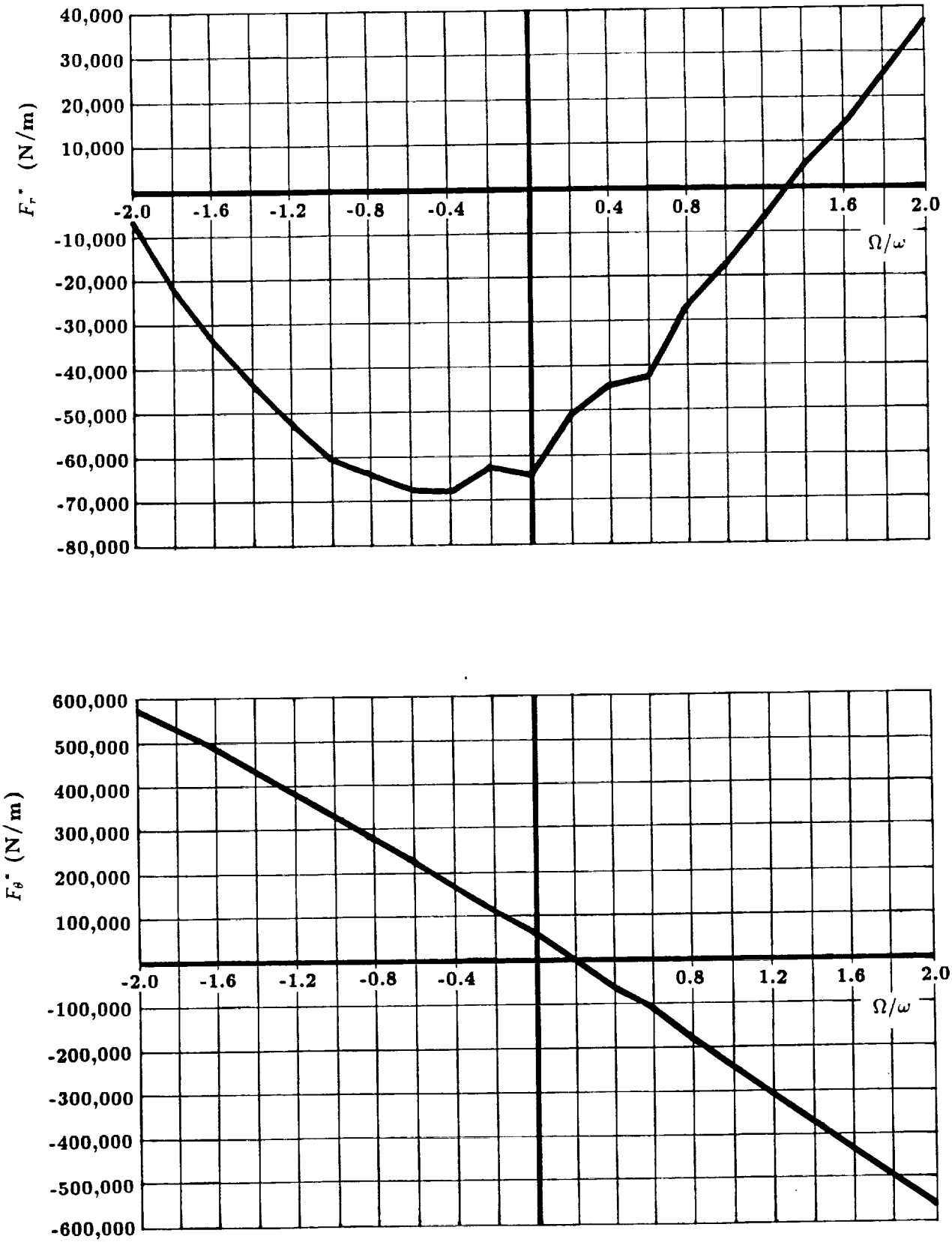


**Fig. 12 Fluid–exerted forces on the whirling rotor**

| ROTORDYNAMIC COEFFICIENTS | CURRENT PERTURBATION MODEL | EXPERIMENTAL MEASUREMENTS BY IWATSUBO AND KAWAI (1984) |
|---|---|---|
| K (N/m) | $6.60*10^4$ | $1.0*10^4$ |
| k (N/m) | $2.20*10^4$ | $0.94*10^4$ |
| C (Ns/m) | $-3.49*10^2$ | $-1.01*10^2$ |
| c (Ns/m) | $-9.19*10^2$ | $-7.75*10^2$ |

**Table 1 Comparison of the rotordynamic coefficients with experimental data for thesingle–chamber seal configuration**

| ROTORDYNAMIC COEFFICIENTS | CURRENT PERTURBATION MODEL | EXPERIMENTAL MEASUREMENTS BY IWATSUBO AND KAWAI (1984) |
|---|---|---|
| K (N/m) | $5.87*10^4$ | $2.30*10^4$ |
| k (N/m) | $6.19*10^4$ | $2.25*10^3$ |
| C (Ns/m) | $1.22*10^4$ | $1.25*10^2$ |
| c (Ns/m) | $-6.60*10^2$ | $-1.75*10^3$ |

**Table 2 Comparison of the rotordynamic coefficients with experimental data for the five–chamber seal configuration**

# Perturbed Flow Structure in an Annular Seal Due to Synchronous Whirl *

**E.A. Baskharone** **

Department of Mechanical Engineering
Texas A&M University
College Station, Texas 77843

This paper provides a thorough examination of the flow field resulting from synchronous whirl of an eccentric rotor in an annular seal under typical operating conditions. A new finite-element-based perturbation model is employed in the analysis, whereby perturbations in the flow thermophysical properties are attributed to virtual distortions in the rotor-to-housing finite element assembly. The numerical results are compared to a recent set of experimental data for a hydraulic seal with typical geometrical configurations and a synchronously whirling rotor. Despite the common perception that perturbation analyses are categorically confined to small rotor eccentricities, good agreement between the computed flow field and the experimental data is obtained for an eccentricity/clearance ratio of 50%. The agreement between the two sets of data is notably better at axial locations where the real-rig flow admission losses have diminished, and up to the seal discharge station. This attests to the accuracy of this untraditional and highly versatile perturbation model in predicting the rotordynamic characteristics of this and a wide variety of conceptually similar fluid/rotor interaction problems.

## Nomenclature

$c$ = nominal seal clearance

$d$ = rotor diameter

$e$ = eccentricity ratio $(\epsilon/c)$

* This research was funded by NASA-Marshall Space Flight Center (Huntsville, Alabama), Contract No. NAS8-37821, technical monitor: James Cannon.

** Associate Professor, Mem. ASME.

PAPER# 3

A Paper Entitled:

# Perturbed Flow Structure in an Annular Seal Due to Synchronous Whirl

(currently under review for publication in the ASME J. of Fluids Engineering)

$F_r^*$ = radial component of the rotor force perturbation

$F_\theta^*$ =tangential component of the rotor force perturbation

$L$ = seal length

$p$ = static pressure

$p_{in}$ = seal inlet pressure

$Re$ = Reynolds number = $2cV_{in}/\nu$

$r_i$ = rotor radius

$Ta$ = Taylor number = $\frac{cU_i}{\nu}\sqrt{\frac{2c}{d}}$

$U_i$ = rotor surface velocity = $\omega r_i$

$V_{in}$ = seal inlet through–flow velocity

$V_r$ = radial velocity component

$V_z$ = axial velocity component

$V_\theta$ = tangential velocity component

$z$ = distance along the seal axis

$\epsilon$ = rotor eccentricity

$\nu$ = kinematic viscosity coefficient

$\rho$ = fluid density

$\Omega$ = whirl frequency

$\omega$ = rotor spinning speed

$()^*$ implies the operator $\frac{\partial()}{\partial\epsilon}$

## Introduction

An unstable operation mode of annular seals is known as cylindrical whirl (Fig. 1), in which the rotor axis precesses around the housing centerline at a finite frequency ($\Omega$). Of the possible vibration mechanisms in this case is synchronous whirl, where the whirl frequency is identical to the rotor speed, and is primarily caused by mass imbalance. In high speed pump applications, the hydrodynamic forces associated with the rotor whirl can be a major contributor to the system stability, and may indeed lead to destructive consequences.

Existing computational tools for predicting the fluid/rotor interaction forces vary in complexity from the simple and widely used bulk–flow model (Childs, 1983) to more detailed finite–difference analyses (e.g. Dietzen et al., 1987, and Tam et al., 1988). These have progressively embraced more of the flow details in the rotor–to–housing passage but, nevertheless, shared a rather disputed simplification that perturbations in the flow thermophysical properties assume a single–harmonic type of circumferential variation. While such a simplification is, for all practical purposes, applicable to the simple annular seal problem (Baskharone and Hensel, 1991b), it is unlikely that the same would hold true for secondary turbomachinery passages which, due to their complex geometry, give rise to flow separation and recirculation even under the unperturbed (centered–rotor) operation mode.

The current study is an extension to a recent investigation (Baskharone and Hensel, 1991a), in which an unconventional perturbation approach to the general fluid–induced vibration problem was devised. The perturbation equations, under the new strategy, were deduced from the flow–governing equations in their discrete finite–element form, rather than the differential form as is traditionally the case. As a result, limitations on the circumferential perturbation pattern and/or the rotor–excitation degrees of freedom, were totally alleviated. The new perturbation model was utilized in computing the rotordynamic coefficients associated with cylindrical and conical rotor

whirl [Baskharone and Hensel (1991b) & (1991c)], as well as a compound rotor excitation that is composed of the two whirling modes (Baskharone and Hensel, 1991d).

Validation of the new perturbation model has so far been focused on verifying the results in a "macroscopic" sense, with the net integrated rotor forces, and the corresponding rotordynamic coefficients being the only variables under examination. In this paper, however, fine details of the perturbed rotor–to–housing flow field are rigorously verified. The intention here is to provide a better understanding of the source of rotordynamic forces which, in turn, should serve the design process itself. The current study was first and foremost motivated by the recent availability of detailed LDA flow measurements in a typical annular seal with a synchronously whirling rotor (Morrison et al., 1992). The outcome of this experimental study is utilized here for the purpose of comparison.

The seal geometry and operating conditions in the current study are identical to those of Morrison et al. (1992). With a length of 37.3 mm, a rotor diameter of 164.1 mm, and a nominal clearance of 1.27 mm, this seal was tested at a rotor speed of 3600 rpm using water as the working medium. These variables gave rise to a Reynolds number (Re) of 24,000 and a Taylor number (Ta) of 6,600. At all times, the rotor whirl frequency was identical to the spinning speed, and the eccentricity ratio ($\epsilon/c$) was fixed at 50 % in the test rig.

## Computational Development.

**Centered–Rotor Flow Field.** The perturbation procedure is initiated by computing this "zeroth–order" flow field, which is clearly axisymmetric. Details of the flow–governing equations, turbulence closure, and finite–element formulation of this relatively simple problem were all discussed by Baskharone and Hensel (1991b), where two sample cases (including the seal under consideration here) were presented. Comparison of the through–flow and swirl velocity profiles in

the rotor–to–housing passage with the experimental data previously reported by Morrison et al. (1991), was also presented, and the agreement between the two sets of data was encouraging.

**Perturbation Analysis.** The centered–rotor flow solution, referenced above, was used in the current study as input to the perturbation analysis phase of the computational procedure. Devised by Baskharone and Hensel (1991a), the perturbation model here is based on what was generically termed the "virtually" deformable finite element concept, where the perturbed flow equations emerge from expansion of the finite–element equations in terms of the rotor eccentricity $\epsilon$. Since no circumferential pattern is pre–imposed on the perturbations of the flow properties, the problem at this point shifts to the fully three–dimensional type, as the rotor eccentricity destroys the flow axisymmetry (Fig. 2). Simultaneously, the flow problem is cast in a rotating–translating frame of reference, which is attached to the whirling rotor at all times (Fig. 2) in order to eliminate the time dependency of the flow field in this case.

**Grid Dependency.** As would naturally be anticipated, the perturbed flow resolution is dependent on the grid resolution which, as the domain three–dimensionality prevails, translates into the number of computational stations in the circumferential direction (Fig. 2). Investigation of this dependency was carried out by varying this number and computing the fluid–exerted forces on the rotor each time. Results of this preliminary step are shown in Fig. 3, where the fluid force components $F_r^*$ and $F_\theta^*$ are obtained by integrating the rotor–surface pressure forces, upon resolution in the radial and tangential directions, over all of the contributing finite element boundaries.

The force trends in Fig. 3 suggest that the radial force is more sensitive to the tangential grid resolution by comparison. The Figure also shows that changes in the force magnitudes becomes acceptably small for a tangential computational–station count that is in excess of 11. In the current

study, this parameter was selected to be 13, as a compromise between a desirably high resolution of the flow properties in the circumferential direction, on one hand, and the CPU time consumption, on the other.

## Results and Discussion

Examples of the "raw" results of the current study are shown in Fig. 4 for the seal middle cross section, as a representative axial location. These are contours of the non–dimensionalized perturbations in the velocity components; namely $cV_z^*/V_{in}$ , $cV_r^*/V_{in}$ and $cV_\theta^*/\omega r_i$, where:

$V_{in}$ is the seal–inlet average through–flow velocity

$\omega$ is the rotor spinning speed

$r_i$ is the rotor radius

$c$ is the seal nominal clearance

with the astrisk implying the operator $\frac{\partial}{\partial \epsilon}$. In this, as well as all remaining Figures, the whirl frequency $\Omega$ is identical to the rotor speed $\omega$, giving rise to the case of a synchronous whirl investigated by Morrison et al. (1992). There is, however, no valid comparison between the results in Fig. 4 and Morrison's flow measurements, since the latter is a combination of the velocity perturbations and the unperturbed (centered–rotor) velocity field.

Examination of Fig. 4 reveals that the maximum perturbation of the axial velocity component occurs in the vicinity of the rotor "pressure" side (where the clearance is smaller than the nominal value), and at a tangential location that lags the minimum–clearance position, by reference to the whirl direction. The radial velocity perturbations in this Figure are clearly smaller than those of the axial velocity, and attains its maximum value near the rotor pressure side as well. The difference, however, is that the the radial component peaks ahead of the minimum–clearance position in the

whirl direction. As for the tangential velocity perturbation in Fig. 3, the peak value appears closer to the housing, and on the "suction" side relative to the rotor.

Figure 5 shows contours of the non–dimensionalized pressure perturbations $(p^{\sim}c/\rho V_{in}{}^2)$ , as well as those of the combined (centered–rotor and eccentricity–related) pressure values in the annulus at the middle of the seal length. The combined pressure values in this Figure correspond to an eccentricity ratio $(\epsilon/c)$ of 50% , and are non–dimensionalized using the seal–inlet static pressure $(p_{in})$. As expected, the peak values, in each plot, occurs on the rotor pressure side, and not at the minimum clearance position as may be intuitively anticipated. Comparison of this observation, as well as those cited above in connection with the velocity perturbations, with the flow measurements by Morrison et al. (1992) was not possible, as the latter involved only the "net" velocity field in the whirling–rotor operation mode, with no pressure measurements whatsoever.

A one–to–one comparison with Morrison's experimental data are presented in Figs. 6 through 10. In these Figures, the velocity component perturbations, corresponding to a rotor eccentricity ratio of 50%, are superimposed on the centered–rotor magnitudes. In assessing the numerical results in these Figures, it was both important as well as interesting to verify a fact that was solidly stated by Morrison et al., that the maximum through–flow velocity magnitude occurs on the pressure side of the rotor, over the early seal sections, but then moves towards the suction side as the flow progresses to the seal downstream sections. Comparison of the computed velocity contours in Figs. 6 through 10 reveals that the numerical results are indeed in agreement with Morrison's observation

In interpreting the computed velocity components (e.g. Fig. 10), it may seem that the larger magnitude of the tangential velocity component "$V_\theta$" in the greater–clearance region is inconsistent with the principle of mass conservation. However, such observation would be valid should the problem at hand be of of such category as that where the axial mass flux is zero (e.g. the case

where the flow is simply swirling beween two parallel endwalls, with no mass flux in the axial direction). The fact is that any valid control volume (in the current problem), to which the $V_\theta$–related mass flux is a contributor, has to have an axial extension between two cross–flow planes. In this case, the mass flux across these two planes has to also be taken into account in applying the continuity equation. With this in mind, and by reference to Figs. 8&10, let us (for instance) consider the left–hand–side half of the seal cross section, between the $z/L = 0.77$ and $z/L = 0.99$ cross sections, as a control volume. As can be seen from the $V_z$ distribution over the left–hand–side halves of these two sections, neither the $V_z$ contours nor the average $V_z$ values are identical. The point can, therefore, be qualitatively made that the net mass flux due to what may appear as an invalid $V_\theta$ distribution over the left–hand–side–halves of the annulus at the two cross sections, is balnced by that due to the The change in the $V_z$–related flux between the two axial locations.

It is important, in comparing the numerical and experimental sets of data, to point out that early sections of the seal (perhaps up to the mid–seal location) are those which no significant agreement would be anticipated. This is largely due to the flow admission losses which would prevail in the actual test rig, whereas the computational model treats this early seal segment as systematically, in the sense of turbulence closure and near–wall analysis, as does the entire seal. This is primarily why the velocity contours become more and more in agreement with the experimental data as the seal exit station is approached (e.g. Figs. 9 and 10). This, in particular, includes the tangential shift of the maximum axial–velocity position from a tangential location in the pressure (small clearance) region, gradually towards the suction side (Figs. 8 through 10) in a manner that is consistent with the flow measurements in these Figures. In fact, one would even go further, in reviewing the flow measurements in Figs. 6 through 10, indicating that the measurements themselves do not exhibit a characteristically similar axial–velocity pattern until the 77% seal–length section is reached.

An interesting phenomenon, which is confirmed both by the numerical results and the flow measurements, is that of flow separation and recirculation near the seal exit station. This, by reference to Figs. 9 and 10, takes place on the rotor suction side, and is more pronounced at the tangential location marked "s" in these two Figures. It is also in Figs. 9 and 10 that the numerical results yield shapes and magnitudes of the velocity contours which are very much consistent with the flow measurements.

Another flow structure, which is equally interesting, involves the tangential velocity distribution and pertains, in particular, to the seal sections at 49% and 77% of the seal length (Figs. 7 and 8). It is seen that there exists a region of reversed tangential velocity in each of these two sections near the housing at the minimum–clearance location. This implies local in–plane flow separation and recirculation in this region. Such flow behavior was apparently suspected (but not confirmed) by Morrison et al. (1992), who stated that: "if a tangential recirculation zone exists, it must be between the stator (referred to as the housing in this paper) and the first radial grid line."

Referring to the circumferential velocity contours in Figs. 8 through 10, in which the numerical and experimental results can be meaningfully compared, one can observe several characteristic differences between the two sets of data. Contrary to the numerical contours, the experimental $V_\theta$ contours feature a local and abrupt fluctuation, midway between the rotor and the housing, at the greatest clearance position. As for the tangential location where the circumferential velocity peaks, one could see (by marching in the clockwise direction) that $V_\theta$ peaks within the first quadrant in both sets of data. However, examination of the experimental contours in Figs. 8 through 10, does not reveal a fixed angular position where the peak value exists, although the angle (measured from the horizontal direction) of minimum $V_\theta$ seems to fluctuate around an average value of $32^o$. This angle, by comparison, is nearly constant in the numerical set of data, and is approximately equal to $59^o$.

Referring to the numerical and experimental results in Figs. 6 through 10, it is important to point out that the uncertainties in the two sets of data are $\pm 6\%$ and $\pm 4.7\%$, respectively. Of these, the The experimental uncertainty was cited by Morrison et al. (1992). As for the numerical results, the uncertainty was deduced from the comparison by Baskharone and Hamed (1981) between the numerical results of a confined–flow problem and the closed–form exact solution of the same problem. The rationale here is that the finite–element formulation, the discretization unit, the matrix–inversion code and the numerical precision (in both computational models) are all identical to one another.

Figure 11 shows a contour plot of the non–dimensionalized pressure perturbation; namely $(p^* c/\rho {V_{in}}^2)$, and the resultant (centered–rotor and whirl–related) magnitudes of the non–dimensionalized pressure $(p/p_{in})$ over the rotor surface. The pressure contours in this Figure are shown on the "unwrapped" rotor surface which is obtained by "splitting" the surface along the lines labeled $[a_1–b_1]$ and $[a_2–b_2]$ in Fig. 1. Due to the lack of pressure measurements in Morrison's study, no experimental verification of the results in Fig. 9 was possible. Examination of the pressure contours in this Figure reveals that the peak value occurs at a tangential location which lags the minimum–clearance position, by reference to the whirl direction. It is conceivable, and indeed likely, that the maximum pressure location is a function of the whirl direction (forward or backward) and/or the the whirl frequency ratio $(\Omega/\omega)$. For the synchronous whirl case under consideration, Fig. 9 shows that the rotor surface pressure peaks to a value of approximately 1.12 of the inlet pressure near the inlet station, and that with the streamwise loss in total pressure (due to friction) this magnitude gradually declines to approximately 0.93 of the inlet pressure at the exit station. Fig. 9 also shows that the maximum and minimum rotor–surface pressure locations hardly change their tangential location over the overwhelming majority of the seal length.

## Concluding Remarks

Since the development of the so–called "virtually" deformable finite–element concept (Baskharone and Hensel, 1991a), the validation of this new approach never went beyond the traditional "macroscopic" means of assessing the ultimate objective of the entire computational procedure; namely the final set of rotordynamic coefficients (Baskharone and Hensel, 1991b,c&d). Such a verification method is perhaps the least accurate, for it was always the global value of integrated rotor–surface pressure that was examined in reality. Recalling that the seal–clearance pressure field itself is among the least sensitive thermophysical properties, it is clear that the current comparative study is the most significant in appraising the mathematically rigorous computational model which centers around this categorically new finite–element–based concept.

The numerical results corresponding to a synchronously whirling rotor of an annular seal are consistent with the flow measurements of Morrison et al. (1992). Agreement of the two sets of results is particularly favorable over the downstream half of the seal, which is where the real–rig flow admission losses have dissipated, and characteristically similar trends of the measurements themselves take place. Contrary to the common perception that perturbation analyses are only applicable to infinitesimally small rotor eccentricities, the favorable results of this study corresponds to an eccentricity that is as high as 50% of the seal nominal clearance. Successful validation of the computational model, under such conditions, underscores the model accuracy and establishes it as perhaps the most versatile perturbation approach, of its nature, in the general area of rotordynamics today.

## Acknowledgment

This study was funded by NASA–Marshall Space Flight Center (Huntsville, Alabama), contract no. NAS8–37821, technical monitor: James Cannon.

## References


Baskharone, E. and Hamed, A., 1981,"A New Approach in Cascade Flow Analysis Using the Finite Element Method," AIAA Journal, Vol. 19, No. 1, pp. 65–71.

Baskharone, E.A. and Hensel, S.J., 1989, "A New Model for Leakage Prediction in Shrouded–Impeller Turbopumps," ASME J. of Fluids Engineering, Vol. 111, pp. 118–123.

Baskharone, E.A. and Hensel, S.J. , 1991, "A Finite–Element Perturbation Approach to Fluid/Rotor Interaction in Turbomachinery Elements. Part 1: Theory," ASME J. of Fluids Engineering, Vol. 113, No. 3, pp. 353–361.

Baskharone, E.A. and Hensel, S.J. , 1991, "A Finite–Element Perturbation Approach to Fluid/Rotor Interaction in Turbomachinery Elements. Part 2: Application," ASME J. of Fluids Engineering, Vol. 113, No. 3, pp. 362–367.

Baskharone, E.A. and Hensel, S.J. , 1991, "Moment Coefficients of Incompressible–Flow Seals with Conically Whirling Rotors," Int. J. of Mechanical Sciences, Vol. 33, No. 2, pp.151–167.

Baskharone, E.A. and Hensel, S.J. , 1991, "Interrelated Rotordynamic Effects of Cylidrical and Conical Whirl of Annular Seal Rotors," ASME J. of Tribology, Vol. 113, No. 3, pp. 470–480.

Childs, D.W. ,1983,"Finite Length Solutions for Rotordynamic Coefficients of Turbulent Annular Seals," ASME J. of Lubrication Technology, Vol. 105, pp. 437–445.

Dietzen, F.J. and Nordmann, R., 1987, "Calculating Rotordynamic Coefficients of Seals by Finite Difference Techniques," ASME J. of Tribology, Vol. 109, pp. 388–394.

Morrison, G.L., Johnson, M.C. and Tatterson, G.B., 1991, "Three–Dimensional Laser Anemometer Measurements in an Annular Seal," ASME J. of Tribology, Vol. 113, pp 421–427.

Morrison, G.L., DeOtte, R.E. and Thames, H.D, 1992, "Turbulence Measurements of High Shear Flow Fields in a Turbomachine Seal Configuration," presented at the Advanced Earth–To–Orbit Propulsion Technology Conference, Huntsville, Alabama.

Tam, L.T., Prezkwas, A.J., Muszynska, A., Hendricks, R.C., Braun, M.J. and Mullen, R.L., 1988, "Numerical and Analytical Study of Fluid Dynamic Forces in Seals and Bearings," ASME J. of Vibration, Acoustics, Stress, and Reliability in Design, Vol. 110, pp. 315–325.

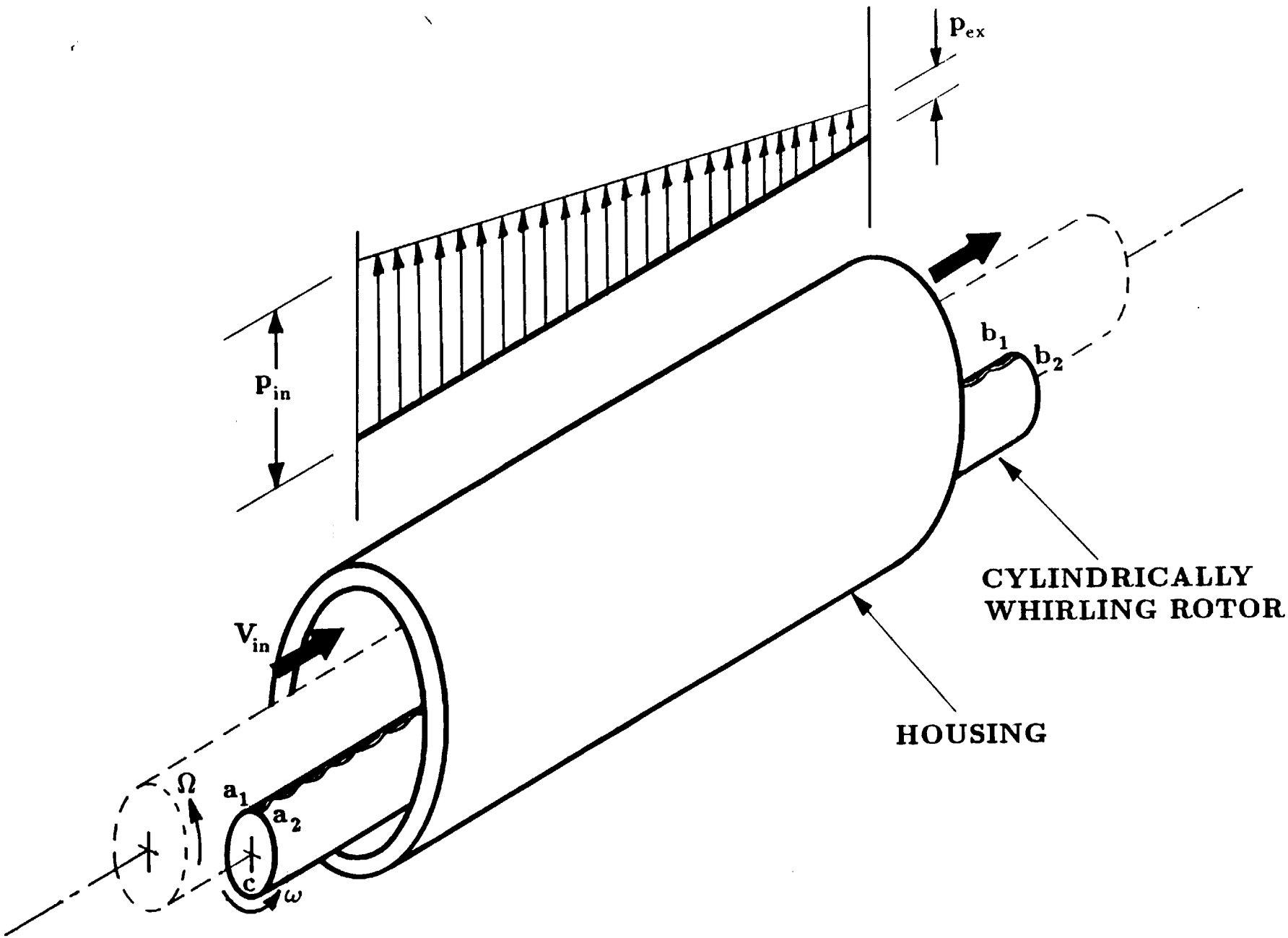


**Fig. 1 Cylindrical whirl in annular seals**

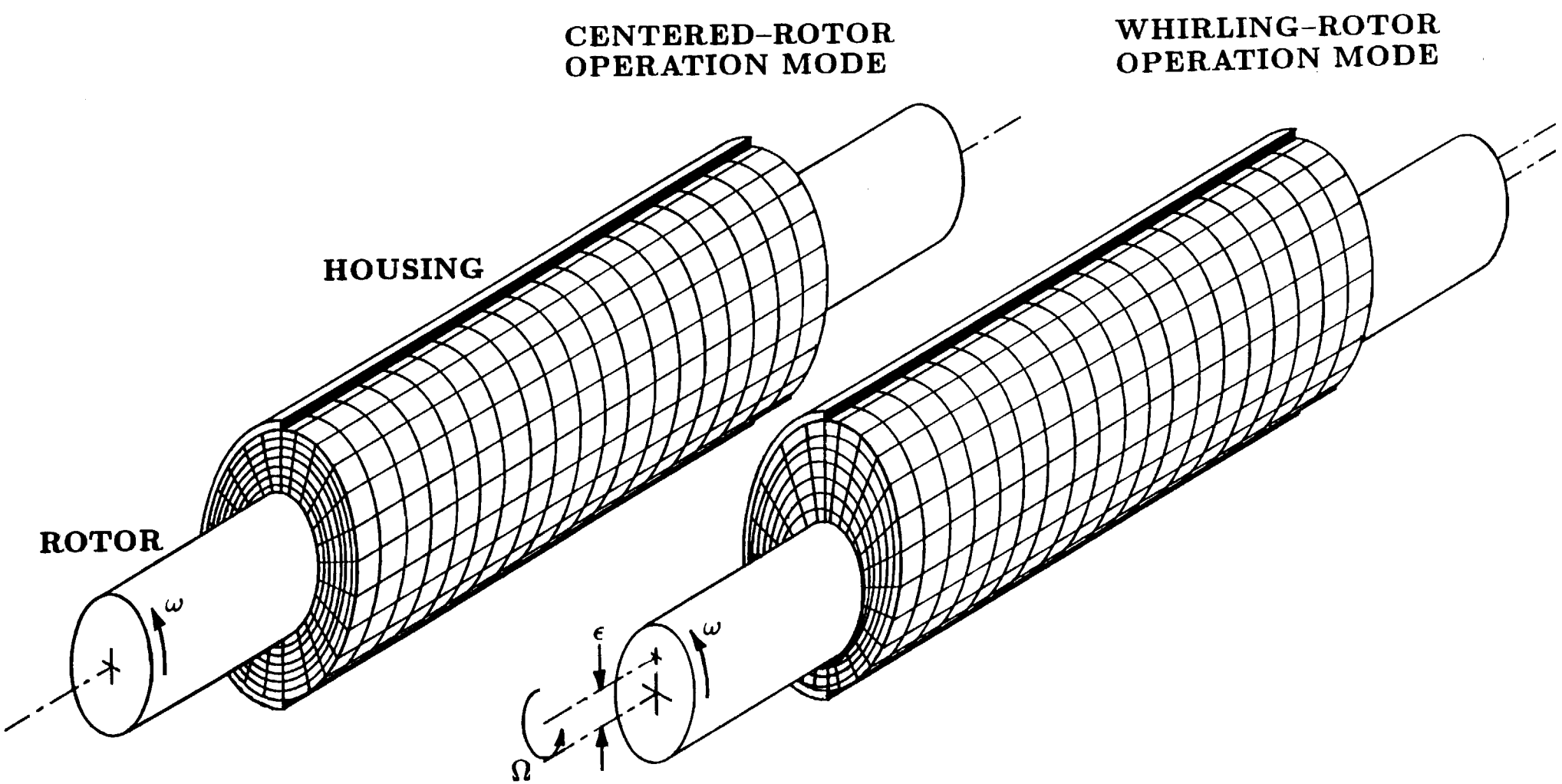


**Fig. 2 Distortion of the rotor–to–housing finite element assembly as a result of the rotor eccentricity**

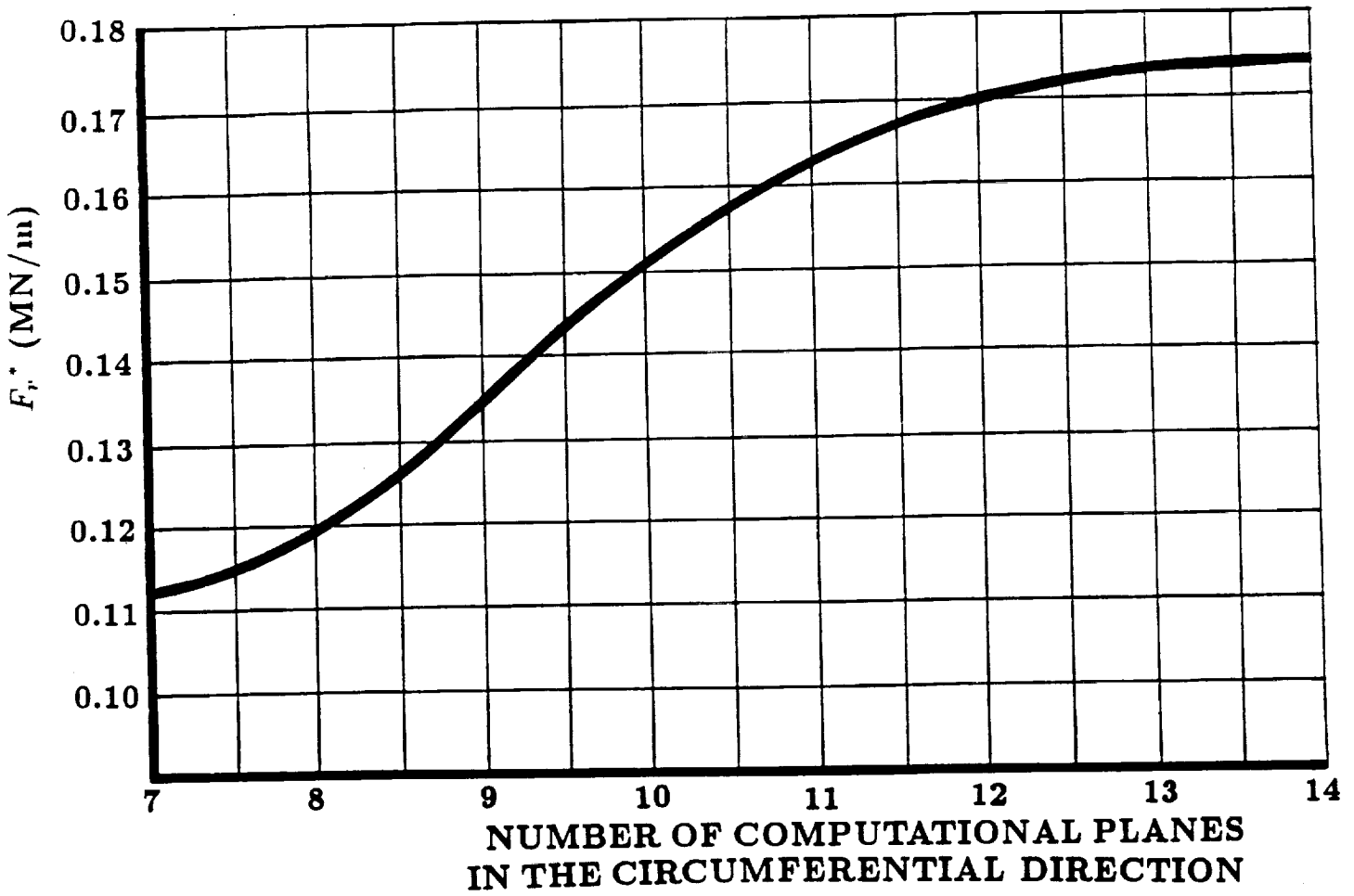


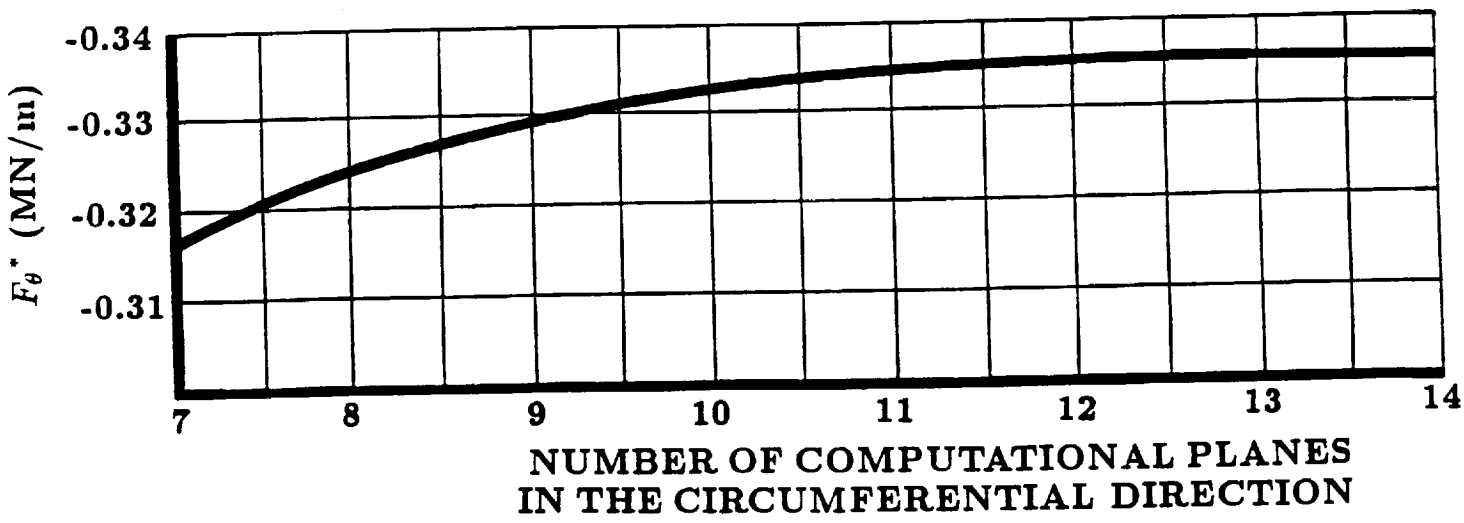


Fig. 3 Relationship between the fluid-exerted forces and the grid resolution in the tangential direction

$z/L = 0.50$

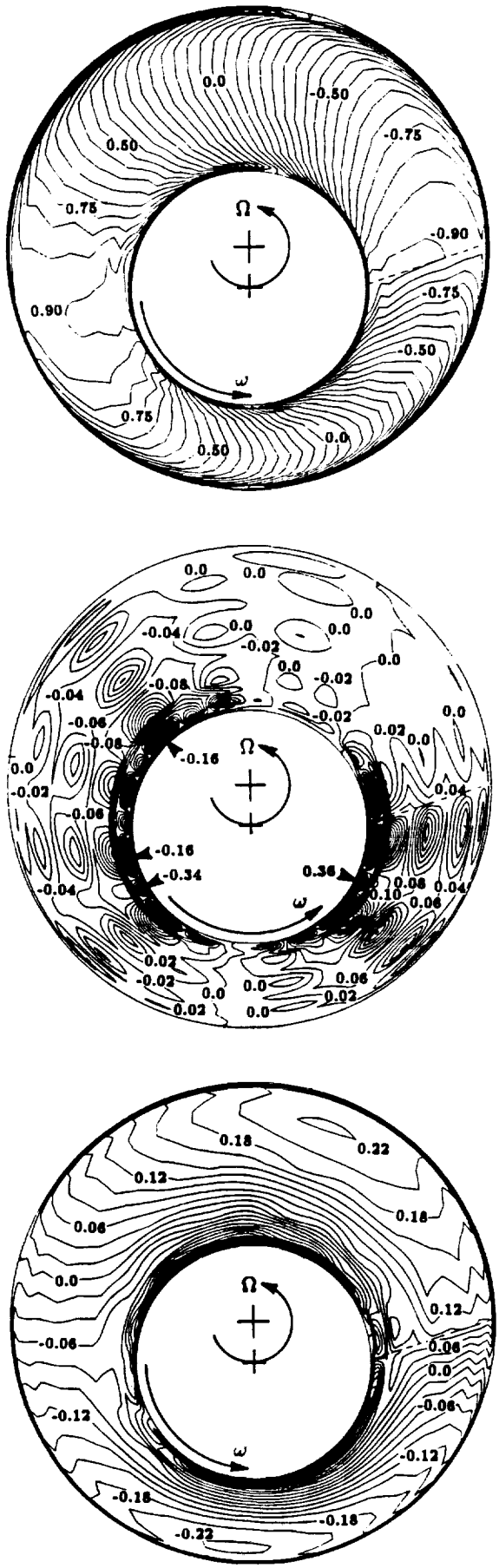


$\frac{c}{V_{in}} \frac{\partial V_z}{\partial \epsilon}$

$\frac{c}{V_{in}} \frac{\partial V_r}{\partial \epsilon}$

$\frac{c}{\omega r_i} \frac{\partial V_\theta}{\partial \epsilon}$

**Fig. 4 Contour plots of the velocity perturbations at 50% of the seal length**

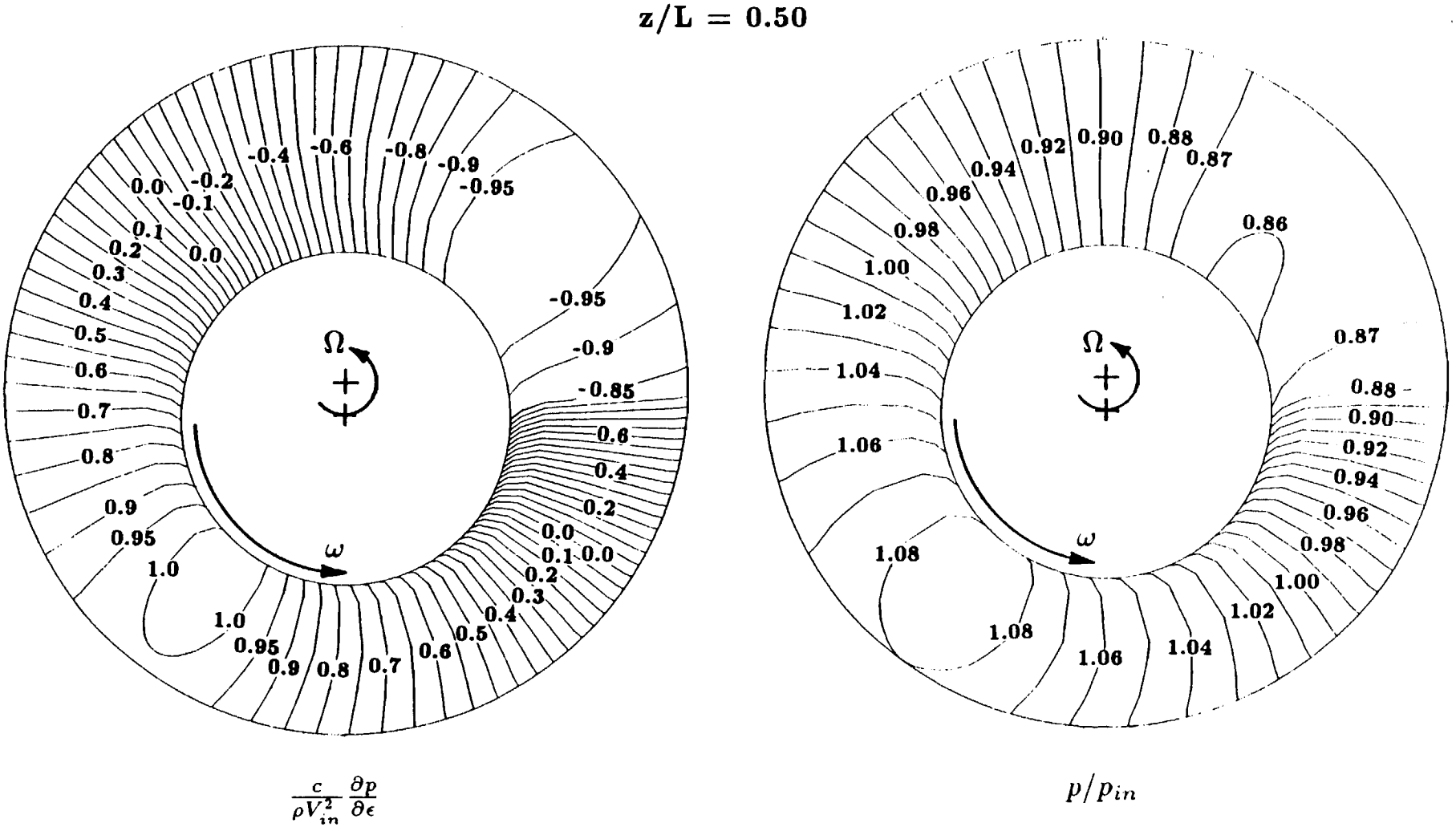


**Fig. 5 Contour plots of the pressure perturbation and the resultant pressure (for a 50% eccentricity ratio) at 50% of the seal length**

NUMERICAL RESULTS

FLOW MEASUREMENTS

$z/L = 0.22$

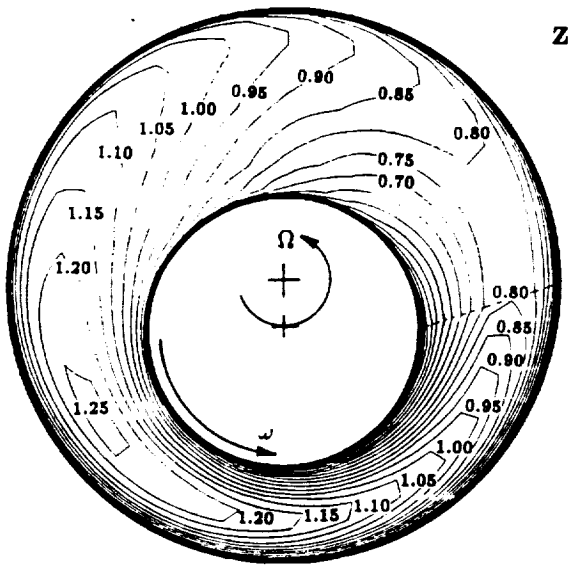


$V_z/V_{in}$

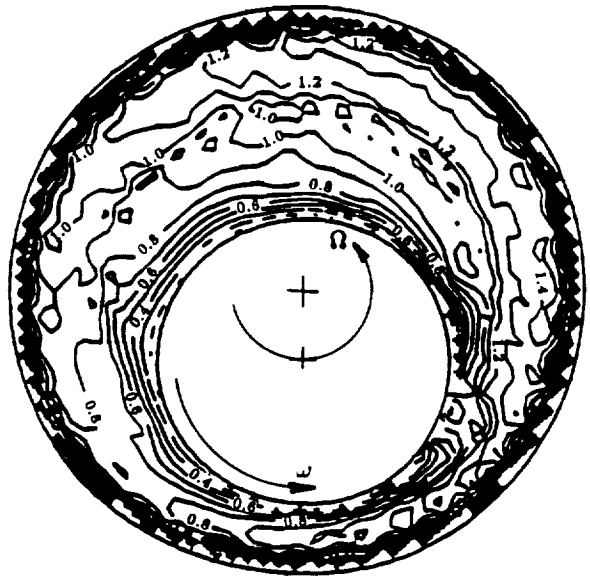


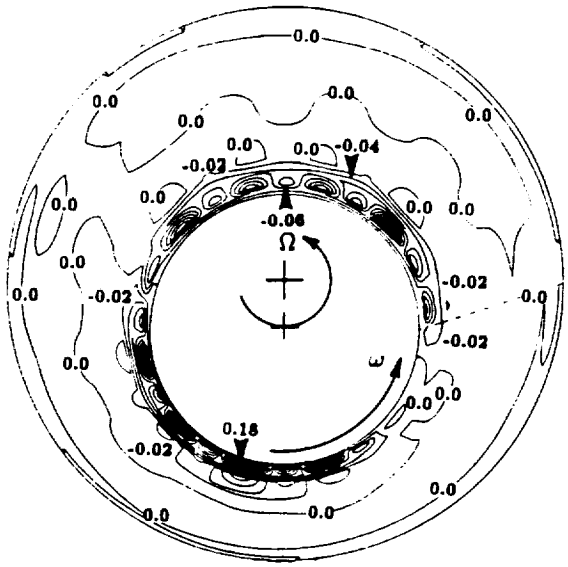


$V_r/V_{in}$

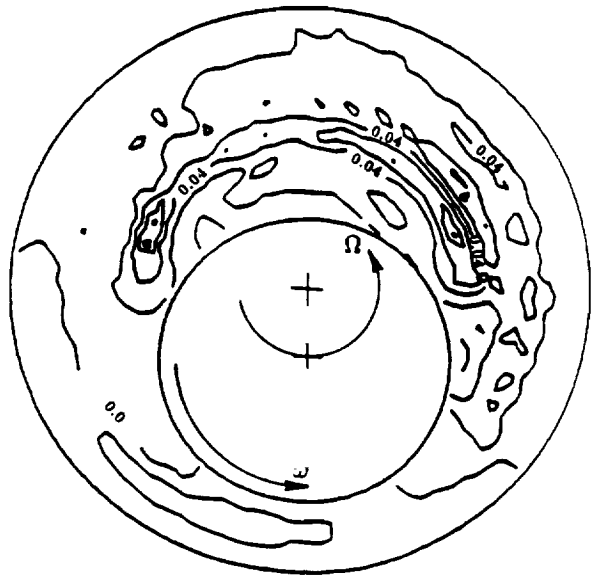


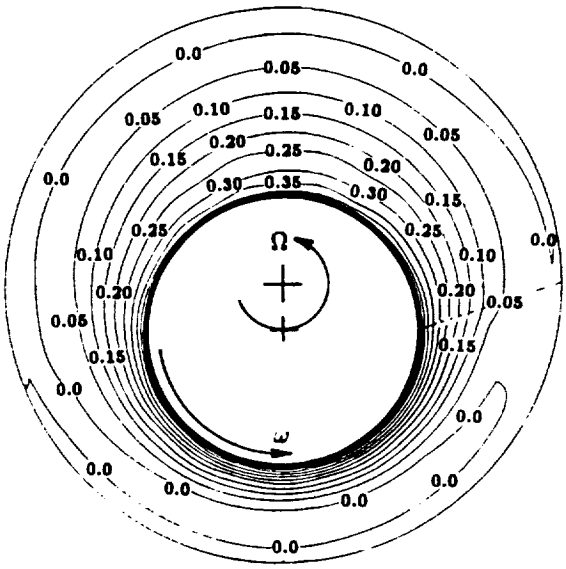


$V_\theta/(\omega r_i)$

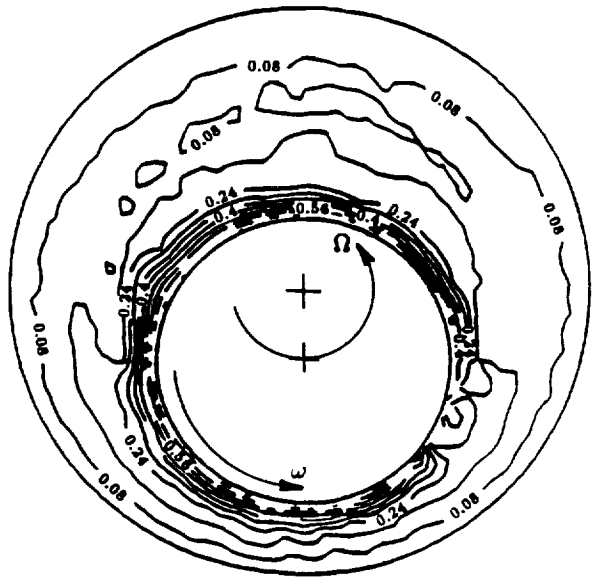


**Fig. 6 Comparison of the velocity distribution at 22% of the seal length (eccentricity ratio = 50%)**

NUMERICAL RESULTS

FLOW MEASUREMENTS

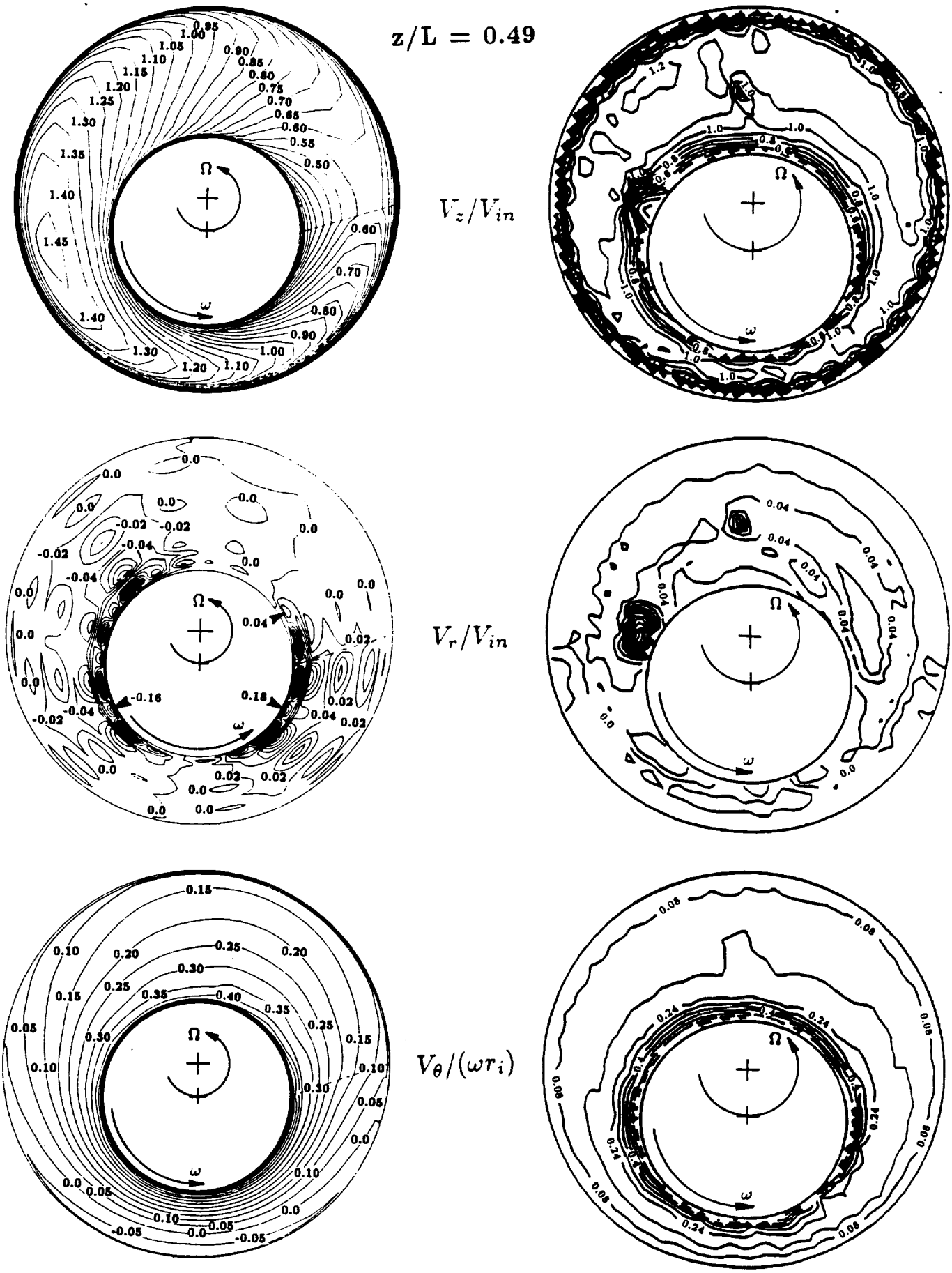


**Fig. 7 Comparison of the velocity distribution at 49% of the seal length (eccentricity ratio = 50%)**

NUMERICAL RESULTS FLOW MEASUREMENTS

$z/L = 0.77$

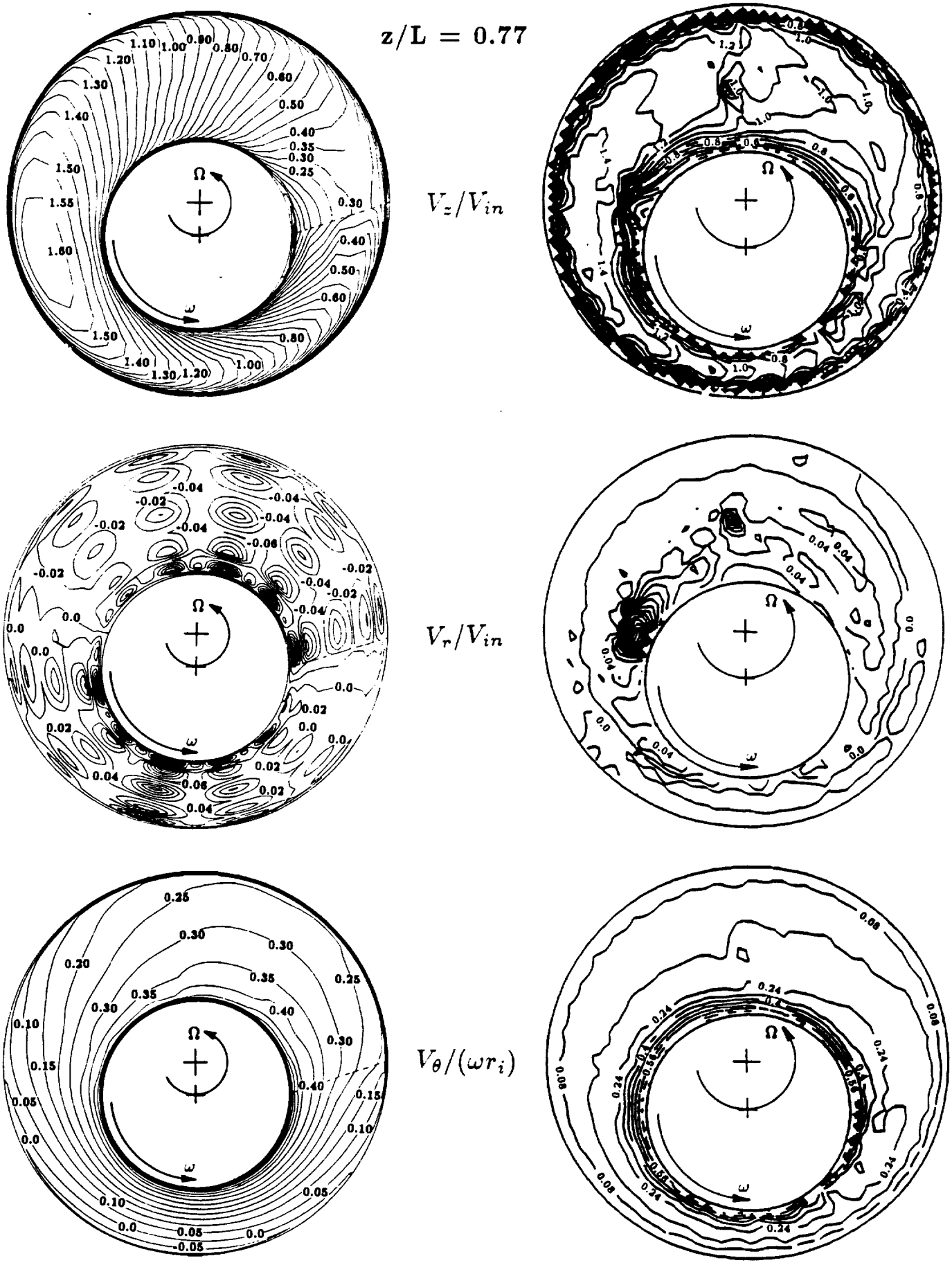


**Fig. 8 Comparison of the velocity distribution at 77% of the seal length (eccentricity ratio = 50%)**

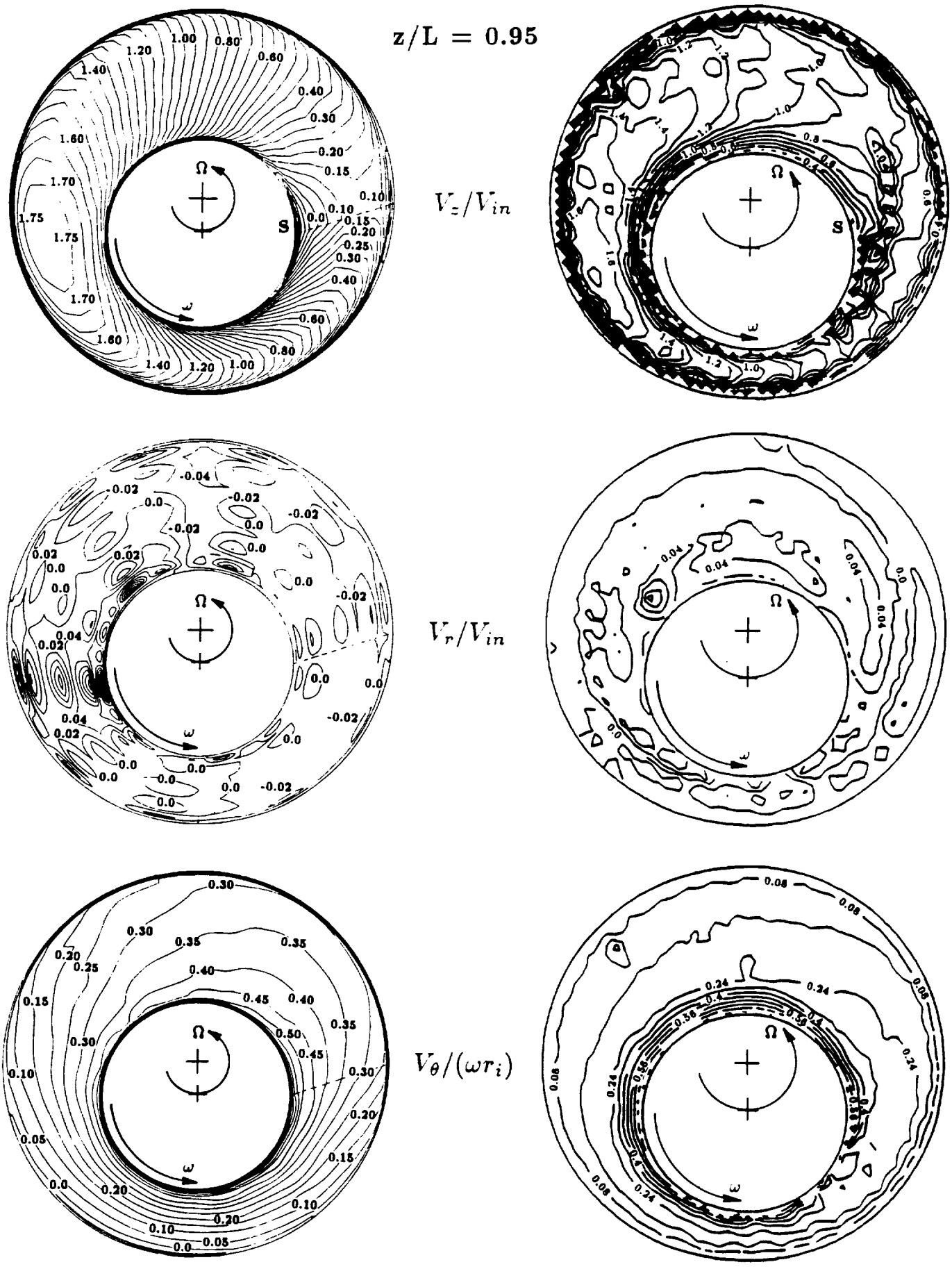


**Fig. 9 Comparison of the velocity distribution at 95% of the seal length (eccentricity ratio = 50%)**

NUMERICAL RESULTS

FLOW MEASUREMENTS

$z/L = 0.99$

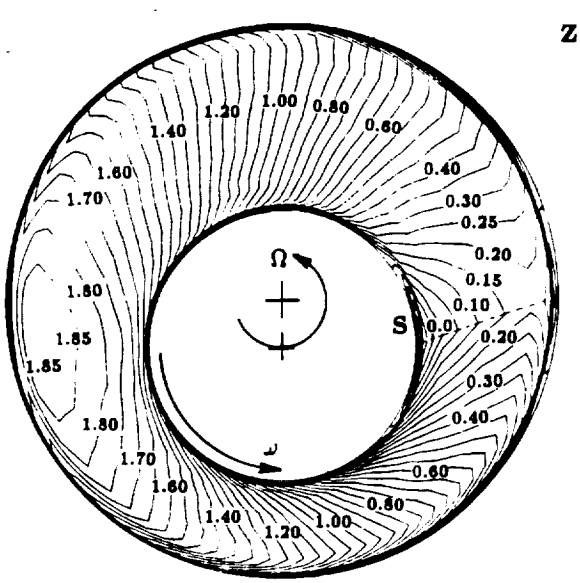


$V_z/V_{in}$

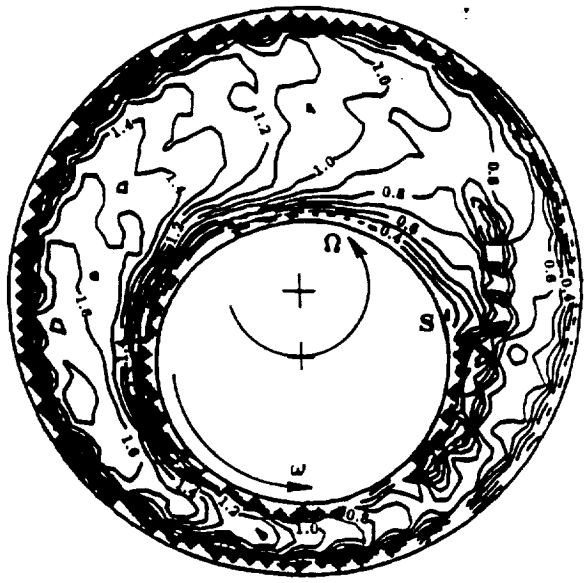


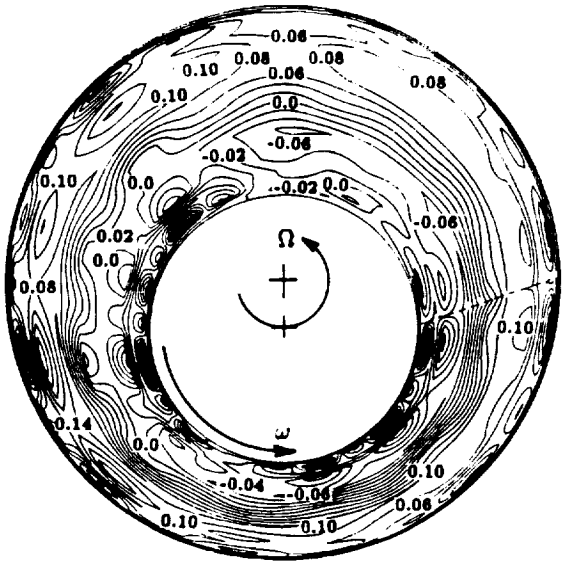


$V_r/V_{in}$

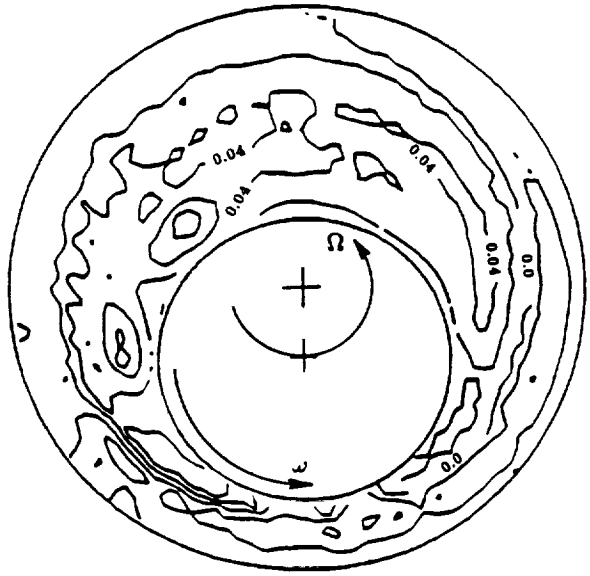


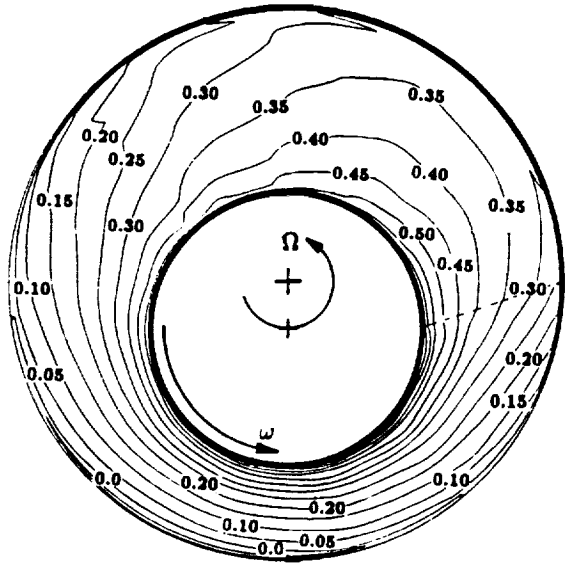


$V_\theta/(\omega r_i)$

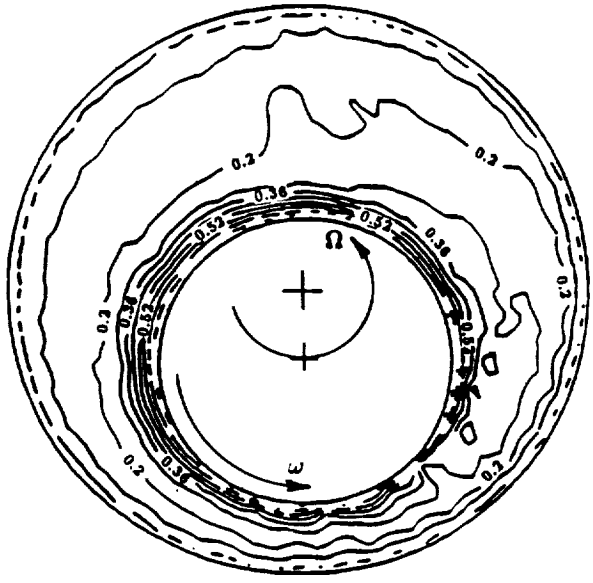


**Fig. 10 Comparison of the velocity distribution at 99% of the seal length (eccentricity ratio = 50%)**

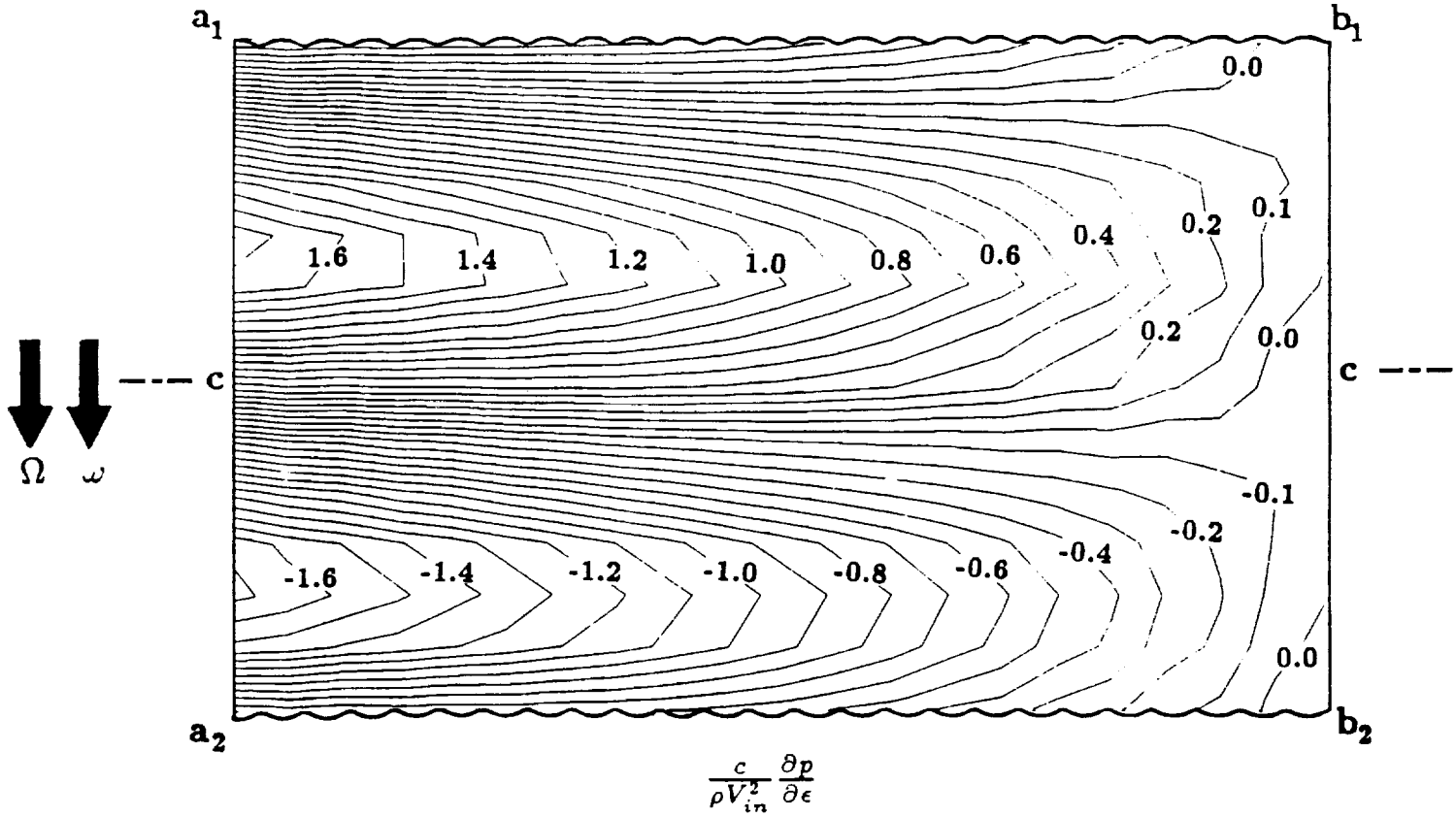


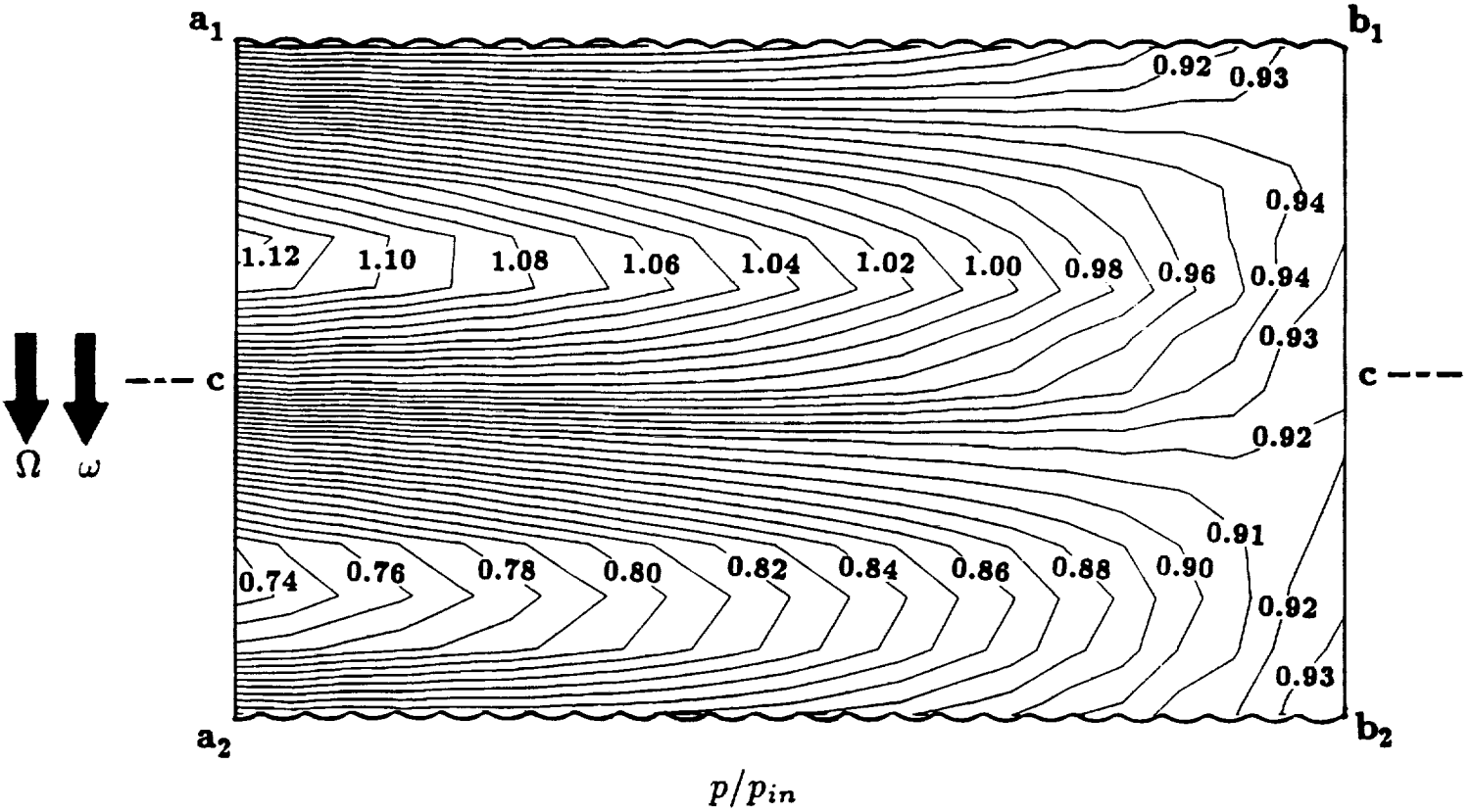


**Fig. 11 Contours of the pressure perturbation and the resultant pressure (for a 50% eccentricity ratio) over the rotor surface**